

ResearchOnline@JCU

This file is part of the following reference:

Osborn, Eric Peter (2016) *Characteristic wind actions on large flat roofed porous canopies*. Masters (Research) thesis, James Cook University.

Access to this file is available from:

<http://researchonline.jcu.edu.au/44649/>

The author has certified to JCU that they have made a reasonable effort to gain permission and acknowledge the owner of any third party copyright material included in this document. If you believe that this is not the case, please contact

*ResearchOnline@jcu.edu.au and quote
<http://researchonline.jcu.edu.au/44649/>*

JAMES COOK UNIVERSITY

**COLLEGE OF SCIENCE,
TECHNOLOGY AND ENGINEERING**

**CHARACTERISTIC WIND ACTIONS
ON LARGE FLAT ROOFED
POROUS CANOPIES**

Eric Peter Osborn

B. Eng (Civil), B.A., M.I.E.Aust

Thesis submitted to the
College of Science, Technology and Engineering
in fulfilment of the requirements for the degree of
Master of Philosophy

February 2016

Acknowledgements

I wish to acknowledge the assistance of my supervisor Associate Professor John Ginger and the staff at the Cyclone Testing Station, Don Braddick, Dennis Smith and research engineer Peter Kim. Acknowledgement is given to Dr John Holmes for his assistance in providing direction to the study and to the staff at Netpro Protection Canopies - Adrian Pradella for his construction of the Models for testing and Claude Grayling and Michael Thompson for their encouragement and sharing of their practical knowledge. I also wish to thank Michael Barbagallo for his testing of the non-porous model and Marcel Olivotto for his assistance in the experimental work and processing the large amounts of data. Finally thank you to my wife Bronwen for her patience and support during this study.

Statement on the Contribution of Others

Nature of Assistance	Contribution	Co-Contributors
Intellectual Support	Data Analysis Editorial Assistance	Michael Barbagallo Marcel Olivotto Assoc Professor John Ginger Therese Farrell
Experimental Testing	Building of Models Wind Tunnel Set Up Model Testing Fabric Porosity Testing	Adrian Pradella Don Braddick, Denis Smith Michael Barbagallo, Marcel Olivotto, Mitchell Humphreys Dr Matthew Mason

Abstract

Large porous protection canopy construction has evolved in Australia over the past 30 years from modest small orchard canopies to large canopies over essential water storages to reduce evaporation and pollution, canopies over large numbers of vehicles for car importers and exporters, and horticultural canopies of over 40 hectares in area. The canopies have proved to be an effective economical method to protect increasing numbers and types of assets from exposure to sun, hail, wind, birds and insects.

Canopy design and construction has evolved from the grass roots with initially no structural engineering design input. As the value of assets protected has increased, the request for structural engineering certification of the canopies has become common. To be able to certify the canopy's structure, the certifying engineer needs to confidently be able to predict the wind actions that may occur. In the past there has been limited structural engineering research undertaken into wind loads on porous structures. The aim of this study is to research the characteristic wind actions normal to large flat roof porous canopies and derive design pressure coefficients. Surface friction actions from wind drag across the surfaces are not researched in this thesis and remain a subject for future research.

Four scale models of a typical porous protection canopy were constructed for testing in the wind tunnel at the Cyclone Testing Station (CTS), James Cook University, Townsville. The models are of identical geometry, but each of different porosity, 0%, 19%, 38% and 58%. The Models were placed in the CTS boundary layer wind tunnel and rotated through 360° at increments of 15°. At each 15° increment, three sets of pressure readings, each for 30 seconds, were taken at a series of pressure taps located on the Model externally and internally. The pressure readings were processed by the wind tunnel transducer into non dimensional pressure coefficients and then adjusted for the boundary layer speed at the height of the Model.

The pressure coefficient results were imported into the analysis software Matlab and Excel and then plotted against the geometry of the canopy. This thesis presents these results graphically with pressure coefficients being plotted against distance. The distance is shown non dimensional as ratios of model width and length to model height.

It is evident from the external pressure results, that the introduction of porosity into the canopy's roof surface causes significant reduction in the magnitude of the wind actions acting on the roof when compared to the non-porous canopy. In contrast, the introduced porosity does not modify the magnitude of the wind actions on the walls greatly, but does alter the coefficient distribution. Internal pressure coefficients were found to decrease in magnitude across the model away from the windward edge.

To predict the resultant wind actions on the canopy surfaces, the simultaneous external and internal pressure coefficients were summed and adjusted using a gust factor in accordance with the Standard AS/NZS 1170.2. The net surface pressure coefficient was then plotted for four wind directions in increments of 15° from 0° to 45° . The results were then combined to find the peak maximum and minimum pressure coefficients for a $\pm 45^\circ$ wind direction sector orthogonal to the structure as required in AS/NZS1170.2.

It was found that the introduction of porosity to the models caused significant reduction in the magnitude of normal roof wind actions. Increasing the magnitude of the porosity caused only minor further reduction. The wind actions on the porous walls do not decrease significantly from the magnitudes of the coefficients on the equivalent non-porous walls, but are distributed differently due to the flow of the wind in and out of the canopy interior through the porous wall and roof surfaces. The derived net pressure coefficient results are summarised in tabular form and provide values for the design of large porous flat roofed canopies under wind load.

Table of Contents

Acknowledgements	2
Statement on the Contribution of Others	3
Abstract	4
List of Figures	10
1. Introduction	15
1.1 Large Protection Canopies.....	15
1.2 Aims and Objectives.....	16
2. Net Protection Canopies in Australia and Previous Research.....	17
2.1 The Development of Net Protection in Australia	17
2.2 Canopy Construction	21
2.3 Benefits of Protection Canopies	25
2.3.1 Horticulture.....	25
2.3.2 Agriculture and Aquaculture	27
2.3.3 Vehicle Protection	29
2.3.4 Water Storage Covers	29
2.3.4 Other applications.....	30
2.4 Relevant Past Research into Loads on Porous Surfaces	32
2.4.1 Wind Loads on Porous Structures (Richards and Robinson, 1999)	34
2.4.2 Design of a Low Cost Wind Resistant Shade Cloth Structure (Donnan et al, 1987).....	38
2.4.3 Integrated Structural Design Methodology for Agricultural Protecting Structures Covered with Nets (Briassoulis and Mistrionis, 2010).....	39
2.4.4 Mean Wind Loads on Porous Canopy Roofs (Letchford et al, 2000)	42
2.4.5 Wind Pressures on Permeably and Impermeably-clad (Robertson et al, 2002)	45
2.5 Review Summary	46
3. Experimental Methodology.....	49
3.1 Overview	49
3.2 The Boundary Layer Wind Tunnel.....	49
3.3 Selection of Test Model Dimensions.....	52
3.3 Models	56
3.3.1 0% Non-Porous Model –Model A.....	56
3.3.2 19% Porous Model – Model B	57
3.3.3 38% Porous Model –Model C.....	58
3.3.4 58% Porous Model - Model D.....	59
3.3.5 Determination of loss coefficient K.....	60

3.4	Testing of Internal Pressure and Combined Internal and External Pressure	64
3.5	Graphical Presentation of the Results.....	65
4.	Wind Tunnel Test Results.....	67
4.1	Model A, Zero Porosity	67
4.1.1	Model A External Pressure Coefficients for $\theta = 0^\circ$	67
4.1.2	Model A External Pressure Coefficients for $\theta = 45^\circ$	71
4.2	Model B, 19% Porosity	74
4.2.1	Model B External Pressure Coefficients for $\theta = 0^\circ$	74
4.2.2	Model B External Pressure Coefficients for $\theta = 45^\circ$	78
4.2.3	Model B Internal Pressure Coefficients.....	81
4.3	Model C, 38% Porosity	88
4.3.1	Model C External Pressure Coefficients, $\theta = 0^\circ$	88
4.3.2	Model C External Pressure Coefficients, $\theta = 45^\circ$	92
4.3.3	Model C Internal Pressure Coefficients.....	95
4.4	Model D, 58% Porosity	99
4.4.1	External Pressure Coefficients for $\theta = 0^\circ$	99
4.4.2	Model D External Pressure Coefficients for $\theta = 45^\circ$	102
4.4.3	Model D Internal Pressure Coefficients	105
4.5	Summary Comparison of Wind Tunnel Pressure results for the four Models.....	105
5.	Net Pressure Coefficients for Large Flat Roof Porous Canopies.....	110
5.1	Net Pressure Coefficient <i>C_{fig,net}</i>	110
5.2	Pressure Coefficient <i>C_{fig,net}</i> , Roof Surface R, Porous Models B, C and D	111
5.2.1	Model B, 19% Porosity	112
5.2.2	Model C, 38% Porosity	114
5.2.3	Model D, 58% Porosity	116
5.3	Review of Roof Coefficients <i>C_{fig,net}</i>	118
5.4	Pressure Coefficient <i>C_{fig,net}</i> , Porous Models B, C and D, Walls W1,W2,W3 and W4	119
5.4.1	Pressure Coefficient <i>C_{fig,net}</i> , Model B, Walls W1,W2,W3 and W4.....	119
5.4.2	Net Pressure Coefficient <i>C_{fig,net}</i> , Model C, Walls W1,W2,W3 and W4	121
5.4.3	Net Pressure Coefficient <i>C_{fig,net}</i> , Model D, Walls W1,W2,W3 and W4	123
5.5.	Comparison of net peak pressure wall coefficient.....	125
6.	Conclusions.....	128
7.	References.....	130
	Appendix A.....	131

Appendix A

A.1 Roof Pressure Coefficient Contour Plots Model B (19% porosity)	132
A1.1 Model B, Roof R, <i>C_{peak.net}/Gu₂</i> Maximum, 0°, 15°, 30°, 45° Wind Directions.....	132
A1.2 Roof Pressure Coefficient Contour Plots	134
Model B, Roof R, <i>C_{peak.net}/Gu₂</i> Minimum, 0°, 15°, 30°, 45° Wind Directions	134
A2. Roof Pressure Coefficient Contour Plots, Model C (38% porous)	136
A.2.1 Model C Roof R, <i>C_{peak.net}/Gu₂</i> Maximum, 0°, 15°, 30°, 45° Wind Directions.....	136
A.2.2 Roof Pressure Coefficient Contour Plots	138
Model C roof, <i>C_{peak.net}/Gu₂</i> Minimum, 0°, 15°, 30°, 45° Wind Directions	138
A3. Roof Pressure Coefficient Contour Plots, Model D (58% porous)	140
A3.1 Model D roof, <i>C_{peak.net}/Gu₂</i> Maximum, 0°, 15°, 30°, 45° Wind Directions	140
A3.2 Roof Pressure Coefficient Contour Plots	142
Model D roof, <i>C_{peak.net}/Gu₂</i> Minimum, 0°, 15°, 30°, 45° Wind Directions	142
A4 Wall Pressure Coefficient Plots, Model B	144
A4.1 Model B. (19% Porous).....	144
A4.2 Model B Side Walls W2, <i>C_{peak.net}/Gu₂</i> , 0°, 15°, 30°, 45° Wind Directions.....	146
A4.3 Model B Wall W3, <i>C_{peak.net}/Gu₂</i> , $\theta = 0°, 15°, 30°$	148
A4.4 Model B Wall W4, <i>C_{p,n}</i> , $\theta = 15°, 30°$	149
A5 Model C, (38° , Porous)	150
A5.1 Windward Wall W1, <i>C_{peak.net}/Gu</i> , $2\theta = 0°, 15°, 30°, 45°$	150
A5.2 Side Wall W2, <i>C_{peak.net}/Gu₂</i> , $\theta = 0°, 15°, 30°, 45°$	152
A5.3 Leeward Wall W3, <i>C_{peak.net}/Gu₂</i> , $\theta = 0°, 15°, 30°$	154
A5.4 Side Wall W4, <i>C_{peak.net}/Gu₂</i> , $\theta = 15°, 30°$	156
A6 Model D 58% Porous.....	157
A6.1 Windward Wall W1, <i>C_{peak.net}/Gu₂</i> , $\theta = 0°, 15°, 30°, 45°$	157
A6.2 Side Wall W2, <i>C_{peak.net}/Gu₂</i> , $\theta = 0°, 15°, 30°, 45°$	159
A6.3 Leeward Wall W3, <i>C_{peak.net}/Gu₂</i> , $\theta = 0°, 15°, 30°$	161
A6.4 Side Wall W4, <i>C_{peak.net}/Gu₂</i> , $\theta = 15°, 30°$	163

List of Tables

Table 2.1 - Measured Wind loads, Force Coefficients (Donnan et al, 1987).....	39
Table 2.2 - Net Pressure Coefficients for an Empty Free Standing Pitched Canopy Roof with Pitch Slope 20° (Briassoulis and Mistriotis, 2010)	40
Table 2.3 - Net Pressure Coefficients for a Fully Blocked Free Standing Canopy Roof with Pitch Slope = 20° (Briassoulis and Mistriotis, 2010)	40
Table 2.4 - Aerodynamic Coefficients for a Flat-roof House (Briassoulis and Mistriotis, 2010)41	
Table 3.1 Loss Coefficients K.....	62
Table 4.1 External Peak and Mean Roof Pressure Coefficients, $\theta = 0^\circ$	105
Table 4.2 Distribution of External Minimum Pressure Coefficients, $\theta = 0^\circ$	106
Table 4.3 External Windward Wall W1 Peak Pressure Coefficients, $\theta = 0^\circ$	106
Table 4.4 External Leeward Wall W3 Peak Pressure Coefficients, $\theta = 0^\circ$	107
Table 4.5 External Side Wall W2 Pressure Coefficients, $\theta = 0^\circ$	107
Table 4.6 External Windward Wall Pressure Coefficients, $\theta = 45^\circ$	107
Table 4.7 External Leeward Wall Pressure Coefficients, $\theta = 45^\circ$	108
Table 4.8 Peak Internal Pressure Coefficients for Porous Models B, C and D.....	108
Table 5.1 Summary of Resultant Pressure Coefficients, Roof R, 19% Porosity	113
Table 5.2 Summary of Resultant Pressure Coefficients, Model C, Roof R, 38% Porosity	115
Table 5.3 Summary of Net Pressure Coefficients, Roof R, 58% Porosity.....	117
Table 5.4 Summary of Roof R Net Pressure Coefficient, <i>C_{fig,net}</i> , $\theta = 0^\circ \pm 45^\circ$	118
Table 5.5 Summary of Wall Net Pressure Coefficient, Wall W1, <i>C_{fig,net}</i> , $\theta = 0^\circ \pm 45^\circ$.	125
Table 5.6 Summary of Wall Net Pressure Coefficient, Side Walls W2, W4, <i>C_{fig,net}</i> , $\theta = 0^\circ \pm 45^\circ$	126
Table 5.7 Summary of Wall Net Pressure Coefficient, Leeward Wall W3, <i>C_{fig,net}</i> , $\theta = 0^\circ \pm 45^\circ$	127

List of Figures

Figure 1.1 Large Free Spanning Canopy over Orbost Clear Water Storage.....	15
Figure 2.1 Canopies for Stone Fruit Orchards at Childers, Queensland.....	17
Figure 2.2 Canopy for Mango Orchard in Northern Queensland.....	19
Figure 2.3 Dam Cover Construction at The Summit, Queensland.....	19
Figure 2.4 Vehicle Protection Canopy.....	20
Figure 2.5 Flat Roofed Canopy Structure Design.....	23
Figure 2.6 Canopy Net Sagging to the Ground with Accumulated Hail between Tree Rows....	24
Figure 2.7 Pitched Hail Protection Canopy for Vehicles.....	24
Figure 2.8 Orchard Canopy.....	25
Figure 2.9 Vegetable Seedling Canopy.....	26
Figure 2.10 Hail Protection Canopy over Seedlings.....	27
Figure 2.11 Shade Covers to Feedlot Cattle Pens.....	28
Figure 2.12 Net Canopy over Fish Breeding Facility.....	28
Figure 2.13 Canopy over Abalone Farm Facilities.....	28
Figure 2.13 Pitched Vehicle Storage Hail Canopy.....	29
Figure 2.14 Clear-span Protection Canopy over Clear Water Storage.....	30
Figure 2.15 Irrigation Channel Cover.....	30
Figure 2.16 Canopy for Waste disposal Facility.....	31
Figure 2.17 Separation of Fluid at a Solid Body's Leading edge.....	33
Figure 2.18 Fluid Flow through and around Porous Body.....	33
Figure 2.19 Loss Coefficients for Round Wire Screens (Richards and Robinson, 1999).....	35
Figure 2.20 Wind Tunnel Arrangement for Testing of Porous Screens.....	36
Figure 2.21 Drag Coefficients for windbreak fences.....	37
(Wind perpendicular to the fence surface, $\theta = 0^\circ$) (Richards and Robinson, 1999).....	37
Figure 2.22 Model Testing Arrangement.....	38
Figure 2.23 Model Configurations for Testing by Letchford et al.....	43
Figure 2.24 - Drag and Lift Coefficients for Three Pitches of a Gable Roof at 0 Degrees Azimuth (Letchford et al, 2000).....	43
Figure 2.25 - Drag and Lift Coefficients for Three Pitches of a Mono-slope Roof at 0° Azimuth (Letchford et al, 2000).....	44
Figure 2.26 - Cross Section of Model of Flat Roofed Shade Structure Tested by Robertson et al.....	45
Figure 2.27 – Mean Pressure Coefficients on the walls and Roof of a Flat Roof Shade House.	46
Figure 2.28 Typical Roof Support Member Loads for Porous and Non- Porous Roof Members	48

Figure 3.1 Turbulence Intensity Profile	50
Figure 3.2 Wind Tunnel Mean Velocity Profile	50
Figure 3.3 Full Scale Large Flat Roofed Porous Canopy used for Scale Modelling	53
Figure 3.4 Scale Model Dimensions	54
Figure 3.5 Tapping Points and Identification Grid	55
Figure 3.6 Connection of Plastic Tubes to Tapping Tubes Model on Turntable in Wind Tunnel	56
Figure 3.7 - View of Underside of Model A with Tapping Tubes.....	57
Figure 3.8 19% Porous Perforated Sheet for Model B.....	57
Figure 3.9 38% Porous Model C using a fine Brass Mesh	58
Figure 3.10 Underside of Model C with Tapping Inserts and Support Trusses.....	58
Figure 3.11 Perforated Sheet with 58% open area Model D.....	59
Figure 3.12 Model D on Turntable	60
Figure 3.13 Close up of Model D on turntable	60
Figure 3.14 Loss factor K and mean upstream speed U_s	63
Figure 3.15 Pressure loss coefficient K as a function of Reynolds number (Letchford et al, 2000)	63
Figure 3.16 Internal Pressure Measurement Tap Locations, Model B and Model C.....	64
Figure 3.17 External Pressure Tap Locations for combined External and Internal Pressure Results, Model B and Model C	65
Figure 3.18 Wall Pressure Measurement Heights $h/3$ and $2h/3$	66
Figure 3.19 Wall and Roof References and Roof Plan View Axes	66
Figure 4.1 Mean External Roof Pressure Coefficient $C_{\bar{p}}$, Zero Porosity Model A, $\theta = 0^\circ$	67
Figure 4.2 Maximum External Roof Pressure Coefficient, $C_{\bar{p}}$, Zero Porosity Model A, $\theta = 0^\circ$	68
Figure 4.3 Minimum External Roof Pressure Coefficients, $C_{\bar{p}}$, Zero Porosity Model A, $\theta = 0^\circ$	69
Figure 4.4 Pressure Coefficients C_p for Windward Wall W1 of Model A, $\theta = 0^\circ$	69
Figure 4.5 External Pressure Coefficients, C_p for Leeward Wall W3 of Model A, $\theta = 0^\circ$	70
Figure 4.6 External Pressure Coefficient, C_p for Side Walls W2 and W4 of Model A, $\theta = 0^\circ$	71
Figure 4.7 Mean External Pressure Coefficient, $C_{\bar{p}}$, Zero Porosity Model A, $\theta = 45^\circ$	71
Figure 4.8 Maximum External Pressure Coefficient, $C_{\bar{p}}$, Zero Porosity Model A, $\theta = 45^\circ$	72
Figure 4.9 Minimum External Roof Pressure Coefficients, $C_{\bar{p}}$, Zero Porosity Model A, Zero Porosity Model A, $\theta = 45^\circ$	72
Figure 4.10 Pressure Coefficients C_p for Windward Walls W1 and W2 of Model A, $\theta = 45^\circ$	73

Figure 4.11 Pressure Coefficients C_p for Leeward Walls W3 and W4 of Model A, $\theta = 45^\circ$..	73
Figure 4.12 Mean External Pressure Coefficient, $C_{\bar{p}}$, 19% Porosity Model B, $\theta = 0^\circ$	74
Figure 4.13 Maximum External Pressure Coefficient, $C_{\bar{p}}$, 19% Porosity Model B, $\theta = 0^\circ$...	75
Figure 4.14 Minimum External Pressure Coefficient, $C_{\bar{p}}$, 19% Porosity Model B, $\theta = 0^\circ$...	75
Figure 4.15 External Pressure Coefficients C_p for Windward Wall W1 of Model B, $\theta = 0^\circ$...	76
Figure 4.16 External pressure Coefficients C_p for Leeward Wall W3 of Model B, $\theta = 0^\circ$	77
Figure 4.17 External Pressure Coefficients C_p for Side Wall W2 of Model B, $\theta = 0^\circ$	77
Figure 4.18 Mean External Pressure Coefficient, $C_{\bar{p}}$, 19% Porosity Model B, $\theta = 45^\circ$	78
Figure 4.19 Maximum External Pressure Coefficient, $C_{\bar{p}}$, 19% Porosity Model B, $\theta = 45^\circ$..	79
Figure 4.20 Minimum External Pressure Coefficient, $C_{\bar{p}}$, 19% Porosity Model B, $\theta = 45^\circ$..	79
Figure 4.21 External Pressure Coefficient C_p Windward Wall W1 of Model B, $\theta = 45^\circ$	80
Figure 4.22 External Pressure Coefficient C_p Leeward Wall W3 of Model B, $\theta = 45^\circ$	81
Figure 4.23 Mean Internal Pressure Coefficient, $C_{\bar{p}}$ Model B, $\theta = 0^\circ$	82
Figure 4.24 Maximum Internal Pressure Coefficient, $C_{\bar{p}}$, Model B, $\theta = 0^\circ$	83
Figure 4.25 Minimum Internal Pressure Coefficient, $C_{\bar{p}}$, 19% Porosity Model B, $\theta = 0^\circ$	84
Figure 4.26 Mean Internal Pressure Coefficient, $C_{\bar{p}}$ Model B, $\theta = 45^\circ$	85
Figure 4.27 Maximum Internal Pressure Coefficient, $C_{\bar{p}}$, Model B, $\theta = 45^\circ$	86
Figure 4.28 Minimum Internal Pressure Coefficient, $C_{\bar{p}}$, 19% Porosity Model B, $\theta = 45^\circ$	87
Figure 4.29 Mean External Pressure Coefficient, $C_{\bar{p}}$, 38% Porosity Model C, $\theta = 0^\circ$	88
Figure 4.30 Maximum External Pressure Coefficient, $C_{\bar{p}}$, 38% Porosity Model C, $\theta = 0^\circ$	89
Figure 4.31 Minimum External Pressure Coefficient, $C_{\bar{p}}$, 38% Porosity Model C, $\theta = 0^\circ$	89
Figure 4.32 External Pressure Coefficients for Windward Wall W1, C_p , Model C, $\theta = 0^\circ$	90
Figure 4.33 External Pressure Coefficients for Leeward Wall W3, C_p , Model C, $\theta = 0^\circ$	91
Figure 4.34 External Pressure Coefficients for Side Wall W2, C_p , Model C, $\theta = 0^\circ$	91
Figure 4.35 Mean External Pressure Coefficient, $C_{\bar{p}}$, 38% Porosity Model C, $\theta = 45^\circ$	92
Figure 4.36 Maximum External Pressure Coefficient, $C_{\bar{p}}$, 38% Porosity Model C, $\theta = 45^\circ$	93
Figure 4.37 Minimum External Pressure Coefficient, $C_{\bar{p}}$, 38% Porosity Model C, $\theta = 45^\circ$	93
Figure 4.38 External Pressure Coefficients, C_p , Windward Wall W1 of Model C, $\theta = 45^\circ$	94
Figure 4.39 External Pressure Coefficients, C_p , Leeward Wall W3 of Model C, $\theta = 45^\circ$	94
Figure 4.40 Mean Internal Pressure Coefficient, $C_{\bar{p}}$ Model C, $\theta = 0^\circ$	95

Figure 4.41 Maximum Internal Pressure Coefficient, $C_{\bar{p}}$ Model C, $\theta = 0^\circ$	96
Figure 4.42 Minimum Internal Pressure Coefficient, $C_{\bar{p}}$, 38% Porosity Model C, $\theta = 0^\circ$	96
Figure 4.43 Mean Internal Pressure Coefficient, $C_{\bar{p}}$ Model C, $\theta = 45^\circ$	97
Figure 4.44 Maximum Internal Pressure Coefficient, $C_{\bar{p}}$ Model C, $\theta = 45^\circ$	98
Figure 4.45 Minimum External Pressure Coefficient, $C_{\bar{p}}$, 38% Porosity Model C, $\theta = 45^\circ$	98
Figure 4.46 Mean External Pressure Coefficient, $C_{\bar{p}}$, 58% Porosity Model D, $\theta = 0^\circ$	99
Figure 4.47 Maximum External Pressure Coefficient, $C_{\bar{p}}$, 58% Porosity Model D, $\theta = 0^\circ$..	100
Figure 4.48 Minimum External Pressure Coefficient, $C_{\bar{p}}$, 58% Porosity Model D, $\theta = 0^\circ$.	100
Figure 4.49 External Pressure Coefficient C_p Windward Wall W1 of Model D, $\theta = 0^\circ$	101
Figure 4.50 External Pressure Coefficient C_p Leeward Wall W3 of Model D, $\theta = 0^\circ$	101
Figure 4.51 External Pressure Coefficient C_p Side Wall W2 of Model D, $\theta = 0^\circ$	102
Figure 4.52 Mean External Pressure Coefficient, $C_{\bar{p}}$, 58% Porosity Model D, $\theta = 45^\circ$	103
Figure 4.53 Maximum External Pressure Coefficient, $C_{\bar{p}}$, 58% Porosity Model D, $\theta = 45^\circ$	103
Figure 4.54 Minimum External Pressure Coefficient, 58% Porosity Model D, $\theta = 45^\circ$	104
Figure 4.55 External Pressure Coefficient C_p Windward Wall W1 of Model D, $\theta = 45^\circ$	104
Figure 4.56 External Pressure C_p for Leeward wall W3 of Model D, $\theta = 45^\circ$	105
Figure 5.1 Maximum Pressure Coefficient $C_{fig,net}$, Model B, Wind direction sector $\theta = 0^\circ \pm 45^\circ$	112
Figure 5.2 Minimum Pressure Coefficient $C_{fig,net}$, Model B, Wind direction sector $\theta = 0^\circ \pm 45^\circ$	113
Figure 5.3 Maximum Pressure Coefficient $C_{fig,net}$, Model C, Wind direction sector $\theta = 0^\circ \pm 45^\circ$	114
Figure 5.4 Minimum Pressure Coefficient $C_{fig,net}$, Model C, Wind direction sector $\theta = 0^\circ \pm 45^\circ$	115
Figure 5.5 Maximum Pressure Coefficient $C_{fig,net}$, Model D, Wind direction sector $\theta = 0^\circ \pm 45^\circ$	116
Figure 5.6 Minimum Pressure Coefficient $C_{fig,net}$, Model D, Wind direction sector $\theta = 0^\circ \pm 45^\circ$	117
Figure 5.7 Maximum and Minimum Net Pressure Coefficient $C_{fig,net}$, Model B, Wall W1	119
Figure 5.8 Maximum and Minimum Net Pressure Coefficient $C_{fig,net}$, Model B Wall W2	120

Figure 5.9 Maximum and Minimum Net Pressure Coefficient <i>C_{fig,net}</i> , Model B Wall W3	121
Figure 5.10 Maximum and Minimum Net Pressure Coefficient <i>C_{fig,net}</i> , Model C Wall W1	121
Figure 5.11 Maximum and Minimum Net Pressure Coefficient <i>C_{fig,net}</i> , Model C Wall W2	122
Figure 5.12 Maximum and Minimum Net Pressure Coefficient <i>C_{fig,net}</i> , Model C Wall W3	122
Figure 5.13 Maximum and Minimum Net Pressure Coefficients <i>C_{fig,net}</i> , Model D Wall W1	123
Figure 5.14 Maximum and Minimum Net Pressure Coefficient <i>C_{fig,net}</i> , Model D Wall W2	124
Figure 5.15 Maximum and Minimum Net Pressure Coefficient <i>C_{fig,net}</i> , Model D Wall W3	124

1. Introduction

1.1 Large Protection Canopies

Large protection canopies are a unique development of structural ingenuity, where extensive areas of woven net are supported by pre-tensioned high tensile cables spanning large distances frequently in excess of 100m. These resilient, lightweight, tensile systems provide great structural efficiency leading to significant cost savings and are quickly erected and easily maintained. They provide a solution to the protection of large areas of valuable assets from sun, hail, wind and birds.

A recent (2013) example of these clear far spanning structures is the Evaporation Canopy constructed over the Orbost Clear Water Storage for East Gippsland Water shown in **Figure 1.1**. The clear storage area covered by this canopy is 100mx140m or 1.4Ha. The lightweight structure is constructed using 12mm diameter high tensile steel pre-tensioned cables with galvanised steel perimeter posts and screw anchors.



Figure 1.1 Large Free Spanning Canopy over Orbost Clear Water Storage

To design and construct these canopies successfully, an understanding of the critical design actions is essential. The weight of the net cover and self weight of the cables are easily quantified, but the porous structure's response to wind is presently little understood with only limited research completed on wind actions on porous canopies.

The large area of net supported by each cable subject to wind loads is significant, but it is evident from current canopy construction, that the wind actions on the porous surfaces are considerably less than the design wind actions on a non-porous roof. Inadequate understanding of the wind loads has led to structural failures during extreme storm events, causing wide-spread

damage to the assets under cover. In the past, the design and development of the net canopy structural systems have developed empirically from a practice base where systems have been tried and extended, modified and refined without structural engineering design. This has mostly led to resilient and serviceable structural systems, but also at times unpredictable structural performance. The challenge for a structural designer is to show that these lightweight structures are structurally adequate for site design winds specified in the wind loading standard AS/NZS 1170.2(2011). No guidance on wind actions at this time is provided in this Standard for the design of porous canopies. Additional information is also required showing how these loads vary with different net porosities and their distribution across the flat roof surfaces and along the porous walls.

Previous studies by Richards and Robinson (1999), Donnan (1987), Letchford et al (2000) Wolbers (1999), Briassoulis and Mistrionis (2010), and Robertson et al (2002) provide research findings into wind loads on porous structures. These studies are reviewed in Chapter 2 and it is shown that, while providing valuable information on wind loads on porous structures, the additional research presented in this thesis has been necessary to investigate wind actions on large porous canopies.

1.2 Aims and Objectives

This research aims to establish pressure coefficients that, combined with the site wind velocity, will enable the structural engineer to predict wind actions on typical enclosed flat roof porous canopies. The resulting design coefficients are intended to form the basis for future inclusion in the design standard AS/NZ1170.2 – Structural Design Actions Part 2: Wind Actions.

The research aims also to study the influence of the degree of porosity on the wind actions, comparing wind actions for various degrees of porosity with those found for an equivalent solid structure.

This is achieved by carrying out a series of wind tunnel experiments to obtain measurements of pressure on external and internal surfaces of scale models, representing porous canopies with different degrees of porosity. The wind tunnel pressure measurements are analysed and presented graphically. The simultaneous internal and external pressures are combined to obtain net pressure coefficients for the structure's surfaces.

The scope of this study does not include wind surface friction actions, which can be significant due to the large roof areas, and dynamic effects from wind actions. These subjects remain for future study.

2. Net Protection Canopies in Australia and Previous Research

2.1 *The Development of Net Protection in Australia*

Large scale net protection structures were initially constructed to protect orchards and crops from hail, wind, temperature extremes, pests and birds. In the past thirty years these structures have become more sophisticated with new systems and methods being developed by commercial companies that specialise in the construction of the canopies. In Australia and New Zealand companies such as Netpro, VP Structures, Superspan and Coastguard Netting have provided these structures for a wide range of agricultural and horticultural projects installing tensioned cable structures that support woven nets with a wide range of shade percentages and porosities. There are examples of similar canopies in Israel, India and South Africa.

The application of the cable structures has been limited to regions of drier climatic conditions, where snow does not occur. The large span cable structures are limited by their lack of capacity to carry the weight of the snow. Net support structures required to support snow loads require stronger nets, more closely spaced support grids and frequently the replacement of the cables with steel trusses leading to significant cost increase.

The canopies can be extensive, adapted to the produce being protected and the irregular layout of the orchard or farm as shown below in **Figure 2.1** where the canopies have followed the orchard footprint.



Figure 2.1 Canopies for Stone Fruit Orchards at Childers, Queensland

One of the first types of net protection for horticulture was the vertical net wind break, constructed to protect kiwi fruit orchards on the North Island of New Zealand from catastrophic wind damage. The success of these structures led to extensive analytical and wind tunnel

research into the wind loads on vertical wind break net structures at Auckland University (Richards and Robinson, 1999). Further research work has continued on their application to control dust and particle dispersion from mineral stockpiles (Cheng-Peng Yeh et al, 2010).

Several New Zealand net protection contractors gained experience in the construction of the vertical wind breaks and identified the potential of net protection canopies, commencing a protection canopy construction company in Stanthorpe, Queensland, an intensive area for fruit growing. This company developed a canopy protection system which evolved into the current Netpro Protection Canopies. Similarly, Superspan commenced constructing net canopies in the 1980's at Flinders, Victoria followed by a number of other contractors.

At James Cook University in 1987, Donnan undertook a project investigating wind pressure on net protection structures for his Bachelor of Engineering Honours thesis, under the supervision of Professor Walker. This work was later published in the proceedings of the First National Structural Engineering Conference (Donnan et al, 1987). The damage to net structures and green-houses by cyclones has been a large cost to the fruit growing industry in the North Queensland region and the need for engineering design was apparent. Donnan, who as a resident in North Queensland had witnessed this damage, constructed a green-house model and tested the normal pressure coefficients for a number of different nets in the Cyclone Testing Station Wind Tunnel. He presented the results in his undergraduate thesis and subsequently in the paper mentioned above.

In 1989, the author was required to report and provide evidence on the collapse of a net shade structure that had been constructed for an orchid grower at Murphys Creek near Toowoomba. This structure had failed during a storm and subsequently there was extensive damage to the valuable imported orchid tissue stock. Substantial loss was incurred by the grower and the implications of failure were significant enough to take the claim by the grower against the contractor to the Supreme Court. The evidence that was presented highlighted the lack of significant testing and research into the wind actions on net structures. It also demonstrated the need for correct detailing, particularly with regard to the connection of the net to the cables.

The demand by orchardists for protection canopies continued to increase for protection of the wide range of fruit grown, including apples, pears, apricots and peaches. Significant losses due to severe hail storms, bird damage and frost had been experienced, creating the need for an effective affordable protection canopy system. Contractors commenced constructing flat canopies over orchards using timber posts, high tensile cables and a range of woven net fabrics with varying levels of shade, hail and bird protection. **Figure 2.2** shows a canopy erected for protection of mangoes.



Figure 2.2 Canopy for Mango Orchard in Northern Queensland

Soon the net canopies were being constructed over a variety of fruit, vegetables and crops at wide spread locations throughout Australia and New Zealand. Abalone growers used the nets to protect their produce from birds and the sun. Parafield Air Port in Adelaide installed a net canopy over a large dam used to collect surface water for pumping back into ground aquifers. The purpose of the canopy was to prevent birds breeding in large numbers on the dam and causing a hazard to the aeroplane engines. Covers were also constructed over water storages to reduce water evaporation and improve water quality as illustrated in **Figure 2.3**.



Figure 2.3 Dam Cover Construction at The Summit, Queensland

A major, current application is the construction of canopies over vehicle storage facilities. Car importers and exporters store large numbers of vehicles before distribution to dealers or export and require protection against hail and the sun as shown in **Figure 2.4**. Car retailers have also constructed the canopies to protect their stock on a smaller scale.



Figure 2.4 Vehicle Protection Canopy

The variety of uses of cable supported canopy systems is constantly developing. The cost effectiveness of the net canopy system is able to be demonstrated by the current (2015) approximate rates of construction:

1. 12mm quad flat canopy, with walls and providing bird, moderate hail, wind and 20%-30% shade protection, cost of construction : \$5.50/m².
2. Pitched hail protection canopy, with hail guard netting and providing, hail, bird, wind and 30% shade protection, cost of construction : \$12-\$15/m².

Traditional alternatives to the net protection canopies include the hooped tunnel green house and steel framed pitched structures. These structures necessarily have smaller clear spans and are used in intensive growing situations where retractable roofs and/or controlled mechanical venting may be applied. The costs of these structures gradually increase from \$15/m² to over \$100/m² depending on the technology and sophistication of the system. The speed of construction and ease of repair and maintenance are also significant advantages of the net structures.

The effectiveness of the net protection canopies has led to insurers offering growers and car storage companies reduced premiums against storm damage if the canopies are installed.

2.2 Canopy Construction

The net canopy structures consist of tensioned woven polyester net roofs and walls supported by a two way grid of pre-tensioned cables, which in turn are supported by steel or timber posts restrained by tie back cables and ground anchorage systems. The nets are manufactured using UV stable polymer threads in weaves that are suitably elastic for tensioning during installation and have adequate strength to carry the wind load and self weight loads. Typically the cloths when tested in a biaxial tension test have two distinct stages of load versus deformation behaviour. The first stage is usually linear up to a tightening of the threads into knots at their intersections. This then leads to a first permanent deformation of the net which then, with increased load, moves into a second stage of response before tensile failure of the fibres. When the nets are loaded to the second stage of deformation, permanent stretching of the nets occurs and replacement is often required. The replacement of failed nets and cables can be carried out quickly, providing a resilient structural system. A wide range of nets is now available from the high porosity low shade nets used for bird protection to the low porosity shade netting providing up to 95% shade. The weaves are diverse and have different strength and tensioning characteristics. A number of companies in Australia, New Zealand and Asia have developed the capacity to produce these cloths with a wide range of weaves, colours and strengths.

High tensile steel cables that are used in this type of canopy are frequently of 6.1mm (7x2mm strands), 7.5mm (7x2.5mm strands) or 12.0mm (19x2.5mm strands) diameters and are currently being manufactured in Australia. The minimum breaking forces of the cables are specified as 31kN, 51kN and 124kN respectively. A project specific pretension force, obtained by experience and past assessment of the deflection once a net is installed, is applied to the cables with an electric or hand winch. The orthogonal tensioned cables provide a structural grid onto which the cloth is able to be clipped. The nets are rolled out in a nominated longitudinal direction with wires woven into the cloth. The wires are connected with plastic clips to the longitudinal cables, which interact with the cross cables to provide a two way support system.

A number of load tested clipping and cable splice connection systems are available on the market. The use of clips and splices that do not damage the net's weave and structure is an essential part of the canopy system. Local wind forces on the clips can be assumed to have peak forces greater than the average roof actions across the roof structure in a manner similar to roof screws fixing metal roof sheeting. Helical cable splices, developed for the power transmission industry, have been adapted successfully, allowing smooth splicing of the cables and avoiding wear points on the cloth.

Generally in the horticultural canopies, timber posts of treated hard wood or radiata pine are used to support the cable and net structure. The external posts are supported by tie back or guy

cables that typically are installed at 45 degrees to a ground anchorage system. The pretension loads applied to the roof and tie back cables act to place the perimeter posts in compression and drive them into a predrilled ground hole. Sometimes a timber or concrete bearing pad is placed under the posts to spread this load in weaker soils. Internal posts are placed to provide support to the cables and reduce deflections to the canopy under the weight of the net and cables. The posts' self weight and frictional anchorage in the ground provide resistance to uplift and can also, where required, be anchored using screw anchors or mass concrete footings. The tie back cable anchors are frequently constructed using a log buried in a trench with a high tensile rod placed through the log and out through the ground for connection of the cable. This system is a convenient method of anchorage, using the materials that are at the site for construction of the superstructure, but is difficult to assess for structural capacity. The back fill to the trench is typically moderately compacted by machine wheel rolling. The pre-tensioning of the roof and tie back cables pulls the log into the side of the trench engaging the passive pressure resistance of the soil. One problem that has occurred with this system is when the anchors are installed in open earth drains surrounding the orchard. The soil becomes saturated during high levels of rain and run-off and the logs have a tendency to be pulled out of the ground. This is avoided by ensuring that there is good drainage away from the anchor locations.

More recently, screw pile anchors have been used to anchor the tie back cables. These anchors can be installed to a measured resistance torque and the required pull out capacity achieved. The use of these anchors has led to the need for geotechnical investigations to be carried out so that the screw pile contractor can estimate the length and capacity of the pile system. The installation of these piles into a weathered non cohesive rock material can lead to the torque resistance being achieved, but the pull out capacity being much lower than that required. The flight of the pile will drill into the non cohesive material but not engage with the weathered rock surrounding. Installation problems also can occur where there are rock floaters or weak wet non cohesive sand. Another alternative in situations where there is shallow rock or non cohesive material is to use bored concrete piers or mass concrete pads. Grouted rock anchors and manta ray anchors have also been used effectively. Frequently, the anchors are the first point of failure for the structure, with required anchorage capacity of over 10 tonnes often specified. Their failure will lead to a progressive collapse similar to the failure of a tent once one guy rope is released.

Figure 2.5 shows a canopy designed to fit a specific site, with cable spacing and post centres chosen to suit the net to be installed and the site design wind.

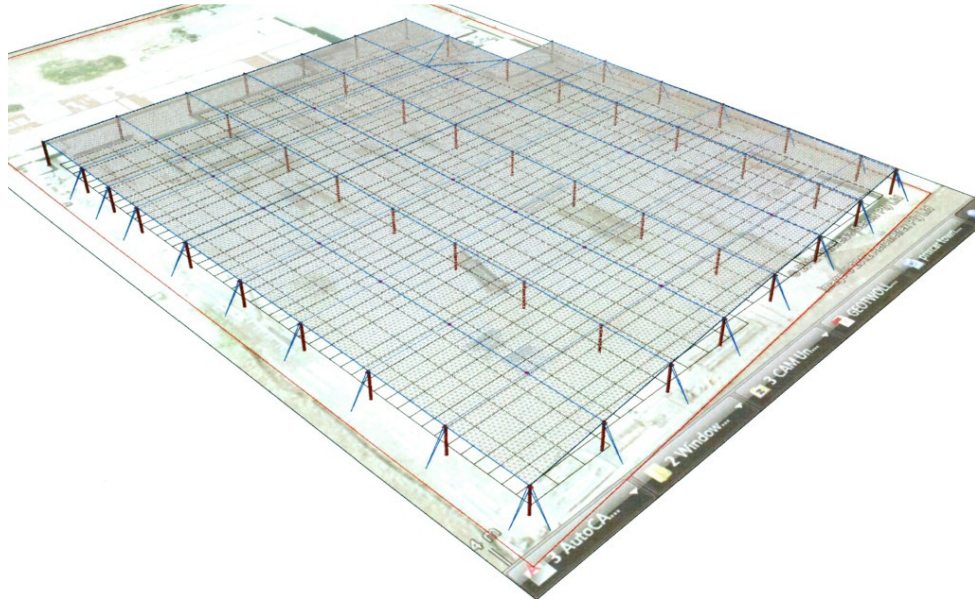


Figure 2.5 Flat Roofed Canopy Structure Design

The flat canopies have been found to have good capacity to withstand wind loads and the self weights of the net and cables, but to have limitations when supporting hail loads. Typically the hail collects in the centre of a rectangular cable supported panel and the net sags to the ground. This extra load sometimes causes cables to break or tie back foundations to be pulled out of the ground. Openings in the centre of the net panels to allow the collected hail to fall through have been introduced. A multiple pitched roof structure with valleys that allow the hail to fall through has been found to be most effective. These structures with their close cable centres and truss type arrangements have proved to be resilient with low deflection. They also attract higher horizontal wind loads than the flat roofs due to the inclined roof sections. In car protection canopy construction, the car parking can be planned so that the hail from the valley falls between the parked vehicles. In orchards, canopies can be constructed with the main cables located over the tree rows, leading to the net sagging to the ground between the trees and minimising damage as shown in **Figure 2.6**.



Figure 2.6 Canopy Net Sagging to the Ground with Accumulated Hail between Tree Rows

Figure 2.7 shows the design of a typical pitched car protection structure. Column centres and cable grids are reduced from usual flat roof cable spacing and additional horizontal roof drag loads, due to the ridge and valley repetitive arrangement, occur.

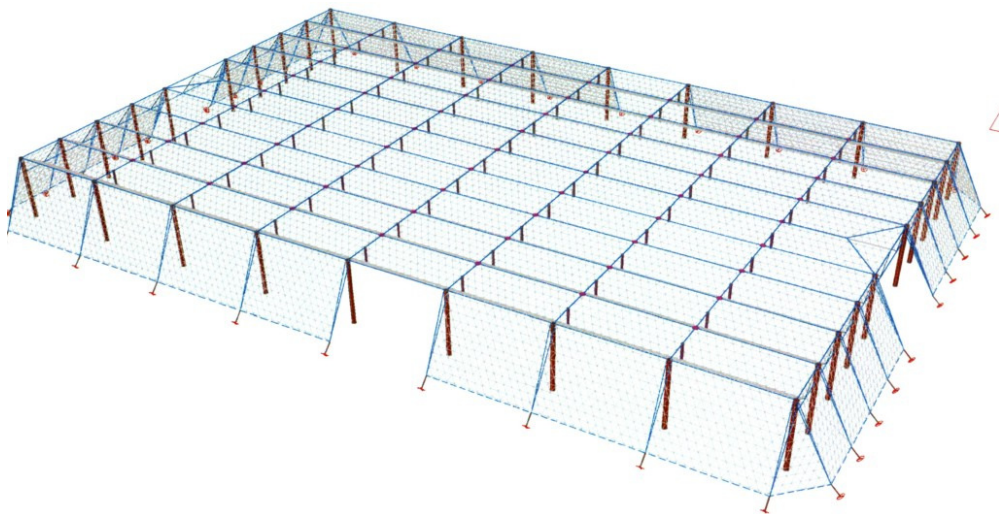


Figure 2.7 Pitched Hail Protection Canopy for Vehicles

The structures developed for protection of vehicles have evolved from the rural structures constructed for growers. The car protection canopies are typically constructed using steel circular hollow section columns and generally higher wind loads are used for their design. Universal Beam sections are used as cantilever edge supports where no space for tie back cables is available.

Dam and reservoir covers can be installed at ground level above the high water level using the steel cable system and screw anchored perimeter supports. Free spanning canopies have been constructed with additional external suspension cables replacing the support provided by internal posts.

2.3 Benefits of Protection Canopies

2.3.1 Horticulture

A number of horticultural trials have been carried out to assess the effectiveness and cost benefits of the net protection canopies for the grower. Middleton (2004) found reduced sunburn, improved fruit colour and skin finish, greater water use efficiency and the elimination of bird damage as benefits of hail netting that may make canopies an economic proposition. Annels et al (2008) reported trials that compared fruit grown under the canopies to fruit without protection. It was concluded that benefits from protective netting over horticulture crops include increased crop reliability, reduced water usage and a reduction in pesticide usage. Production benefits included increased pack-out of first grade fruit as a result of reduced environmental damage.

The Australian Fruitgrower, in the October 2007 issue confirmed the benefits that might be gained by installing net protection: reduced sunburn, wind damage, increased bird and pest control, hail protection, insect control and water saving (Netpro et al, 2007). The canopy structure tends to have some measure of a greenhouse effect, creating a modified climate or microclimate for the produce that allows growers to control their production and quality and to fulfil their supply quotas with more confidence. **Figure 2.8** shows a typical arrangement for an orchard canopy. The choice of colour and degree of shade will depend on what benefits the grower primarily wishes to obtain from the canopy. A balance between adequate shade and adequate sunlight for growth is an example of the outcomes that need to be examined.



Figure 2.8 Orchard Canopy

The development of a fruit fly proof net has also added to the potential benefits of a net protective canopy. The Qld Department of Primary industries reported that netting protection trials with stone fruit, a highly susceptible crop, proved to be highly effective. Fruit flies and other larger insect pests were excluded. As well as being almost completely chemical free, the quality of the fruit was found to improve significantly (DPI, 2008).

Similar benefits were found to occur for vegetable growers when net canopies, as shown in **Figure 2.9**, were constructed. Environmentally susceptible vegetables such as capsicums benefited greatly from the protection structures. An article in the Southern Free Times (Robinson, 2007) described the benefits of growing vegetables inside a domestic net protection structure clad with the fruit fly netting. Insect protection, hail protection and moderating of temperature variation were some of the benefits observed. Additionally the creation of a manageable growing facility meant greater productivity of home grown produce, reducing the carbon footprint for a sustainable future.



Figure 2.9 Vegetable Seedling Canopy

Pitched canopies, as shown in **Figure 2.10**, similar to the canopies built to protect vehicles from hail provide greater hail protection to produce. The valleys of the canopy open up and allow the collected hail to fall through. Beds are laid out so that the canopy falls between the plant beds.



Figure 2.10 Hail Protection Canopy over Seedlings

Retractable net systems for orchards have also been developed in areas such as Batlow in Southern NSW where snow falls in the winter.

The simplicity and economy of the cable and post construction system allows for adaptation to special climate or crop needs. With the rapid growth of the world's population and demand for food, it can be guaranteed that the canopies, with their relatively low construction cost, will have a greater role in increasing efficient food production. The growers association Horticulture Australia Limited actively promotes the use of the protective canopies through sponsoring research into effectiveness and application in Australia. Completed research projects include Building Codes and Greenhouse Construction. This study investigates the relevance and applicability of current building standards to protective structures and a further project is Investigation of Low Cost Protective Cropping for Vegetable Growers.

2.3.2 Agriculture and Aquaculture

A balance between shade and exposure to sunlight has been achieved for feedlot cattle pens, by installing shade covers over sections of the pen still allowing the pens to dry out, but also provide shade for the cattle. This is illustrated in **Figure 2.11**. Heat fatigue and sunstroke have previously been significant issues for feedlot operators. The benefits to the cattle are described as very positive in the article in the Australian Lot Feeders Association's publication (ALFA Feedlotting) where it is noted that greater provision of shade area for feedlot cattle has produced the best possible result for the Australian grain fed beef industry (ALFA Feedlotting, 2005). The \$40M feedlot Grassdale in Southwest Queensland constructed in 2008 and since expanded has adopted this approach and currently there is significant interest in Texas and Arizona, USA.



Figure 2.11 Shade Covers to Feedlot Cattle Pens

Nets have also been constructed over fish production facilities, **Figure 2.12**, providing protection from birds that prey on the fish and also reducing evaporation.



Figure 2.12 Net Canopy over Fish Breeding Facility

Abalone farmers have also constructed nets over their production facilities; see **Figure 2.13**, to provide shade and protection from birds.



Figure 2.13 Canopy over Abalone Farm Facilities

2.3.3 Vehicle Protection

Large numbers of vehicles are imported into Australia each year as well as exported from the local car manufacturing plants. Vehicle importers receive the cars from the port and store the vehicles while they are processed and prepared for delivery to the many car dealerships. Protection from weather extremes including hail is provided to the high value vehicle stock as shown in **Figure 2.13**. Recent hail damage events have led to an increase in the construction of these canopies.



Figure2.13 Pitched Vehicle Storage Hail Canopy

A number of vehicle protection canopy failures have occurred due to a lack of professional engineering design, where there has been little understanding of the structural forces resulting from wind actions. Typically the inadequate sizing of the cables and cable anchorage has led to the failures. It is now standard practice for local government authorities to request structural certification for these structures. This has made research into the characteristic wind actions on porous structures critical.

2.3.4 Water Storage Covers

The major benefit in using net covers over water storages is reduction in evaporation. A project by CSIRO Textile and Fibre Technology Division with Gale Industries and East Gippsland Water examined the benefits of the net covers (Finn and Barnes, 2007), which included reducing light levels to prevent algal and plant growth, reducing wind-borne contaminants and reduction of evaporation. Data was collected from two covered storages and it was found that the water quality was enhanced and water evaporation reduced.

Further research at the National Centre for Engineering in Agriculture, University of Southern Queensland was carried out on a cover installed over a dam at The Summit in Queensland. Tests showed that the cover has the potential to reduce evaporation by 70% (Schmidt, 2007)

With the cost of water increasing and severe fluctuations in season conditions, the reduction of evaporation is becoming increasingly necessary. An increased number of covers for water storages have been constructed in the last two years as shown in **Figure 2.14**.



Figure 2.14 Clear-span Protection Canopy over Clear Water Storage

Irrigation channels, shown in **Figure 2.15**, have also been covered to reduce evaporation.



Figure 2.15 Irrigation Channel Cover

2.3.4 Other applications

Some other applications that are common include bird protection canopies over water reservoirs and effluent ponds to prevent the nesting of birds at these facilities and the construction of canopies over waste disposal facilities, shown in **Figure 2.16**, to prevent litter and dust spreading. Bird aviaries including an eagle enclosure have also been constructed.



Figure 2.16 Canopy for Waste disposal Facility

The development of canopy protection systems for ore and aggregate stockpiles in areas where the prevention of dust is necessary is also being investigated. Presently vertical wind breaks are used to reduce the wind speeds and dust creation and a structural system to cover a large stockpile is currently being developed. The canopies as shown above, offer a low cost way to provide protection over large areas of produce, stock and other assets.

2.4 Relevant Past Research into Loads on Porous Surfaces

The pressures acting on porous surfaces, when subject to the flow of a fluid, have been investigated by a number of researchers using mathematical and experimental methods over the past 60-70 years. However, the complexities of this research have resulted in limited outputs for application in structural design codes. For the most part, the research has concentrated on the flow of the fluid normal to the porous surface. Examples of this research include Annand (Annand, 1953) and Hoerner (Hoerner, 1965) who both investigated the resistance to air flow by wire gauzes, and, following on, research by Richards and Robinson (Richards and Robinson, 1999), who investigated the wind pressures on porous wind breaks. Subsequently Donnan (Donnan et al, 1987), Letchford (Letchford et al, 2000), Briassoulis (Briassoulis and Mistrionis, 2010) and Robertson (Robertson et al, 2002) carried out investigations to determine the wind pressures on porous canopies. Donnan, Letchford and Briassoulis investigated open canopies without internal pressure, while Robertson modelled an enclosed horticultural structure and measured external and internal pressures. These studies found that the loads acting on the porous elements are influenced by the degree of porosity and the construction (weave of nets) of the porous material, the flow velocity characteristics (magnitude and intensity) and type of fluid. The angle of the porous element to the flow of the fluid has also been identified as significant, but research into the actions resulting from the flow of a fluid parallel to a porous surface have not been considered in detail, as these forces were not considered significant. Although relatively small, these actions for a fluid flowing parallel to the surface are significant for large flat roof canopies due to the large roof areas on which the actions act.

The flow of a fluid around a building structure, termed a bluff structure as distinct from a streamlined structure similar to an aeroplane wing, is characterised by forces acting perpendicular to and parallel to the structure's surfaces and a disturbance or separation of the fluid at the leading edges of the structure (Holmes, 2007). The velocity of the fluid approaches zero at contact with the non-porous surface of a structure creating boundary layer flow where the velocity varies from zero at the surface to the free fluid velocity away from the surface of the structure. **Figure 2.17** shows the separation of the fluid at the leading edge.

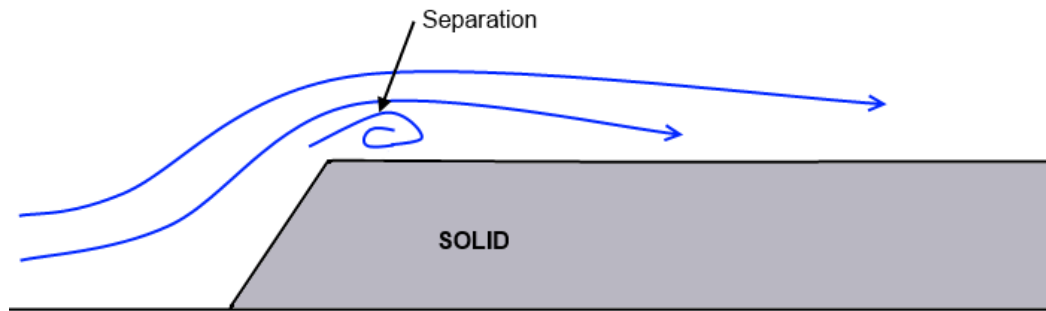


Figure 2.17 Separation of Fluid at a Solid Body's Leading edge

The porous surface of a structure will modify the velocity, forces and separation by having both a part of the fluid resisted and deflected by the structure and a part that flows through the surface and into the interior. The wind velocity instead of being reduced to zero by a non-porous barrier is decreased by a factor determined by the properties of the porous surface as shown in **Figure 2.18**.

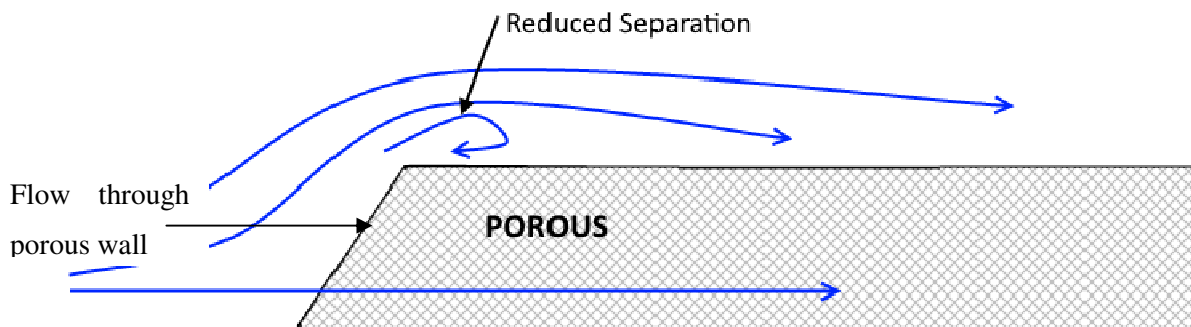


Figure 2.18 Fluid Flow through and around Porous Body

Holmes (Holmes, 2007) introduces a porosity factor K_p , which is dependent on the solidity δ (i.e. the ratio of the solid area to the total area of the surface), which leads to a modification of the perpendicular (drag) force C_D to $C_{D,\delta}$ as defined in **Equation 2.1**.

$$C_{D,\delta} = C_D \cdot K_p \quad (2.1)$$

K_p does not vary linearly with respect to the degree of porosity (Holmes, 2007). It can be expected with a porous canopy structure that the separation at the leading edge (wall and roof intersection) will largely disappear.

The Reynolds number, a property of the fluid flow through the porous material (influenced by the velocity, turbulence and characteristic dimension of the porous surfaces openings), is identified as influential on the resulting forces on the structure. The Reynolds number is the ratio of fluid inertia forces in the flow to the viscous forces on the solid body or element. Viscous forces are present in the surface boundary layers that are created at each opening in the porous surface where, for example with a woven net, forces are generated around each solid element by the flow of air through the net.

To investigate previous research on these characteristics of wind loads on porous structures, a review of research on porous structures was carried out resulting in the following research papers concerning wind loads on porous structures being studied.

2.4.1 Wind Loads on Porous Structures (Richards and Robinson, 1999)

This paper written by Richards and Robinson presents the results of research at Auckland University that investigated the wind's actions on vertical porous screens and net wind breaks. This investigation presents analytical and experimental results obtained from past research, theoretical analysis, wind tunnel measurements at Auckland University and also field measurements on full scale wind breaks.

The fluid pressure on a porous screen perpendicular to the fluid flow is characterised by a loss coefficient (k) which is dependent on the screen porosity (β) and also the screen's construction or weave, in the case of a fabric. The porosity is calculated by dividing the screen open area by the total screen area. The manner of construction of the porous material will vary the flow through the material and the resulting Reynolds number.

Previous research by Annand (Annand, 1953), Hoerner (Hoerner, 1965) and the Engineering Science Data Unit, London (Engineering Science Data Unit, 1972) into the magnitude of the loss coefficient are presented and the authors' analysis of the geometry of the screens leads to their refinement of the relationship between porosity and the loss coefficient. This is presented in the **Figure 2.19** (Richards and Robinson, 1999). Equation 8 shown graphically is compiled from the results obtained for the loss behaviours at low porosities and at high porosities and is reproduced in **Equation 2.2** (Richards and Robinson, 1999).

$$k(\beta, \text{Re} > 2000, \text{round}) = \left(\frac{(1-\beta)^8}{\beta^8} + (1-\beta)^4 / (1-0.75(1-\beta))^8 \right)^{0.25} \quad (2.2)$$

k = pressure loss coefficient of the porous surface

β = the surface porosity and $1-\delta$

Re = Reynolds Number for screen with round cylindrical elements

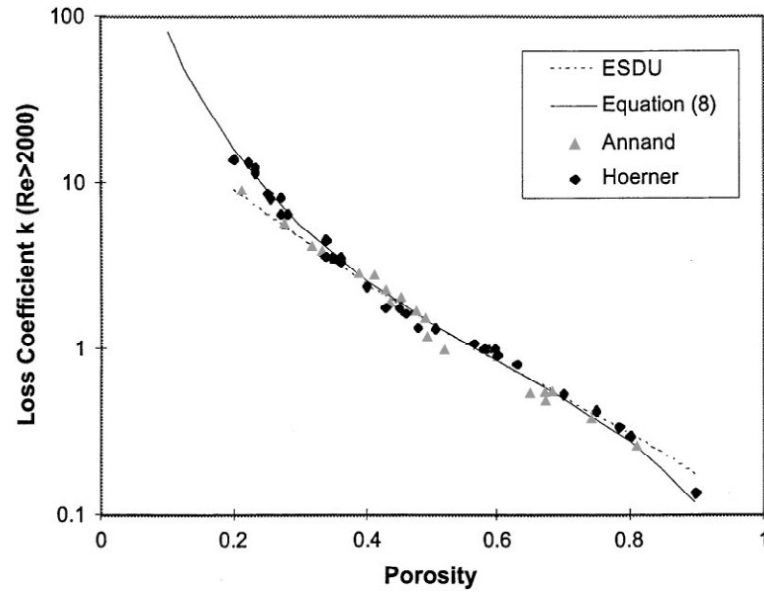


Figure 2.19 Loss Coefficients for Round Wire Screens (Richards and Robinson, 1999)

The authors introduce the concept of an effective or reference porosity (β_e) based on the loss through a round wire mesh screen. The loss through a differently constructed screen can be related to this value. The pressure loss across the porous screen (ΔP) can be expressed by the following **Equation 2.3** (Richards and Robinson, 1999):

$$\Delta P = k 0.5 \rho V_T^2 \quad (2.3)$$

ρ = Density of air

V_T = Volume rate or air per unit area

k = Loss coefficient dependent on porosity, type of construction and Reynolds number R_e

The Reynolds R_e number is derived from **Equation 2.4** (Richards and Robinson, 1999)

$$R_e = \rho V_T d / \mu \quad (2.4)$$

d = the characteristic screen dimension

μ = kinematic viscosity of air

The reference characteristic screen dimension d may be defined as the dominant fibre diameter or in the case of a perforated plate, the typical hole diameter, but must be kept consistent when comparing Reynolds number of different screens.

Richards and Robinson found that the loss coefficient remained relatively constant for Reynolds numbers greater than 2000, but increased at lower Reynolds numbers, with a ratio of approximately 3 occurring between $R_e 2000$ and $R_e 100$. Woven net fabrics were found to have R_e values of the order of several hundred and loss coefficients increasing with reduced area

porosity β . The loads on the canopy surfaces perpendicular to the air flow can be expected to be significant.

Wind tunnel tests of the round wire screens were carried out at Auckland University to provide data comparative to predicted theoretical results. Porous fabrics were tested in a closed 300mm x 300mm wind tunnel to obtain their loss coefficients and then were mounted on a 300mm x 1500mm frame in a 1500mm x 1500mm wind tunnel as illustrated in **Figure 2.20**. Forces were measured parallel and perpendicular to the frame for a range of angles to the wind flow.

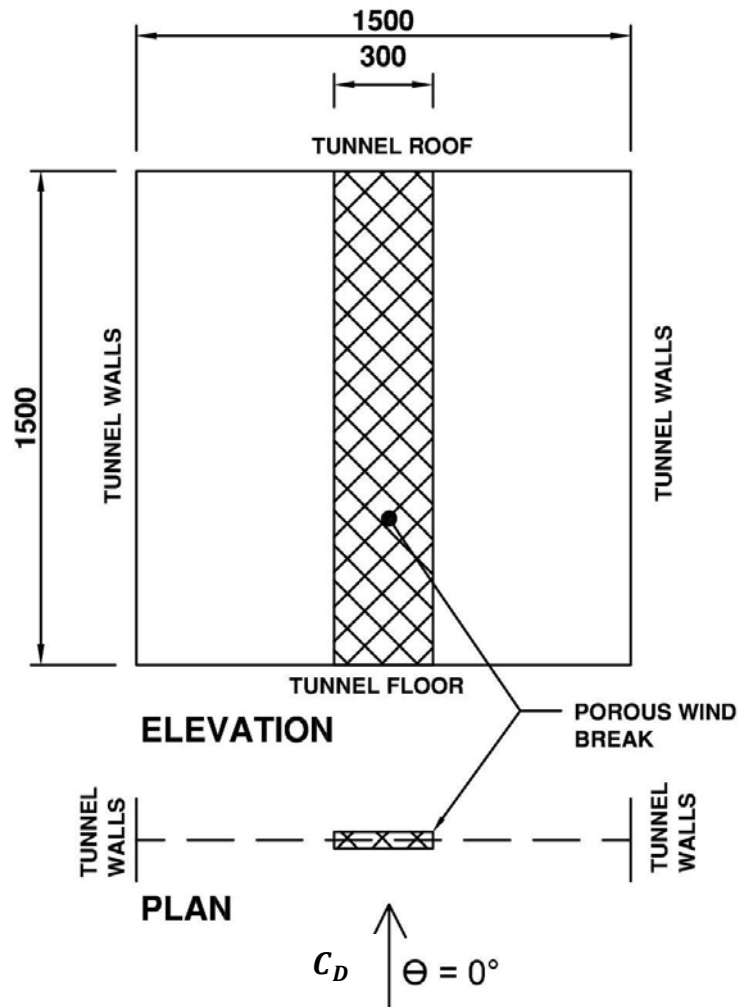
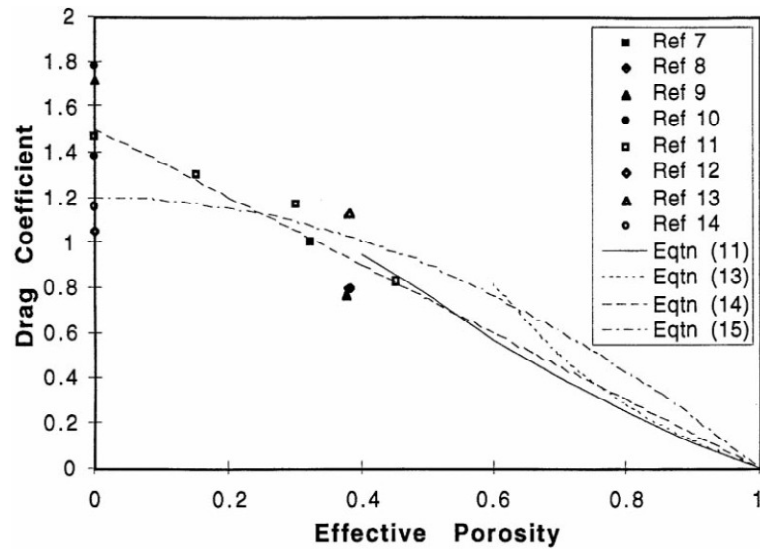


Figure 2.20 Wind Tunnel Arrangement for Testing of Porous Screens

This research found that the drag coefficient C_D on a porous wind break fence, both theoretically and from the wind tunnel test results, decreases almost linearly with the effective porosity of the tested screen. **Figure 2.21** shows this variation. The drag coefficient C_D , is defined as the pressure coefficient for the wind normal to the vertical wind break front surface with the positive direction towards the surface.



**Figure 2.21 Drag Coefficients for windbreak fences
(Wind perpendicular to the fence surface, $\theta = 0^\circ$) (Richards and Robinson, 1999)**

The various references made in the legend of the figure refer to research results obtained from research by Richardson, Painter, Seginer, Robertson and Hagen testing the wind pressures on freestanding wall structures. The equations refer to equations derived from research and momentum theory. It is seen that there is reasonable correlation between all the results.

From these results it can be concluded that the wind acting perpendicular to a porous net surface will produce significant forces that need to be allowed for in the design of the windbreak structure.

The angle of the wind on a porous surface was also investigated and the effective loss coefficient (k) was found to be reduced by $\cos^2\theta$, where θ = angle between wind direction and a normal to the surface. This leads to the effective porosity increasing and the loads decreasing as θ increases from 0° to 90° . From this research it can be expected that the drag forces on the walls of a large porous canopy will be greatest when $\theta = 0^\circ$.

The research has relevance to this project, defining the key factors that influence the wind resistance of a porous surface as degree of porosity, Reynolds number and direction of wind relative to the porous structure. The results for pressure coefficients on a free standing porous wind break show that wind forces on the structure diminish with increased porosity. Additionally the wind loads diminish as the direction of the wind on the surface varies from perpendicular to parallel. The research however does not consider the pressures on an enclosed canopy structure with walls and roof. To be able to understand the wind forces on a large protective canopy, additional wind tunnel testing of scaled porous canopy models is required that will allow the influence of the wind parallel to the roof and the interaction between resulting external and internal pressures to be investigated.

2.4.2 Design of a Low Cost Wind Resistant Shade Cloth Structure (Donnan et al, 1987)

This research project was carried out at James Cook University. Wind tunnel testing was carried out on 1:100 scale models of a cable and post supported net structure. The full scale size of the structure investigated was 3.25m high and 21 metres deep. Four different porosities were tested: non-porous, 90% shade, 70% shade and 50% shade. The % shade is defined by percentage of light blockage of the screen and is influenced by the solid area of the net, the net construction and also the net colour. It generally closely approximates the solidity of the net and is often used as a first estimate for solidity and hence porosity. The models were mounted on a three component force balance to allow measurement of the resultant drag and lift forces. The test arrangement is shown in **Figure 2.22**.

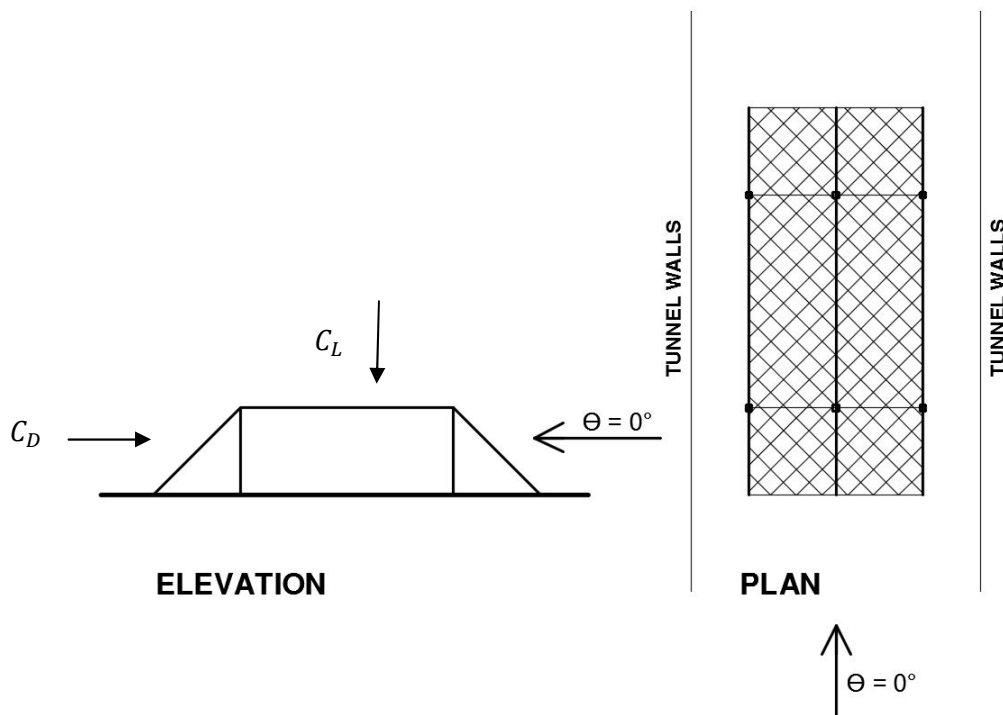


Figure 2.22 Model Testing Arrangement

The results are presented as force coefficients C_L on the model's plan surface (lift coefficient with negative value for suction away from the structure's surfaces) and C_D in the model's front surface (drag coefficient with positive value towards the structure's front surface). The derivation of these values is shown in **Equations 2.5** and **2.6**.

$$C_L = \frac{F_L}{q_h A_p} \quad (2.5)$$

$$C_D = \frac{F_D}{q_h A_f} \quad (2.6)$$

Where F_L , F_D = lift and drag forces respectively, A_p , A_f are the projected plan and frontal areas and q_h the wind pressure at roof height.

The results presented in **Table 2.1** shows that the overall drag forces increase with porosity, the non-porous model showing the lowest drag. The lift forces however decreased significantly with the introduction of small amounts of porosity, but did not increase significantly with increasing porosity.

Table 2.1 - Measured Wind loads, Force Coefficients (Donnan et al, 1987)

	Drag C_D	Lift C_L
AS 1170.2 (non-porous)	0.90	-0.32
Non-porous	0.93	-0.72
90% Shade	1.00	+0.10, -0.17
70% Shade	1.10	+0.06, -0.16
50% Shade	1.15	+0.06, -0.13

These results provide indication that the lift pressure coefficients on the roof of a large porous flat canopy will be of lower magnitude than the lift coefficients for a non-porous roofed canopy. The results also indicate that the drag pressures on the walls of the canopy will be similar or greater than that for a non-porous windward facing wall. The results presented give the resultant overall forces on the canopy, but do not provide any information on the distribution of the pressure for example on the leeward wall of the model. Net pressure coefficients for all the canopy surfaces are required for the structural design of large flat roof canopies and hence further research is required beyond that presented in this paper.

2.4.3 Integrated Structural Design Methodology for Agricultural Protecting Structures Covered with Nets (Briassoulis and Mistrionis, 2010)

Briassoulis and Mistrionis at the Agricultural University of Athens, Department of Agricultural Engineering, present in this paper a comprehensive summary of recent research that has been carried out for the determination of wind loads on porous structures (Briassoulis and Mistrionis, 2010). It is concluded that the wind load reduction for a porous net relative to a non-porous cover is not proportional to the porosity of the net, and additionally depends on the position of the net relative to the wind flow.

A summary of results obtained for wind breaks is presented, referencing Richards and Robinsons' work together with pressure coefficients provided by the Eurocode 1 and ANSI Standard. Also provided is a summary of results obtained for a porously clad elevated panel under wind load. They comment: '... the determination of load requirements represents the first step in the design procedure. However, the calculation of loads for porous agricultural protecting structures has not been the subject of any national or European standard or code of

practice.' The paper also emphasises the load carrying capacity and mechanisms of the net, particularly relevant where frequent snow and hail loads are to be carried by the nets, reflecting the different climatic conditions in Greece and Southern Europe from those in Australia.

A comprehensive review of current research into loads on net structures is presented with reference to their own previous work and the work by Richards and Robinson, Letchford et al (2000) and Robertson et al (2002). They present results from their research for a freestanding pitched roof canopy with a roof slope of 20°, a height at the ridge of 5m and width of 4.8m. The structure is considered unblocked and blocked underneath. The results have been obtained using numerical methods with Computational Fluid Dynamics (CFD) numerical modelling and are shown in **Tables 2.2** and **2.3**.

In the tables solidity refers to (1 - porosity). The pressure coefficient C_{p-net} is the net pressure coefficient for the forces acting on the canopy roof. The windward C_{p-net} refers to the windward half of the canopy roof and the leeward to the leeward half of the roof.

Table 2.2 - Net Pressure Coefficients for an Empty Free Standing Pitched Canopy Roof with Pitch Slope 20° (Briassoulis and Mistrionis, 2010)

Name of Net	Solidity %	C_{p-net} Windward	C_{p-net} Leeward
FRU26	18	0.1	-0.1
OMBR70	46	0.2	-0.2
BIO 50	67	0.4	-0.2
OMBR 70	79	0.4	-0.3
AGREW	96	0.5	-0.5
FILM	100	-0.5	-1.0
EUROCODE	100		-0.9

The pressures increased when the structure was modelled as fully blocked under, where there is solidity under the canopy roof preventing free flow of the wind beneath. It is noted that the Eurocode-1 (CEN, 2005b) provides C_f values only for non-porous canopies. The non-porous film result is significantly different than the Eurocode value, but it is not commented upon by the authors.

Table 2.3 - Net Pressure Coefficients for a Fully Blocked Free Standing Canopy Roof with Pitch Slope = 20° (Briassoulis and Mistrionis, 2010)

Name of Net	Solidity %	C_{p-net} Windward	C_{p-net} Leeward
FRU26	18	0.0	-0.2
OMBR70	46	0.0	-0.7
BIO 50	67	-0.4	-1.4
OMBR 70	79	-0.6	-1.6
AGREW	96	-1.3	-1.7
FILM	100	-2.3	-1.8
EUROCODE	100	-1.3	

Briassoulis and Mistrionis also used numerical methods to predict the pressure coefficients on a flat porous roof with a height of 4m and width of 4.8m shown in **Table 2.4**. The zones referred to in the table G,H,I are defined by Eurocode1 : a) G-zone ($x < h/5$); b) H-zone($h/5 < x < h$); and c) I-zone ($h < x$), where x is the distance from the windward eave and h is the height of the flat roof.

Table 2.4 - Aerodynamic Coefficients for a Flat-roof House (Briassoulis and Mistrionis, 2010)

Name of net	Solidity (%)	C_p -net h/5 G-Zone	C_p -net h H-Zone	C_p -net >h I-Zone
LIBEC30	29	0.0	0.0	0.0
SHNT	60	-0.1	-0.1	-0.1
OMBR 70	79	-0.3	-0.2	-0.3
FILM	100	-2.6	-1.1	-0.8
EUROCODE	100	-1.2	-0.7	-0.2/0.2

The results show the large reduction in magnitude of coefficients from non-porous to the most porous material, where zero coefficients are predicted. Additionally, for the porous roofs, the pressures do not vary significantly with distance across the roof.

The paper also considers snow and hail loads and proposes that for a canopy constructed in a temperate climate, provision for a minimum hail load should be allowed for when designing the net. This has not necessarily been the case in Australia where large net spans for flat roofs have been chosen to gain site coverage and the net has been repaired or replaced if damaged by hail. As discussed in this chapter, there has also been the development of pitched roof designs which allow the shedding of the hail. Other loads considered are the permanent self weight of the net and structure and also loads from covered orchard trees within the canopy interacting with the net. The net permanent loads are given as being in the range of 15g/m^2 to 180g/m^2 . This is similar to the nets used in Australia where some of the higher level shade nets weigh 250g/m^2 . Generally loads from the trees have been ignored in Australia as they are designed with good clearance from the trees, but may be relevant in some orchard conditions. Load combination factors are considered with reference to the European Codes.

The paper presents research into the design and load carrying capacity of the net. Non linear finite element analysis can be used to analyse the net's capacity once the net's behaviour under load is tested and physical properties for the weft and warp directions are determined. The support of the net with cables is considered and the concept of analysing the cover as an orthotropic membrane system proposed.

In conclusion the paper proposes that the design methodology presented ‘...can lead to designs at a minimum construction and material cost satisfying simultaneously well established margins of safety in accordance with the relevant provisions of the Eurocodes.’

The numerical modelling of a flat roofed shade house has produced results that can be compared with the wind tunnel testing of the porous models in this project, but does not provide adequate information to provide peak wind load coefficients for the design of a large net canopy. The information on the distribution of the pressure coefficients across the walls and roof are limited and the results provided are only for a wind direction of $\theta = 0^\circ$ normal to the modelled canopy. Additional research to that presented is again identified as being necessary.

2.4.4 Mean Wind Loads on Porous Canopy Roofs (Letchford et al, 2000)

This paper presents the results of research at the University of Queensland where wind loads on free pitched and mono-slope porous roofs of varying slope were predicted by wind tunnel testing (Letchford et al, 2000). Research was carried out into the loss of pressure which occurs when a normal wind flows through a porous surface. The loss of pressure was compared for a number of commercial net fabrics and perforated metal screens used in the test models. The representation of porosity as a physical ratio of (1- the solid area) divided by the total area is refined by the introduction of an experimentally based loss coefficient K which is defined in **Equation 2.7**. This approach is similar to the work Richards and Robinson reviewed in Section 2.4.1 where Richards and Robinson used both theoretical and experimental approaches to establish the loss coefficient for a number of materials.

$$K = \frac{P_u - P_d}{\rho \bar{U}^2 / 2} \quad (2.7)$$

where K = loss coefficient

P_u = upstream static pressure

P_d = downstream static pressure

\bar{U} = average approach velocity

ρ = air density

Similar area porosity fabrics or screens, which show different pressure losses because of differing construction, are compared with the loss coefficient K. This allows the pressure measurements on the porous perforated mesh models to be related to and compared with commercial shade fabrics.

The models tested were open under the roof with no walls or blockage. **Figure 2.23** shows the model configurations.

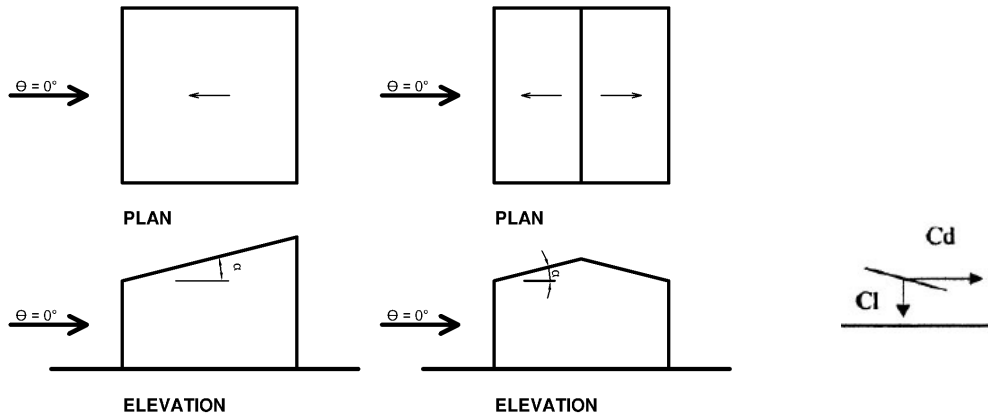


Figure 2.23 Model Configurations for Testing by Letchford et al

A series of models constructed with steel perforated plate surfaces were placed in the wind tunnel and forces on the particular model were measured by force balance or pressures measured through tapping tubes connected to the model. The perforated plates were tested for pressure loss under a normal wind flow and compared with nets of varying porosity which were also tested for pressure loss under normal wind flow.

The mean force coefficients measured on the canopy models were plotted against the porosity of the material tested. The forces were expressed as coefficients derived from the mean dynamic pressure at eaves height and the projected area. The drag coefficients, C_d and lift coefficients C_l are as shown in **Figure 2.23**. The results for the pitched roof models are shown in **Figure 2.24**.

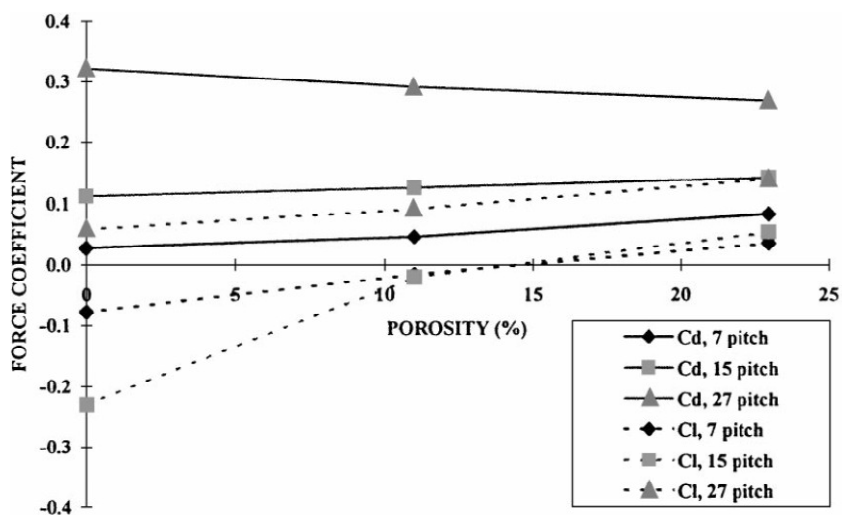


Figure 2.24 - Drag and Lift Coefficients for Three Pitches of a Gable Roof at 0 Degrees Azimuth (Letchford et al, 2000)

For the lowest pitched roof of 7° the mean force coefficients vary between -0.1 and 0.1, similar to the numerical results of Briassoulis (Briassoulis and Mistriotis, 2010), although model dimensions differ between the two projects. Drag values increase significantly with increased pitch, but decrease with porosity for the 27° canopy. The lower pitches however show an increase in drag coefficient with porosity. The authors used flow visualisation on a 15° gable roof and found ‘... that porosity induces flow through the windward roof preventing reattachment beneath this section of the roof and thereby increasing both the upper surface load through increased stagnation area and lower surface load through prevention of pressure recovery after reattachment. It was found that, for steeper pitch roofs, the reattachment does not occur so readily.’ It is also concluded that: ‘... the leeward roof experiences reduced loading because the separation bubble formed on the upper surface at the ridge line is vented somewhat while the lower surface experiences a much more significant wake effect from the flow through the windward roof section’ (Letchford et al, 2000).

The influence of wind flowing through the windward section and the venting of the separation bubble at the ridge indicate that porous structures will behave differently from non-porous structures under wind load. The free, mono-slope roof results are shown in **Figure 2.25**.

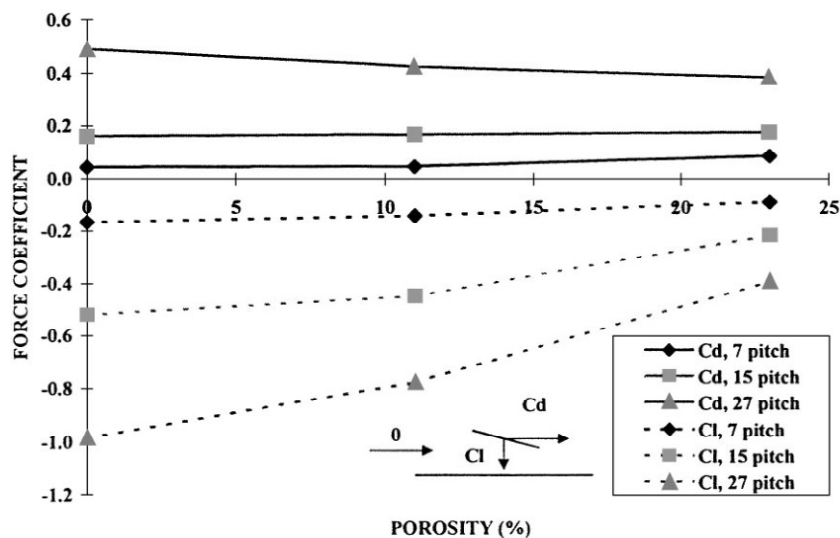


Figure 2.25 - Drag and Lift Coefficients for Three Pitches of a Mono-slope Roof at 0° Azimuth (Letchford et al, 2000)

As the pitch reduces and approaches the flat roof, the drag and lift coefficients reduce to below ± 0.2 . Significantly the lift coefficients decrease with increase in porosity for all of the pitches, for the 7 degree pitch, the drag coefficient increases slightly with porosity.

The paper does not present research into enclosed canopies with flat roofs and walls, but provides insight into a successful methodology of measuring wind forces on porous surfaces.

The lowest pitched roof (7°) model provides results that indicate the likely wind action behaviour on a flat roof.

2.4.5 Wind Pressures on Permeably and Impermeably-clad (Robertson et al, 2002)

Robertson et al carried out wind tunnel testing on a shade house with a flat roof of 6m span and 1.68m height and rounded eaves (radius of curvature 0.33m), shown in **Figure 2.26 (Robertson et al, 2002)**. Testing was done at a scale of 1:2 and insect and shade net together with non-porous film were used in the testing. The open area of the two nets was measured under a microscope and the pressure loss coefficients for a flow normal to these porous materials were also measured.

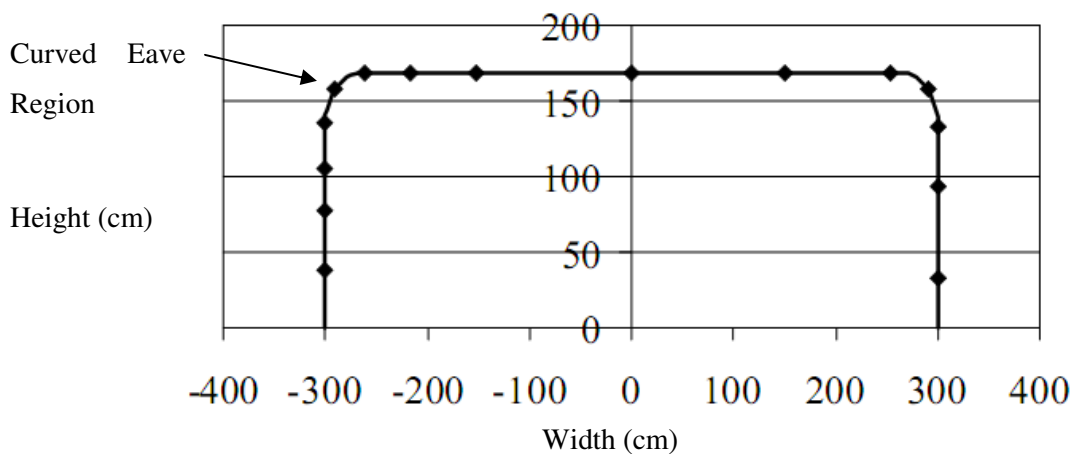


Figure 2.26 - Cross Section of Model of Flat Roofed Shade Structure Tested by Robertson et al

The units in this figure are in centimetres and the horizontal and vertical axes show the horizontal and vertical dimensions of the model cross-section.

The following mean external pressure results in **Figure 2.27** (Robertson et al, 2002) were obtained for a solid film, insect net of 33% open area and a shade net of 39% open area. The coefficient C_{pc} is the mean external pressure coefficient measured in the wind tunnel with positive direction towards the shade house surface.

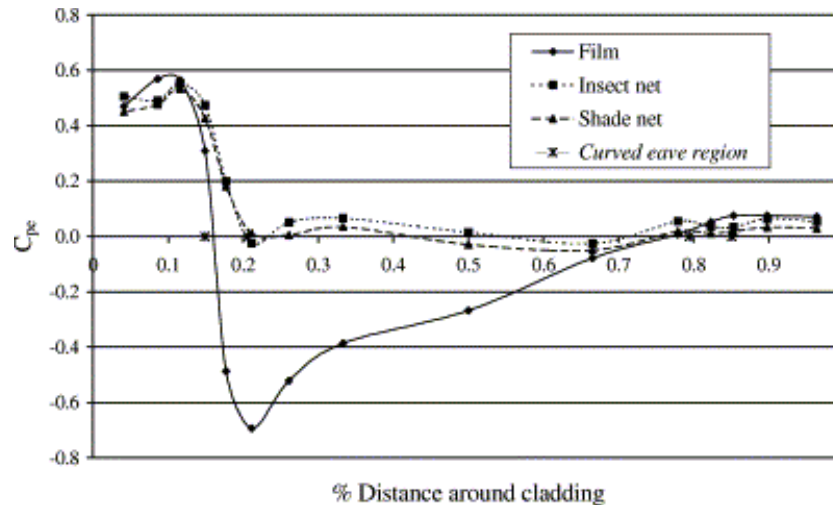


Figure 2.27 – Mean Pressure Coefficients on the walls and Roof of a Flat Roof Shade House

The first section of the graph shows the film and two nets producing a similar positive pressure coefficient of 0.5 to 0.6 on the wall of the model. At the curved eaves area there is significant change from the drag pressure coefficients measured on the wall, with the maximum uplift pressure coefficient for the solid film being -0.7 on the roof after separation of the wind from the structure occurs. The roof pressure coefficients for the insect and shade net reduce to within +/- 0.1, showing little separation effects at the wall roof intersection. The authors conclude: 'the principal findings were that the high external suction developed over parts of each structure when impermeably clad were destroyed when permeably clad, resulting in virtually no net uplift'. Additionally the positive drag pressures on the wind ward wall was found to be virtually unaffected by the porosity.

The internal pressure coefficients measured were found to be consistently small for the two net structures (< 0.05), although it is commented that there may have been a bleeding of the internal pressure through the gable ends due to the experimental set up. The authors comment that further experimental work needs to be carried out to provide reliable data for the design of porous clad structures. This would include varying the wind direction relative to the porous clad structure, additional measurement of the internal pressure to ensure no leakage of air is occurring and also more roof pressure measurements.

2.5 Review Summary

From the research reviewed, the wind velocity at a porous surface is reduced, but not to zero as with a non-porous surface. The flow of air through the surface to the interior of a canopy creates an internal pressure, and the difference of this internal pressure to external pressure at the canopy's external surface determines the net wind action normal to the surface. The reduction of the air velocity through the porous surface is influenced by the porosity of the structure's

material, the material's construction, or in the case of nets, the weave, and the Reynolds number generated by the air flow through the material.

Porosity is both presented in terms of measured open area divided by total area and also in terms of a loss coefficient which also takes into account the construction of the porous material. Richards and Robinson determine the loss coefficient both theoretically and experimentally and also present the concept of an equivalent porosity referenced to the loss coefficient of a round wire screen. Letchford et al determined experimentally the loss coefficients for the various model screens used in their wind tunnel research and compare these loss coefficients with those of commercial porous fabrics.

Donnan, Robertson et al and Letchford et al have carried out wind tunnel testing to measure wind actions on constructed scale models. Donnan's model was a flat roofed open structure, whereas Letchford et al investigated monoslope and pitched roof models of typical greenhouse structures. Robertson et al investigated an enclosed green house model measuring both external and internal pressure coefficients. Briassoulis and Mitriotis used numerical computer modelling to investigate the pressure coefficients on a range of mono slope and pitched porous structures.

The results from the wind tunnel testing and numerical modelling, show that porosity leads to significant reduction in wind actions on the roof of a flat or low pitched roofed structure. Mean lift forces on the flat or low pitched porous roofs tended towards zero, whereas the wind actions on the walls were found to be of similar magnitude to the actions on a non-porous cladding.

The large canopies being studied by this project have large cable spacing and spans, generating significant cable forces and displacements under small wind pressures. Although the wind actions on the porous roof surfaces can be expected to be small in comparison to the pressures on a non-porous roof surface loaded in the same conditions, the large roof tributary load areas to the cables generate large actions on the structure. This is illustrated in **Figure 2.28**, showing a 14m spaced cable, with design wind pressure of 1kPa and pressure coefficient of -0.1, resulting in a distributed load $q = -1.4\text{kN/m}$. This can be compared to the wind load that acts on a purlin supporting a steel clad roof with design wind pressure = 1kPa, uplift pressure coefficient of -1.1 and purlin spacing = 1.2m, producing a similar force/m of -1.32kN/m. If the porous roof design coefficient for the cable load varies from -0.1 to -0.2 or -0.05, it can be seen that the total load is halved or doubled, illustrating the sensitivity of the load to very slight changes of the pressure coefficient.

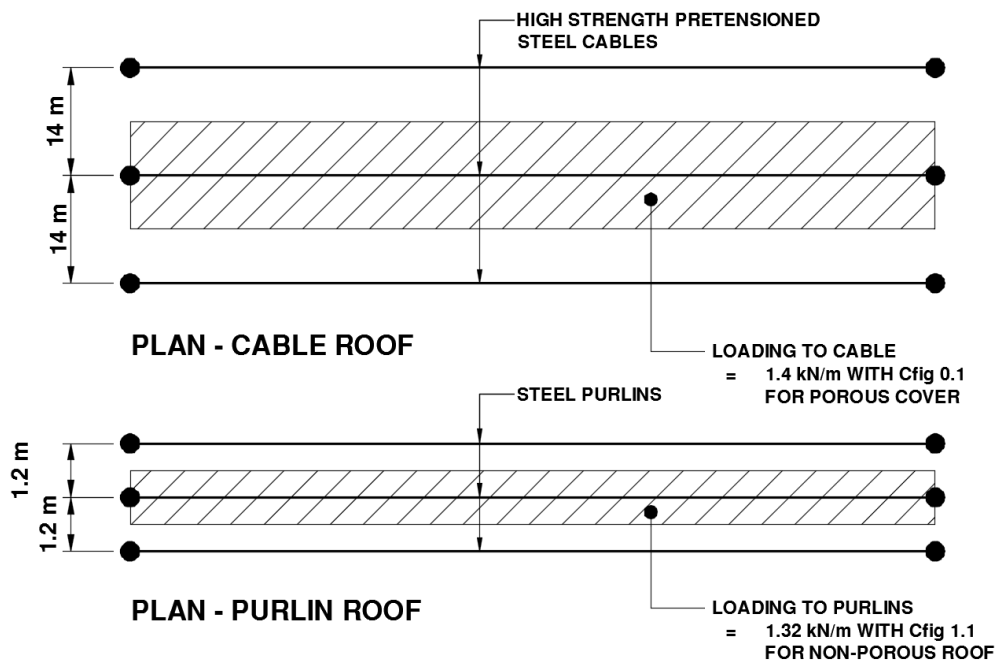


Figure 2.28 Typical Roof Support Member Loads for Porous and Non-Porous Roof Members

The gaps in current research indicated by the literature survey include:

- The research reviewed has only been carried out on relatively small greenhouse structures with much larger height to breadth ratios than are present in the large flat canopies.
- There are no in-depth studies of the resulting wind actions on large flat porous roofs.
- There are no results for wind actions on sloping walls which are prevalent in the large protective canopy industry.
- The research presents the measured mean pressure coefficients rather than the peak maximum and minimum coefficients.
- There is limited measurement of internal pressures in enclosed canopies and no study of the variation of internal pressure along a porous structure's interior.
- There is no examination of the resulting actions from the wind direction changing through 360°

This project seeks to fill these gaps by wind tunnel scale model testing of a series of flat roofed canopy models with varying porosity.

3. Experimental Methodology

3.1 Overview

In this study, the characteristic distribution of wind actions on large flat porous canopies has been investigated by testing scale models of a typical protective canopy in the Boundary Layer Wind Tunnel at the Cyclone Testing Station, James Cook University. Four models of identical geometry were constructed, each with different cladding to vary the porosity, but maintaining identical dimensions. Pressure taps were fixed to the external surfaces of the models and several taps installed inside the model to measure internal pressure. The taps were connected to the wind tunnel's Dynamic Pressure Measurement System (DMPS) with tuned plastic tubes. A series of test pressure measurement runs on each model was then carried out, with the wind direction relative to the model being varied in 15° increments.

The pressures recorded by the DMPS were analysed and adjusted for the wind velocity at the model's roof relative to the wind velocity measured at a height of 500mm. Mean, maximum and minimum pressure coefficient results are presented graphically and analysed for changes in magnitude, due to the different porosities of the models. Net pressure coefficients on the models' surfaces are then derived by finding the peak values of the sum of simultaneous external and internal pressures at each tap location using the time based history of the data recorded. These values are divided by a gust factor squared to provide a pseudo-steady coefficient value consistent with the design coefficients specified in AS/NZS 1170.2 (2011). The coefficients are reviewed and conclusions drawn on the behaviour of large porous flat roof canopies under wind actions.

3.2 The Boundary Layer Wind Tunnel

The atmospheric boundary layer wind tunnel is located at the Cyclone Testing Station in the College of Science, Technology and Engineering at James Cook University (JCU). The 22.0m long tunnel has a cross section of 2.0m high x 2.5m wide. A 2.43m diameter 5 blade fan is located at the downstream end of the tunnel with a diffuser. The fan is powered by a 45kW Brook squirrel cage induction motor with a variable speed drive.

The atmospheric boundary layer was modelled to a length scale of 1/250 by installing a 250mm trip board and carpet to the tunnel floor to provide a suitable roughness to represent a Terrain Category 2 as defined in AS/NZS 1170.2(2011).

The turbulence intensity of the wind tunnel set up is shown in **Figure 3.1** with comparison to the turbulence intensity profile specified in AS/NZ1170.2 for terrain category 2, where

turbulence intensity I_u is defined as the ratio of the fluctuating component of the wind speed to the mean speed.

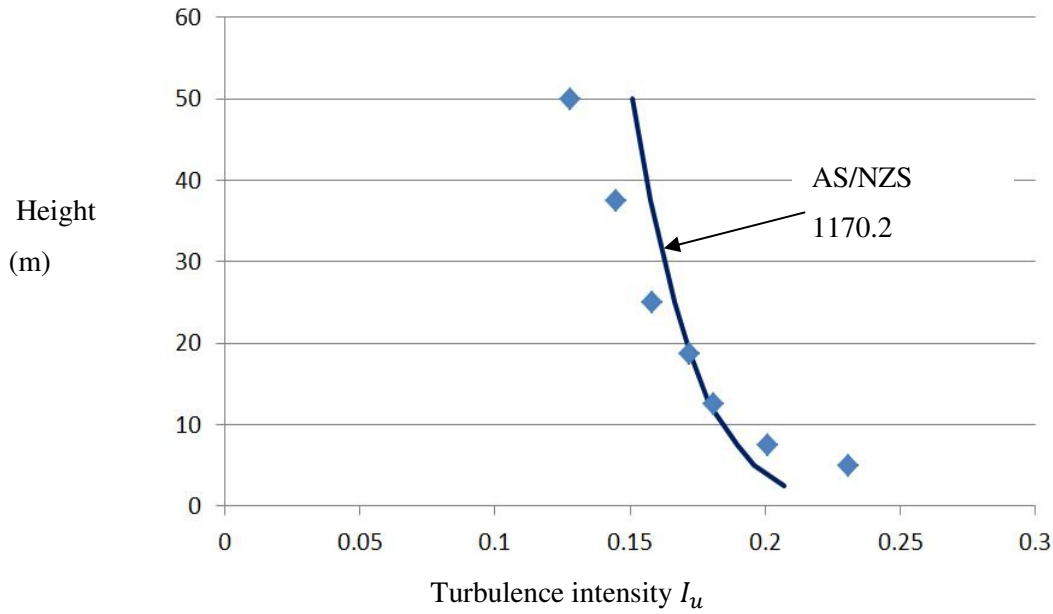


Figure 3.1 Turbulence Intensity Profile

Figure 3.2 shows the wind tunnel mean velocity profile with comparison to AS/NZS 1170.2 terrain category 2 profile.

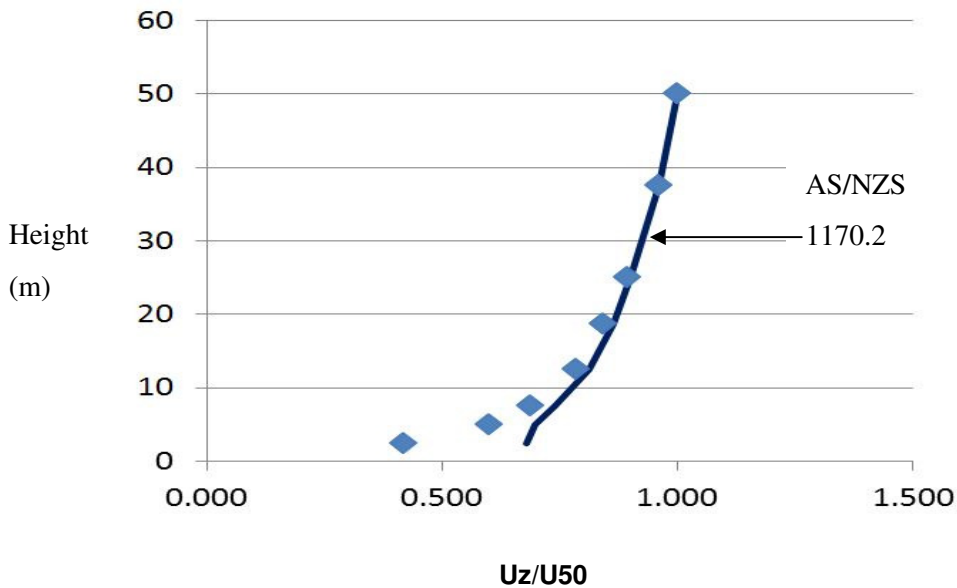


Figure 3.2 Wind Tunnel Mean Velocity Profile

A length scale $L_r = 1/250$ and a velocity scale $U_r = 1/2.5$ are used for the experiments. This gives the time scale T_r calculated by **Equation 3.1**.

$$T_r = L_r / U_r = \frac{1/250}{1/2.5} = 1/100 \quad (3.1)$$

For a 30 second test, the modelled wind duration T is found by **Equation 3.2**.

$$T = 30 \times 100 / 60 = 50 \text{ minutes} \quad (3.2)$$

A pitot tube is located 500mm above the floor upstream of the model to measure the static and total head for calculation of wind velocity in the tunnel.

The models, built at the scale $1/250$, were individually placed on a turntable just upstream of the fan. The turntable is able to rotate 360° to test multiple wind directions and was rotated in increments of 15° for the tests.

The pressure tapping tubes installed on the models were connected with tuned 1.5mm plastic tubes to the transducer, the Turbulent Flow Instrumentation (TFI) DPMS. The DPMS houses a pressure module of 64 pressure channels, each with its own pressure transducer. The system is capable of sampling data at very high frequency. The pressure transducers and tubing frequency response for the data acquisition system are calibrated by the manufacturer.

All pressures were filtered at 625Hz and sampled simultaneously at 1250Hz for 30 seconds. The minimum, mean, maximum and standard deviation of the wind pressure at each tap was then calculated by the recording software. Performing three tests at each location allowed for a mean of each of these to be calculated and provides a measure of variability.

The results were normalised using the wind tunnel mean velocity profile, converting from the velocity measured at 500mm above the floor of tunnel to the velocity at roof height of model (25mm) using the relationship given in **Equation 3.3**.

$$Cp_h = Cp_{500} \times \left(\frac{1}{x}\right)^2 \quad (3.3)$$

Cp_h = pressure coefficient at required height (roof of model, 25mm)

Cp_{500} = pressure coefficient at 500mm height

Normalising factor (Velocity ratio) for 25mm height $x = 0.605$

The mean, maximum and minimum pressure coefficients were found using **Equation 3.4**.

$$C_{\bar{p}} = \frac{\bar{p}}{\frac{1}{2}\rho\bar{U}_h^2}, \quad C_{\hat{p}} = \frac{\hat{p}}{\frac{1}{2}\rho\bar{U}_h^2}, \quad C_{\check{p}} = \frac{\check{p}}{\frac{1}{2}\rho\bar{U}_h^2} \quad (3.4)$$

\bar{p} , \hat{p} , \check{p} are mean, maximum and minimum pressures

$\rho = \text{Density of air}$

$\bar{U}_h = \text{Mean wind speed at roof height of 25mm in model scale}$

Chapter 4 presents the external and internal pressure coefficient results graphically for $\theta = 0^\circ$ and 45° wind directions. The results are investigated for the influence of the porosity on the resulting wind pressure coefficients and compared with the non-porous model.

3.3 Selection of Test Model Dimensions

Net protection canopies have frequently a footprint of several hectares, fitting the land area of asset to be protected. A full scale structure of roof area 196mx196m and 6.25m high was selected as a typical canopy for modelling after investigating the dimensions of large protective canopies constructed in Australia. These dimensions also suit the typical 14m roof cable spacing often used in practice to accommodate the common 14m net roll width. Walls inclined at 45° were adopted, a typical arrangement which allows the side netting to be supported by the inclined tie back cables, creating additional protected space. The inclined walls have the added benefit of providing improved aerodynamic characteristics of the structure compared to vertical wall construction, leading to reduced wind actions on the structure. The height of 6.25m is typical for large flat canopies and allows room for mobile machinery to operate and the growth of plants as well as good air circulation. The ratio of height to width and length is small (0.031), a significant feature of the large net structures. The geometry of the full sized structure modelled is shown in **Figure 3.3**.

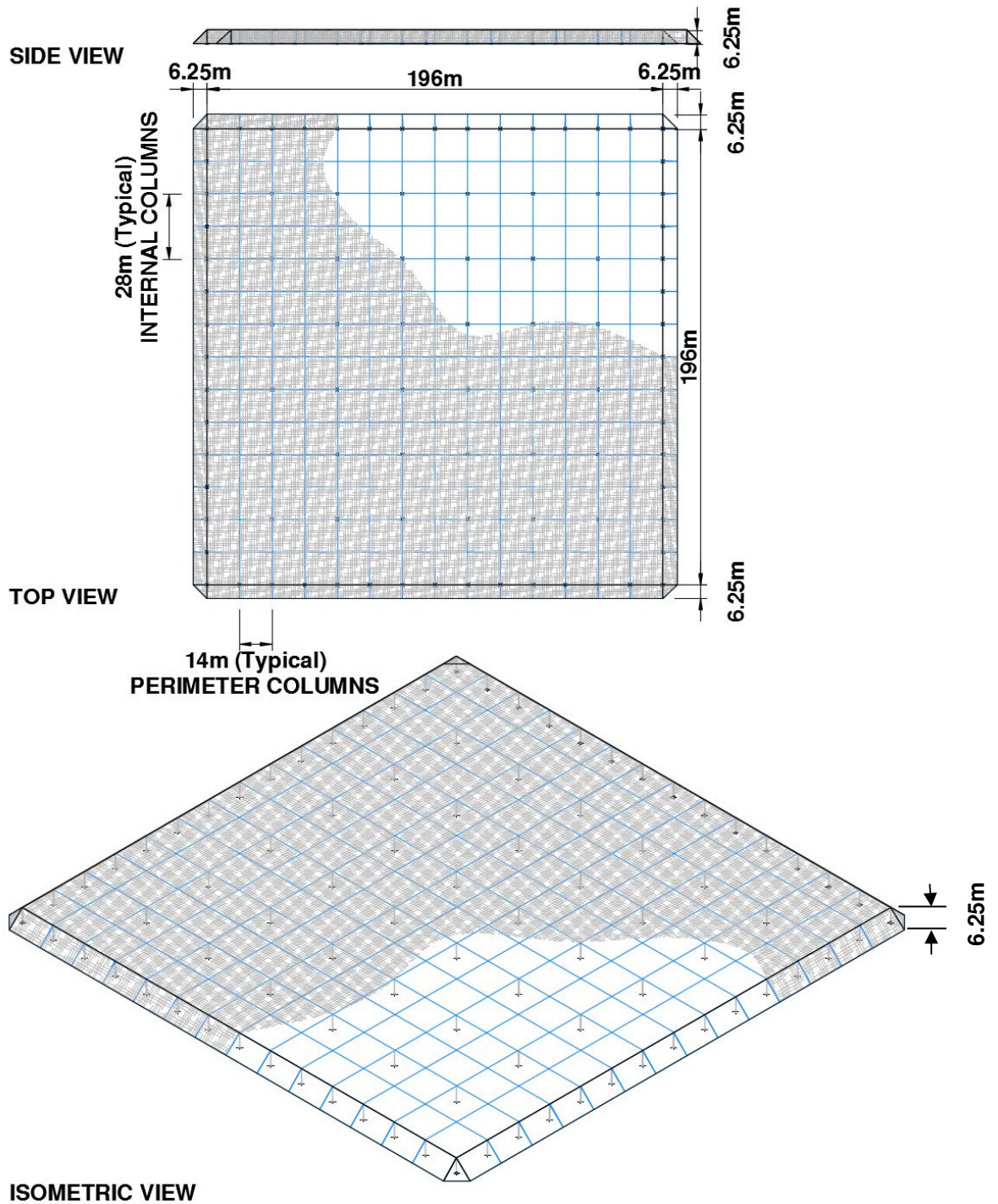


Figure 3.3 Full Scale Large Flat Roofed Porous Canopy used for Scale Modelling

This selected canopy structure was modelled at a scale of 1:250. This gives a model roof size of 784mm square and a height of 25mm as shown in **Figure 3.4**. The overall footprint including the sloping walls is 834mm x 834mm which was a suitable size for placement in the wind tunnel. The wind direction for the testing is shown as the angle θ .

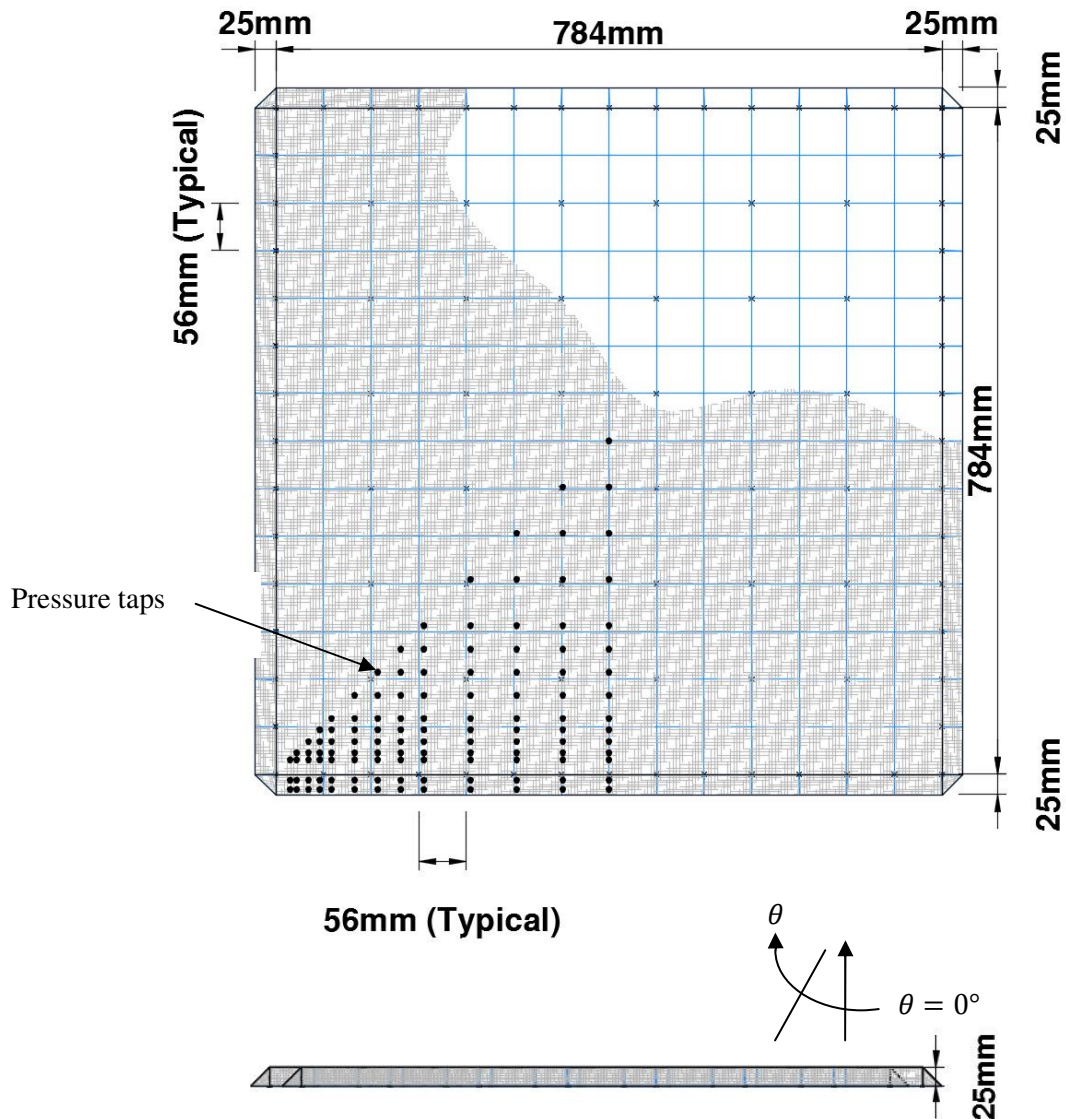


Figure 3.4 Scale Model Dimensions

The symmetry of the models allows the tapping of one eighth of the model, which can then be rotated to achieve pressure test results for the full roof and wall areas. The first non-porous model was tapped across one quarter of the model and the three porous models tapped across one eighth. **Figure 3.5** shows the detailed dimensions of the locations of the tapping points and labelling. A grid system of alphabetic letters and numbers was set up to identify each tapping point e.g. A5. This allowed the plastic connecting tubes to be tagged with the tapping point name and be identified at the numbered transducer channel. Results then could be identified and related to the correct tapping point on the structure.

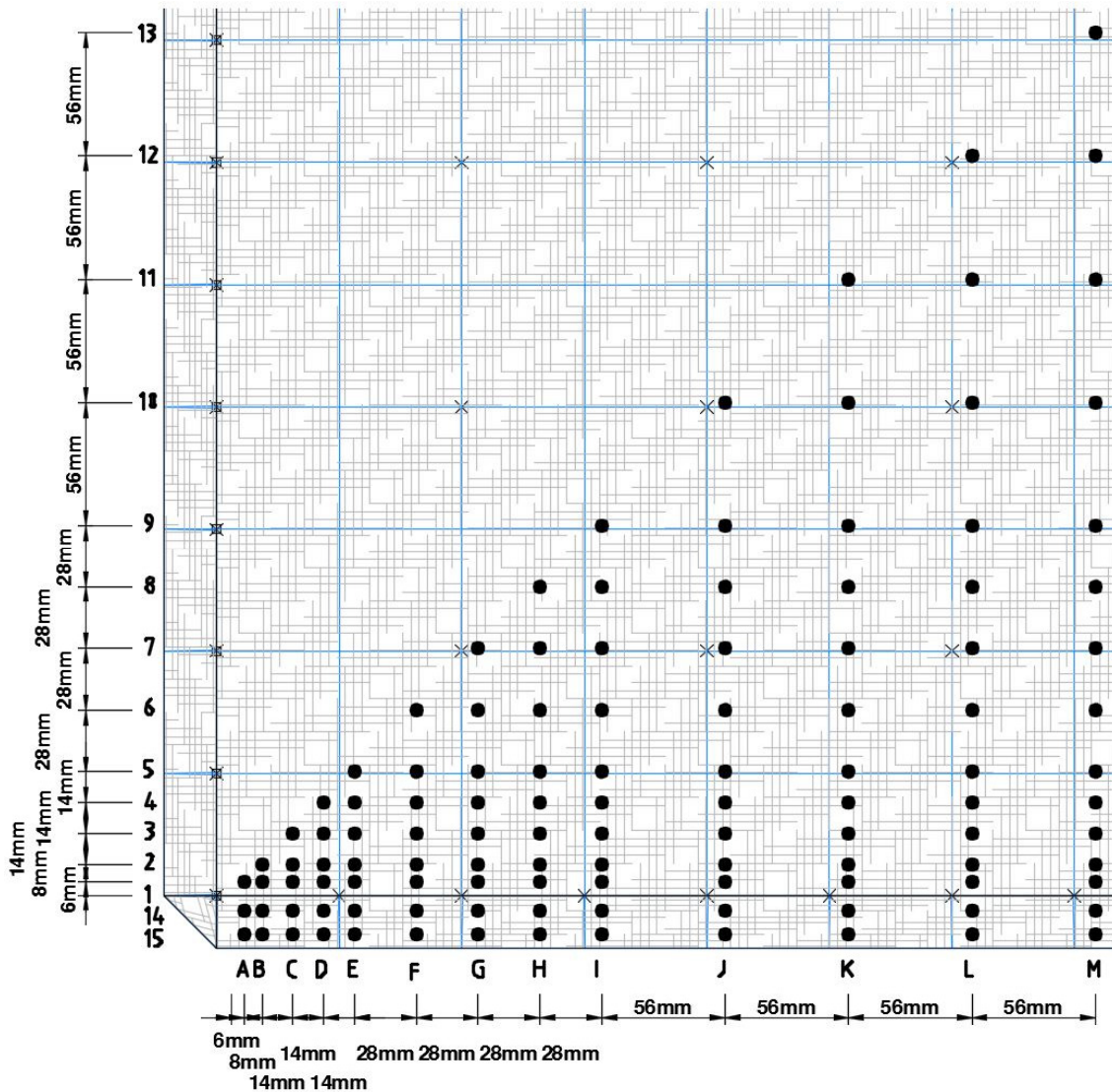


Figure 3.5 Tapping Points and Identification Grid

The external pressure measurement arrangement allows up to 62 tapping points on the external surface of the model and one point internally, located centrally on the model floor, to be connected and measured during one run of measurements. One additional measurement channel is used to measure the wind speed upstream from the model at 500mm above the wind tunnel floor using the pitot tube installed for this purpose. Two separate test runs of the model were required to allow testing at all the tapping points in the eighth sector. The points were distributed across the sector with a greater density of points close to the roof edge to examine edge separation effects and associated higher external pressures. Two rows of taps were located on the walls at one third (8mm) and at two thirds height (16mm). The model was rotated through 360 degrees in the tunnel in increments of 15 ° and tested three times at each location. This sequence of tests was repeated twice providing six sets of results for each tap location at each increment of rotation.

The model was placed on the turntable and the tapping tubes, welded onto the Model surfaces, were connected via the tuned plastic tubes to the transducer channels. The base of the Model was sealed with the tapping tubes connected to each side of the non-porous floor to ensure that no air flowed through the base of the model. Initial tests on the porous models showed that leakage through the bottom had a significant effect on the results with the air flow through the model being diverted out the floor opening and altering the internal pressure conditions. Large downward forces were measured on the roof surface.

Figure 3.6 shows the model on the turntable in the wind tunnel and the connection of the plastic tubes to the tapping points.

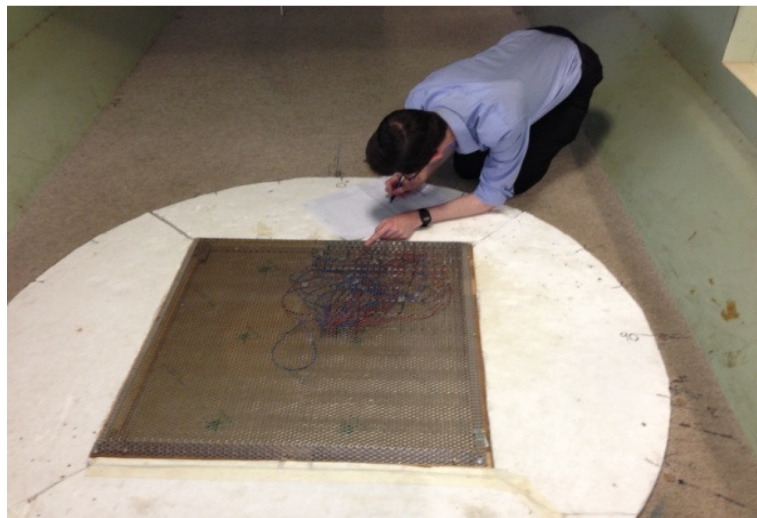


Figure 3.6 Connection of Plastic Tubes to Tapping Tubes Model on Turntable in Wind Tunnel

3.3 Models

Four models were constructed to the dimensions described in Section 3.2 with varying porosity. These porosities were 0% (non-porous), 19%, 38% and 58%.

3.3.1 0% Non-Porous Model –Model A

Model A was constructed from non-porous perspex and pressure taps drilled and tubes then glued in place as shown in **Figure 3.7**. This model was tested for comparison with the porous models and also with the pressure coefficients for large flat roofs given in the design standard AS/NZS 1170.2:(2011).



Figure 3.7 - View of Underside of Model A with Tapping Tubes

The model was sealed around the edges so that no internal pressure variation was generated by the wind in the tunnel. Only external pressure measurements were recorded.

3.3.2 19% Porous Model – Model B

The 19% model tested was constructed from a perforated steel sheet to the same dimensions of the non-porous model A. The open area porosity was calculated as 19% with 6.3mm diameter holes at 13.8mm centres. A section of the perforated sheet is shown in **Figure 3.8**.

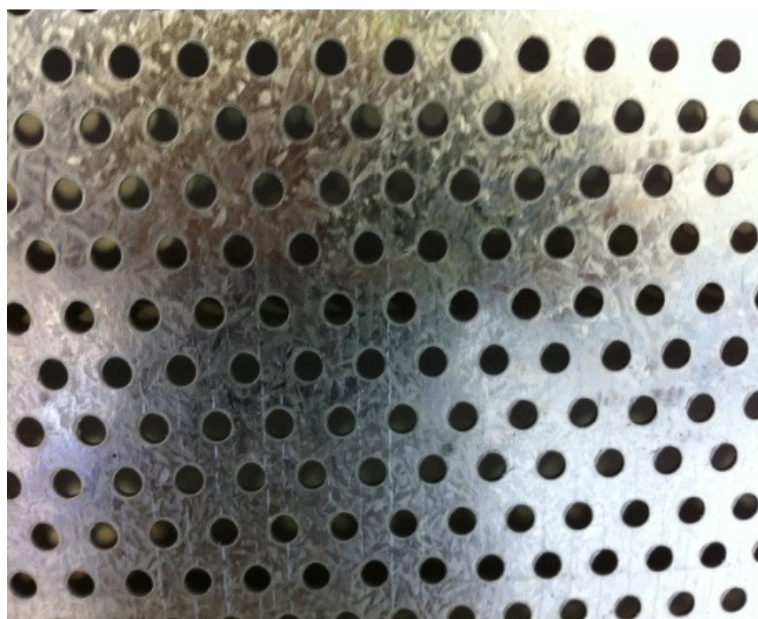


Figure 3.8 19% Porous Perforated Sheet for Model B

The tapping tubes were welded to the solid sections of the plate surface and connection of the plastic connecting tubes was aided by the rigidity of the plate model.

3.3.3 38% Porous Model –Model C

The 38% porous model tested was constructed using a fine brass mesh, which provided a similar material to a woven net with a regular grid of round strands, and is shown in **Figure 3.9** and **Figure 3.10**. The porosity by open area was measured as 38%. Tapping tubes were brazed onto the mesh, which was a time consuming exercise. The flexibility of the mesh made connections of the PVC connecting tubes slow and several of the small insert cylinders were pushed through the mesh during the connection process. The mesh was supported by light metal trusses.



Figure 3.9 38% Porous Model C using a fine Brass Mesh



Figure 3.10 Underside of Model C with Tapping Inserts and Support Trusses

The fine brass mesh used in the model is constructed with wire of diameter 0.18mm and with apertures of 0.315mm width. Barbagallo (Barbagallo, 2011) tested the mesh used for this model in a circular 600mm diameter wind tunnel at James Cook University and found that the pressure was reduced by 32% across the screen by measuring the difference between the static upstream and downstream pressures. The pressure loss factor was calculated using **Equation 2.7**(refer Section 2.4.4) as presented by Letchford et al (2000). This pressure drop percentage is not directly applicable to the model and its testing, due to the model being subject to external wind actions parallel to the roof surface and an internal pressure from the wind flow through the porous surfaces into the interior of the model. The inclination of the model walls at 45° also varied from the vertical mesh arrangement in the 600mm diameter wind tunnel. The loss coefficient of the brass mesh can compared to the loss coefficients of other porous materials including commercially used net fabrics and the perforated metal screens used on Models B and D.

3.3.4 58% Porous Model - Model D

A second model made from perforated steel sheet, with a greater open area percentage giving a porosity of 58%, was tested. The holes are 8mm in diameter and at 10mm centres on a 60° angle between rows as shown in **Figure 3.11**.



Figure 3.11 Perforated Sheet with 58% open area Model D

Figure 3.12 shows Model D placed on the turntable in the wind tunnel and **Figure 3.13** shows a close up of the corner of the model.



Figure 3.12 Model D on Turntable



Figure 3.13 Close up of Model D on turntable

This model has significantly higher porosity than the three other models tested (0%, 19% and 38%).

3.3.5 Determination of loss coefficient K

A series of measurements of pressure reduction across a number of commercial net fabric and the perforated metal screens used for Models B and D was undertaken by Mason at the University of Queensland in collaboration with the author and Netpro (Mason, 2016). The

measurements were carried out in the School of Civil Engineering's wind tunnel which is an open loop facility with two adjoining 760mm x 760mm x 1180mm test sections. A 25mm wide support frame was installed between the two test sections to mount each of the porous materials onto. The mounting frame has the effect of causing flow contraction due to the air passing through the smaller cross sectional area of the frame and varying the mean upstream and downstream wind speeds. This flow contraction varies from the testing referred to by C.W. Letchford et al , and referred to in 2.4.4 of this thesis and also the testing by Barbagallo of the Model C gauze fabric where no similar contraction occurred . The loss coefficient K is found by **Equation 3.5** which allows for the change in mean wind speeds up and downstream of the frame.

$$K = \frac{(P_{s,u} - P_{s,d}) + \rho(U_u^2 - U_d^2)/2}{\rho \bar{U}^2/2} \quad (2.7)$$

where K = loss coefficient

$P_{s,u}$ = upstream static pressure

$P_{s,d}$ = downstream static pressure

U_u = measured upwind wind speed

U_d = measured downwind wind speed

ρ = air density

The averages of the experimental results are shown in **Table 3.1** with the additional brass gauze (used in Model C) loss coefficient result from the testing at James Cook University by Barbagallo

Table 3.1 Loss Coefficients K

Porous Material	K
M1, Model B perforated sheet	32
M2, Model D perforated sheet	2.5
Brass Gauze	0.90
F1, 95 % shade cloth	51
F2, Heavy quad cattle shade	7.2
F3, 12mm Quad fabric	0.64
F4, 16mm Quad fabric	0.43
F5, 24mm Quad fabric	0.43
F6, 20mm bird net fabric	0.27

The results show that the loss coefficients for the Model B sheet (porosity by measured area of 19%) and Model D (porosity by measured area of 58%) are less than the coefficient for the 95% heavy shade cloth and slightly greater than the heavy cattle shade cloth with approximately 70% shade. The loss coefficient for the brass gauze is significantly less than that of the Model D perforated sheet which has higher area porosity, indicating that the wind flow through the mesh is greater than the perforated sheet. The loss coefficient K results are plotted against upstream wind speed U_s in **Figure 3.14**. **Figure 3.15** presents the pressure loss coefficients found by Letchford et al (2000) plotted against the material's Reynolds number.

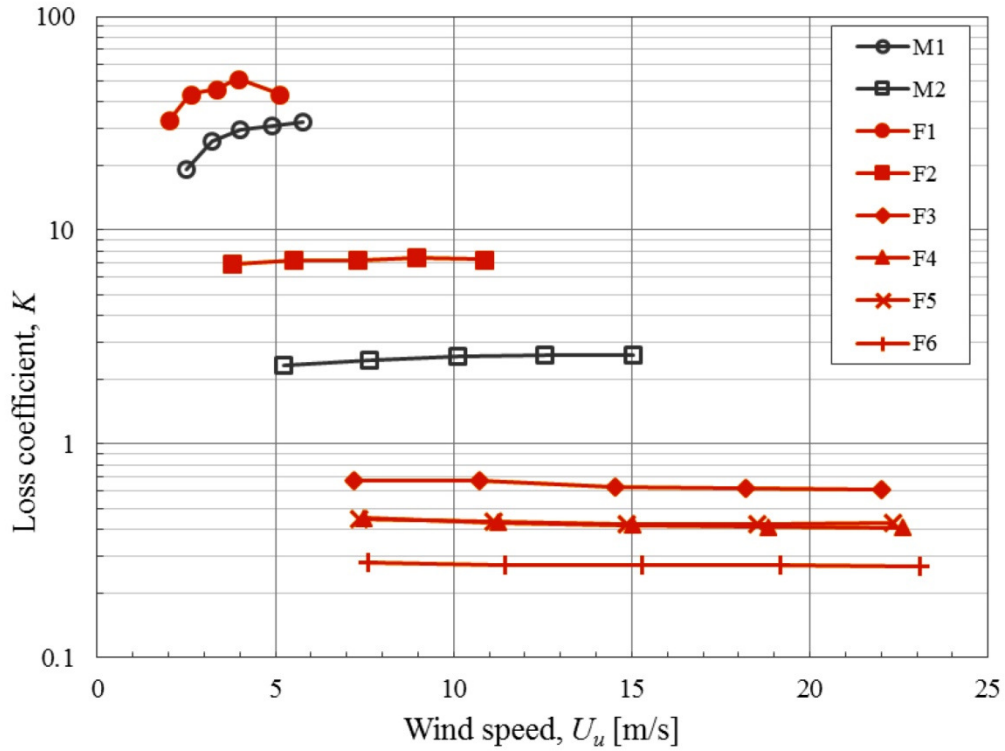


Figure 3.14 Loss factor K and mean upstream speed U_s

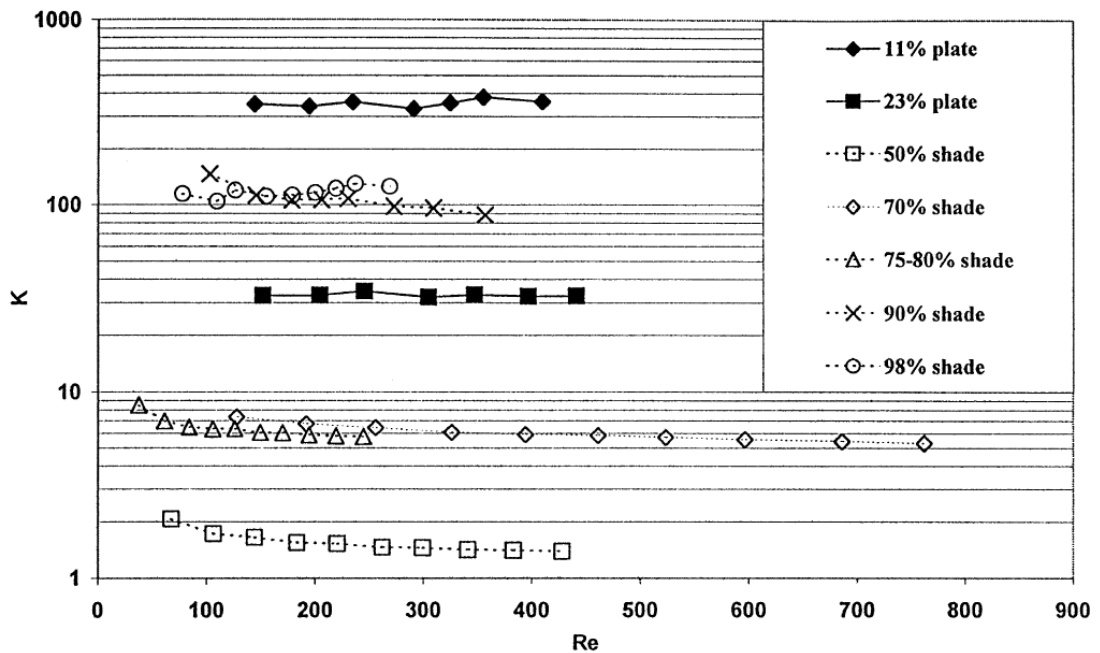


Figure 3.15 Pressure loss coefficient K as a function of Reynolds number (Letchford et al, 2000)

The pressure loss coefficient results shown in **Figure 3.15** are of a similar order to the results in **Figure 3.14** but demonstrate the variability of the loss coefficient for different materials and fabric weaves.

The loss factors presented can be used when applying the experimental results presented in this thesis to the design of commercial fabric structures that are constructed from the net materials referred to above (F1 –F6).

3.4 Testing of Internal Pressure and Combined Internal and External Pressure

It was identified that the internal pressure varies in magnitude along the model due to the wind passing through the porous models. Initially just one internal pressure measurement was taken in the centre of the model floor, but to obtain better understanding of the changing internal pressure and more accurate combined external and internal pressure results, testing of the internal pressure distribution across the floors of two of the porous models, Model B and Model C was undertaken. The arrangement across one-eighth of the model is shown in **Figure 3.16**. As for the external pressure measurements the model, was rotated through 360° to obtain a full model distribution of internal pressure.

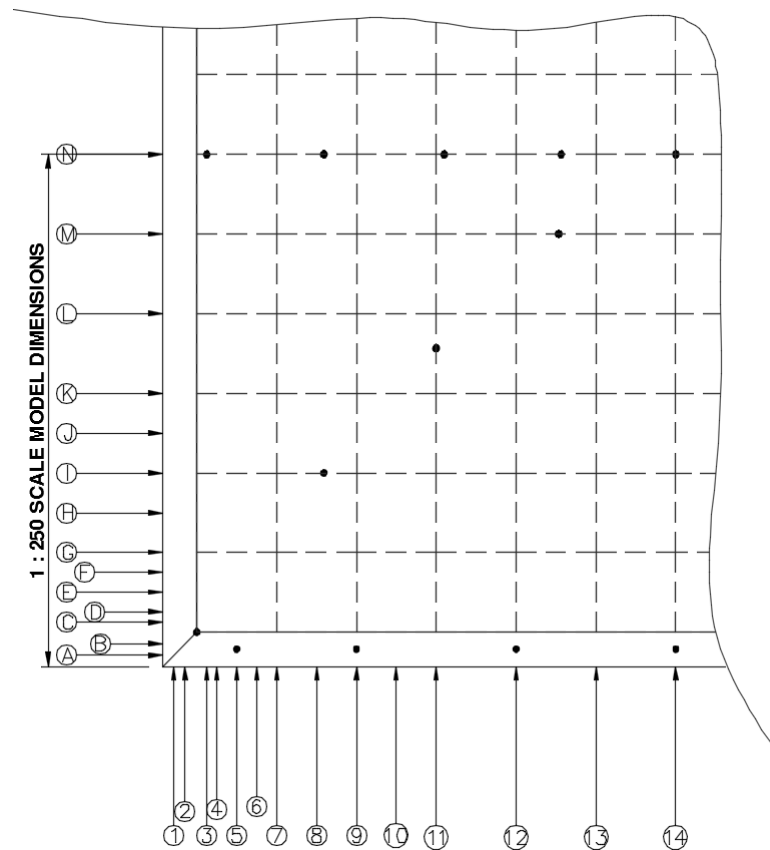


Figure 3.16 Internal Pressure Measurement Tap Locations, Model B and Model C

To measure the simultaneous internal and external pressures on Models B and C the number of external taps were reduced so that there was less interference to the internal wind flow from attached tubes. **Figure 3.17** shows the arrangement of external taps used and also references the internal tap measurement with which each external tap measurement was combined to obtain net pressure resultant values.

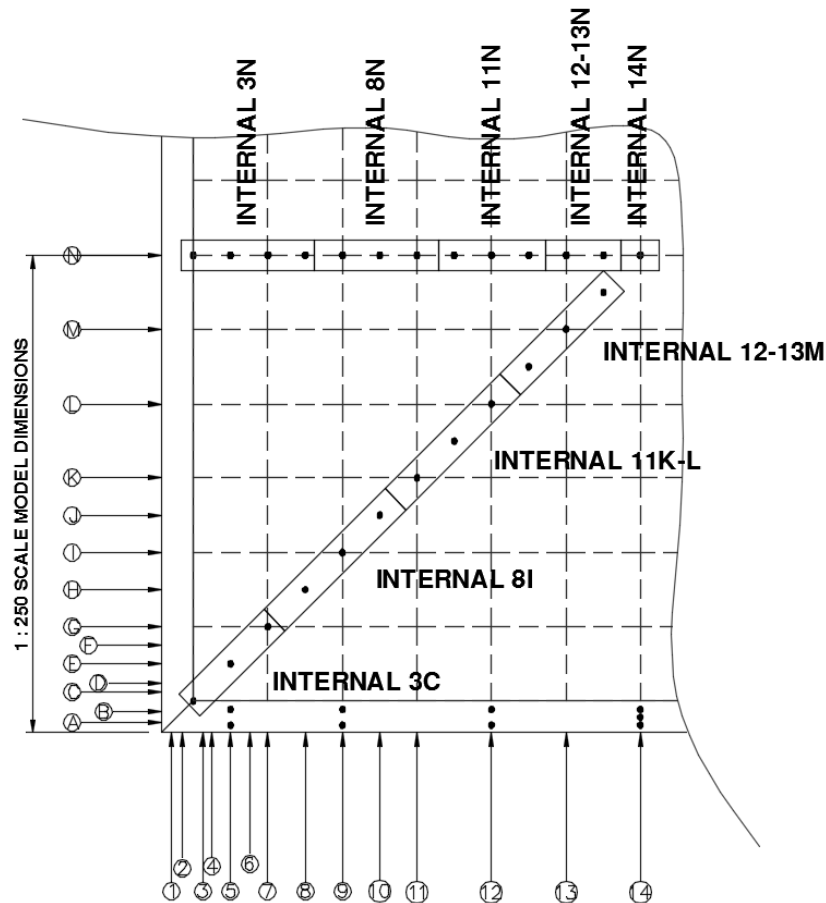


Figure 3.17 External Pressure Tap Locations for combined External and Internal Pressure Results, Model B and Model C

3.5 Graphical Presentation of the Results

In Chapter 4, the external roof pressure coefficient distributions for 0° and 45° directions are presented in colour contour plots of the complete roof surface, using the Matlab software to generate the plots. The horizontal and vertical axes of the plots are to the model dimensions divided by the height of the model h , creating a non-dimension plot from the model results. The pressures are shown by different graded colours referenced to a colour scale adjacent to the plot. In all of the pressure contour plots for the roofs of the four models, red indicates the maximum value and blue the minimum value as shown on the side bar with intermediate colours indicating the grading across the surface.

The wall pressures were measured across the walls at two vertical heights, $h/3$ and $2h/3$ as shown in **Figure 3.18** and are graphed with the vertical axis showing the pressure coefficient and the horizontal axis showing the dimensionless distance referenced to height h across the wall. The walls are referenced as **W1**, **W2**, **W3** and **W4** as shown in **Figure 3.19**. The roof is referenced as **R**. The positive directions of the wall drag coefficients and the roof lift coefficients are also shown

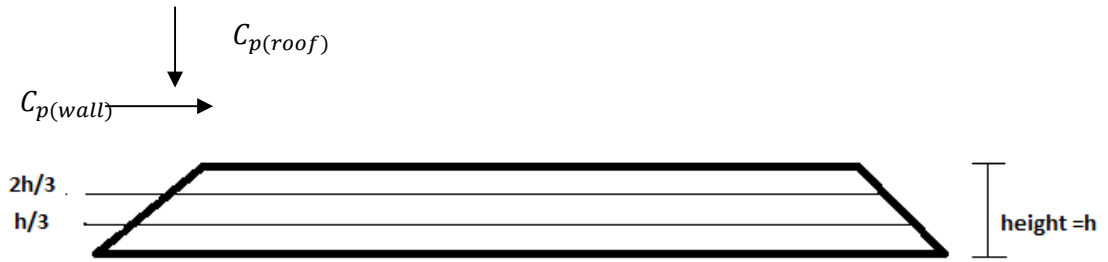


Figure 3.18 Wall Pressure Measurement Heights $h/3$ and $2h/3$.

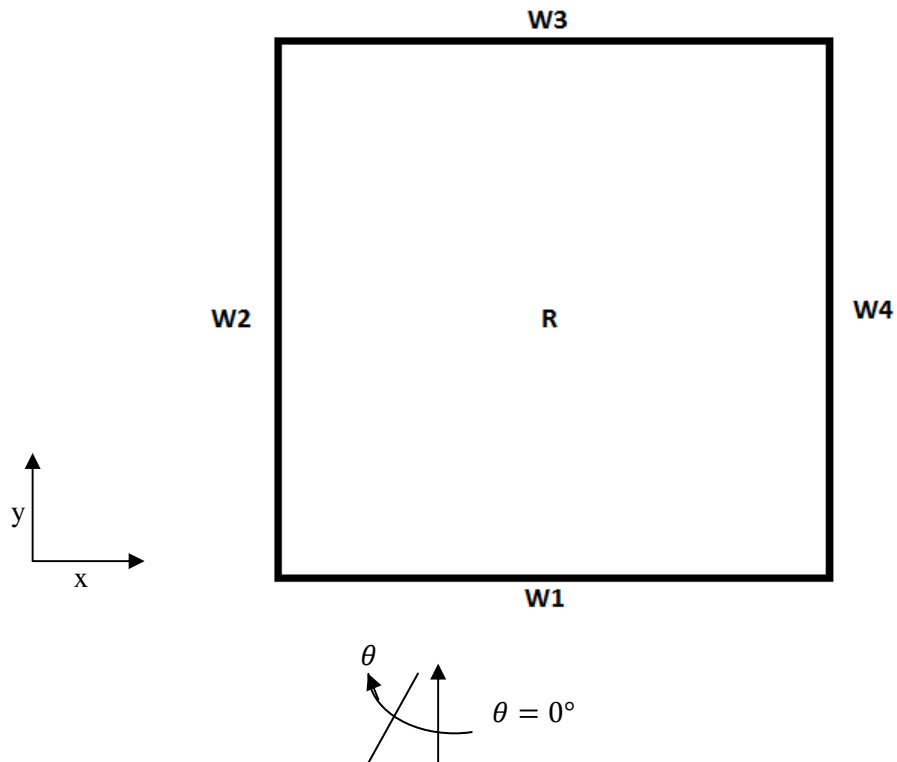


Figure 3.19 Wall and Roof References and Roof Plan View Axes

In Chapter 5, the net pressure coefficients $C_{fig,net}$ are derived from the internal and external measurements and are presented in a graphical form showing the distributions across the models' surfaces. These are compared between models and commentary is provided on the trends and variations with increasing porosity.

In Appendix A, the contour plots of the net peak directional pressure coefficients for the three porous models B, C and D are presented for 0° , 15° , 30° and 45° wind directions.

In Chapter 6 conclusions are drawn from the research, presenting the key results and identifying areas for future research into large porous canopies.

4. Wind Tunnel Test Results

The measured external pressure coefficient results for the four models are presented graphically for wind directions $\theta = 0^\circ$ and $\theta = 45^\circ$. Measured internal pressures are also presented and comparisons of the results between the four models are made. The experimental results obtained include also the external pressure coefficient measurements for $\theta = 15^\circ$ and $\theta = 30^\circ$ which have been used in Chapter 5 for the derivation of design coefficients.

4.1 Model A, Zero Porosity

4.1.1 Model A External Pressure Coefficients for $\theta = 0^\circ$

The test results for the non-porous Model A based on the wind speed at 500mm height in the tunnel were exported into an Excel spread sheet and normalised as discussed in Chapter 3, by factoring the results for the lower wind speed at the height of the model (25mm). **Figures 4.1, 4.2 and 4.3** show the contour plots of the mean, maximum and minimum external roof pressure coefficients C_{pe} that were obtained for $\theta = 0^\circ$ on roof surface R. As discussed in Chapter 3, vertical and horizontal axes show distance in increments of the height 'h' with the x and y dimensions of the model divided by the height 'h'. This is typical for all contour plots presented. The right side bar shows the pressure coefficients with red denoting the highest positive value and blue the highest negative.

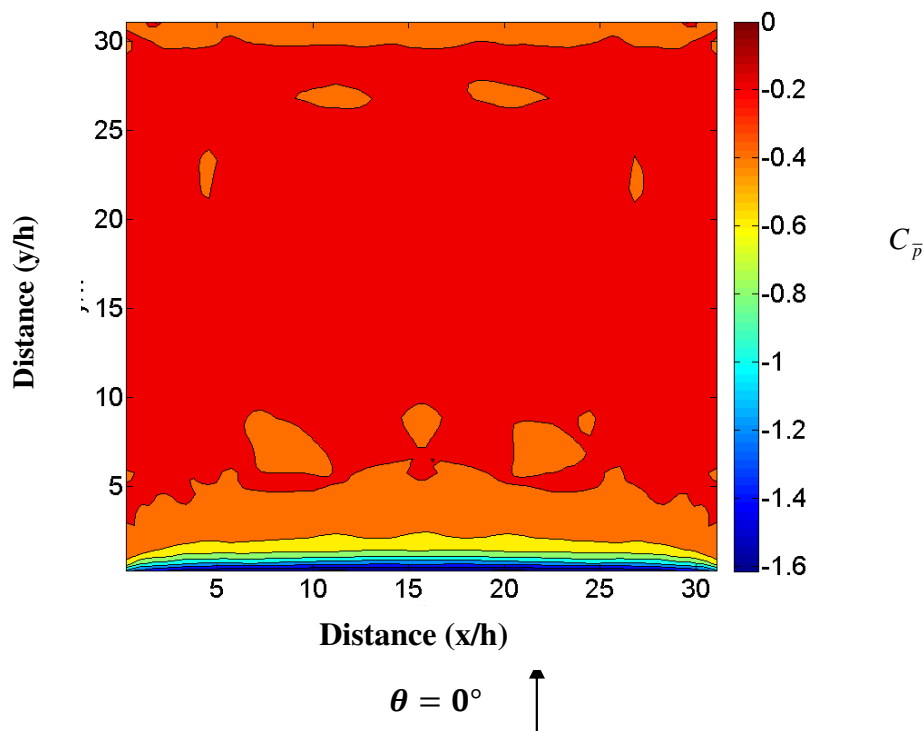


**Figure 4.1 Mean External Roof Pressure Coefficient $C_{\bar{p}}$,
Zero Porosity Model A, $\theta = 0^\circ$**

Figure 4.1 shows that the highest mean suction coefficient occurs at the windward edge and then rapidly reduces with distance away from the front edge. The mean value reduces to a value of -0.2 over a distance of approximately $6h$ and then remains constant until there is a slight increase $2h$ away from the leeward edge.

The downward pressure coefficients shown in **Figure 4.2** vary from 0 to 0.6 with a reduction at the windward and leeward edges. At the windward edge there is zero downward pressure recorded.

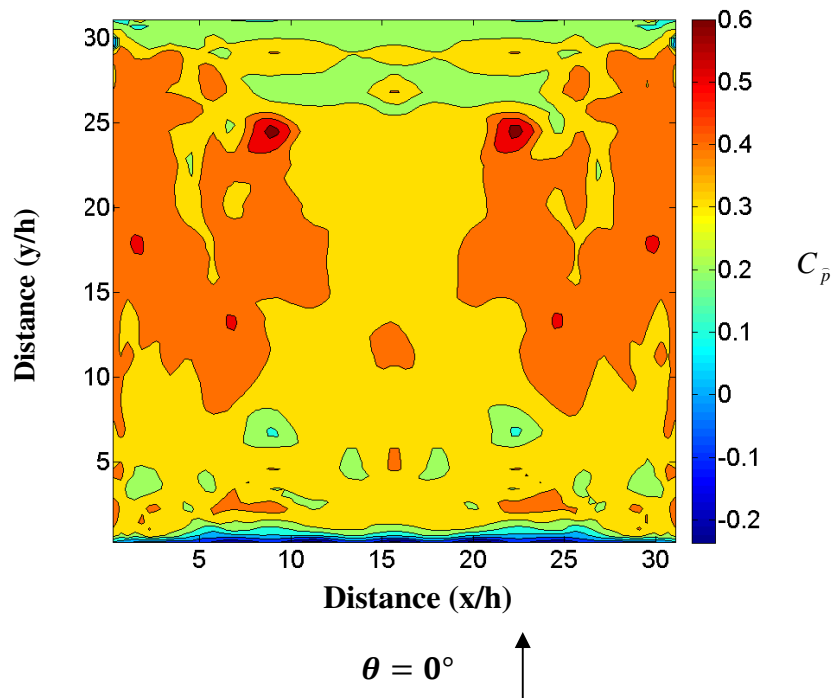


**Figure 4.2 Maximum External Roof Pressure Coefficient, $C_{\bar{p}}$, Zero Porosity
Model A, $\theta = 0^\circ$**

Figure 4.3 shows a minimum pressure coefficient distribution similar to the mean pressure coefficient contours, but with higher values and no increase at the leeward edge. The values peak at the windward edge and reduce over a distance of approximately $5h$, then remain constant across the surface. This can be attributed to the separation of the wind flow at the wall and roof intersection. The 45° wall slope makes the separation less abrupt than for a vertical wall. The distribution is similar to the design minimum pressure specified for a large flat roof in AS1170.2 (2011).

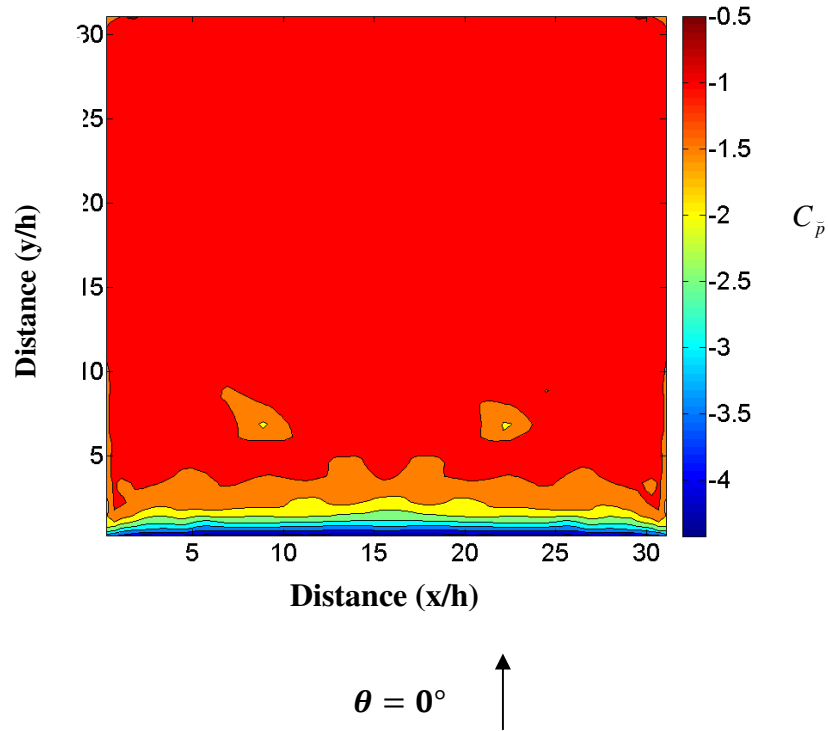


Figure 4.3 Minimum External Roof Pressure Coefficients, C_p , Zero Porosity Model A, $\theta = 0^\circ$

The wall pressure measurements were taken at vertical heights of $h/3$ and $2h/3$ on the wall surface with 45° slope. The results for the mean, maximum and minimum wall pressure coefficients are shown in **Figures 4.4, 4.5, and 4.6** for Walls W1, W3 and W2.

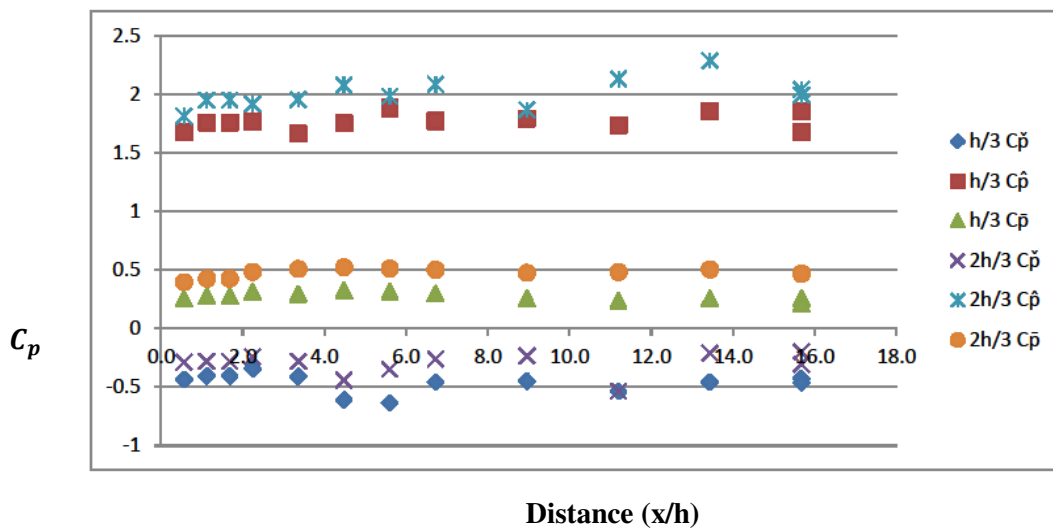


Figure 4.4 Pressure Coefficients C_p for Windward Wall W1 of Model A, $\theta = 0^\circ$

Figure 4.4 presents the pressure coefficients on the windward wall W1 across half the wall's width (the distribution being symmetrical around the wall's centreline) with a highest magnitude of +2.3 at a height of $2h/3$. The pressures are relatively evenly distributed across the wall width and increase in magnitude slightly at $2h/3$ from the maximum magnitudes at $h/3$, due to the wind speed increasing as it approaches the wall-roof intersection. The mean values show an even distribution of inward pressure with mean values slightly higher at $2h/3$. Minimum suction pressure coefficients are shown, varying between -0.2 and -0.6, demonstrating that the inclined walls are subject to both positive and negative pressures for this wind direction.

The positive pressure coefficients on the leeward wall W3 shown in **Figure 4.5**, vary from 0 to +0.3. The mean coefficients vary between -0.6 to -0.3 suction. The minimum suction coefficients show a distribution with peak magnitudes of -1.8 over the distance $2h$ from the wall corner reducing to -1.0 over the next $2h$ distance and then averaging -0.8 across the middle section of the wall.

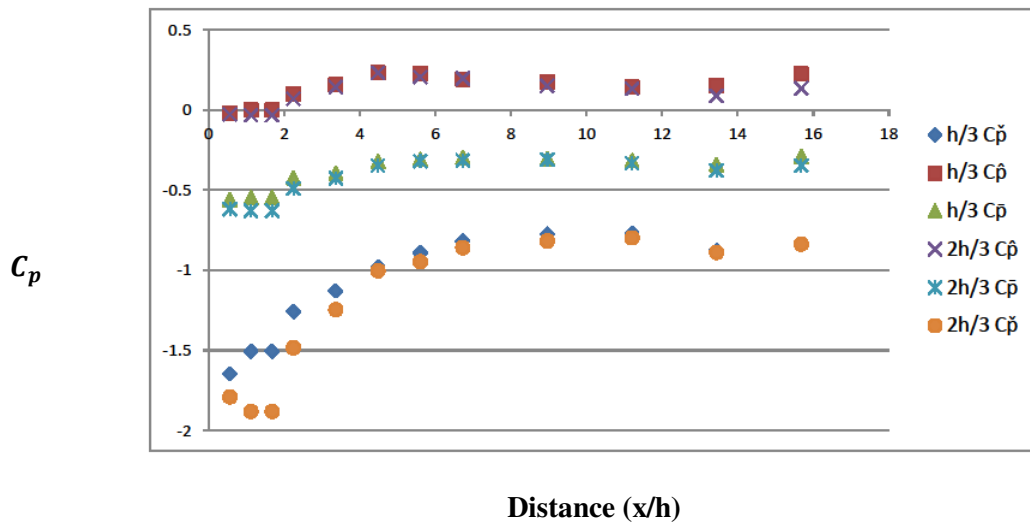


Figure 4.5 External Pressure Coefficients, C_p for Leeward Wall W3 of Model A, $\theta = 0^\circ$

The side wall coefficients presented in **Figure 4.6** for the full length of the wall, as symmetry of the pressure coefficient results around the wall centreline does not apply, commence with the highest suction coefficient at the windward corner of -2.4 and diminish after a distance of $2h$ along the wall to -0.6. There is a slight increase in suction at the leeward corner. The mean coefficients are suction pressure coefficients, reducing gradually along the wall from windward to leeward corners. The maximum pressure coefficients are relatively constant along the wall with a slight increase in the measurement at $2h/3$ at the leeward corner.

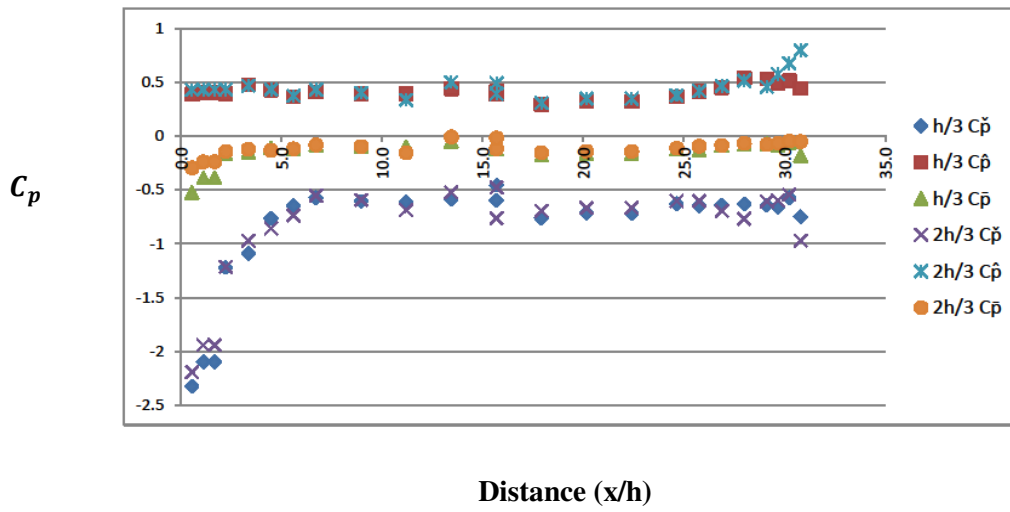


Figure 4.6 External Pressure Coefficient, C_p for Side Walls W2 and W4 of Model A, $\theta = 0^\circ$

4.1.2 Model A External Pressure Coefficients for $\theta = 45^\circ$

The pressure coefficient contour plots for the mean, maximum and minimum pressures on the roof surface R of the non-porous Model A for $\theta = 45^\circ$ wind direction are shown in Figures 4.7, 4.8 and 4.9.

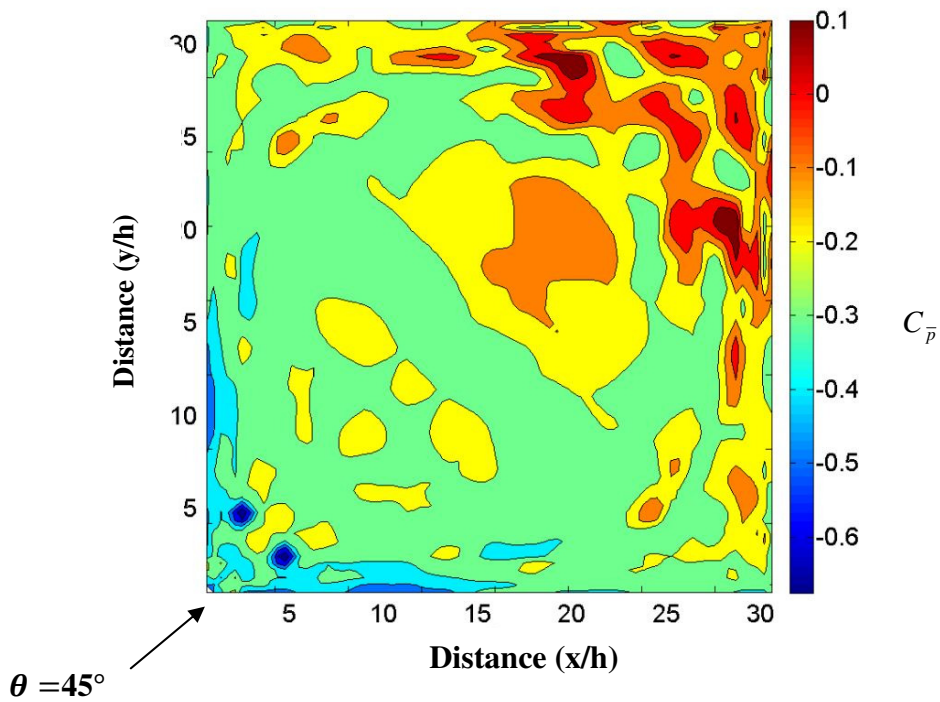


Figure 4.7 Mean External Pressure Coefficient, $C_{p\bar{}}$, Zero Porosity Model A, $\theta = 45^\circ$

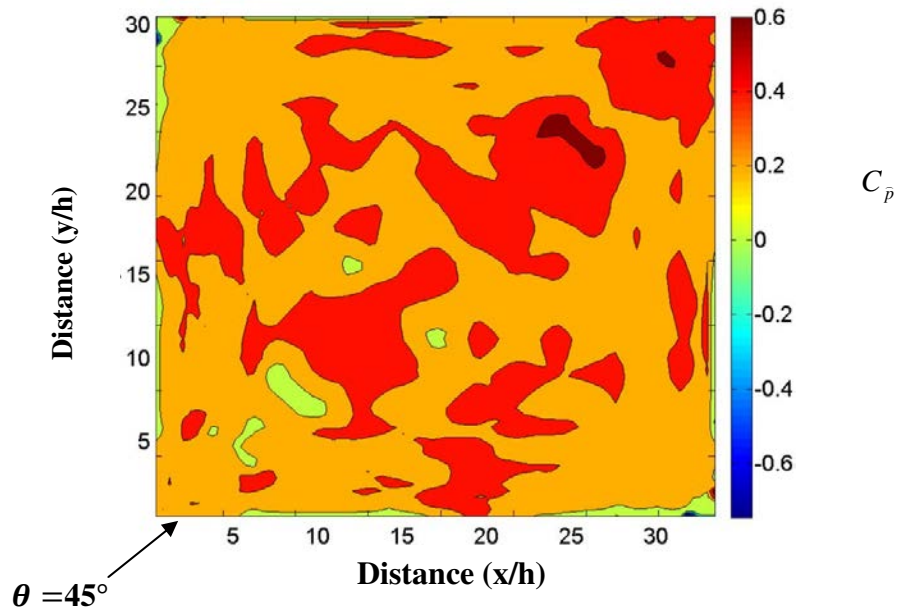


Figure 4.8 Maximum External Pressure Coefficient, $C_{\bar{p}}$,
Zero Porosity Model A, $\theta = 45^\circ$

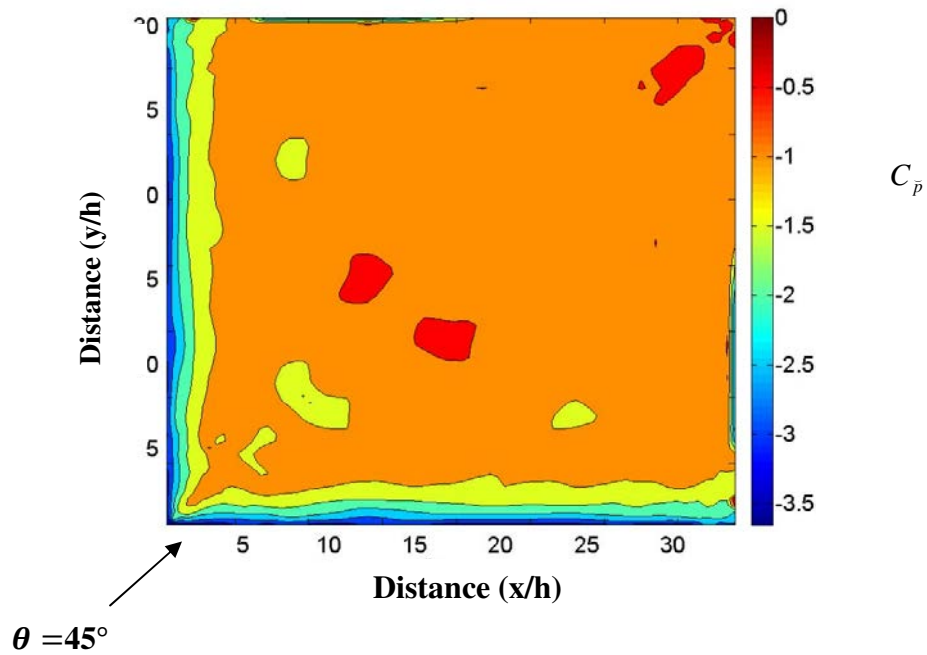


Figure 4.9 Minimum External Roof Pressure Coefficients, $C_{\bar{p}}$,
Zero Porosity Model A, Zero Porosity Model A, $\theta = 45^\circ$

The peak minimum and maximum coefficients are similar in magnitude to the results for 0° wind direction and the mean coefficients slightly less. The suction values reduce with distance rapidly away from the two windward walls W1 and W2 and the downward values vary between

0 and 0.6. The external pressure coefficients on the windward walls W1 and W2 and leeward walls W3 and W4 subject to the 45° wind are presented in **Figures 4.10 and 4.11**.

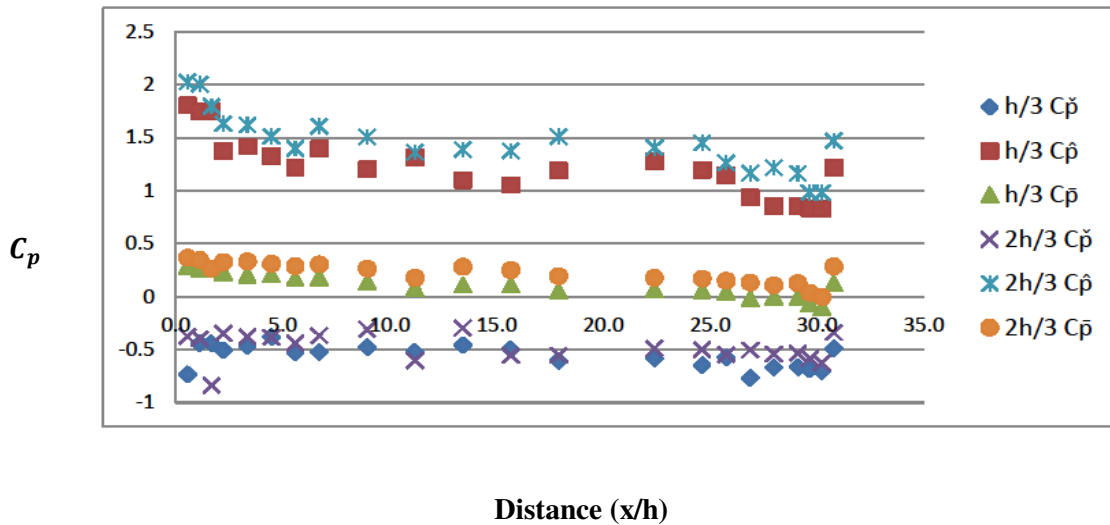


Figure 4.10 Pressure Coefficients C_p for Windward Walls W1 and W2 of Model A, $\theta = 45^\circ$

The mean pressure coefficients on walls W1 and W2 vary from +0.4 at the windward corner to 0.0 at 1h before the leeward corner. There is a slight increase then at the leeward corner. This trend is shown also in the maximum positive pressure coefficients varying from 2.0 at the windward corner to 1.0 at a distance 1h from the leeward corner. The suction values are relatively constant across the length of the wall averaging -0.5.

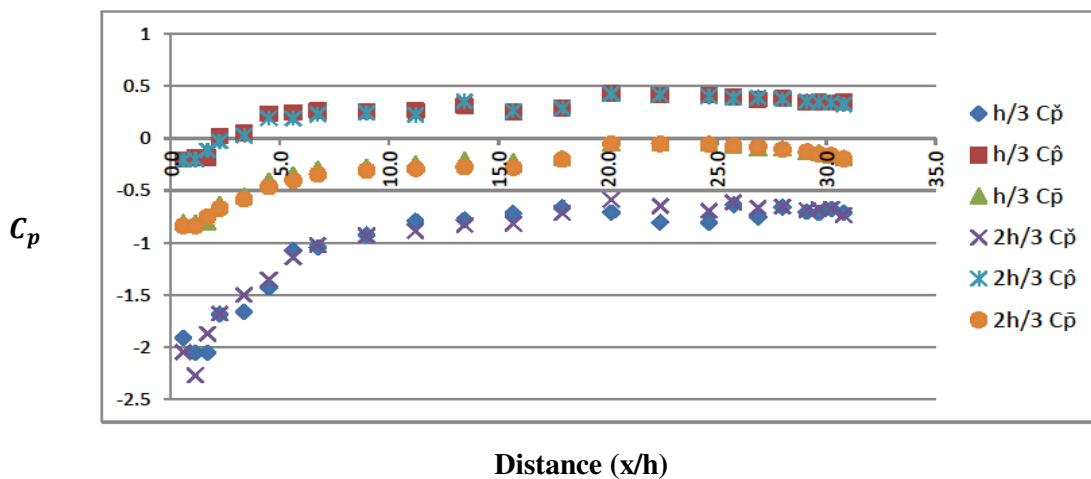


Figure 4.11 Pressure Coefficients C_p for Leeward Walls W3 and W4 of Model A, $\theta = 45^\circ$

The pressure coefficients on the leeward walls W3 and W4 show a reversal of the trends shown on walls W1 and W2. The minimum and mean suction coefficients are highest at the windward corner reducing gradually to approximately the halfway point of the walls width and then remaining relatively constant along to the far corner. The maximum pressure coefficients are smaller in magnitude and are lowest at the windward corners.

4.2 Model B, 19% Porosity

4.2.1 Model B External Pressure Coefficients for $\theta = 0^\circ$

The mean, maximum and minimum external pressure coefficients for the roof surface R are shown for the 19% porous Model B in **Figures 4.12, 4.13** and **4.14**, for $\theta = 0^\circ$.

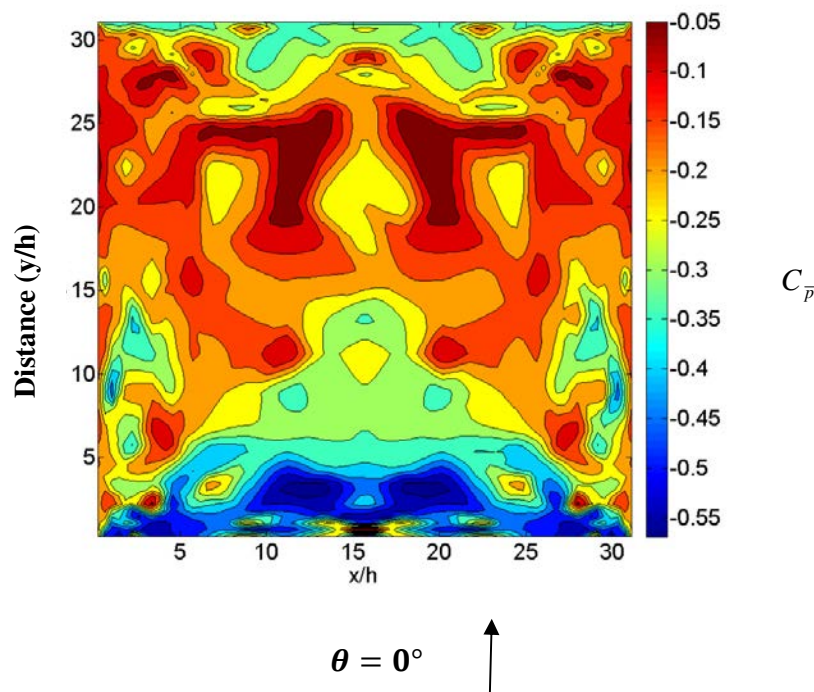


Figure 4.12 Mean External Pressure Coefficient, $C_{\bar{p}}$, 19% Porosity Model B, $\theta = 0^\circ$.

The mean pressure coefficients vary from -0.56 to -0.05 in comparison to -1.6 to 0 for the non-porous Model A. Model B also shows a more gradual reduction in pressure from the windward edge compared to Model A.

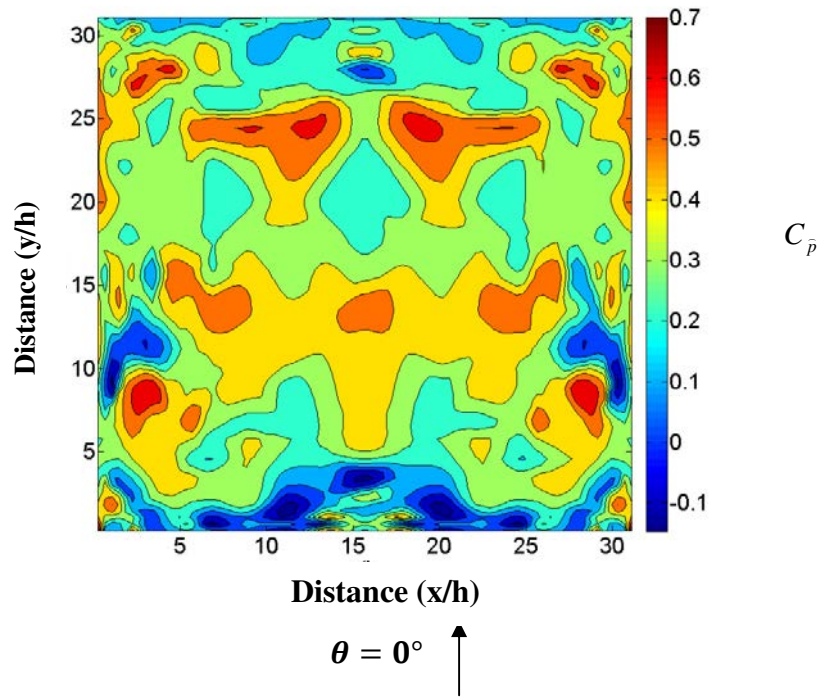


Figure 4.13 Maximum External Pressure Coefficient, $C_{\bar{p}}$,
19% Porosity Model B, $\theta = 0^\circ$.

The maximum downward external roof pressure coefficients shown are of similar magnitude to the non-porous Model A, ranging from 0 to +0.7. At the windward edge zero downward pressure was measured, similar to Model A.

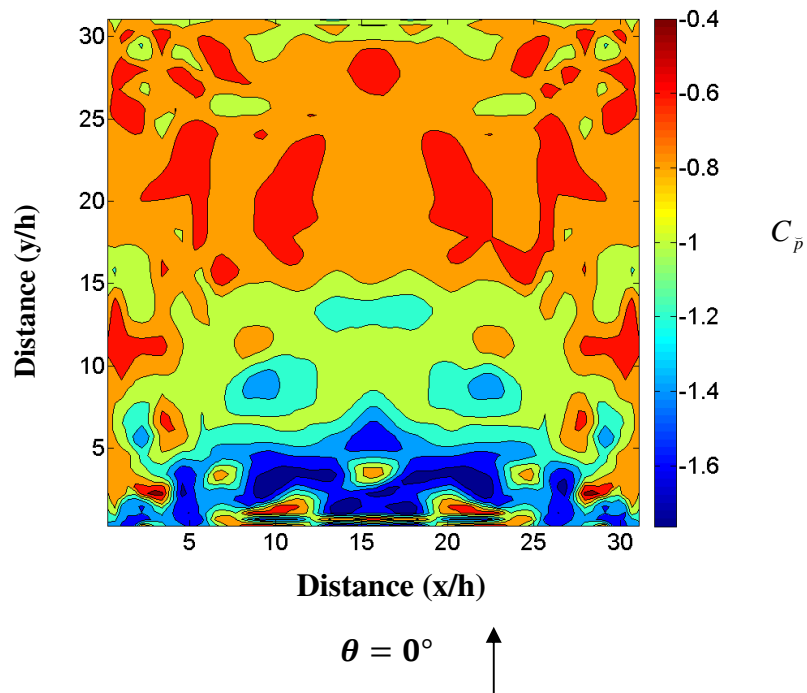


Figure 4.14 Minimum External Pressure Coefficient, $C_{\bar{p}}$,
19% Porosity Model B, $\theta = 0^\circ$.

The minimum external pressure coefficients shown in **Figure 4.14** have a similar distribution to the mean values. The largest magnitude at the windward edge (-1.70) is significantly less than the peak coefficient (-4.5) measured at the windward edge of Model A, demonstrating the reduced separation of the wind at the edge of the porous model.

The Model B wall external pressure coefficient distributions are shown in **Figures. 4.15, 4.16, 4.17**, with pressure coefficients measured at heights $h/3$ and $2h/3$ plotted vertically against distance across the model horizontally. The plots for Walls W1 and W3 present pressure coefficients for half the distance across the model only. The plots are symmetrical around the centre line of the model.

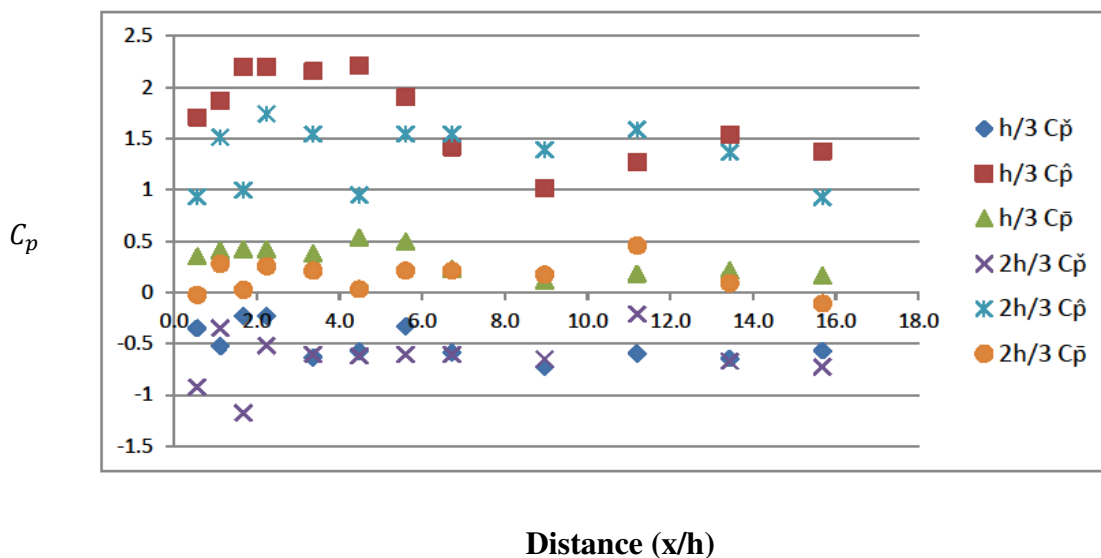


Figure 4.15 External Pressure Coefficients C_p for Windward Wall W1 of Model B, $\theta = 0^\circ$.

Figure 4.15 shows the peak wall pressure coefficient of 2.2 occurs at $h/3$ height and reduces to a peak value of 1.8 at $2h/3$. Peak suction coefficients of -1.0 were measured at $2h/3$ and the mean values vary between 0 and 0.5. The peak maximum coefficient 2.2 is similar to the peak measured on Model A (2.3) indicating that the porosity has not influenced significantly the pressure coefficients.

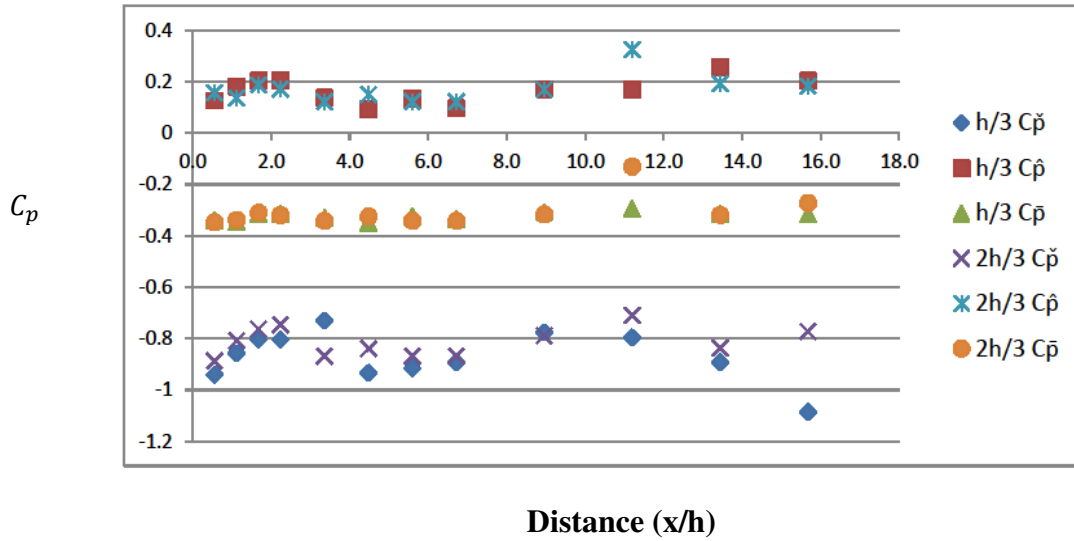


Figure 4.16 External pressure Coefficients C_p for Leeward Wall W3 of Model B, $\theta = 0^\circ$.

The Wall 3 coefficients in **Figure 4.16** show minimum coefficients of -0.7 to -1.1, less than the peak suction value of -1.5 measured on Model A. The mean coefficient distribution is similar to the Model A mean values and the maximum coefficient 0.3, is equal to the maximum for Model A.

The side wall W2 pressure coefficients are shown in **Figure 4.17**

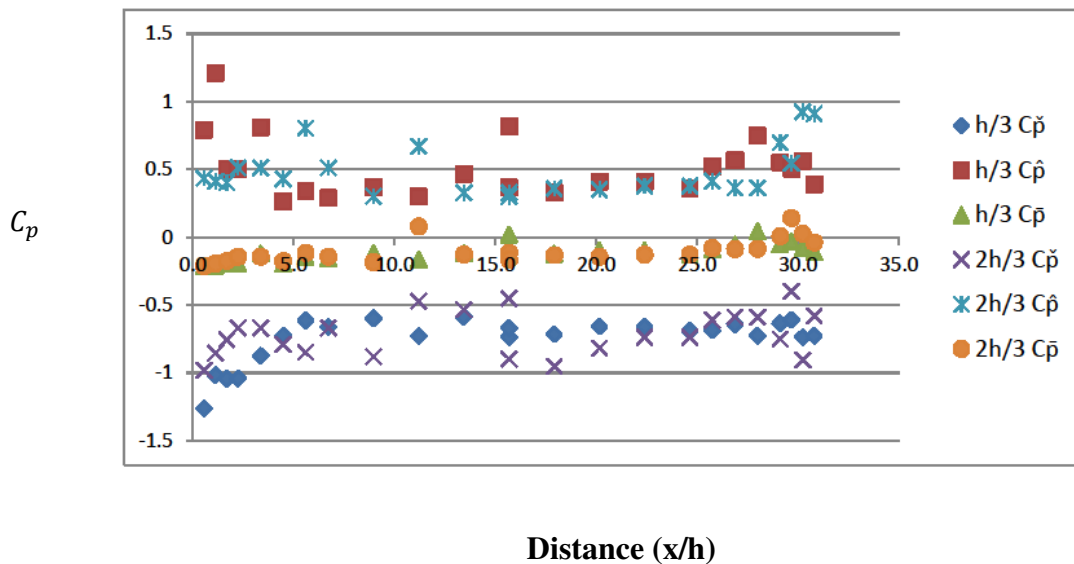


Figure 4.17 External Pressure Coefficients C_p for Side Wall W2 of Model B, $\theta = 0^\circ$

Side wall coefficients vary from -1.3 to +1.2. The mean varies between 0 and -0.02. Peak values occur at the windward corner end of the wall similar to non-porous Model A (-2.5) but of lower magnitude (-1.2). The decrease in positive pressure coefficients along the side wall is more gradual than the decrease on the non-porous Model A side wall and the peak maximum of -1.3 is reduced from -2.6 for the non-porous model. The porosity reduces the suction along the side wall.

4.3.2 Model B External Pressure Coefficients for $\theta = 45^\circ$

The external pressure coefficient results for the roof surface R for $\theta = 45^\circ$ wind direction are shown in the following **Figures 4.18, 4.19** and **4.20**.

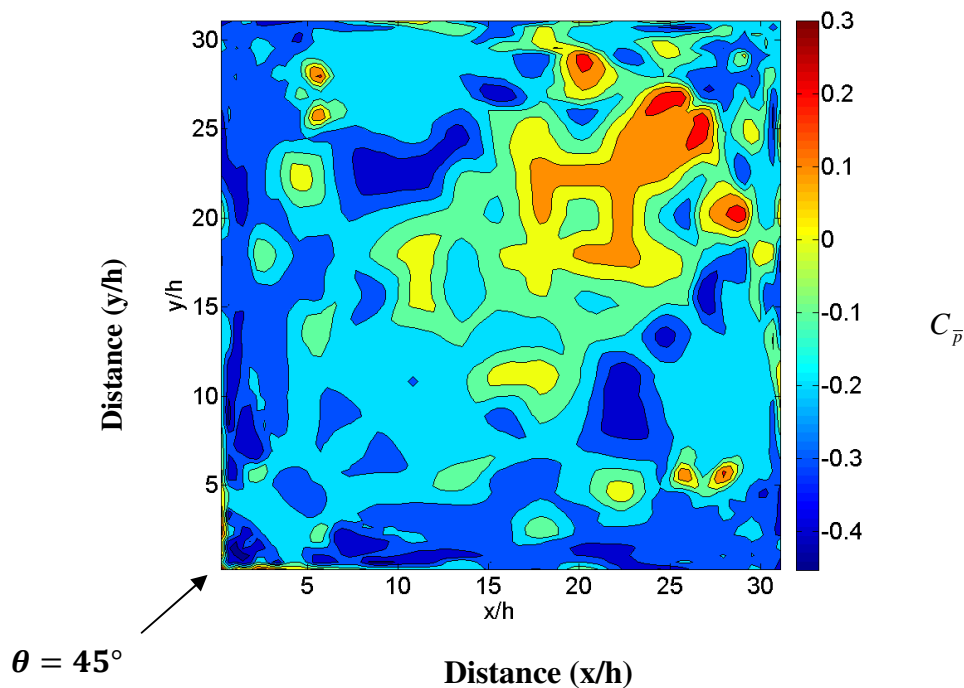


Figure 4.18 Mean External Pressure Coefficient, $C_{\bar{p}}$, 19% Porosity Model B, $\theta = 45^\circ$

Figure 4.18 shows the mean coefficients distribution with a peak magnitude at the windward corner of -0.45, slightly less than that for the 0° direction (-0.55). An area approximately $10h \times 10h$ in the middle of the downwind half and on the diagonal has mean positive downward pressure coefficients. Otherwise the mean pressure coefficients are negative suction coefficients. This is a similar distribution to Model A.

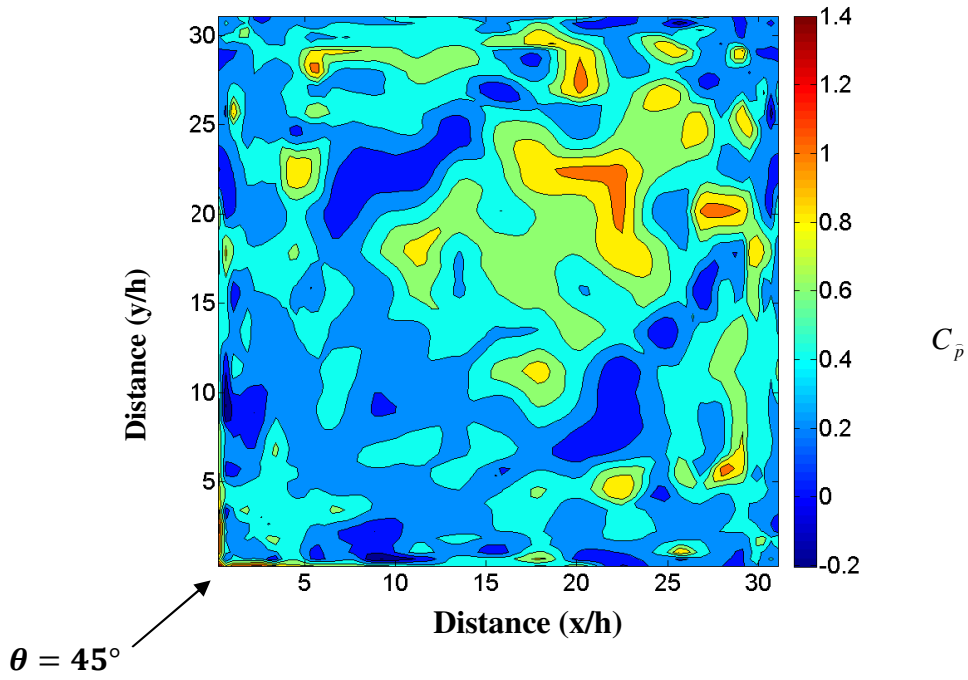


Figure 4.19 Maximum External Pressure Coefficient, C_p ,
19% Porosity Model B, $\theta = 45^\circ$

Figure 4.19 shows maximum pressure coefficients ranging from 0 to 1.4. The peak downward coefficient (1.4) is higher than for Model A (0.6) indicating influence from the flow through the porous wall and roof surfaces as the shape narrows to the model corner.

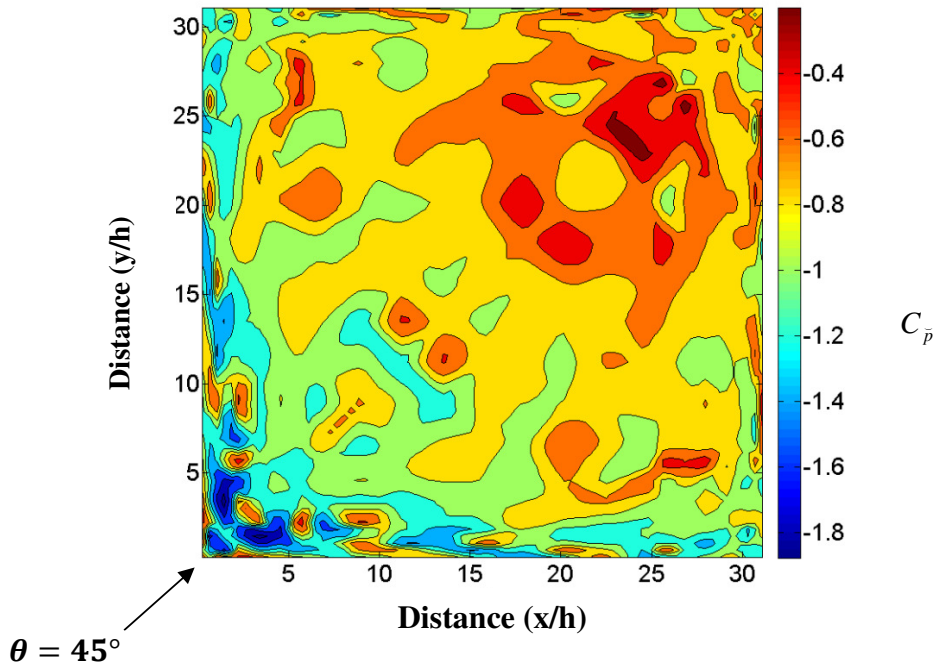


Figure 4.20 Minimum External Pressure Coefficient, C_p ,
19% Porosity Model B, $\theta = 45^\circ$

The minimum coefficients range from -1.9 at the windward corner to -0.4 on the downwind half of the roof. The corner peak coefficient (-1.9) is slightly greater in magnitude than the peak minimum coefficient (-1.7) for $\theta = 0^\circ$.

The wall pressure coefficients for $\theta = 45^\circ$ are shown in **Figures 4.21** and **4.22**. The plots show the pressure for one of the two walls that receive the wind (windward W1 and W2, leeward W3 and W4).

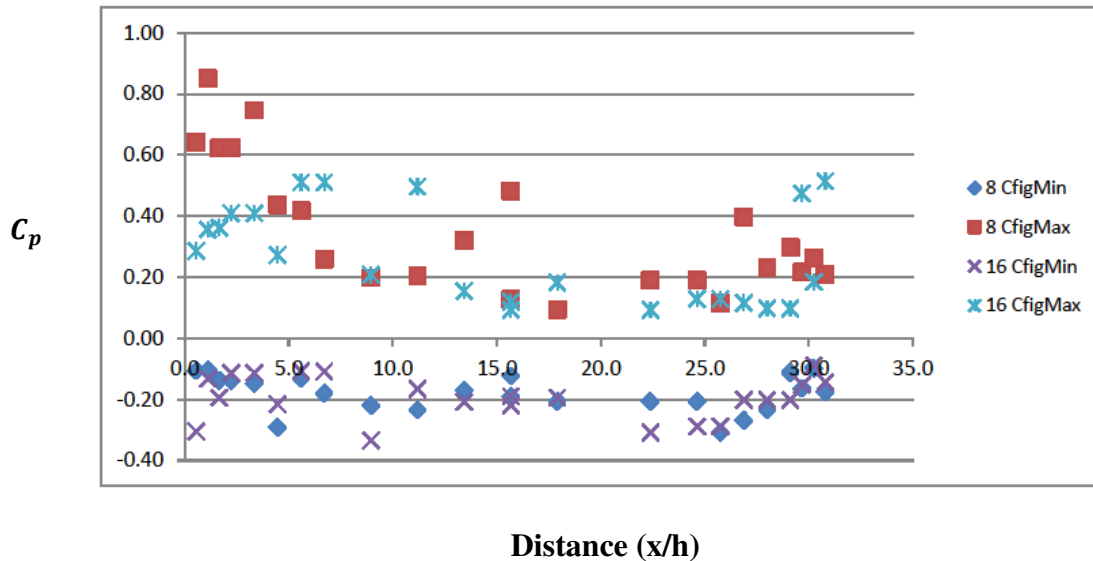


Figure 4.21 External Pressure Coefficient C_p Windward Wall W1 of Model B, $\theta = 45^\circ$

Figure 4.21 shows the peak positive pressure value at height $h/3$ is close to the windward corner and greater in magnitude (2.6) than the 0° windward wall peak value (2.2) and also the peak value for Model A (2.0). There is a gradual reduction in the maximum value at $h/3$ along the wall away from the windward corner. The maximum pressure coefficient at $2h/3$ varies between 0.3 and 1.6. The minimum pressure coefficient varies between -1 and -0.2, similar to the results for $\theta = 0^\circ$.

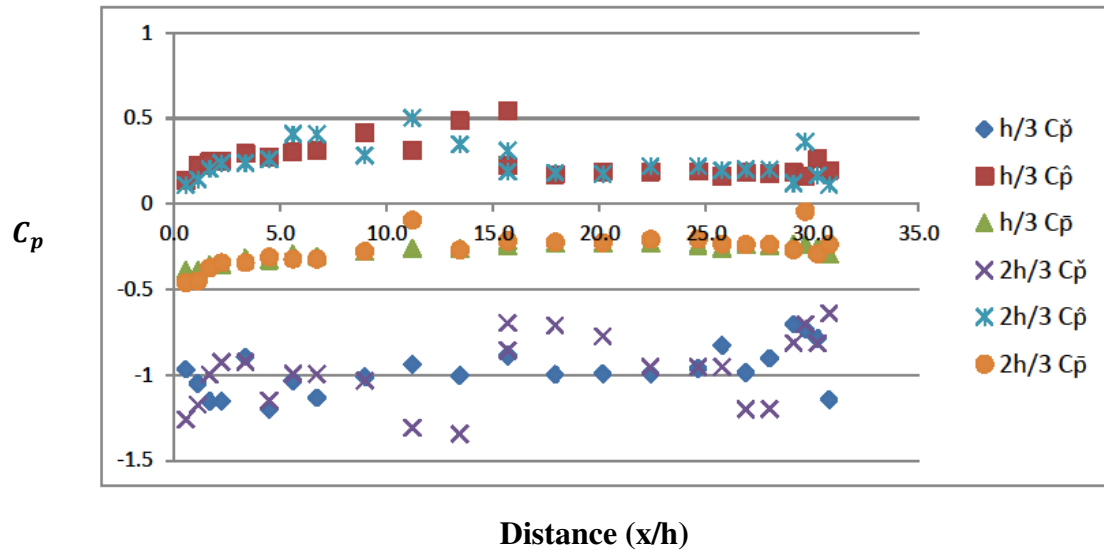


Figure 4.22 External Pressure Coefficient C_p Leeward Wall W3 of Model B, $\theta = 45^\circ$

Figure 4.22 shows Wall W3 maximum and minimum values are slightly higher than for $\theta = 0^\circ$ with a similar distribution.

4.2.3 Model B Internal Pressure Coefficients

The internal pressures were measured across the floor of the model as described in section 3.4 of this thesis, where measurement taps are shown placed on the diagonal, width and length of the model. The contour plots in **Figures 4.23, 4.24** and **4.25** present the resulting graded pressure distributions based on these measurements. A variation of internal pressure along the model due to the flow of the air through the model is shown. Pressures in the side regions of the model, due to the influence of flow through the porous walls, vary from the pressure along the centreline of the model.

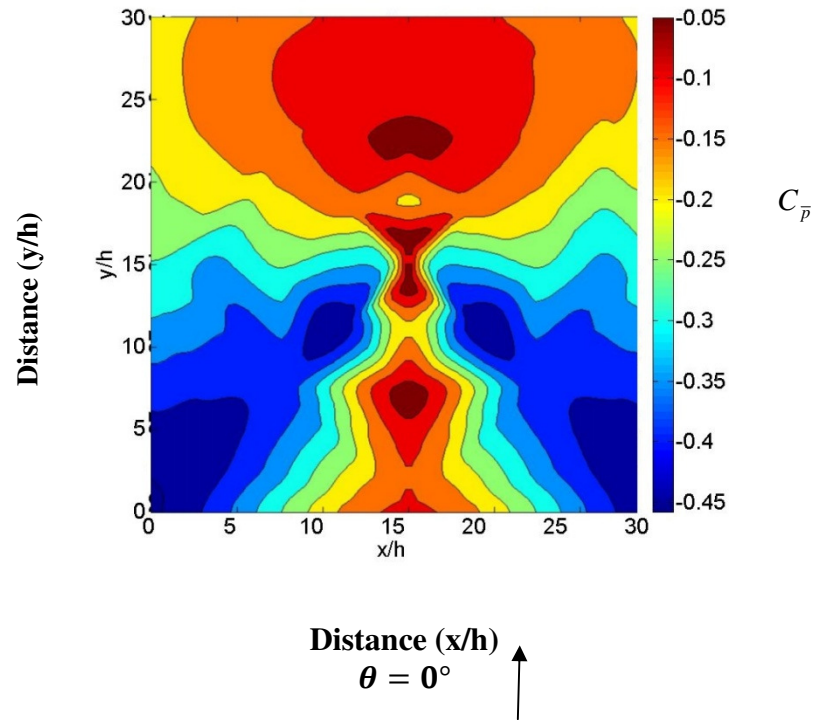
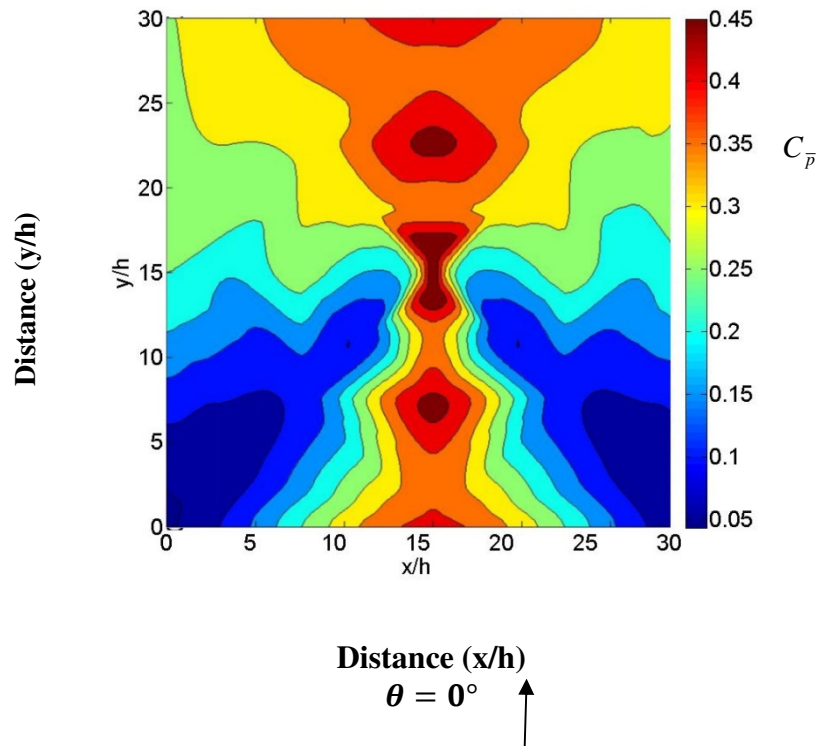


Figure 4.23 Mean Internal Pressure Coefficient, $C_{\bar{p}}$

Model B, $\theta = 0^\circ$

The mean negative internal pressure causes an inward suction on the internal model surfaces generated by the air flowing through the porous model. It is greatest at the upwind corners of the model and reduces along the centre of the model and in the downwind half.



**Figure 4.24 Maximum Internal Pressure Coefficient, $C_{\bar{p}}$,
Model B, $\theta = 0^\circ$**

The maximum internal pressure coefficients acting on the internal surfaces of the model are relatively constant down the centreline of the model with a value of 0.45 but decrease in the downwind corners of the model to 0.05. The maximum pressures increase across the model in contrast to the minimum pressures.

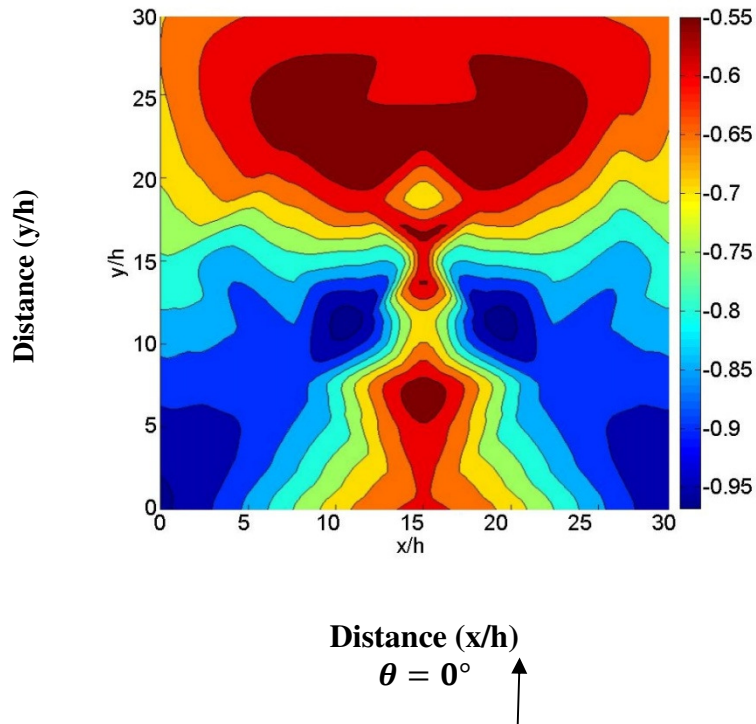


**Figure 4.25 Minimum Internal Pressure Coefficient, $C_{\bar{p}}$,
19% Porosity Model B, $\theta = 0^\circ$**

The minimum internal pressure coefficients show a similar distribution to the mean pressure coefficients varying from -0.95 to -0.55 and decreasing across the model.

Figures 4.26, 4.27 and 4.28 show the internal pressure distributions for $\theta = 45^\circ$

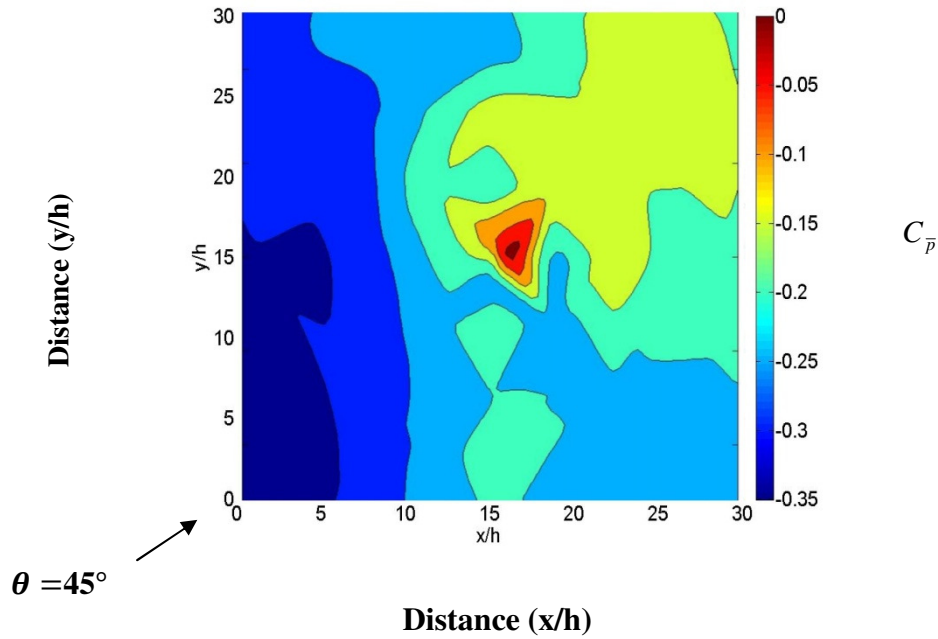


**Figure 4.26 Mean Internal Pressure Coefficient, $C_{\bar{p}}$
Model B, $\theta = 45^\circ$**

The mean internal pressure distribution for $\theta = 45^\circ$ shows the mean pressure decreasing across the diagonal of the model away from the windward corner. The lack of symmetry is due to internal rows of taps being not on the main axes of the model. A more even distribution would occur with additional taps, however additional measurement tubes internally will also disturb the wind flow through the model.

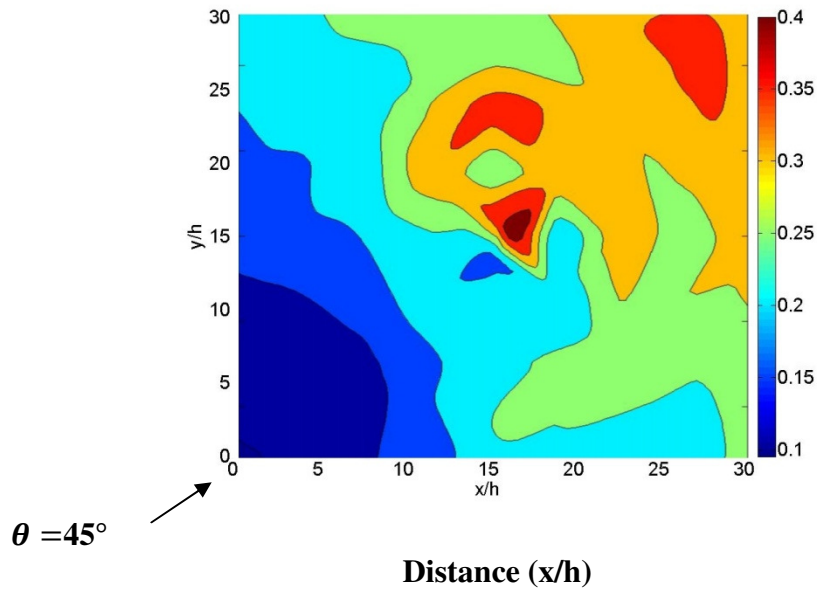


**Figure 4.27 Maximum Internal Pressure Coefficient, C_{p_i} ,
Model B, $\theta = 45^\circ$**

The maximum values show an increase in magnitude across the model diagonal away from the windward corner.

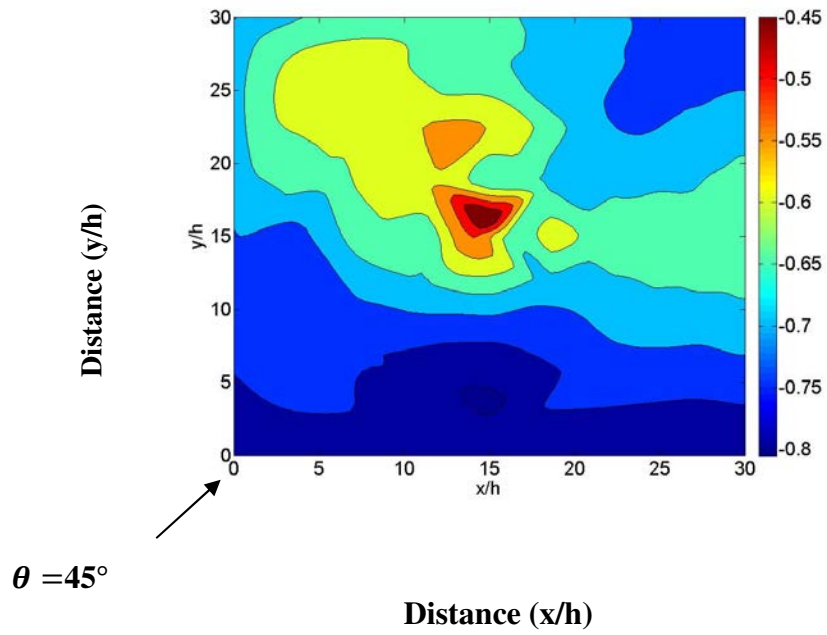


**Figure 4.28 Minimum Internal Pressure Coefficient, $C_{\bar{p}}$,
19% Porosity Model B, $\theta = 45^\circ$**

The minimum results show a range of values from -0.8 to -0.45.

4.3 Model C, 38% Porosity

4.3.1 Model C External Pressure Coefficients, $\theta = 0^\circ$

The external roof pressure contours for the porous Model C with the fine bronze mesh and 38% porosity, were plotted in the same manner as the Models A and B results. **Figures 4.29, 4.30 and 4.31** show the mean, maximum and minimum pressure external coefficients on roof surface R for $\theta = 0^\circ$.

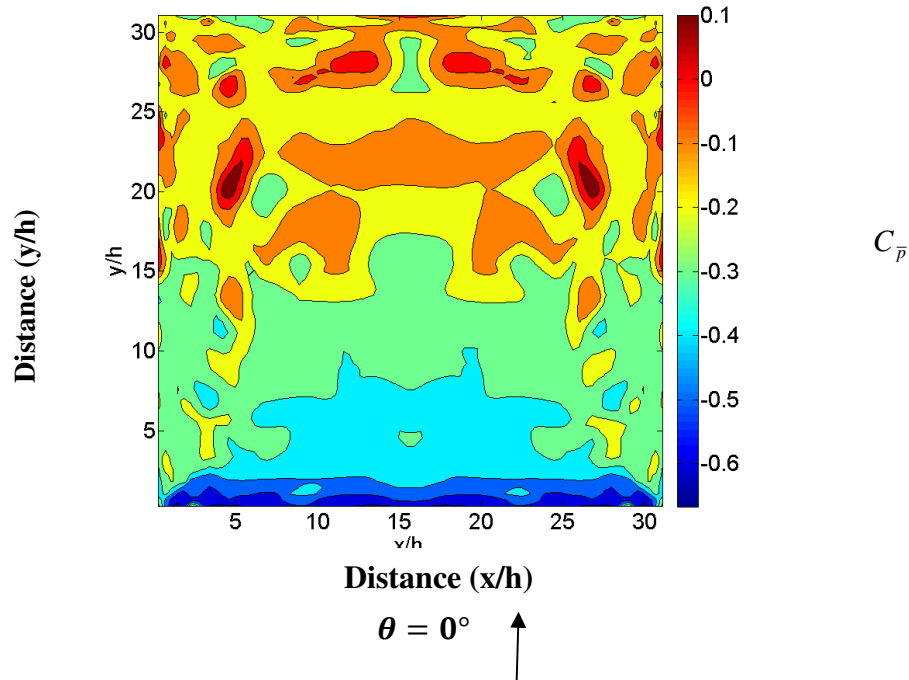


Figure 4.29 Mean External Pressure Coefficient, $C_{\bar{p}}$, 38% Porosity Model C, $\theta = 0^\circ$

Figure 4.29 shows the largest mean suction pressure coefficients are experienced near the windward edge. No mean downward pressure coefficients were shown on the Model B mean plot, indicating the greater porosity is influencing the pressure distribution in the downwind half.

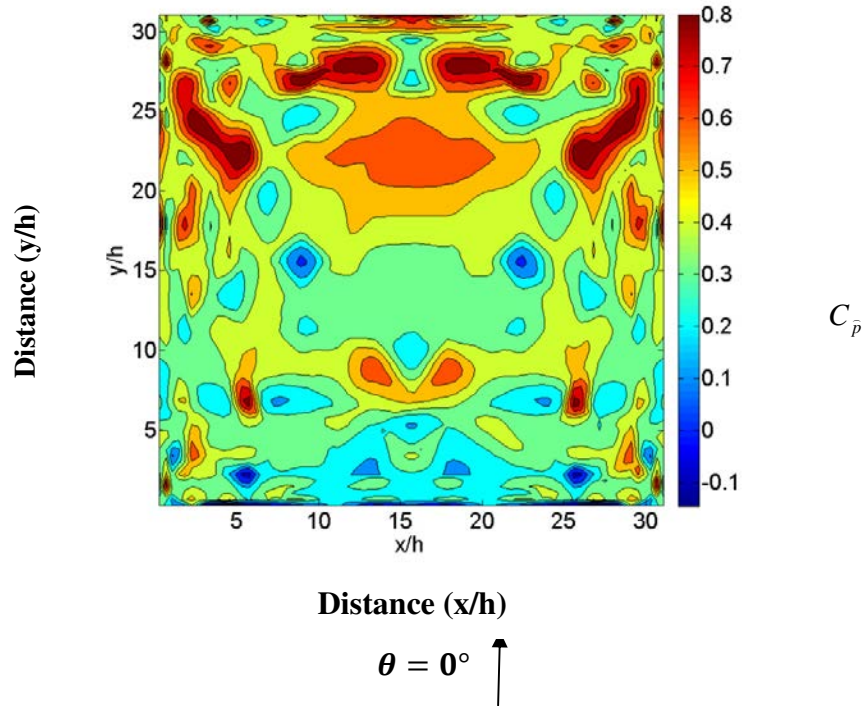


Figure 4.30 Maximum External Pressure Coefficient, $C_{\bar{p}}$,
 38% Porosity Model C, $\theta = 0^\circ$

The maximum positive pressures presented in **Figure 4.30** show a slight increase in magnitude towards the downwind half of the roof, but are generally small in magnitude, varying from zero to 0.8. This distribution is similar to Model B.

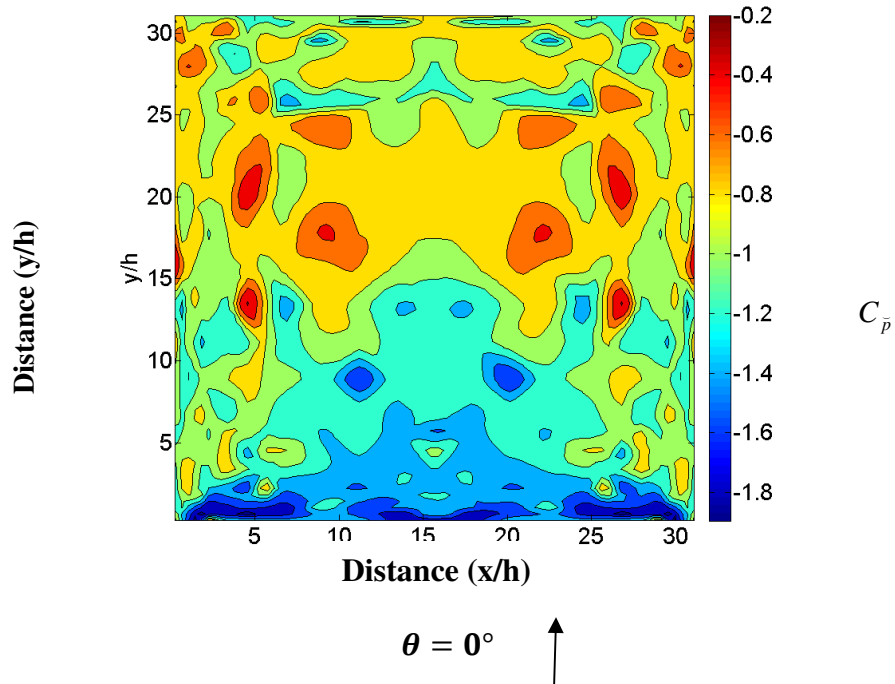


Figure 4.31 Minimum External Pressure Coefficient, $C_{\bar{p}}$,
 38% Porosity Model C, $\theta = 0^\circ$

Figure 4.31 shows the peak suction coefficients with a similar distribution to the mean coefficients, but with low suction coefficients in the downwind half. The peak value at the upwind edge of -1.9 reduces gradually with distance from the windward edge.

The external pressure coefficient plots on Walls W1, W3 and W2 for wind direction $\theta = 0^\circ$ are presented in **Figures 4.32** and **4.33** and **4.34** with the mean, maximum and minimum coefficients for the $h/3$ and $2h/3$ heights plotted against the distance/ h across the model. The windward W1 and leeward W3 plots show half of the wall width, the second half being symmetrical to the first half in pressure distribution. The side wall W2 is shown with the distribution along the full length of the wall to show the change in pressure along the wall's length.

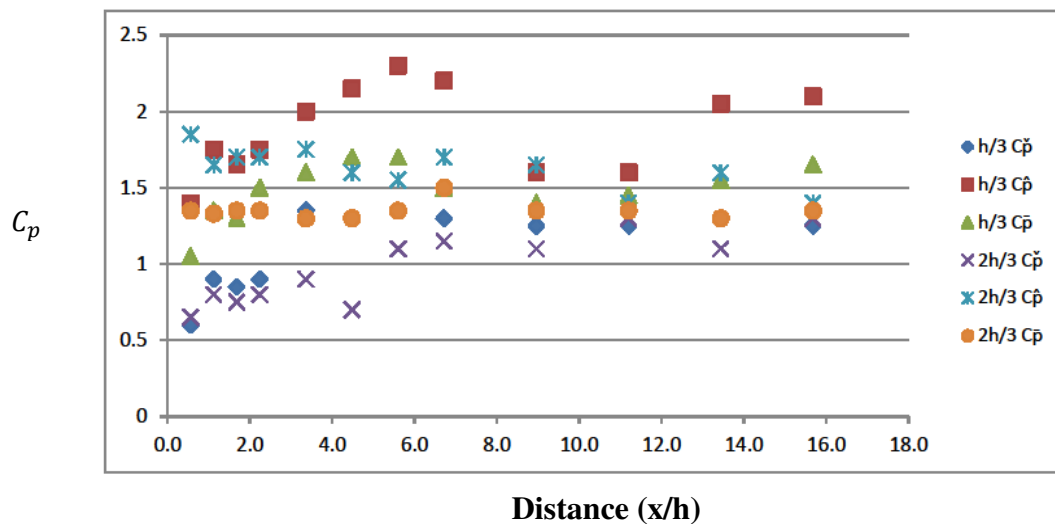


Figure 4.32 External Pressure Coefficients for Windward Wall W1, C_p , Model C, $\theta = 0^\circ$

The maximum external wall pressure coefficients on the windward Wall W1, shown in **Figure 4.32** at the $h/3$ and $2h/3$ heights, vary between 1.4 and 2.4. The mean and minimum coefficients are also positive showing that the front wall is always receiving drag pressure under wind load. This differs from the non-porous model where minimum suction pressures were recorded. The mean coefficients vary from 1.0 to 1.8, higher than the non-porous model. The maximum values vary between 1.5 and 2.4 and are slightly less on average than the non-porous model.

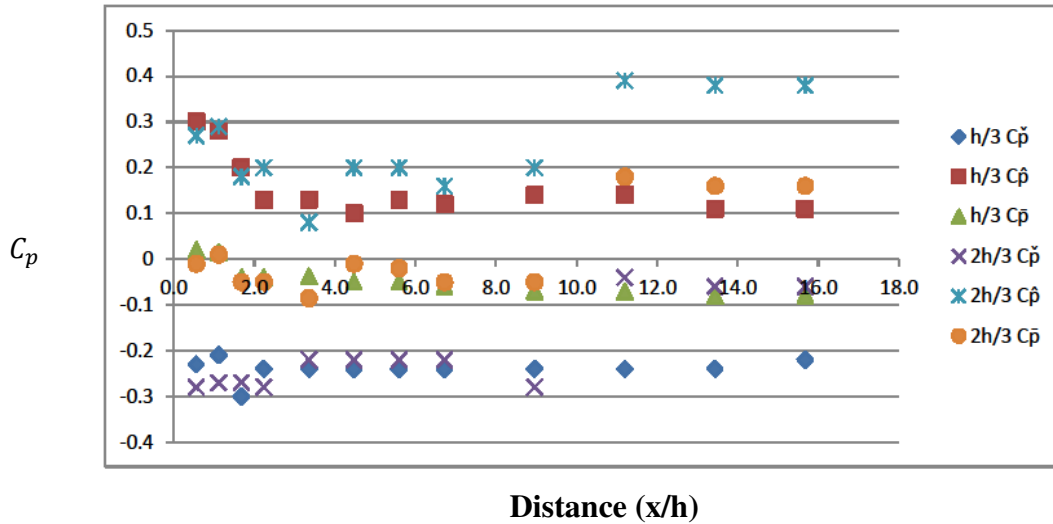


Figure 4.33 External Pressure Coefficients for Leeward Wall W3, C_p , Model C, $\theta = 0^\circ$

The leeward wall W3 coefficients, shown in **Figure 4.33**, are of smaller magnitude than the W1 coefficients, with a variation of peak values between +0.4 and -0.3. The maximum and mean values are greatest in the centre of the full wall width. At this central location the suction coefficients are lowest. The non-porous model results differed, showing lower maximum pressure coefficients and suction coefficients of lower magnitude.

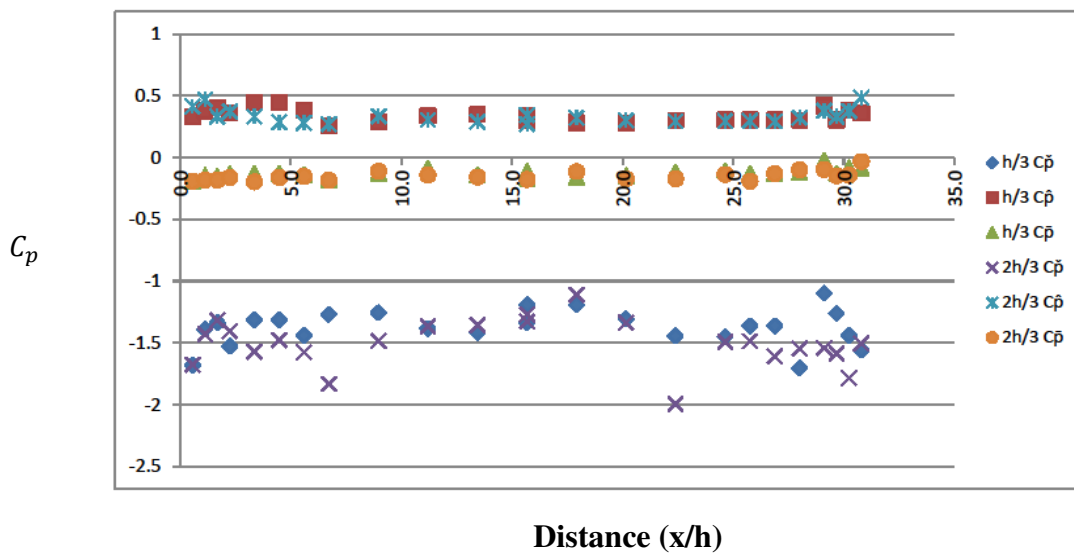


Figure 4.34 External Pressure Coefficients for Side Wall W2, C_p , Model C, $\theta = 0^\circ$

The side wall W2 coefficients, shown in **Figure 4.34** vary between -2.0 and 0.5 with mean coefficients of -0.1 to -0.2. There is little change along the length of the wall away from the windward corner showing a more even distribution than that for the non-porous Model A and

also the porous Model B, which show the pressures diminishing with distance away from the windward corner and higher peak coefficients at the windward corner.

4.2.2 Model C External Pressure Coefficients, $\theta = 45^\circ$

The external pressure coefficients on roof surface R of Model C for $\theta = 45^\circ$ are shown in Figures 4.35, 4.36 and 4.37.

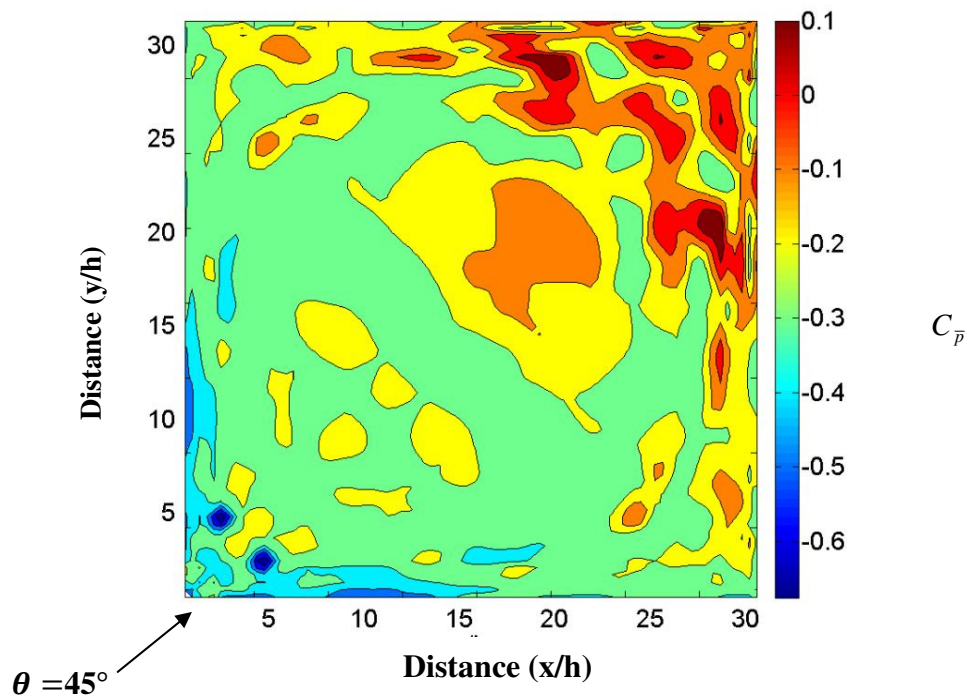
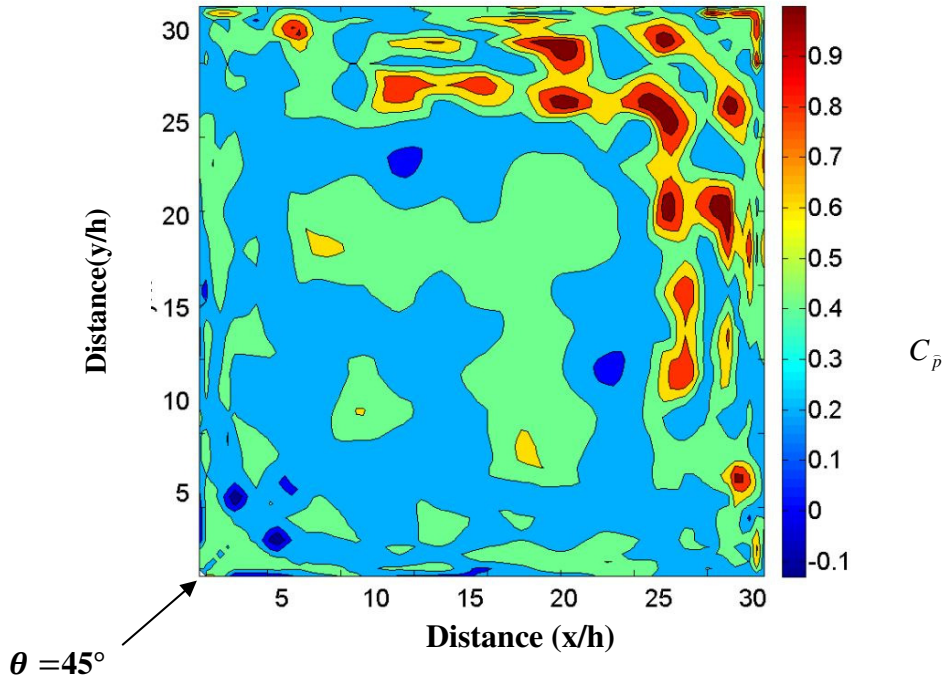


Figure 4.35 Mean External Pressure Coefficient, $C_{\bar{p}}$, 38% Porosity Model C, $\theta = 45^\circ$

The range of the mean coefficients shown in **Figure 4.35** is similar to the results for $\theta = 0^\circ$. The mean pressure coefficients in the far downwind section of the roof are positive downward similar to Model B.



**Figure 4.36 Maximum External Pressure Coefficient, $C_{\bar{p}}$,
38% Porosity Model C, $\theta = 45^\circ$**

The coefficients shown in **Figure 4.36** are similar to the $\theta = 0^\circ$ maximum downward coefficients, with increase in magnitude towards the downwind corner.

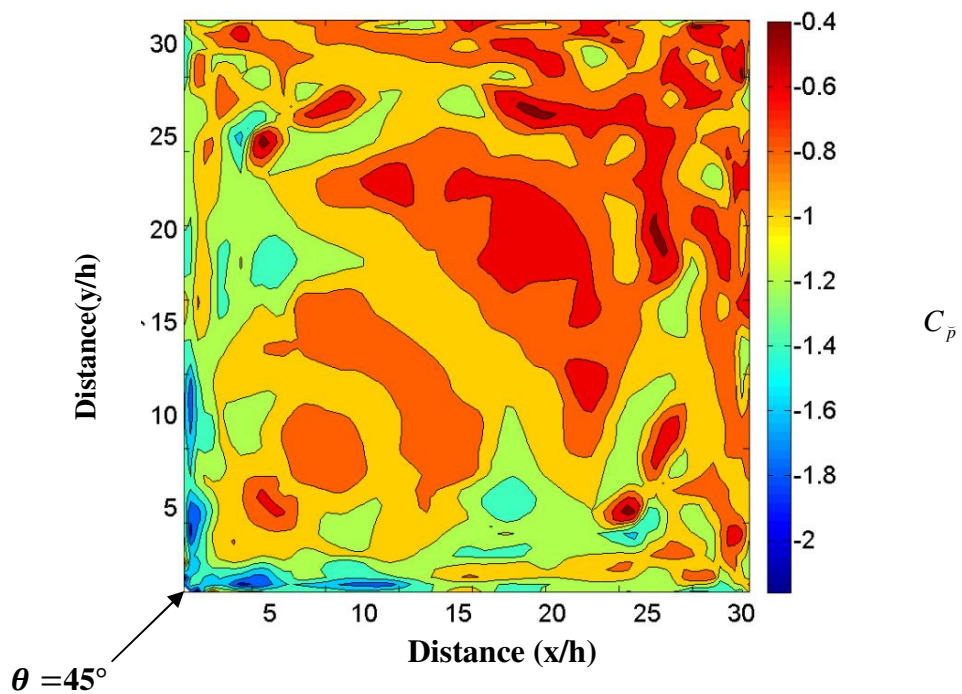


**Figure 4.37 Minimum External Pressure Coefficient, $C_{\bar{p}}$,
38% Porosity Model C, $\theta = 45^\circ$**

The range of minimum external coefficients shown in **Figure 4.37** is similar to the results for $\theta = 0^\circ$ varying from -2.0 at the windward edge to -0.4 in the downwind half.

The wall coefficients obtained for $\theta = 45^\circ$ are shown in **Figures 4.38 and 4.39**.

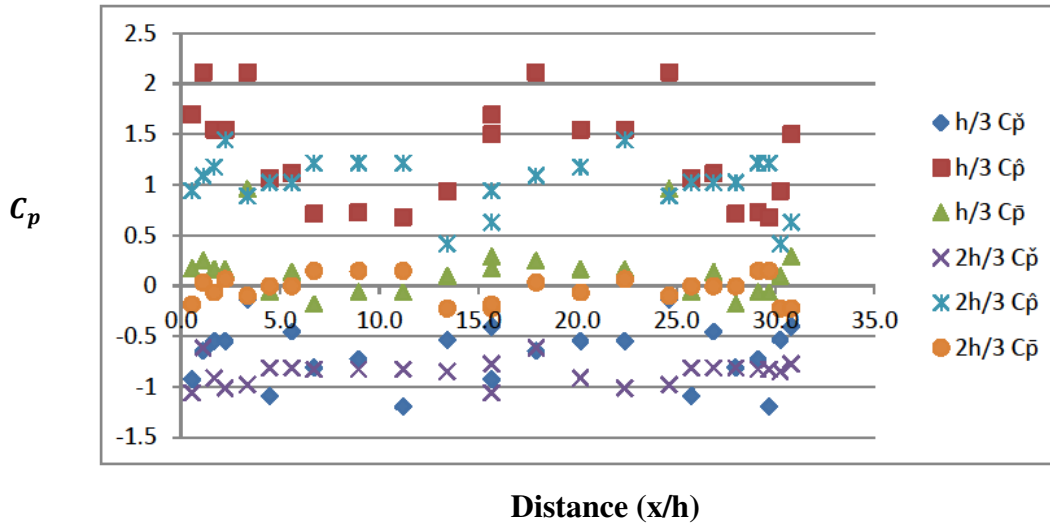


Figure 4.38 External Pressure Coefficients, C_p , Windward Wall W1 of Model C, $\theta = 45^\circ$

Figure 4.38 shows the maximum peak value on wall W1 for the 45° wind direction is 2.1, which is similar to the maximum peak value of 2.3 for the 0° wind direction. A minimum peak coefficient of -1.1 is also shown in **Figure 4.38**, which differs from the results for $\theta = 0^\circ$, where no suction pressures were recorded.

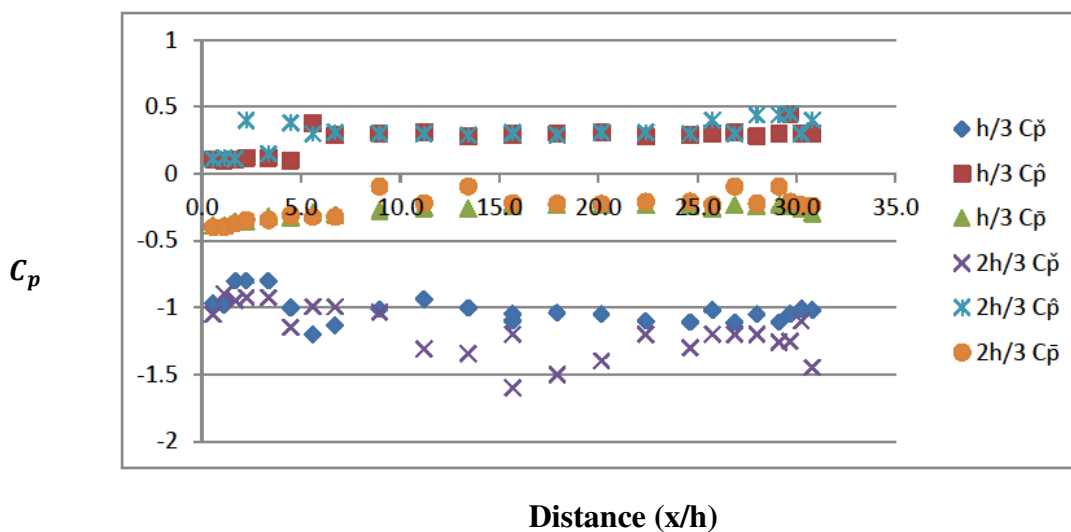


Figure 4.39 External Pressure Coefficients, C_p , Leeward Wall W3 of Model C, $\theta = 45^\circ$

Figure 4.39 shows for $\theta = 45^\circ$, the W3 wall pressure coefficients have peaks of +1.6 and -1.1 which are greater in magnitude than the coefficients +0.4 and -0.3 for $\theta = 0^\circ$.

4.3.3 Model C Internal Pressure Coefficients

The mean, maximum and minimum internal pressure coefficients were measured in a similar manner to Model B and with the tap arrangement described in 3.4.

The results are presented in **Figures 4.40, 4.41 and 4.42**

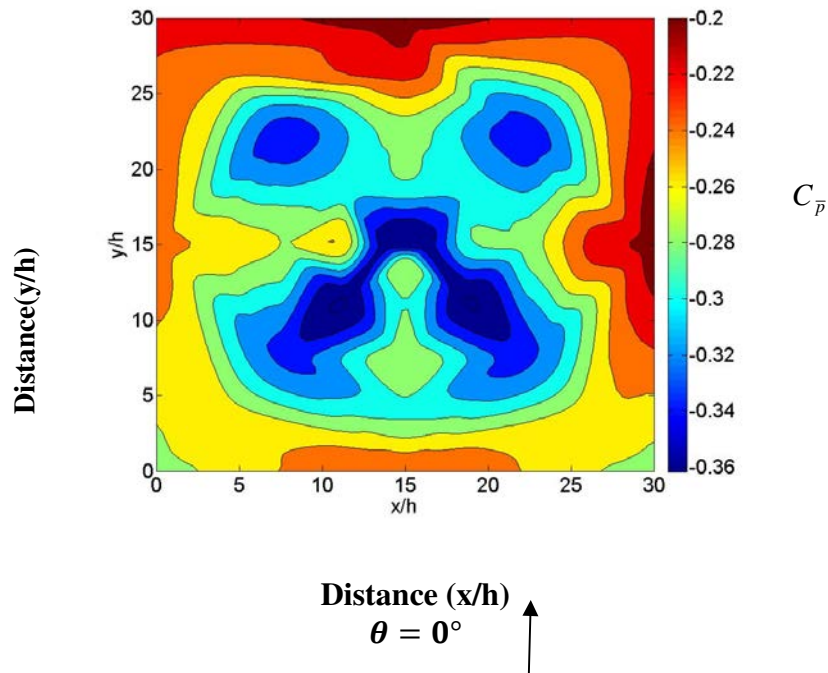


Figure 4.40 Mean Internal Pressure Coefficient, $C_{\bar{p}}$
Model C, $\theta = 0^\circ$

Figure 4.40 shows only small change in the mean internal pressure across the model with a trend of decreasing magnitude at the leeward edge. The increased porosity and also mesh construction (lower loss coefficient) has created a more even distribution to the mean internal pressure measured in Model B.

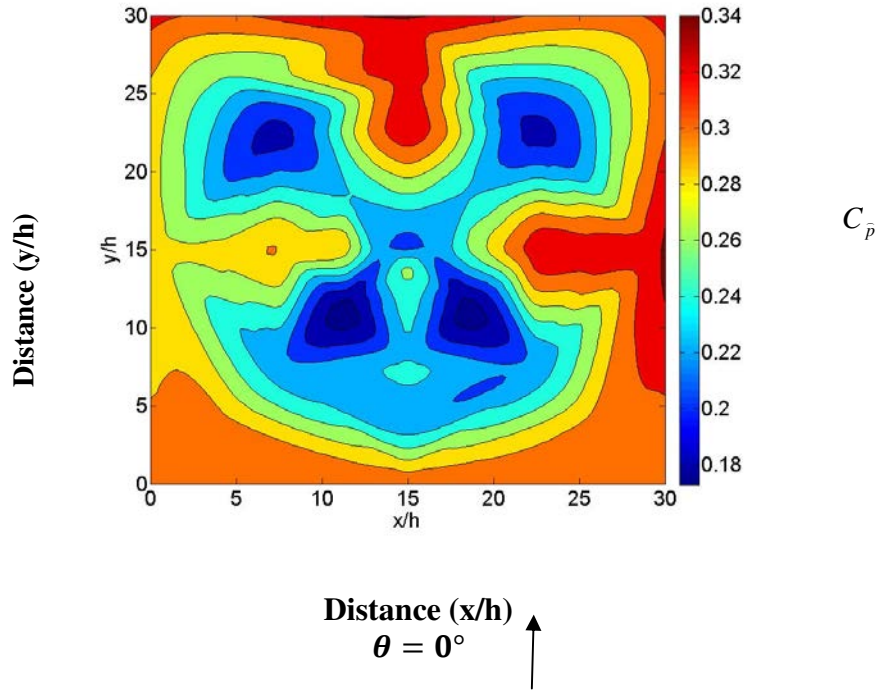


Figure 4.41 Maximum Internal Pressure Coefficient, $C_{\bar{p}}$
Model C, $\theta = 0^\circ$

The maximum internal pressures also show small variation across the model with the greatest magnitudes occurring at the leeward edge as air passes out through the leeward wall.

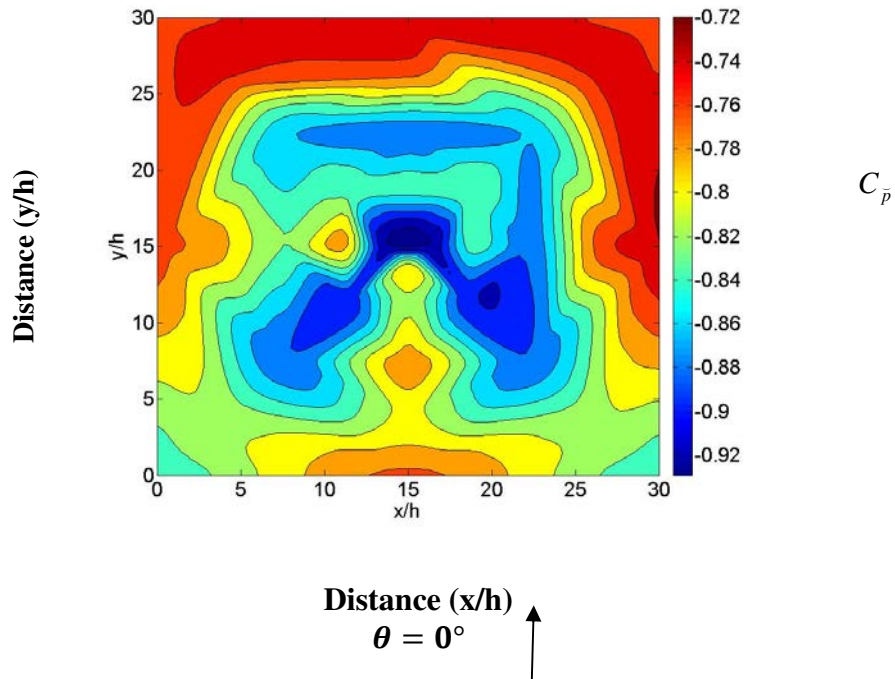
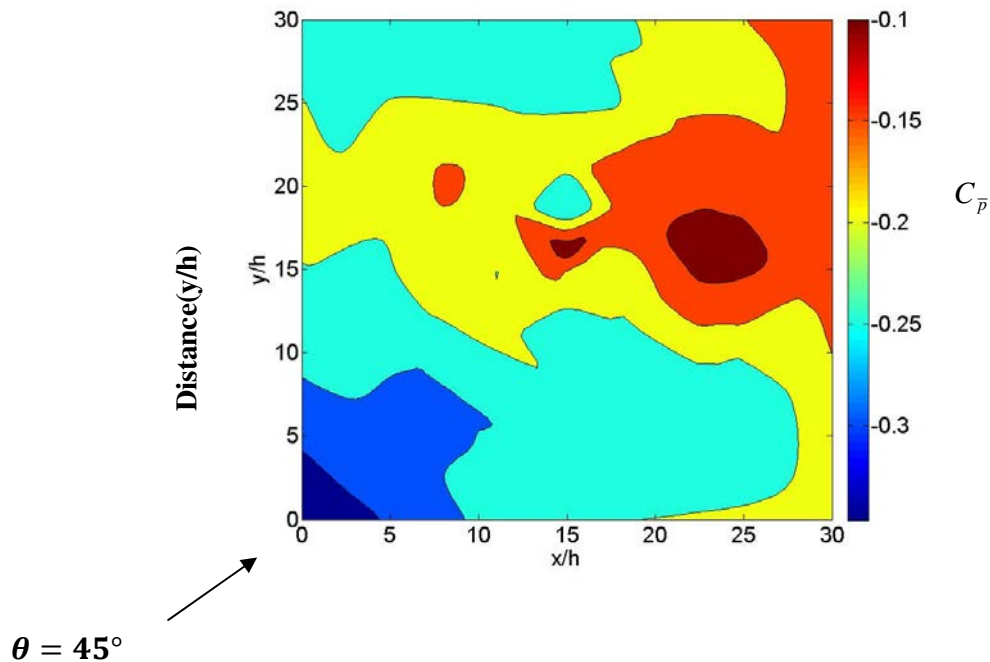


Figure 4.42 Minimum Internal Pressure Coefficient, $C_{\bar{p}}$,
38% Porosity Model C, $\theta = 0^\circ$

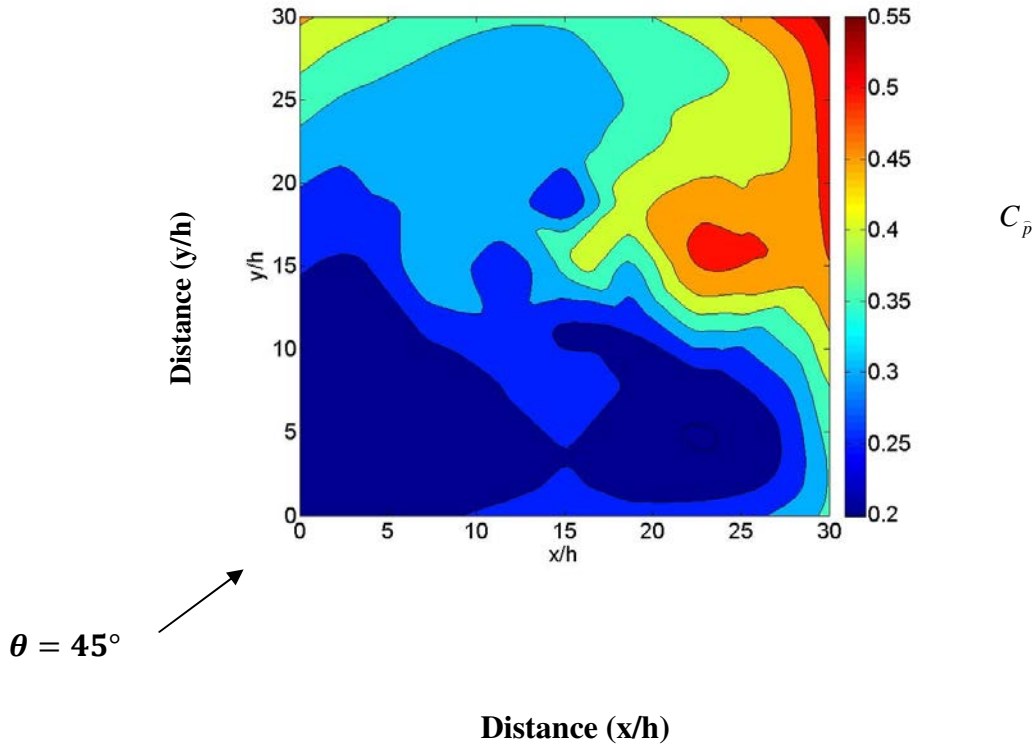
The minimum internal pressure distribution is similar to the mean. Magnitudes vary between -0.92 and -0.72.

Figures 4.43, 4.44 and 4.45 present the internal pressure measurement for $\theta = 45^\circ$



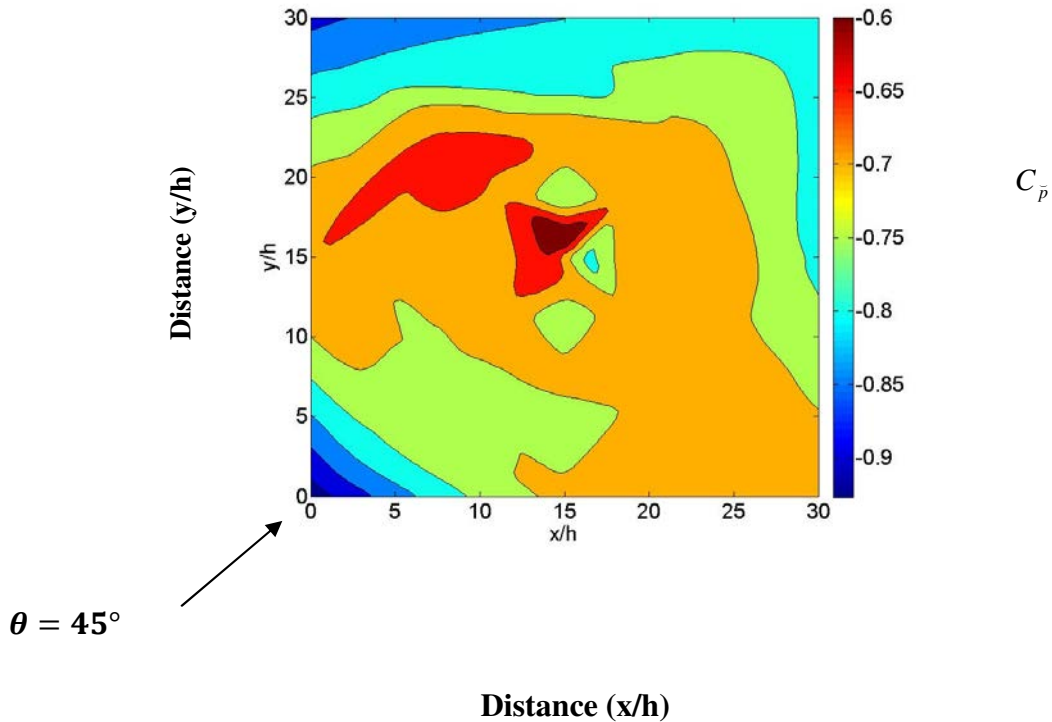
Distance (x/h)
Figure 4.43 Mean Internal Pressure Coefficient, $C_{\bar{p}}$
Model C, $\theta = 45^\circ$

The mean values for $\theta = 45^\circ$ in **Figure 4.43** show a variation from -0.35 to -0.1 across the diagonal of the model.



Distance (x/h)
Figure 4.44 Maximum Internal Pressure Coefficient, $C_{\bar{p}}$
Model C, $\theta = 45^\circ$

The maximum values in **Figure 4.44** vary across the diagonal from 0.2 to 0.55 at the leeward corner.



Distance (x/h)
Figure 4.45 Minimum External Pressure Coefficient, $C_{\bar{p}}$,
38% Porosity Model C, $\theta = 45^\circ$

The minimum internal pressure shown in **Figure 4.45** vary from -0.95 to -0.6 in the centre of the model.

4.4 Model D, 58% Porosity

4.4.1 External Pressure Coefficients for $\theta = 0^\circ$

The mean, maximum and minimum external pressure coefficients for the 58% porous Model D for $\theta = 0^\circ$ are presented in **Figures 4.46, 4.47, and 4.48**

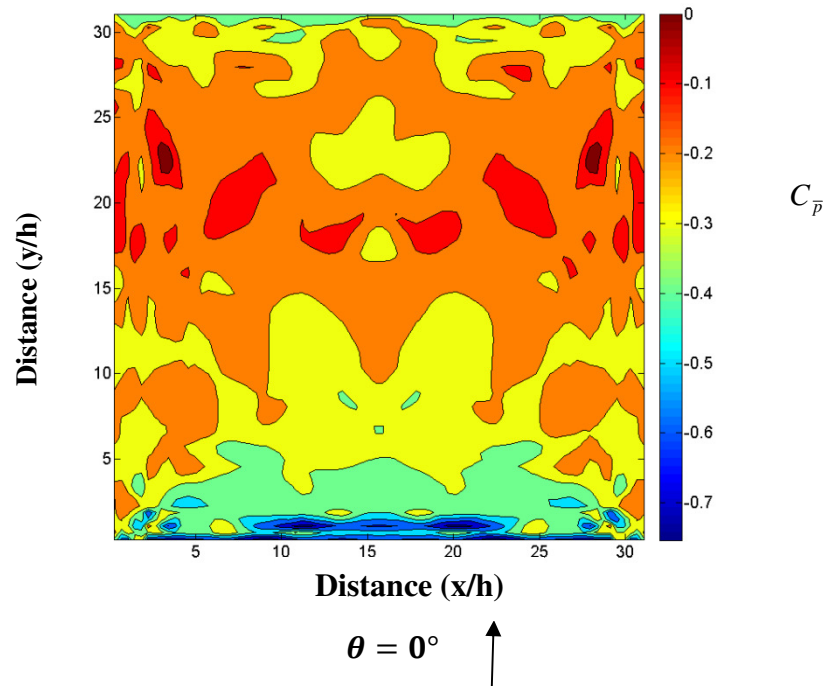
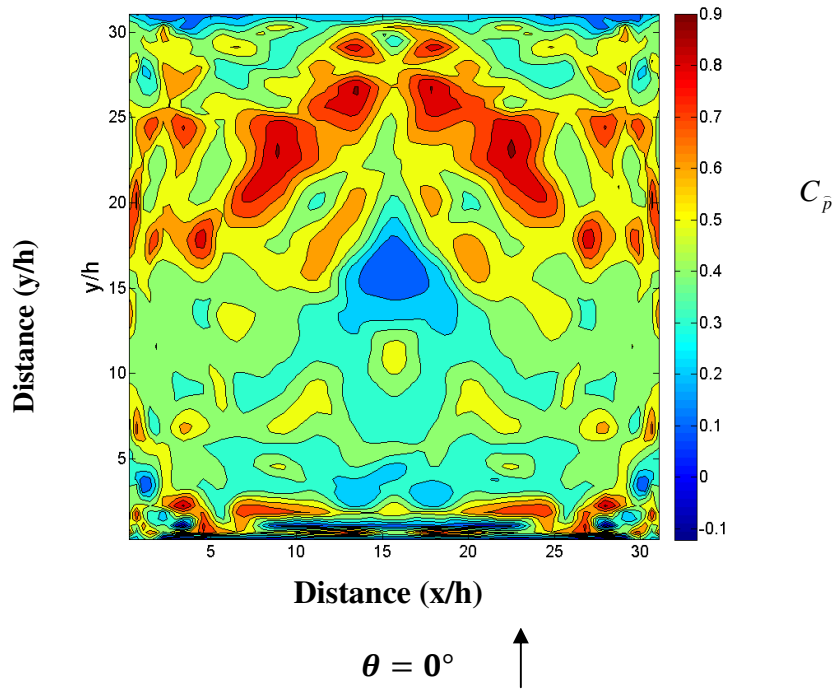


Figure 4.46 Mean External Pressure Coefficient, $C_{\bar{p}}$, 58% Porosity Model D, $\theta = 0^\circ$

Mean coefficients shown in **Figure 4.46** are of similar magnitudes to those for Models B and C. The maximum suction zone at the windward edge extends a smaller distance than for Models B & C, indicating that with increase in porosity, the wind separation at the roof edge diminishes.



**Figure 4.47 Maximum External Pressure Coefficient, $C_{\bar{p}}$,
58% Porosity Model D, $\theta = 0^\circ$**

Figure 4.47 shows higher downward values in the downwind half similar to Models B and C. Pressure coefficients vary from 0 to +0.9.

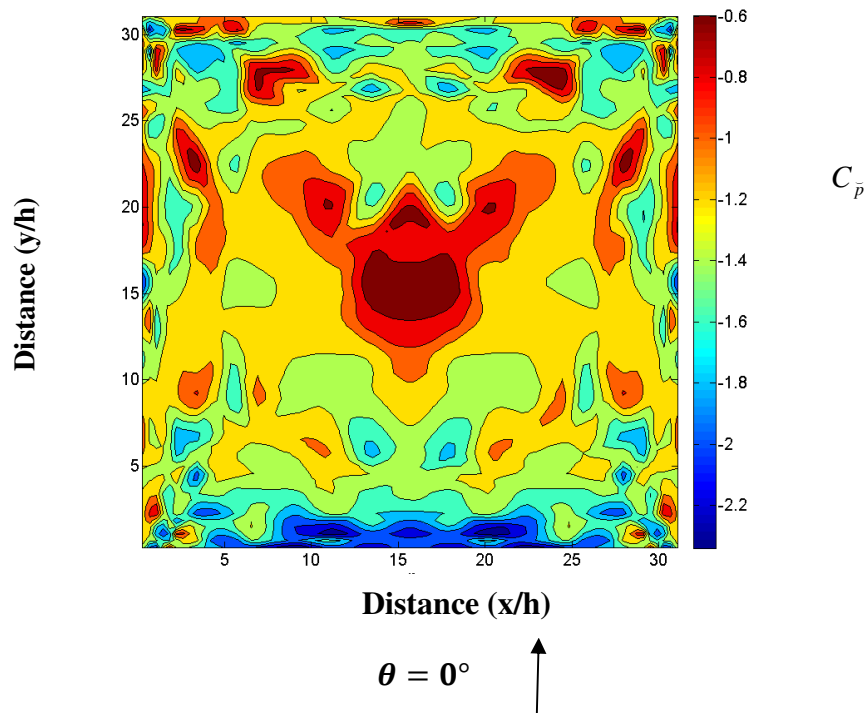


**Figure 4.48 Minimum External Pressure Coefficient, $C_{\bar{p}}$,
58% Porosity Model D, $\theta = 0^\circ$**

The peak suction coefficients shown in **Figure 4.48** vary between -2.2 and -0.6. The peak edge suction are of greater magnitude than the less porous models, but of shorter depth across the roof. There are also greater magnitudes of suction towards the leeward edge.

The wall pressure plots for Model D are shown in **Figures 4.49, 4.50, 4.51**.

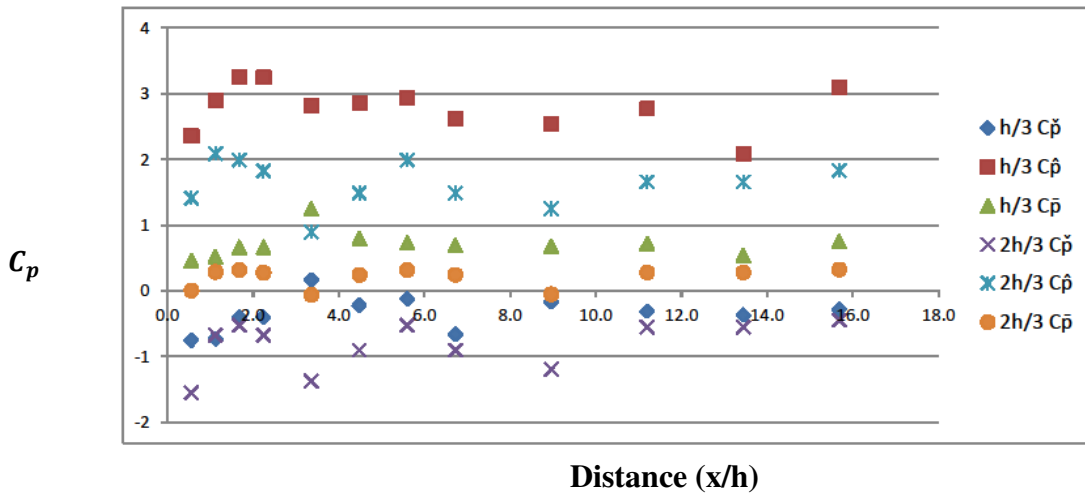


**Figure 4.49 External Pressure Coefficient C_p
Windward Wall W1 of Model D, $\theta = 0^\circ$**

Figure 4.49 shows the peak drag W1 wall values are +3.2 at h/3 and +2.1 at 2h/3. These values show an increase in magnitude from the lower porosity and non-porous models.

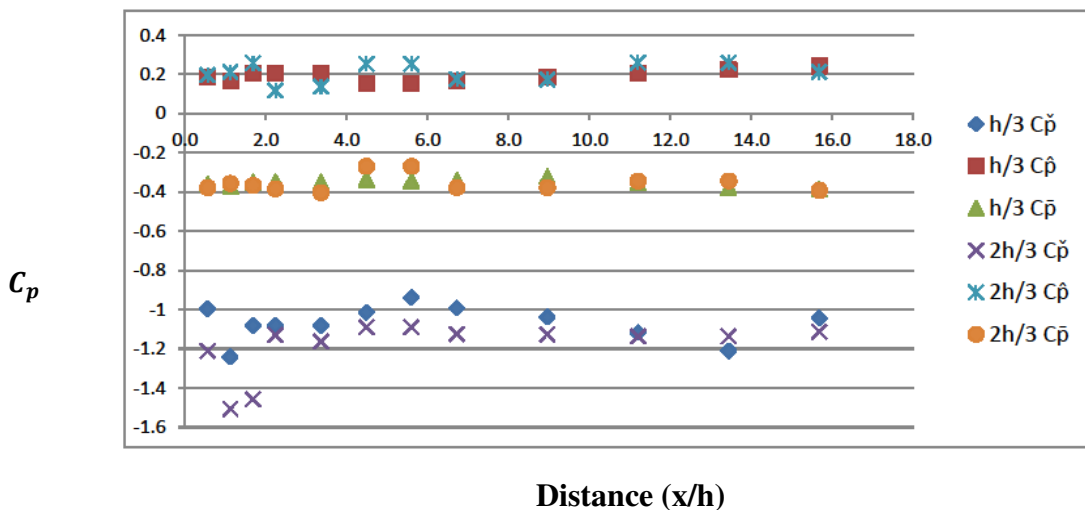


**Figure 4.50 External Pressure Coefficient C_p
Leeward Wall W3 of Model D, $\theta = 0^\circ$**

Figure 4.50 shows W3 wall coefficients are relatively constant in value with height and distance across the model and vary from -1.5 to .25. The peak minimum coefficient magnitude

is slightly greater than for Models B and C, indicating the greater porosity has influence on the suction pressure on W3.

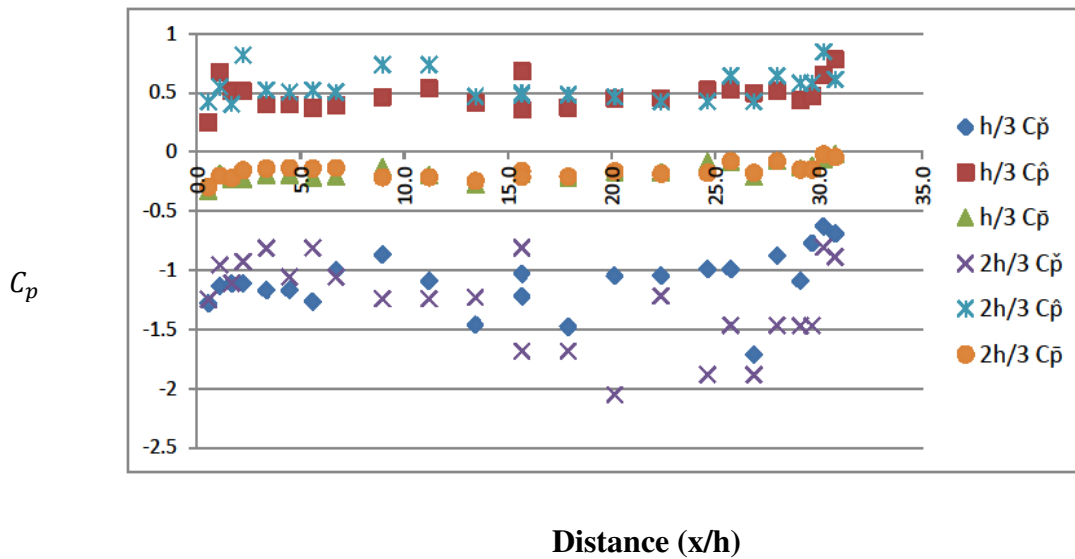


**Figure 4.51 External Pressure Coefficient C_p
Side Wall W2 of Model D, $\theta = 0^\circ$**

Figure 4.51 shows the mean pressure coefficient diminishes from -0.3 to zero at the leeward end. The Maximum pressure coefficient is relatively constant, fluctuating around 0.5, and the minimum coefficient slightly more erratic but averaging -1.3.

4.4.2 Model D External Pressure Coefficients for $\theta = 45^\circ$

Figures 4.52, 4.53 and 4.54 show the roof pressure coefficient distributions on roof surface R for the 45° wind direction.

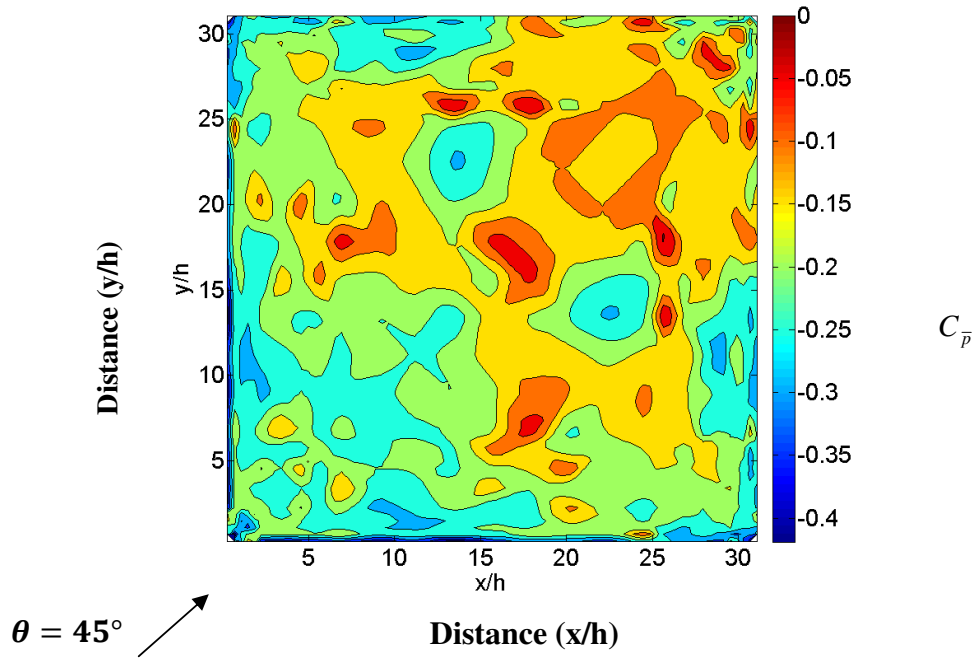


Figure 4.52 Mean External Pressure Coefficient, $C_{\bar{p}}$, 58% Porosity Model D, $\theta = 45^\circ$

The mean pressure coefficients shown in **Figure 4.52** have a similar distribution to the other porous models. The peak value of -0.45 is less than the peak value for $\theta = 0^\circ$.

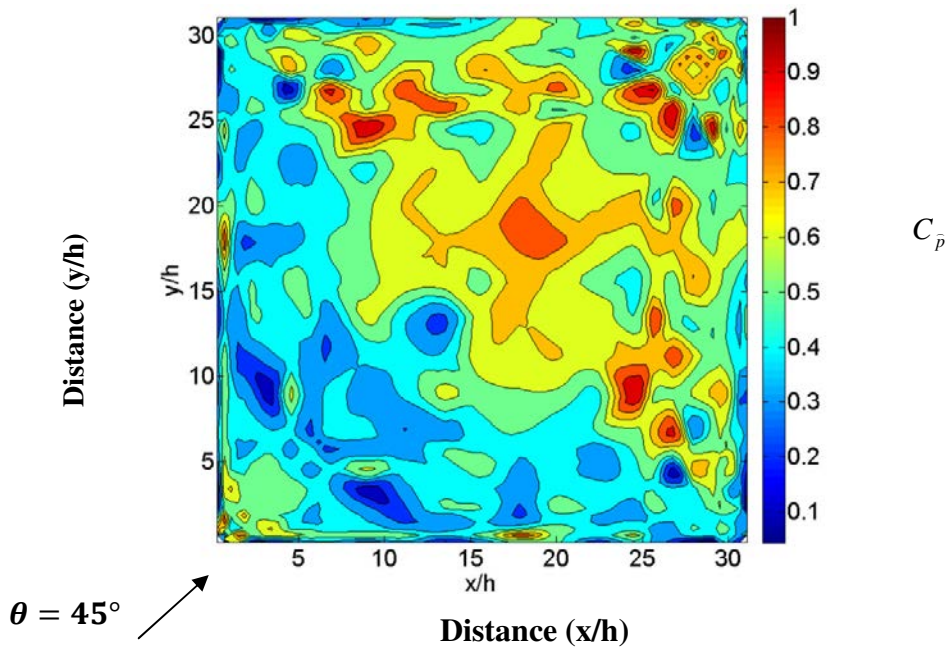


Figure 4.53 Maximum External Pressure Coefficient, C_p , 58% Porosity Model D, $\theta = 45^\circ$

The maximum pressure coefficients shown in **Figure 4.53** vary from 0 to 1.0 and are similar in magnitude to Model B and Model C.

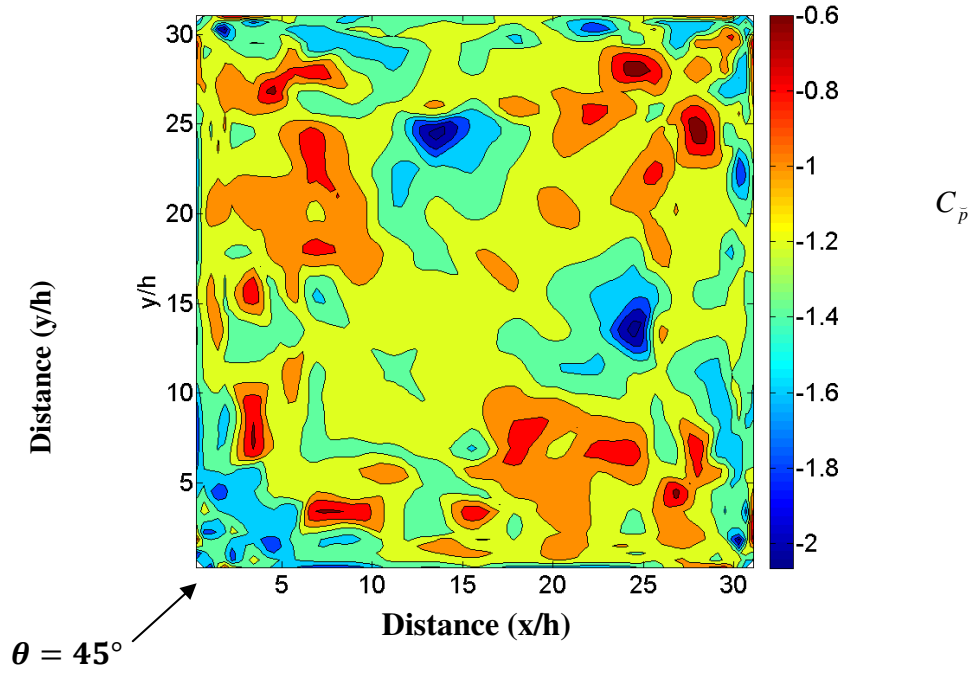


Figure 4.54 Minimum External Pressure Coefficient, 58% Porosity Model D, $\theta = 45^\circ$

Figure 4.54 shows the peak minimum pressure coefficients have similar distribution and magnitude to the other porous models.

The wall results are shown in Figs. 4.55 and 4.56.

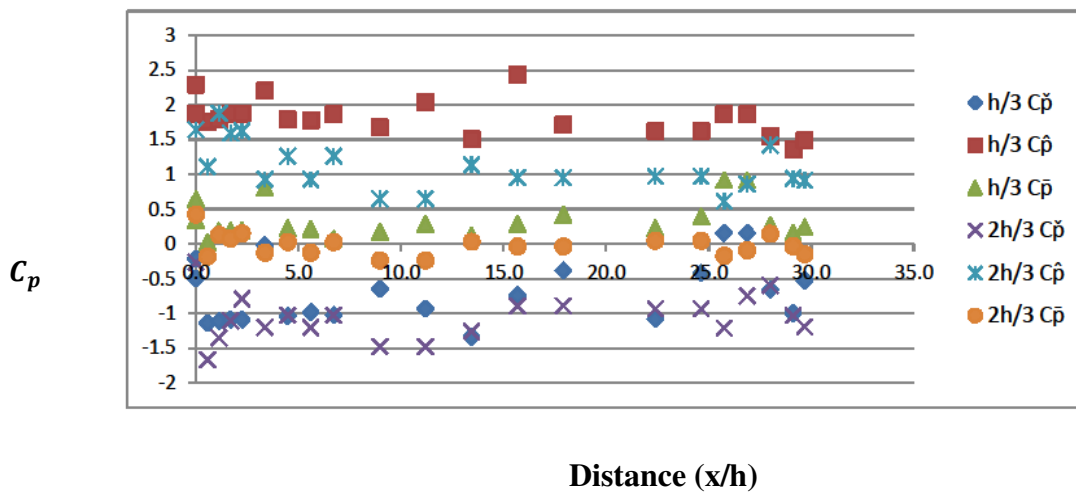


Figure 4.55 External Pressure Coefficient C_p Windward Wall W1 of Model D, $\theta = 45^\circ$

Figure 4.43 shows the pressure coefficients on wall W1 have slightly lower magnitudes to $\theta = 0^\circ$ pressure coefficients.

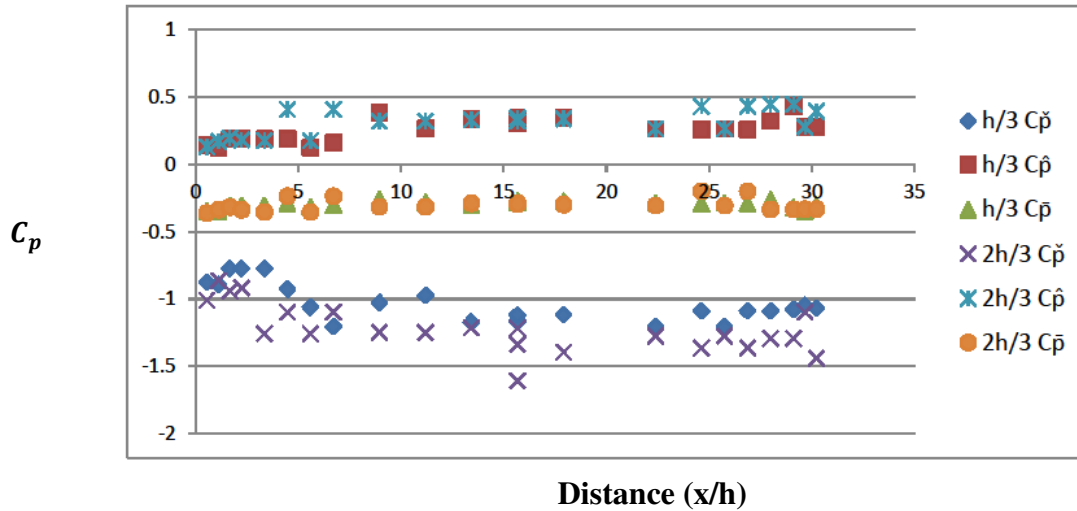


Figure 4.56 External Pressure C_p for Leeward wall W3 of Model D, $\theta = 45^\circ$

Figure 4.56 shows the pressure coefficients on wall W3 are similar in magnitude to the $\theta = 0^\circ$ pressure coefficients.

4.4.3 Model D Internal Pressure Coefficients

The mean, maximum and minimum internal pressure coefficients were measured only at the centre of the floor of the model:

Mean internal pressure = -0.38

Maximum internal pressure = 0.31

Minimum internal pressure = -1.46

4.5 Summary Comparison of Wind Tunnel Pressure results for the four Models

The external pressure results are compared in **Table 4.1** which shows the range of mean values and peak minimum and maximum results for the four Models.

Table 4.1 External Peak and Mean Roof Pressure Coefficients, $\theta = 0^\circ$

Model (porosity%)	$C_{\bar{p}}$ (maximum)	$C_{\bar{p}}$ (minimum)	$C_{\bar{p}}$ (mean) Range
Model A (0%)	0.6	-4.2	-1.6 to -0.2
Model B (19%)	0.7	-1.7	-0.55 to -0.05
Model C (38%)	0.8	-1.9	-0.65 to 0.1
Model D (58%)	0.9	-2.3	-0.8 to 0

The results indicate that the introduction of porosity leads to a significant reduction in the external mean and minimum roof suction pressures. The minimum and maximum external magnitudes increase slightly with increasing porosity.

Table 4.2 shows the distribution of minimum external pressure coefficients with distance from the edge using the height of model 'h' as the distance interval.

Table 4.2 Distribution of External Minimum Pressure Coefficients, $\theta = 0^\circ$

Distance From windward Edge	Model A $C_{\bar{p}}$ Minimum	Model B $C_{\bar{p}}$ Minimum	Model C $C_{\bar{p}}$ Minimum	Model D $C_{\bar{p}}$ Minimum
0-0.5h	-4.2	-1.6	-1.9	-2.3
0.5h-h	-2.5	-1.6	-1.9	-2.2
h-2h	-1.5	-1.6	-1.6	-2.1
2h-3h	-1.0	-1.6	-1.5	-1.6
3h-8h	-0.5	-1.6	-1.4	-1.2
8h -16h	-0.5	-1.0	-1.4	-1.0
>16h	-0.5	-0.8	-0.8	-0.8

The porous models have a more gradual reduction in suction pressure with distance away from the windward leading edge, but do not reduce in value to the same extent as the non-porous Model with distance. The three porous models all show a reduction in pressure to a common value of -0.8. Model D with the greatest porosity has the highest magnitude suction at the windward edge (-2.3). It can be concluded that the degree of porosity does have a small effect on the external pressure coefficients in the upwind half, the magnitude increasing with porosity.

Tables 4.3 to 4.5 show the summary of peak pressure coefficient results for the windward, leeward and side wall results for the 0° wind direction.

Table 4.3 External Windward Wall W1 Peak Pressure Coefficients, $\theta = 0^\circ$

Model (porosity%)	$C_{\bar{p}}$ (maximum)	$C_{\bar{p}}$ (minimum)	$C_{\bar{p}}$ (mean) Range
Model A (0%)	2.3	-0.5	0.5
Model B (19%)	2.2	-1.2	0 to 0.5
Model C (38%)	2.3	0.5	1.2 to 1.8
Model D (58%)	3.2	-1.2	0 to 1.1

The most porous Model D shows the highest windward pressure. The other models were all similar. Uplift pressures occurred on the models due to the 45° degree wall slope.

Table 4.4 External Leeward Wall W3 Peak Pressure Coefficients, $\theta = 0^\circ$

Model (porosity %)	$C_{\bar{p}}$ (maximum)	$C_{\bar{p}}$ (minimum)	$C_{\bar{p}}$ (mean) Range
Model A (0%)	0.2	-1.9	-0.6 to -0.3
Model B (19%)	0.5	-1.1	-0.4 to -0.1
Model C (38%)	0.4	-0.3	-0.1 to 0.15
Model D (58%)	0.25	-1.5	-0.4 to -0.3

Model C with the brass gauze and lowest loss coefficient has the lowest suction coefficient.

Table 4.5 External Side Wall W2 Pressure Coefficients, $\theta = 0^\circ$

Model (porosity %)	$C_{\bar{p}}$ (maximum)	$C_{\bar{p}}$ (minimum)	$C_{\bar{p}}$ (mean) Range
Model A (0%)	0.5	-2.4 to -0.6	-0.5 to -0.1
Model B (19%)	0.7	-1.7 to -0.5	-0.3 to 0
Model C (38%)	0.5	-2.0 to -1.1	-0.2
Model D (58%)	0.7	-2.1	-0.3 to 0

The porous Models C and D side wall pressures do not diminish gradually from the front windward corner in the same way as the non-porous model, but are of a more consistent pressure along the wall. The most porous model showed higher lift values in the second half by distance from the windward corner. It is evident that the flow of air through the wall is influencing these results.

The results for the wind in the 45° direction acting on the walls are compared in **Tables 4.6 and 4.7**.

Table 4.6 External Windward Wall Pressure Coefficients, $\theta = 45^\circ$

Model (porosity %)	$C_{\bar{p}}$ (maximum) Range	$C_{\bar{p}}$ (minimum) Range	$C_{\bar{p}}$ (mean) Range
Model A (0%)	2.0 to 1.0	-0.6	0.3 to 0.1
Model B (19%)	2.6 to 0.6	-1.0 to -0.3	0 to 0.5
Model C (38%)	2.1 to 0.6	-1.1 to 0	0 to 1.0
Model D (58%)	2.5 to 0.6	-1.5	0 to 1.0

The windward wall 45° direction peak results are similar in magnitude to the 0° windward wall results.

Table 4.7 External Leeward Wall Pressure Coefficients, $\theta = 45^\circ$

Model (porosity %)	C_p (maximum) Range	C_p (minimum) Range	$C_{\bar{p}}$ (mean) Range
Model A (0%)	2.0 to 1.0	-0.6	0.3 to 0.1
Model B (19%)	2.6 to 0.6	-1.0 to -0.3	0.5 to 0
Model C (38%)	2.1 to 0.6	-1.1 to 0	0 to 1.0
Model D (58%)	0.5	-1.3	-0.5 to -0.

The leeward results show minimum values similar to the 0° results. There are greater positive pressures present except for Model D.

Table 4.8 presents the peak internal pressure results for the porous models.

Table 4.8 Peak Internal Pressure Coefficients for Porous Models B, C and D

Model (porosity %)	C_p (maximum)	C_p (minimum)	$C_{\bar{p}}$ (mean)
Model B (19%)	0.4	-0.98	-0.35
Model C (38%)	0.35	-0.9	-0.35
*Model D (58%)	0.31	-1.46	-0.38

*Model D measured only at one central location.

The results for Models B and C are similar.

The external pressure results show the following significant features:

- The suction roof uplift pressure coefficients for the porous models are significantly less in magnitude than for the non-porous model.
- The roof uplift values are greatest at the windward edge and gradually reduce across the upwind half of the roof. The rate of reduction in value is slower than for the non-porous model.
- The degree of porosity does not significantly influence the uplift pressure coefficients, but a slight increase in magnitude with increasing porosity occurs.
- The downward roof pressure coefficients are similar to the non-porous model pressure coefficients.
- The windward wall maximum coefficients are similar or greater than those for the non-porous model. The peak pressure coefficient is highest for the most porous model (Model D)
- The leeward wall suction coefficients are similar for the non-porous and porous Models B and D. Model C with the fine brass mesh is significantly smaller.

- The side wall pressure coefficients for the porous models do not reduce gradually with distance away from the windward corner in the same way the coefficients for the non-porous model do. It is evident that the flow of air through these walls is influencing the results.

5. Net Pressure Coefficients for Large Flat Roof Porous Canopies

5.1 Net Pressure Coefficient $C_{fig.net}$

The results in Chapter 4 demonstrated significant differences between the porous models' external roof and wall pressure coefficient trends and those for the non-porous model. In particular, there is significant reduction in magnitude of the external pressure suction coefficients on the porous model roof surfaces. Design coefficients also are required to take into account the concurrent actions of both external and internal pressures.

To derive net surface design pressure coefficients $C_{fig.net}$ for the porous models, the complete time based processor data was analysed by Matlab software to find the maximum and minimum combinations of external and internal pressure on the porous surfaces at any one instance of time. The summation of the simultaneous internal and external pressure measurements gives the resultant pressure at each tapping location and from this, the peak value obtained. Initially the external pressure results were summed with an internal pressure measurement only at the centre of the model. Subsequently the internal pressure variation across the model was studied in Models B and C by a series of measurements described in Section 3.4 and presented in Sections 4.2.3 and 4.3.3. The internal pressure measurements were combined with external pressure results obtained at similar x-y coordinates measured at the same instance of time.

From this analysis, the maximum positive (downward) and negative (uplift) $C_{fig.net}$ values at each tap location were found from the compiled results for 0° , 15° , 30° and 45° directions to provide maximum and minimum pressure coefficients for the orthogonal direction ($\theta = 0^\circ$) influenced by winds across $\pm 45^\circ$ sector as required by AS/NZ1170.2(2011)

To standardise the derived results with the design pressure coefficients given in AS/NZS 1170.2 (2011), the results were modified by a gust factor in **Equation 5.1**.

$$C_{fig.net} = C_{peak.net} / G_u^2 \quad (5.1)$$

$$C_{p.net} = C_{p.ext} - C_{p.int}$$

$$G_u = \text{gust factor} = 1.76$$

$$C_{fig.net} = \text{aerodynamic shape factor}$$

$$C_{peak.net} = \text{the peak value of } C_{p.net}$$

$$C_{p.ext} = \text{external pressure coefficient}$$

$$C_{p.int} = \text{internal pressure coefficient}$$

The gust factor is the ratio of the expected maximum gust wind speed within a specified period to the mean wind speed. In AS/NZS 1170.2 (2011) the basic wind speed for design is a 0.2 second gust measured at 10m height in open terrain. By dividing the peak coefficients with the gust factor a pseudo-steady coefficient is obtained to be combined with the pressure from the peak site wind speed.

Contour plots and graphs of the resulting maximum and minimum $C_{p,net}/G_u^2$ coefficients for the tested wind directions are presented in Appendix A.

5.2 Pressure Coefficient $C_{fig,net}$, Roof Surface R, Porous Models B, C and D

The net roof pressure coefficient $C_{p,net}/G_u^2$ contour diagrams for the three porous models are presented in Appendix A for the four wind directions 0° , 15° , 30° and 45° . As described in Chapter 3, the models were tapped in an eighth sector and rotated through 15° increments, providing measurements that could be combined in symmetry to give the distribution for the total roof.

The variation of pressure with distance is considered using the increment of distance equal to the height of the model 'h' = 25mm. This is consistent with the approach used in AS/NZS1170.2 (2011) for flat roofs to specify changes in the magnitude of the external pressure coefficient with distance across the roof.

These results for the $0^\circ \pm 45^\circ$ wind direction sector are combined to find peak suction and drag pressure actions for the combined results. This follows the approach of AS/NZS1170.2 (2011) which states the following:

'The building orthogonal design wind speeds ($V_{des\theta}$) shall be taken as the maximum cardinal direction site wind speed ($V_{sit\beta}$) linearly interpolated between cardinal points within a sector $\pm 45^\circ$ to the orthogonal direction being considered (see Figures 2.2 and 2.3). NOTE: That is, $V_{des\theta}$ equals the maximum value of site wind speed ($V_{sit\beta}$) in the range $[\beta = \theta \pm 45^\circ]$ where β is the cardinal direction clockwise from true North and θ is the angle to the building orthogonal axes.'

Following from this, the peak wind actions for an orthogonal wind direction with $\theta = 0^\circ$ are obtained from the peak pressure coefficients in the $\pm 45^\circ$ sectors. The contour plots for the three porous models that follow show the coefficients $C_{fig,net}$ found from these combined results.

5.2.1 Model B, 19% Porosity

The pressure coefficient contours for Model B, presented in Appendix A for the four recorded wind directions are shown combined in **Figures 5.1** and **5.2** which present the maximum and minimum resultant coefficients for the wind direction sector $\theta = 0^\circ \pm 45^\circ$.

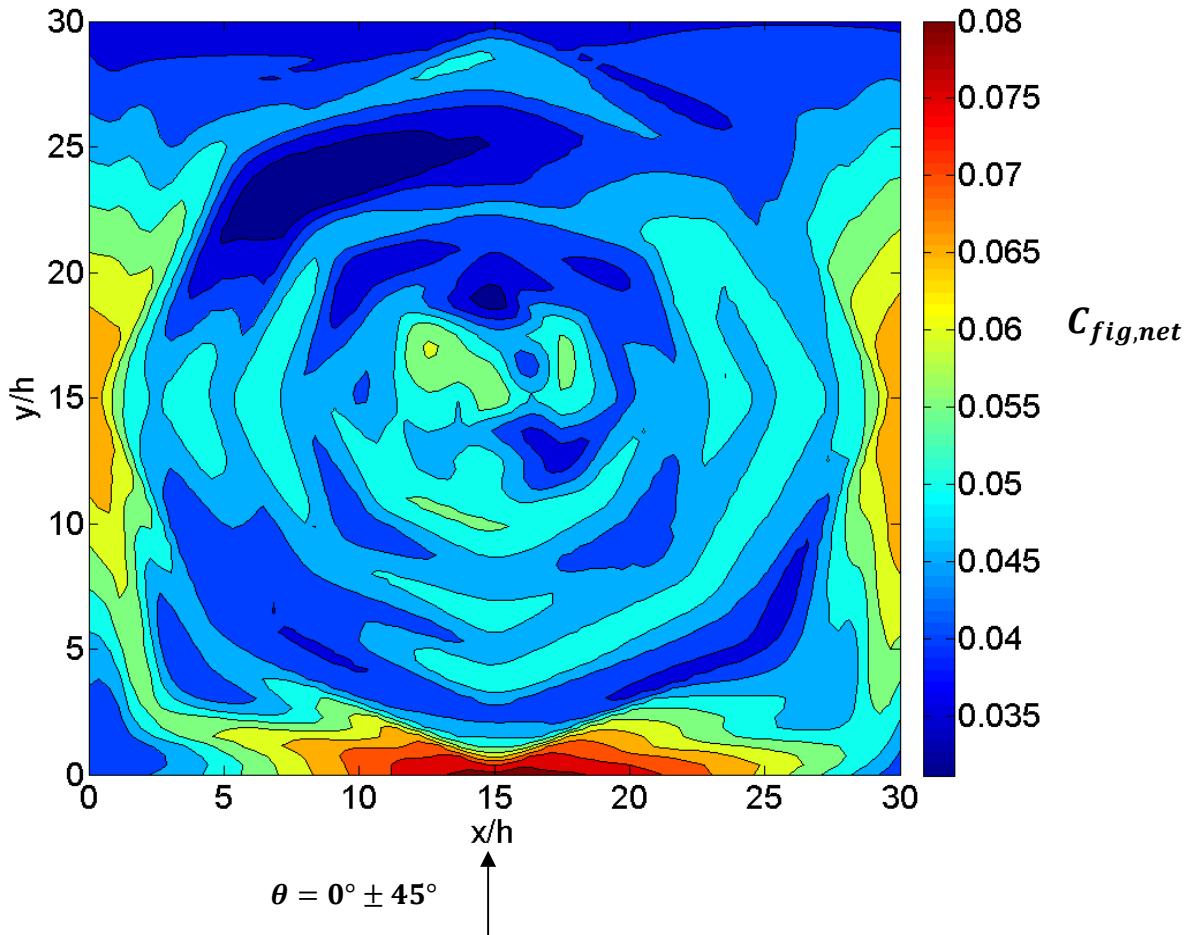
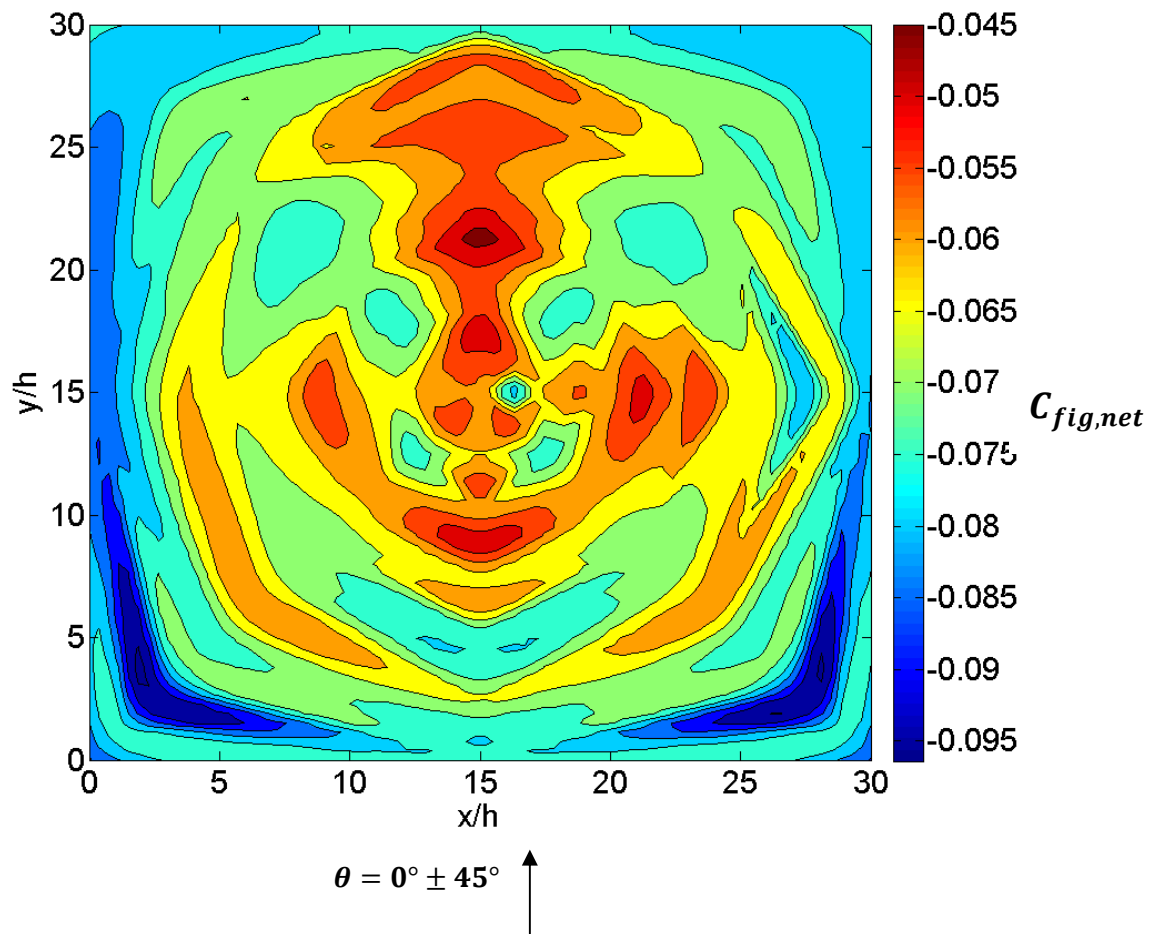


Figure 5.1 Maximum Pressure Coefficient $C_{fig,net}$, Model B, Wind direction sector $\theta = 0^\circ \pm 45^\circ$

The contour plot in **Figure 5.1** shows the maximum downward pressure coefficients on Roof R varying from 0.035 to +0.08. The peak values occur at the model edges with a value of 0.08 at the front roof edge in the centre of the model and -0.065 at the centre of the two side walls. The summation of the internal pressure measurement with the aligning external roof measurement leads to a more even net pressure distribution than the distribution resulting from combining one central internal measurement with the external pressure measurements across the roof.

From these results an average coefficient of +0.05 can be used for design when analysing the whole structure and a peak value of +0.08 when analysing local roof areas within $2h$ from the edge.



**Figure 5.2 Minimum Pressure Coefficient $C_{fig,net}$, Model B,
Wind direction sector $\theta = 0^\circ \pm 45^\circ$**

Figure 5.2 shows the minimum pressure coefficients greatest in magnitude on the windward edge and sides with a peak minimum coefficient of -0.095 in a region 2h -3h from the roof edge. There is then a region in the central part of the model from 3h to 15h with a minimum coefficient decreasing from -0.08 to -0.045. The actions are summarised in **Table 5.1**.

Table 5.1 Summary of Resultant Pressure Coefficients, Roof R, 19% Porosity

Distance from Structure Edge	$C_{fig,net}$ max	$C_{fig,net}$ min
0-2h from windward and side edges	0.08	-0.08
2h-3h from all edges	0.05	-0.095
3h-15h from all edges	0.04 average	-0.07 average

5.2.2 Model C, 38% Porosity

The pressure coefficient contours presented in Appendix A for Model C in the four recorded wind directions are shown combined in **Figures 5.3** and **5.4**, which present the resulting maximum and minimum coefficients for the wind direction sector $\theta = 0^\circ \pm 45^\circ$.

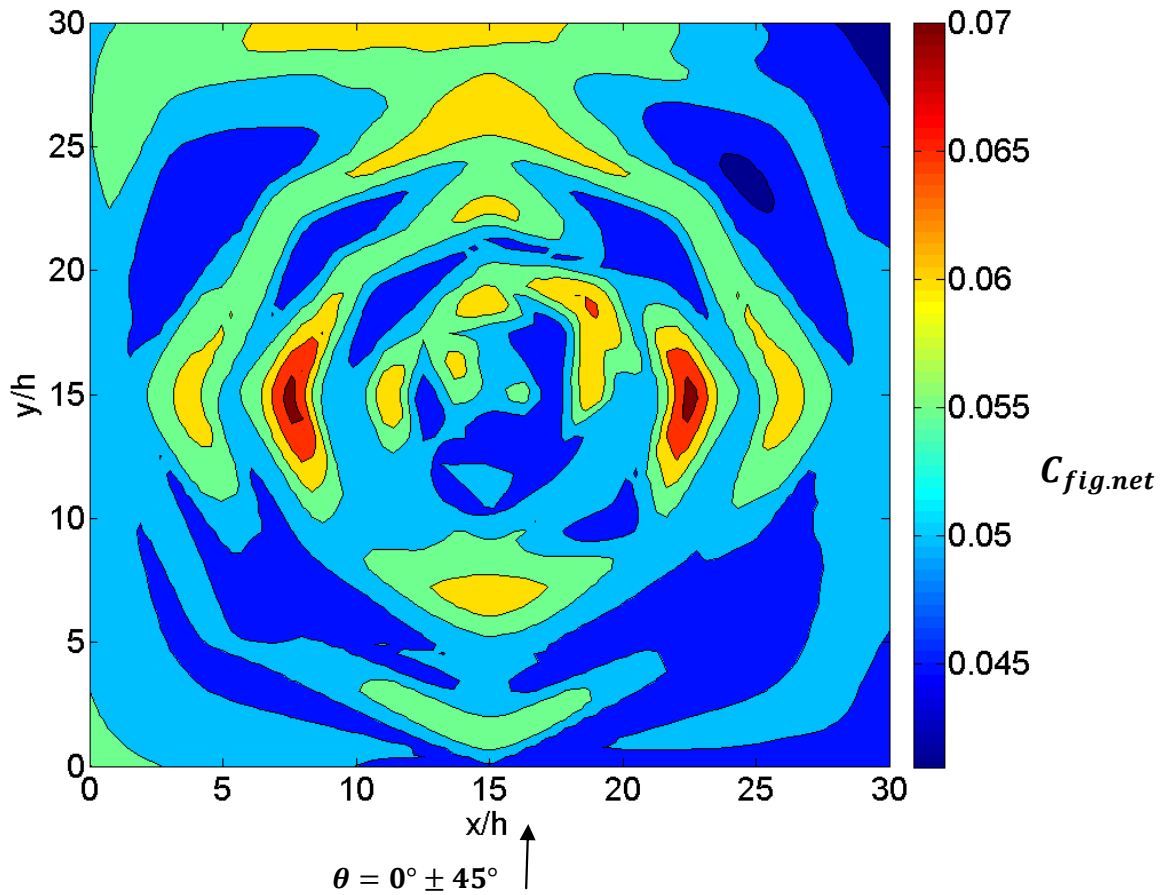


Figure 5.3 Maximum Pressure Coefficient $C_{fig.net}$, Model C,
Wind direction sector $\theta = 0^\circ \pm 45^\circ$

The maximum downward coefficients range in magnitude from +0.04 to +0.07. The distribution shows the 45° wind producing peak maximum results in the downwind half as the model width narrows towards the far corner.

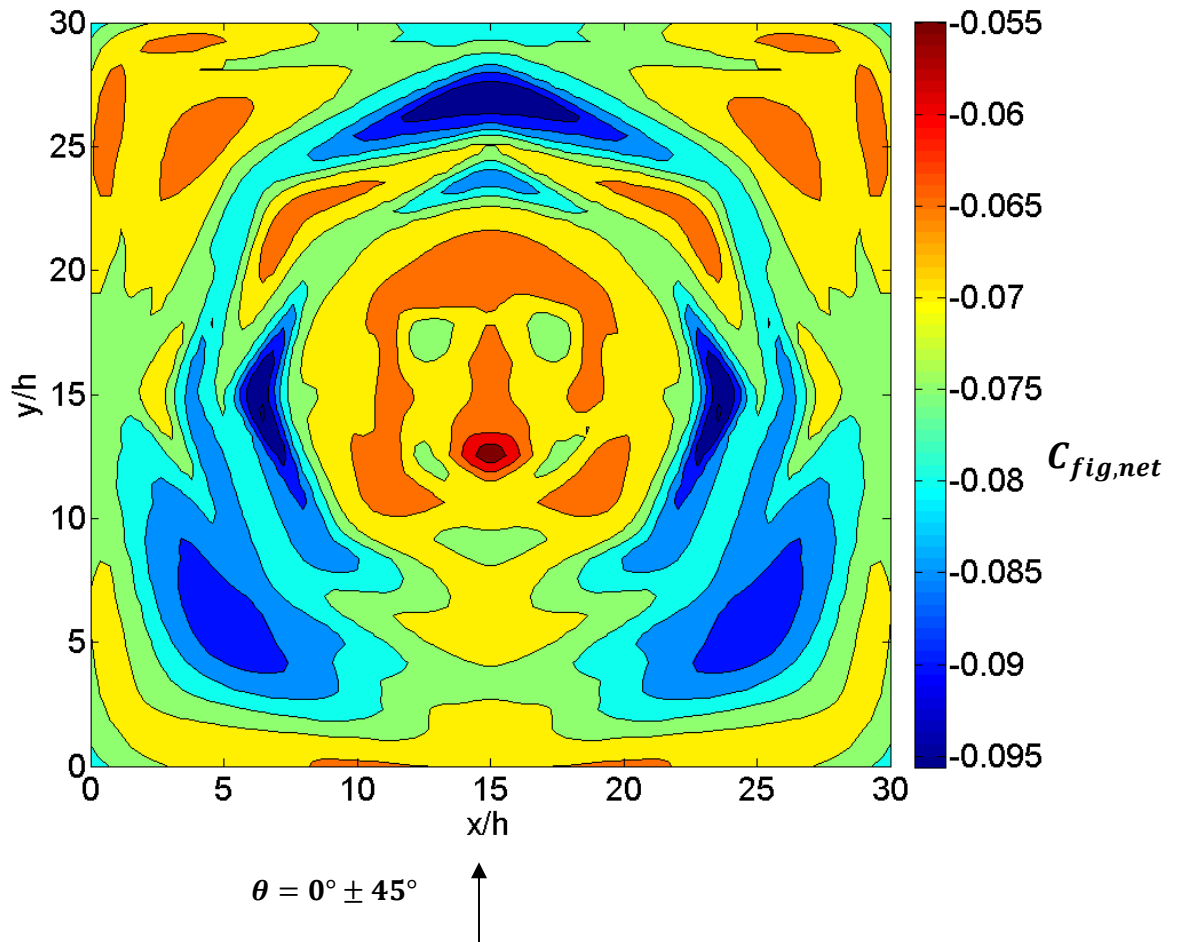


Figure 5.4 Minimum Pressure Coefficient $C_{fig,net}$, Model C, Wind direction sector $\theta = 0^\circ \pm 45^\circ$

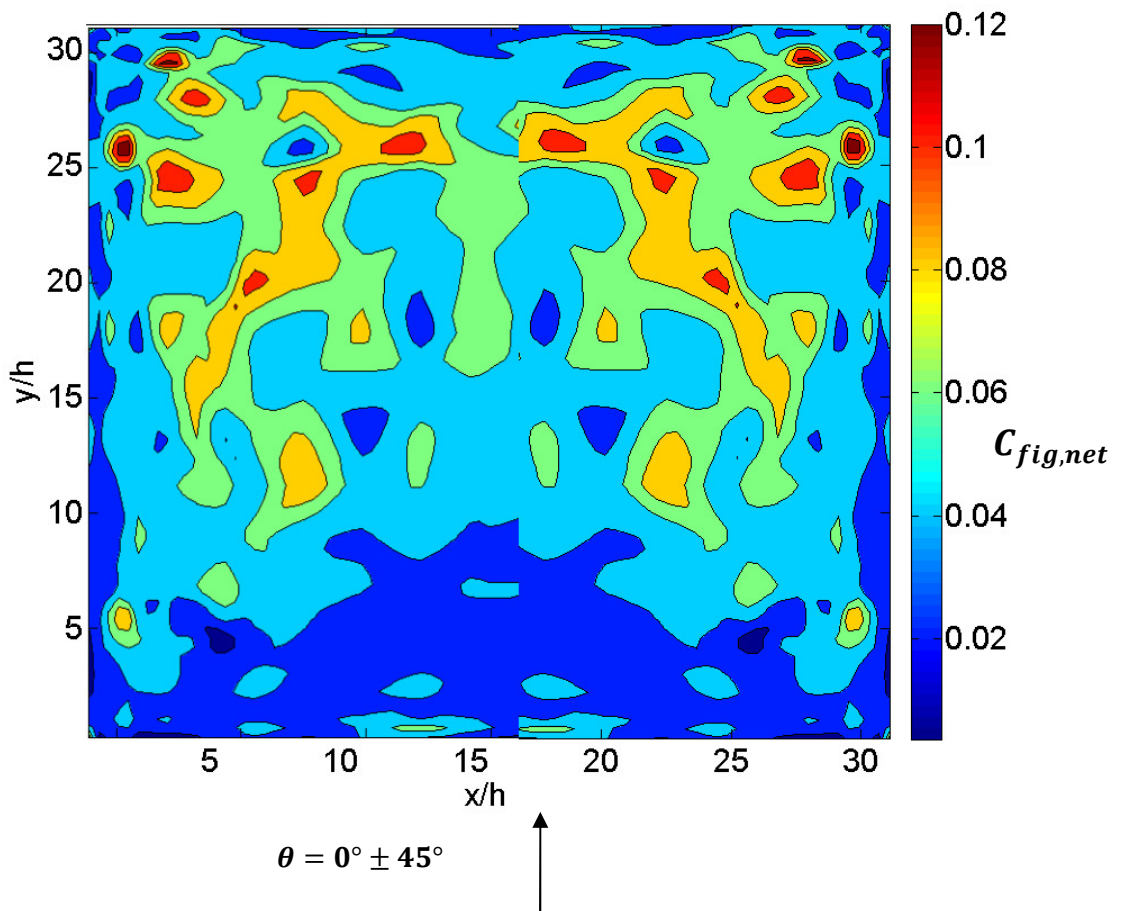
Figure 5.4 shows a similar minimum pressure range to Model B. The peak values of -0.095 are in region 3h-8h from the edges. The central roof section reduces to values between -0.075 and -0.045. The results are summarised in **Table 5.2**.

Table 5.2 Summary of Resultant Pressure Coefficients, Model C, Roof R, 38% Porosity

Distance from Structure Edge	$C_{fig,net}$ max	$C_{fig,net}$ min
0-3h from all edges	0.05	-0.07
3h-8h from all edges	0.05	-0.09
Central area > 8h from edge	0.05	-0.07

5.2.3 Model D, 58% Porosity

The pressure coefficient contours presented in Appendix A for Model D in the four recorded wind directions are combined in **Figures 5.5** and **5.6** which present the resulting maximum and minimum coefficients for the wind direction sector $\theta = 0^\circ \rightarrow 45^\circ$. Note that these resultant pressures are based on the summation of the external coefficients measured across the model with the internal pressure measured at one central point and therefore do not reflect as accurately the net pressure distribution compared to the results for Models B and C.



**Figure 5.5 Maximum Pressure Coefficient $C_{fig,net}$, Model D,
Wind direction sector $\theta = 0^\circ \pm 45^\circ$**

The maximum pressure coefficients in the upwind half of the roof vary between 0 and 0.06. In the downwind half there is a similar distribution to Model B and Model C with peaks occurring under the 45° wind direction with a coefficient magnitude range of +0.06 to +0.12.

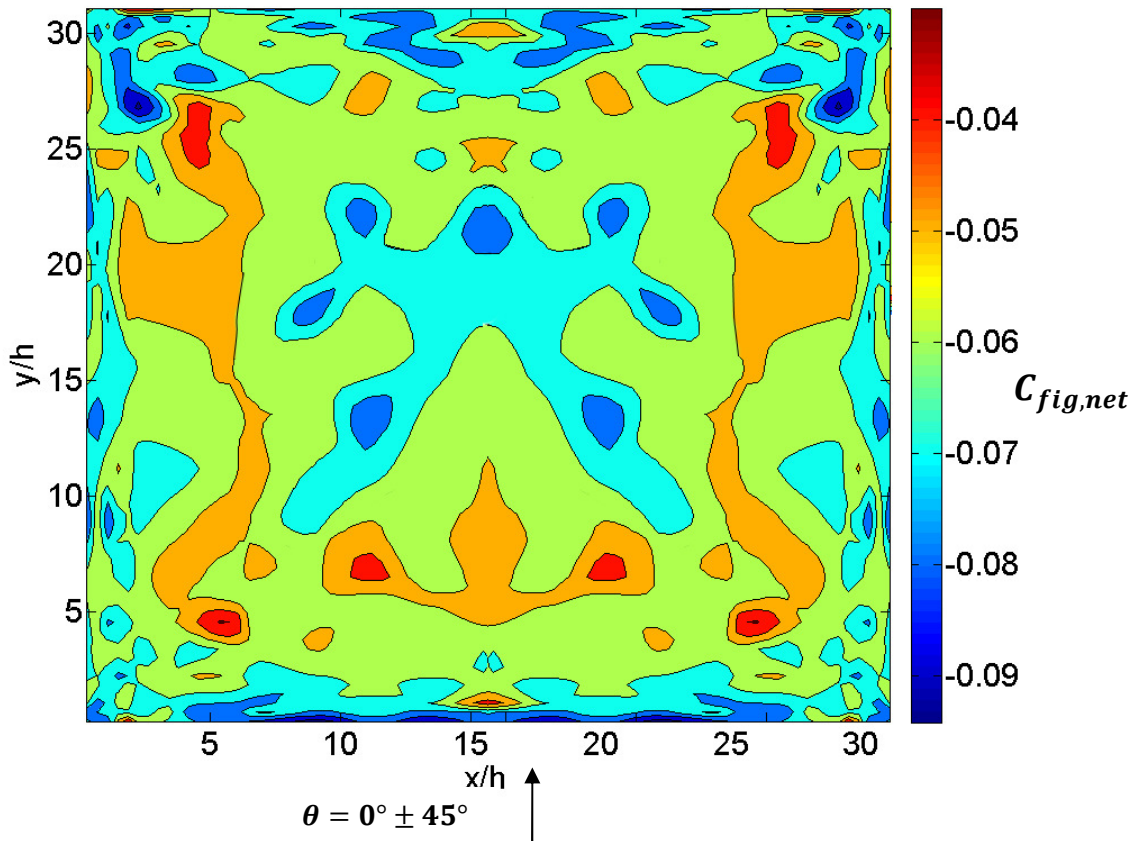


**Figure 5.6 Minimum Pressure Coefficient $C_{fig,net}$, Model D,
Wind direction sector $\theta = 0^\circ \pm 45^\circ$**

The minimum coefficients presented in **Figure 5.6** show magnitudes varying between -0.09 and -0.07 in a perimeter edge region of $3h$ width. For the majority of the surface the coefficient magnitudes vary between -0.05 and -0.07, averaging -0.06

The results are summarised in **Table 5.3**.

Table 5.3 Summary of Net Pressure Coefficients, Roof R, 58% Porosity

Distance from Structure Edge	$C_{fig,net}$ max	$C_{fig,net}$ min
0-3h from all edges	0.04	-0.08
> 3h from all edges, upwind half of roof	0.04	-0.06
> 3h from all edges, downwind half of roof	0.06	-0.06
Area 15hx15h downwind half	0.08	-0.06
Area 10hx10h in central section of roof	0.06	-0.08

5.3 Review of Roof Coefficients $C_{fig,net}$

Table 5.4 presents a summary of the Roof R net pressure coefficients for the three porous Models obtained by averaging the contour plotted results across the roof. The table should be used as a guide and reference to the detailed contour plots be made when carrying out a vigorous analysis of a flat roofed enclosed porous canopy.

Table 5.4 Summary of Roof R Net Pressure Coefficient, $C_{fig,net}$, $\theta = 0^\circ \pm 45^\circ$

Distance from Edge	Model B Maximum $C_{fig,net}$	Model B Minimum $C_{fig,net}$	Model C Maximum $C_{fig,net}$	Model C Minimum $C_{fig,net}$	Model D Maximum $C_{fig,net}$	Model D Minimum $C_{fig,net}$
*0-1h	0.08	-0.08	0.05	-0.07	0.04	-0.06
*1h-2h	0.08	-0.08	0.05	-0.07	0.04	-0.06
*2h-3h	0.05	-0.095	0.05	-0.07	0.04	-0.06
*3h-8h	0.05	-0.07	0.05	-0.09	0.04	-0.06
>8h	0.05	-0.07	0.05	-0.07	0.04	-0.06

* The pressures from 0 to 3h are to be applied to the four sides of the canopy

From this summary the following trends can be noted:

- (i) The maximum pressure coefficients vary only slightly with increased porosity and are predominantly slightly less in magnitude than the minimum suction coefficients.
- (ii) The minimum coefficients reduce slightly with increased porosity.
- (iii) The pressure variations across the three porous models are small.
- (iii) The results for Model D have been derived by extrapolating the results from models B and C with consideration of the derived results using only one central internal pressure measurement.
- (iv) The external design coefficients in AS1170.2 presented for the design of large flat roofs are significantly greater than the porous model net pressure coefficients. Excluding local factors which magnify the coefficients by 1.5 or 2.0 depending on the location, the largest magnitude coefficient is -0.9 located 0-1h from the roof edge. It is apparent that there is an interaction between the internal and internal pressures in the porous models leading towards and equalisation of pressure and resulting in small net coefficients.

5.4 Pressure Coefficient $C_{fig,net}$ Porous Models B, C and D, Walls W1, W2, W3 and W4

The net peak pressure wall coefficients that results after the summation of the external and internal pressure coefficients occurring at one time divided by G_u^2 is presented in Appendix A graphically. $C_{p,net}/G_u^2$ is plotted against the distance across the wall divided by the canopy height h and has been measured at heights $h/3$ and $2h/3$.

The results for the four wind directions have then been combined to present maximum and minimum pressure coefficients for the $\pm 45^\circ$ wind direction sector and a design orthogonal wind $\theta = 0^\circ$, following the approach used for the roof surface R. These combined results are presented graphically for each model.

5.4.1 Pressure Coefficient $C_{fig,net}$ Model B, Walls W1, W2, W3 and W4

Figure 5.7 presents the combined maximum and minimum pressure coefficients $C_{fig,net}$ on wall W1, the front windward wall for $\theta = 0^\circ$. The average values across the wall found by Matlab using the test data are shown with a broken line. The maximum coefficient ranges between 0.6 and 0.35 for the height $h/3$ and 0.55 to 0.35 at the height $2h/3$. The average maximum coefficient is 0.45 at $h/3$ and at $2h/3$, with peak value of 0.6. The slight reduction in value in the upper half of the wall can be attributed to the increase of the wind speed around the structure at the wall roof intersection.

The minimum values range between -0.05 and -0.3 at a height of $2h/3$ and -0.1 to -0.2 at $h/3$

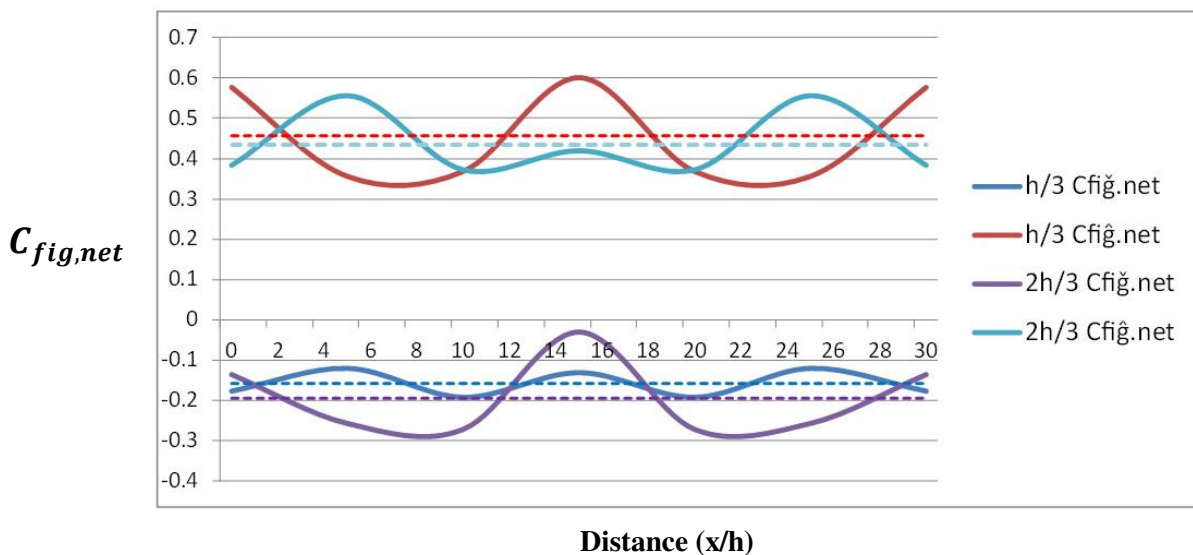


Figure 5.7 Maximum and Minimum Net Pressure Coefficient $C_{fig,net}$, Model B, Wall W1

Figure 5.8 shows the combined net pressure coefficient results for Walls W2 and W4, side walls. The maximum values vary between 0.9 and 0.2 , diminishing away from the windward corner. The minimum pressure coefficients vary between -0.25 and -0.05. The greater positive values produce inward actions on the side walls which differ significantly from the wind actions on a non-porous side wall where out ward actions are of most significance for design.

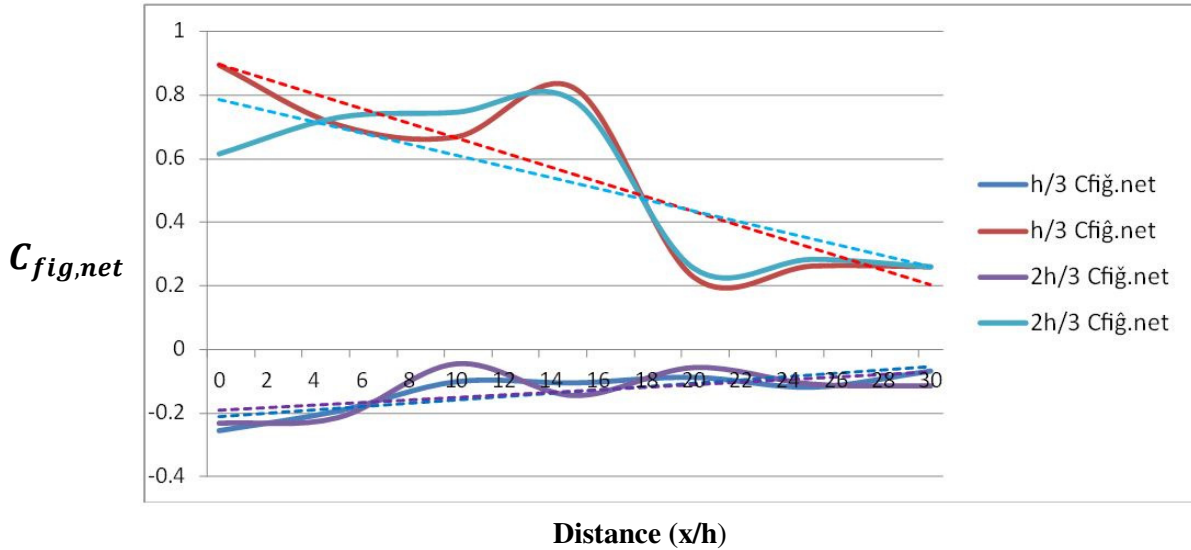


Figure 5.8 Maximum and Minimum Net Pressure Coefficient $C_{fig.net}$, I W2

Figure 5.9 presents the net maximum and minimum pressure coefficients for wall W3. Maximum pressure coefficients vary between 0.3 and 0.55 for the two measurement heights and the minimum between -0.3 and -0. 45. Mean peak values are +0.4 and -0.15. Similar to the side wall wind actions, the dominant design action is the inward positive force, again differing form the actions on a non-porous zero porosity leeward wall. It is evident that the air passing through the interior of the model and out through the large roof surface causes the side and rear walls to experience inward wind actions.

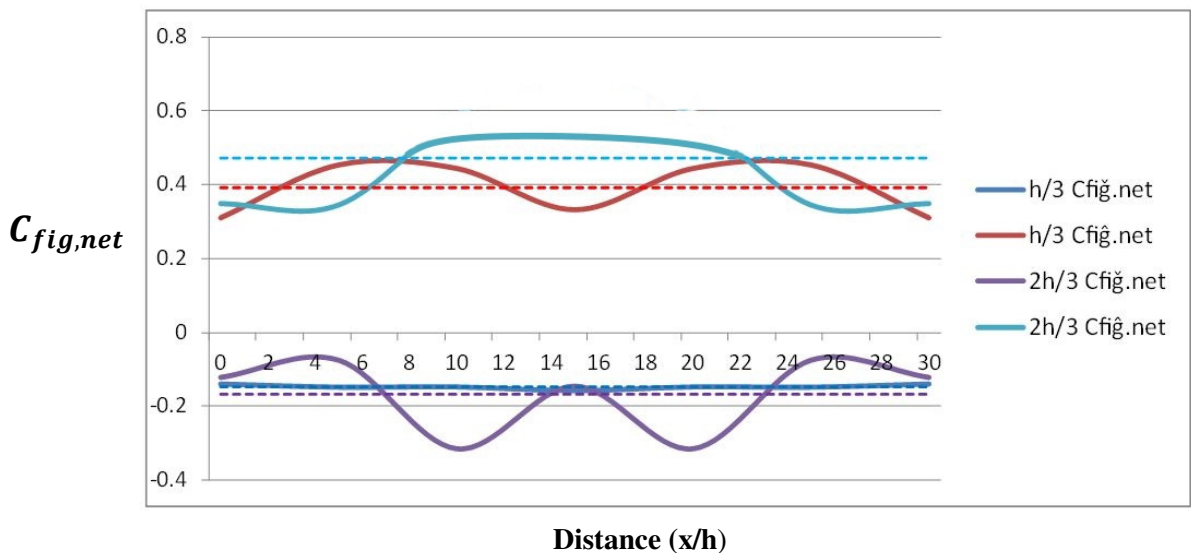


Figure 5.9 Maximum and Minimum Net Pressure Coefficient $C_{fig,net}$, Model B Wall W3

5.4.2 Net Pressure Coefficient $C_{fig,net}$, Model C, Walls W1, W2, W3 and W4

Figure 5.10 presents the combined net peak pressure coefficients for wall W1 of Model C which has a porosity of 38% and mesh construction. The maximum coefficients vary between 0.4 and 0.5 for both measurement heights. The peak suction coefficients range between -0.1 and -0.4. A maximum design coefficient of 0.5 is indicated. The minimum coefficient averages -0.25.

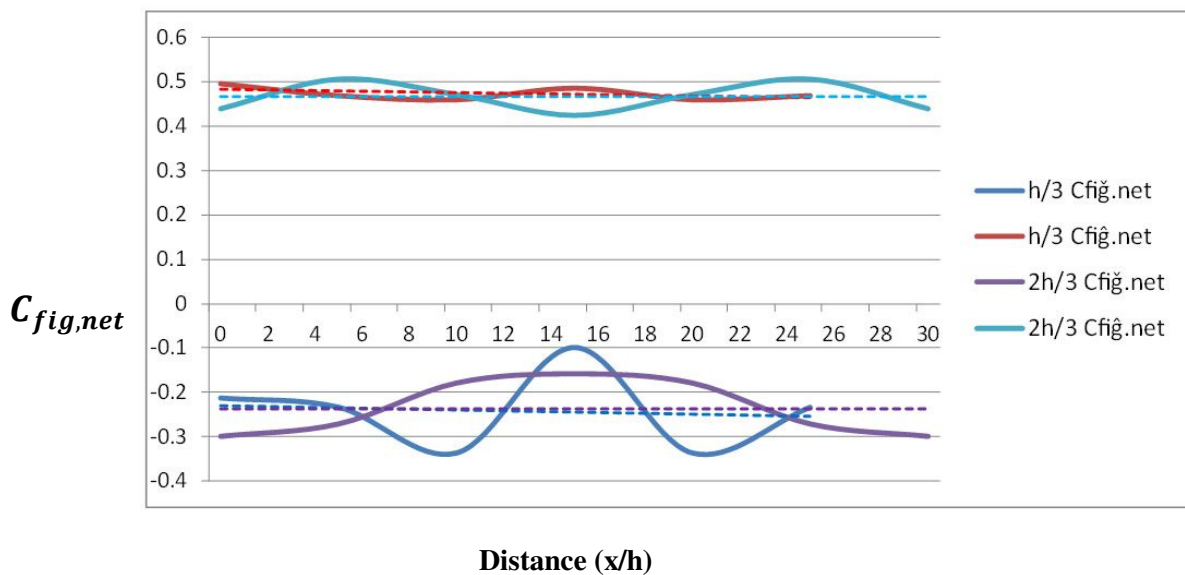


Figure 5.10 Maximum and Minimum Net Pressure Coefficient $C_{fig,net}$, Model C Wall W1

The side walls W2 and W4 net peak pressure coefficient results are presented in Figure 5.11. The maximum coefficient is greatest in magnitude (0.6) at the front corner and at a height of $h/3$, similar to Model B. The maximum coefficient reduces to 0.4 along the wall. The peak minimum coefficient averages -0.1 across the wall. The pressures show the side walls being drawn inward by the flow of the wind through the model's interior and out through the porous roof and walls.

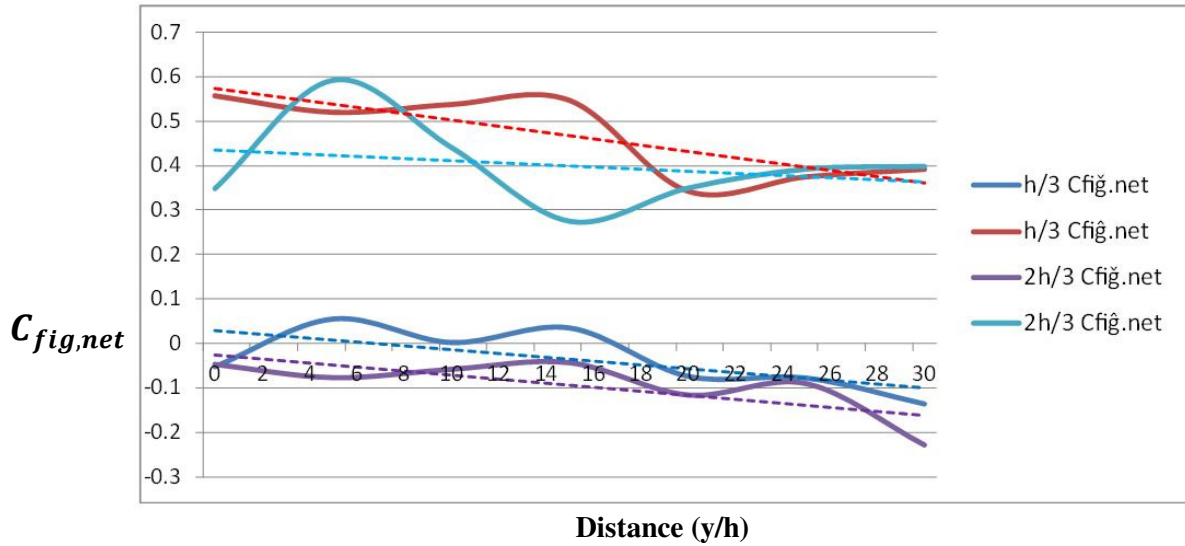


Figure 5.11 Maximum and Minimum Net Pressure Coefficient $C_{fig,net}$, Model C Wall W2

Figure 5.12 shows the peak net coefficients for Wall W3. The maximum coefficients average +0.3 and the net peak minimum coefficients average -0.15 across the wall. The inward pressure on the wall, similar to the side walls indicates an inward suction on the wall as the air flows out through the large roof area.

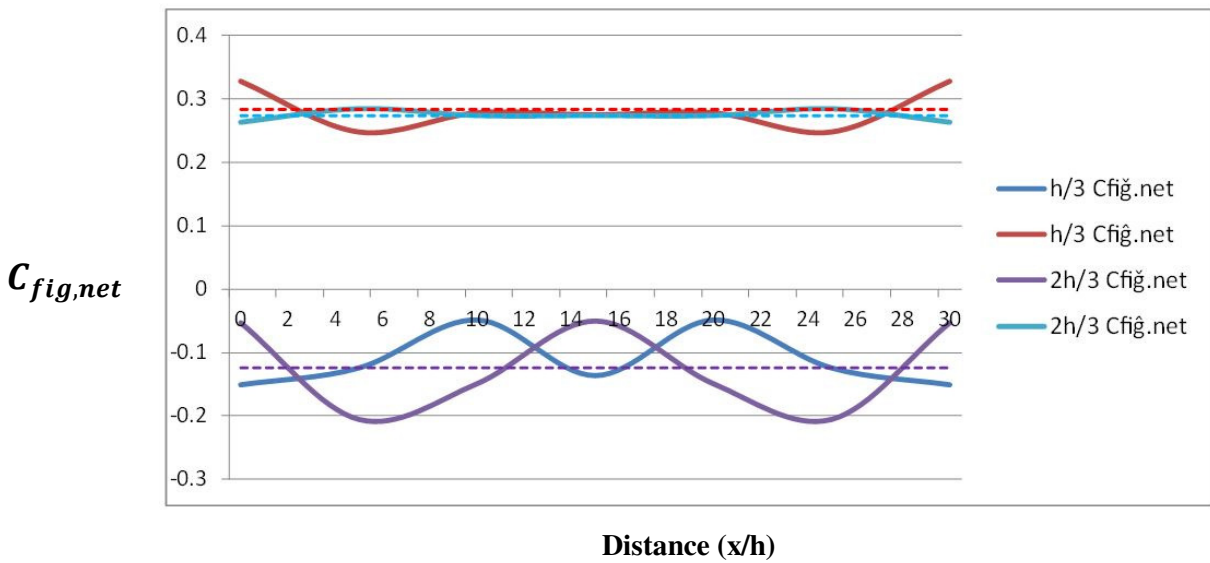


Figure 5.12 Maximum and Minimum Net Pressure Coefficient $C_{fig,net}$, Model C Wall W3

5.4.3 Net Pressure Coefficient $C_{fig,net}$, Model D, Walls W1, W2, W3 and W4

Figure 5.13 presents the net pressure coefficient results for wall W1, Model D. These results were calculated using the one central internal measurement of internal pressure and are not as accurate as for the two previous models where internal pressure measurements across the model area were used. The mean maximum coefficient at $h/3$ is 0.7 and 0.5 at $2h/3$ as compared to mean values of 0.45 to 0.5 for Models B and C. The peak minimum coefficients vary between -0.4 and -0.1 with a mean of -0.3.

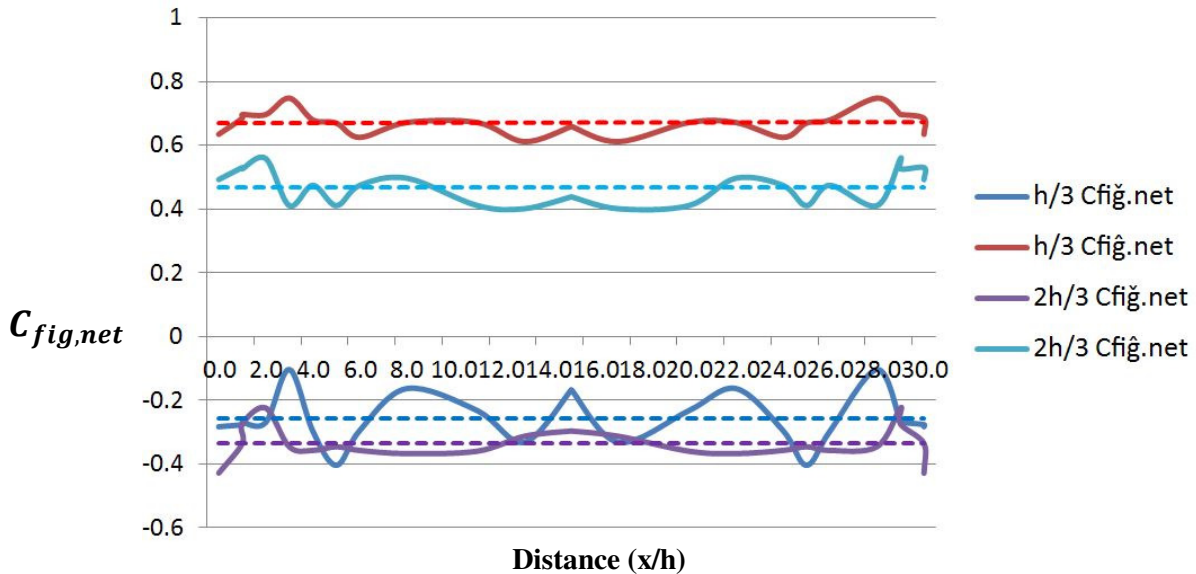


Figure 5.13 Maximum and Minimum Net Pressure Coefficients $C_{fig,net}$, Model D Wall W1

Figure 5.14 shows the net peak pressure coefficients for side walls W2 and W4. The maximum pressure coefficients vary between 0.2 and 0.4 at height $2h/3$ and 0.35 and 0.6 at height $h/3$. The peak pressure of 0.6 occurs at the leeward end of the wall. The minimum pressure coefficients for both heights vary between -0.2 and -0.4 for the length of the wall. This distribution is significantly different to the side wall wind action distributions for Models B and C indicating that the varied distribution of internal pressure measured in Models B and C has significant effect on these results.

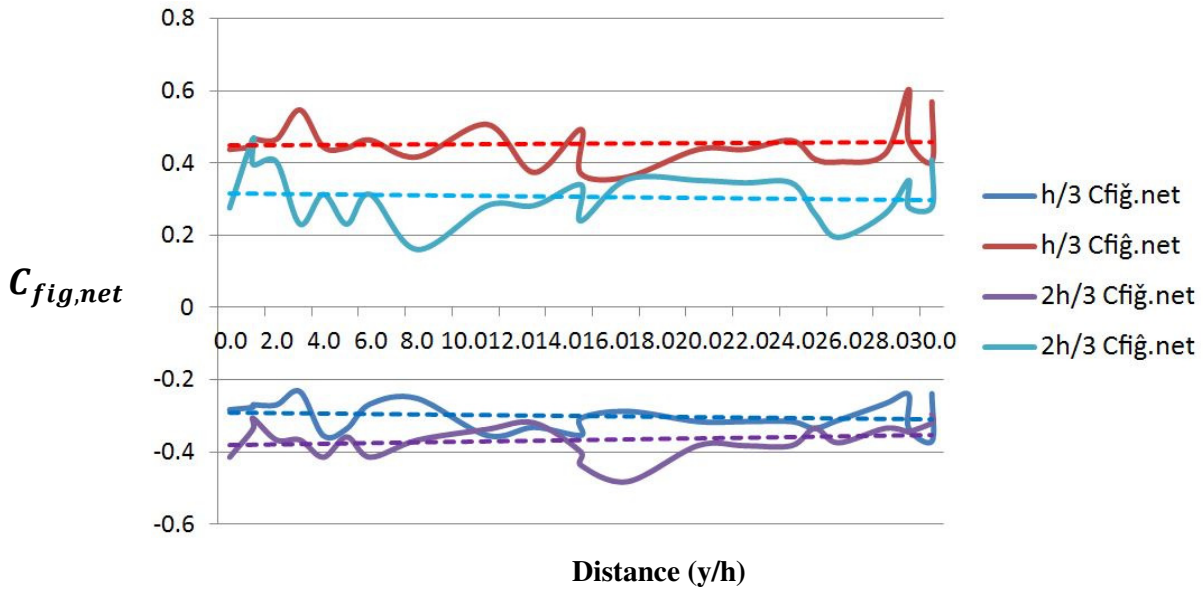


Figure 5.14 Maximum and Minimum Net Pressure Coefficient $C_{fig,net}$, Model D Wall W2

The net peak pressure coefficient results for leeward wall W3 are shown in **Figure 5.15**. The maximum coefficient results do not show any significant fluctuation across the model and average at 0.10. The minimum pressure coefficients vary between -0.3 and -0.4 with slightly higher magnitudes at height 2h/3. The mean minimum coefficient is -0.35. Similar to the side walls, the distribution at the leeward wall is different to the results for Model B and C where the variation in internal pressure was included.

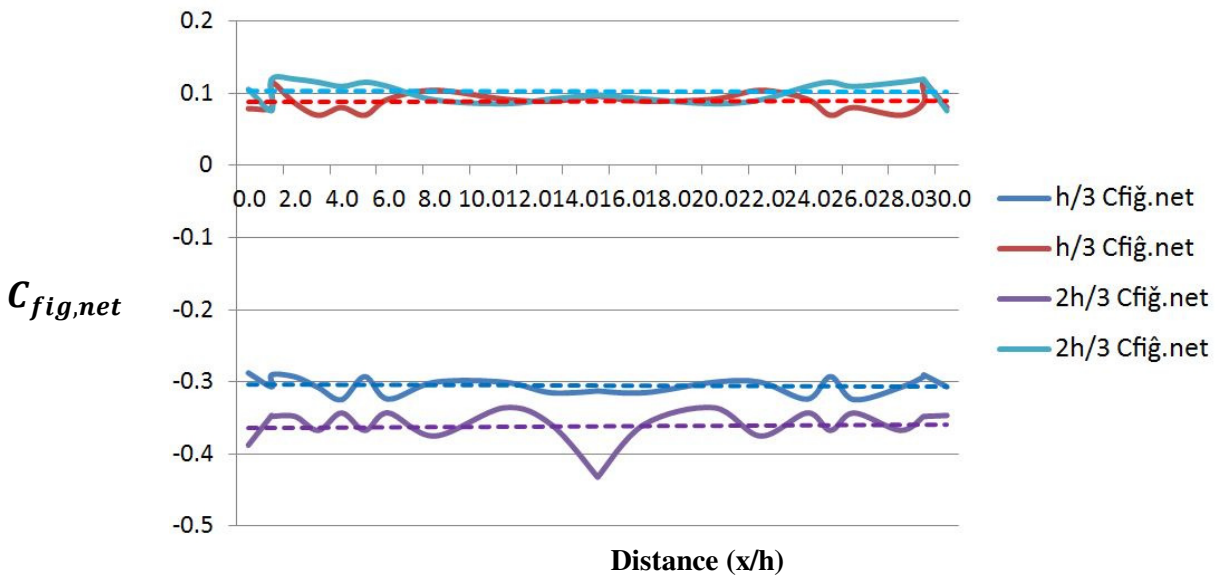


Figure 5.15 Maximum and Minimum Net Pressure Coefficient $C_{fig,net}$, Model D Wall W3

5.5. Comparison of net peak pressure wall coefficient results

Table 5.5 presents a summary of the graphed wall pressure coefficient results for the windward wall W1 of Models B and C. The Model D results for walls W1, W2 W3 and W4 have been derived through a combination of extrapolation of the Models B and C results and the derived results for Model D using one central point of internal pressure measurement.

Table 5.5
Summary of Wall Net Pressure Coefficient, Wall W1, $C_{fig,net}$, $\theta = 0^\circ \pm 45^\circ$

Distance from Corner	Height	Model B Max C_{fig}	Model B Min C_{fig}	Model C Max C_{fig}	Model C Min C_{fig}	Model D Max C_{fig}	Model D Min C_{fig}
0-1h	h/3	0.6	-0.3	0.5	-0.3	0.5	-0.3
	2h/3	0.6	-0.3	0.5	-0.3	0.5	-0.3
1h-5h	h/3	0.5	-0.3	0.5	-0.3	0.5	-0.3
	2h/3	0.5	-0.3	0.5	-0.3	0.5	-0.3
>5h	h/3	0.6	-0.3	0.5	-0.3	0.5	-0.3
	2h/3	0.6	-0.3	0.5	-0.3	0.5	-0.3

Table 5.5 shows a slight reduction in the maximum pressure with increase of porosity.

The magnitudes of the windward wall pressure coefficients are of the same order but slightly less than the external wall coefficients measured on Model A. The peak maximum coefficient for the non-porous Model A shown in **Table 4.3** is 2.3 and, when divided by G_u^2 , is equal to 0.74. This coefficient has no internal pressure component and will increase where internal suction is present. AS1170.2 (2011) presents external windward wall coefficients for a vertical wall of 0.7 to 0.7 to 0.8 depending on the structures height and elevation. Viscous or frictional forces and the internal pressure are combining to create the porous structure coefficients of a significantly greater magnitude than the roof coefficients.

Table 5.6 presents a summary of the graphed wall pressure coefficient results for the side walls W2 and W4.

Table 5.6
Summary of Wall Net Pressure Coefficient, Side Walls W2, W4, $C_{fig,net}$, $\theta = 0^\circ \pm 45^\circ$

Distance from Corner	height	Model B Max C_{fig}	Model B Min C_{fig}	Model C Max C_{fig}	Model C Min C_{fig}	Model D Max C_{fig}	Model D Min C_{fig}
0-2h	h/3	0.9	-0.2	0.5	0	0.5	-0.1
	2h/3	0.7	-0.2	0.5	-0.1	0.5	-0.1
2h-16h	h/3	0.7	-0.2	0.5	0	0.5	-0.1
	2h/3	0.7	-0.2	0.5	-0.1	0.3	-0.1
>15h	h/3	0.5	-0.1	0.4	-0.1	0.3	-0.1
	2h/3	0.5	-0.1	0.4	-0.1	0.3	-0.3

The side wall results in **Table 5.6** show positive inward pressures acting on the walls that peak at the windward corner.

These results differ from that expected for a non-porous wall where outward suction coefficients are the dominant design action, diminishing with distance from the windward edge (refer to Model A results **Figure 4.4**). The flow of air through the porous structure is drawing the side walls inwards.

Table 5.7 presents the leeward wall pressure coefficient results.

Table 5.7
Summary of Wall Net Pressure Coefficient, Leeward Wall W3, $C_{fig,net}$, $\theta = 0^\circ \pm 45^\circ$

Distance from Corner	height	Model B Max C_{fig}	Model B Min C_{fig}	Model C Max C_{fig}	Model C Min C_{fig}	Model D Max C_{fig}	Model D Min C_{fig}
0-6h	h/3	0.4	-0.2	0.3	0	0.3	-0
	2h/3	0.4	-0.1	0.3	-0.2	0.3	-0.1
6h-22h	h/3	0.5	-0.3	0.3	-0.1	0.3	-0.1
	2h/3	0.5	-0.2	0.3	-0.1	0.3	-0.1
>22h	h/3	0.4	-0.1	0.3	-0.1	0.3	-0.1
	2h/3	0.4	-0.2	0.05	-0.2	0.3	-0.1

Table 5.7 shows that the inward pressure magnitude is largest for Model B and reduces for Model C.

The derived net wall pressure coefficients demonstrate that the degree of porosity has a small to moderate influence on the resultant values. It is apparent that the porosity of the structure sets up different pressure patterns on the side and leeward walls compared to the actions predicted for non-porous structures.

With reference to the pressure loss coefficient results presented in **Table 3.1**, the results presented for the three models can be related to large porous structures with porous fabric cladding of various types. The Model B loss coefficient of 32 is between the loss coefficient of the heavy 95% shade cloth ($K = 51$) and the heavy quad cattle shade (7.2). Model D ($K=2.5$) and Model C ($K=0.9$) have loss coefficients between the 70% cattle shade and the 12mm Quad fabric ($K= 0.64$).

6. Conclusions

The application and construction of large flat roofed porous canopies in Australia has grown steadily over the past 30 years. The canopies have proved to be an economical and effective method to protect assets from weather extremes (sun, wind, frost and hail) which may cause damage. Assets commonly protected include horticultural and agricultural crops and animals, water reservoirs, large vehicle storage compounds and waste management facilities. There is an urgent need for the wind actions on these canopies to be researched and quantified to assure safe and economical design.

There have been limited studies into wind actions on porous structures. It is concluded that this subject is a complex and extensive subject for research. The wind actions that result are essentially different from the resulting wind actions on non-porous structures.

This study has carried out experimental wind tunnel testing to investigate the wind actions that result on large flat roofed porous canopies. The external wind pressure coefficients f have been presented graphically for four models of identical geometry and varying porosity, 0%, 19%, 38% and 58%. The internal pressure coefficients within the models, also obtained by experimental measurement, have been summed on a time basis with the simultaneously occurring external pressure coefficients to find the resultant maximum and minimum net pressure coefficients.

The net pressure coefficient results for the porous models have been presented graphically and the results, found over $\pm 45^\circ$ wind direction sector, have been combined to give maximum and minimum values for design at various locations on the structures roof and walls.

The key findings of this research are:

- The net pressure coefficients on porous roofs are significantly lower than the coefficients for an equivalent non-porous roof. The peak uplift coefficients vary between -0.06 and -0.1.
- Increase in porosity decreases the magnitude of the roof minimum and maximum pressure coefficients by small amounts.
- At the wall to roof intersection there is less separation or disturbance of the wind than would occur on a non-porous structure.
- It was found that the maximum roof downward pressure coefficients are generated by the $\theta = 45^\circ$ wind.
- The internal pressure coefficients reduce in magnitude in the downwind half of the models.
- The wind pressures on the porous walls are of greater magnitude than the roof actions.

- The side wall coefficients show maximum design magnitudes of inward coefficients which peak at the windward corner. This differs from that expected for a non-porous structure and can be attributed to the wind flow through the porous structures.

This project has provided a strong basis for the structural design of large flat roofed porous canopies for normal wind actions. Pressure coefficient variations are likely to occur due to different wall slopes, dominant openings and blockage by assets beneath the net. Additional future research is required to further investigate these factors. The influence and magnitude of wind surface friction actions also requires investigation.

In conclusion it can be seen that the study of wind actions on large porous canopies is a relatively untouched field of research. The continuing growth in application of these structures is certain to drive this research forward. As the world's population increases and the demand for food, water and shelter also grows, it can be confidently predicted that large porous canopies will have a vital role in assisting to meet these demands.

7. References

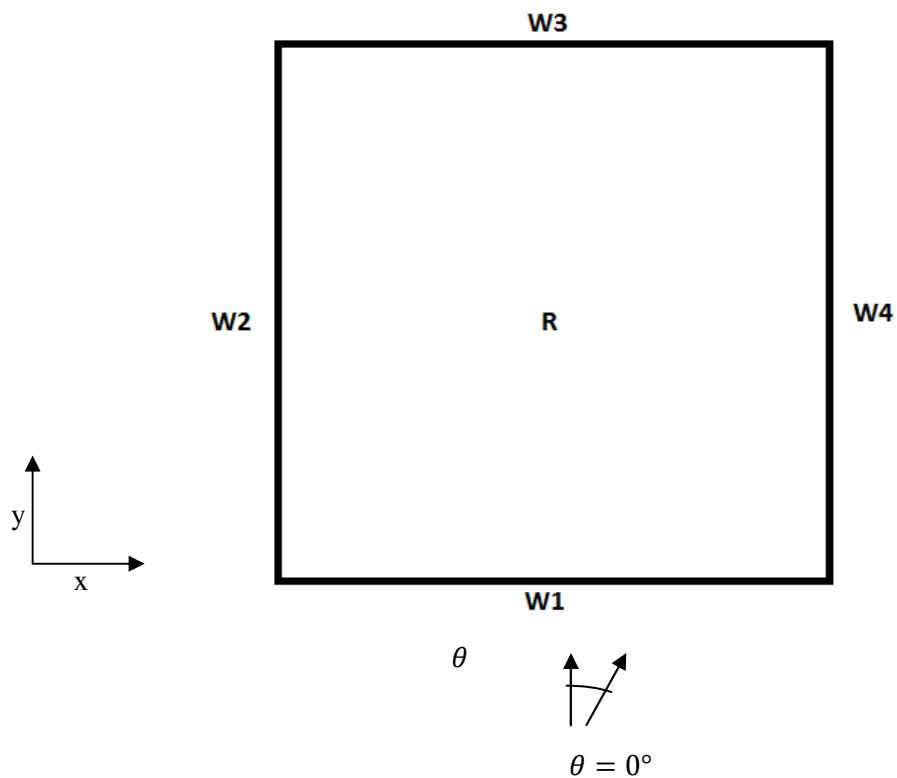
- ALFAFEEDLOTTING 2005. Big inroads in managing summer heat risk. *Lotfeeding*.
- ANNAND 1953. The resistance to air flow of wire gauzes. *Journal Royal Aeronautical Society* 57.
- BARBAGALLO. 2011. *Wind Loads on Large Flat Porous Buildings*. Bachelor of Engineering with Honours (Civil Engineering), James Cook University.
- BRIASSOULIS & MISTRITIS 2010. Integrated structural design methodology for agricultural protecting structures covered with nets. *Biosystems Engineering*, 105, 205-220.
- CHENG-PENG YE ET AL 2010. An investigation into the sheltering performance of porous windbreaks under various wind directions. *Journal of Wind Engineering and Industrial Aerodynamics*.
- DONNAN ET AL 1987. Design of a Low Cost Wind Resistant Shade Cloth Structure. *First National Structural Engineering Conference 1987*. Melbourne.
- DPI. 2008. *Nets prove effective in fruit fly control* [Online]. Queensland. Available: <http://www2.dpi.qld.gov.au/horticulture/14832.html>
- ENGINEERING SCIENCE DATA UNIT, L. 1972. ESDU72009.
- FINN & BARNES 2007. The Benefits of Shade-Cloth Covers for Potable Water Storages. *CSIRO - Gale Pacific - EGW*.
- HOERNER 1965. Fluid Dynamic Drag. *Published by Author*.
- HOLMES 2007. Wind Loading of Structures.
- LETCHFORD ET AL 2000. Mean wind loads on porous canopy roofs. *Journal of Wind Engineering and Industrial Aerodynamics*.
- MASON 2016. Measurement of pressure loss coefficients for porous fabrics. University of Queensland.
- NETPRO ET AL 2007. Netting and permanent structures. *Australian Fruit Grower*.
- RICHARDS & ROBINSON 1999. Wind Loads on Porous Structures. *Journal of wind Engineering and Industrial Aerodynamics* 83, 455-465.
- ROBERTSON ET AL 2002. Wind pressures on permeably and impermeably-clad structures *Journal of Wind Engineering and industrial Aerodynamics*, 90, 461-474.
- ROBINSON 2007. The Vegie House. *Southern Free times*.
- SCHMIDT 2007. Controlling Evaporation Loss from Water Storages using NetPro Shade cloth. *NCEA Publication No 1000580/3*.

Appendix A**Porous Models B, C and D**

Roof R Pressure Coefficient Maximum and Minimum Contour Plots,
 $C_{peak,net}/G_u^2$

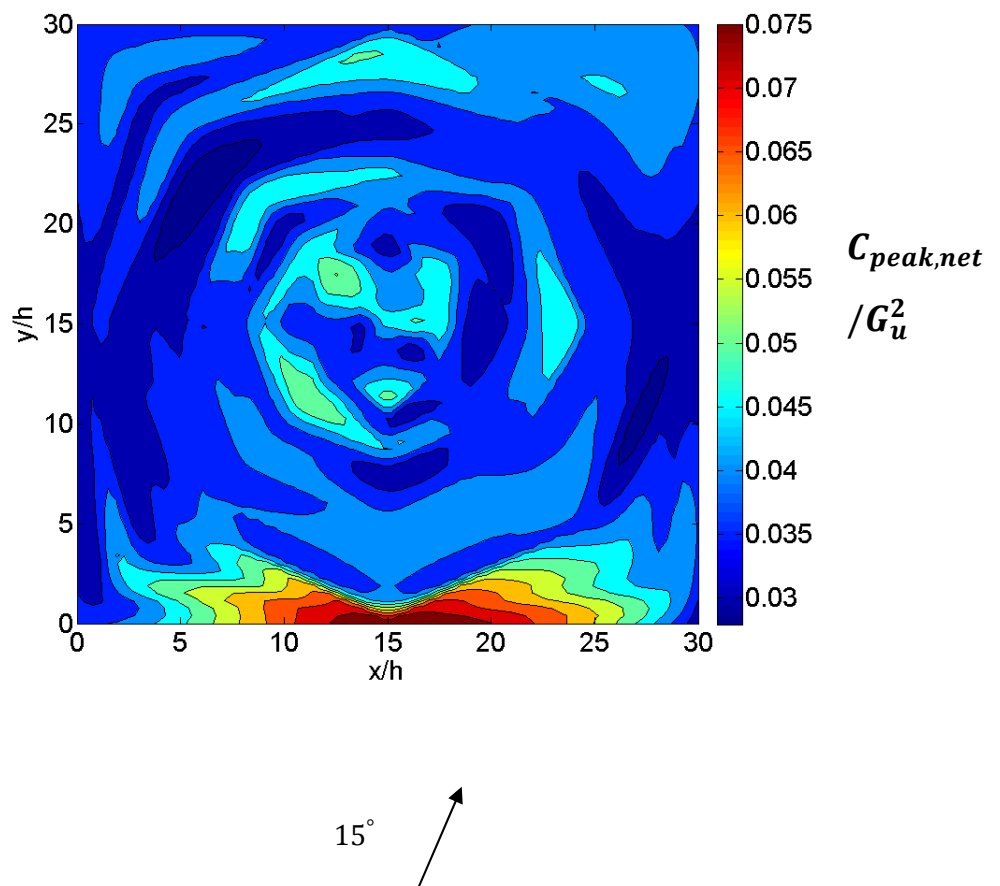
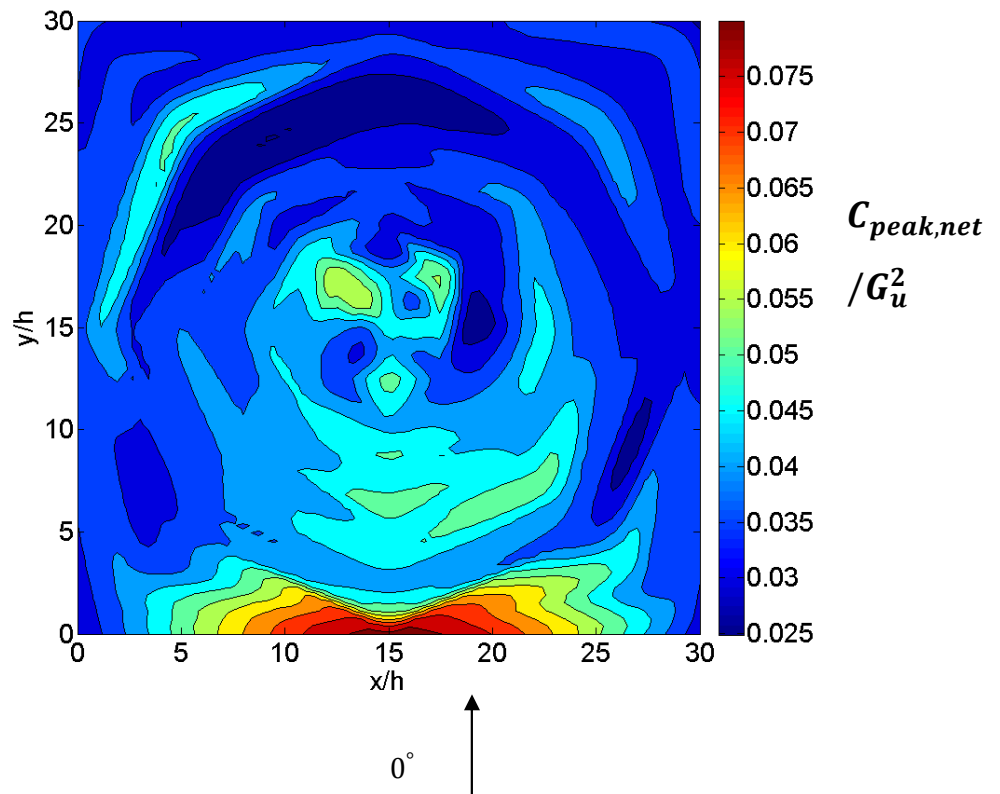
Walls W1, W2 and W3 Pressure Coefficient Maximum and Minimum
Graphs, $C_{peak,net}/G_u^2$
(refer also to section 5.1)

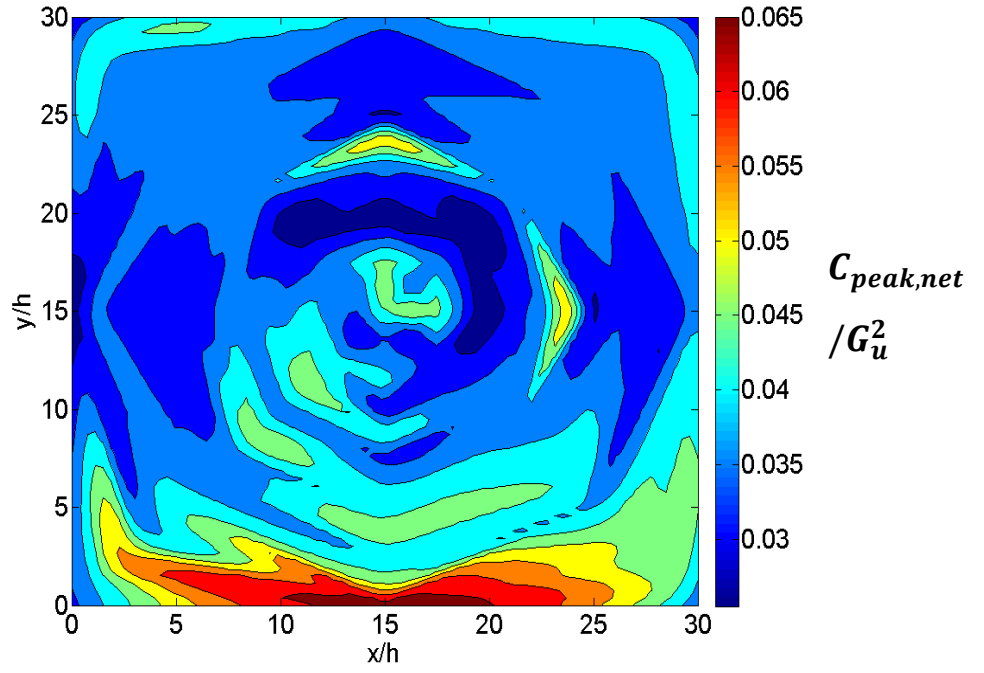
Wind Directions $\theta = 0^\circ, \theta = 15^\circ, \theta = 30^\circ, \theta = 45^\circ$



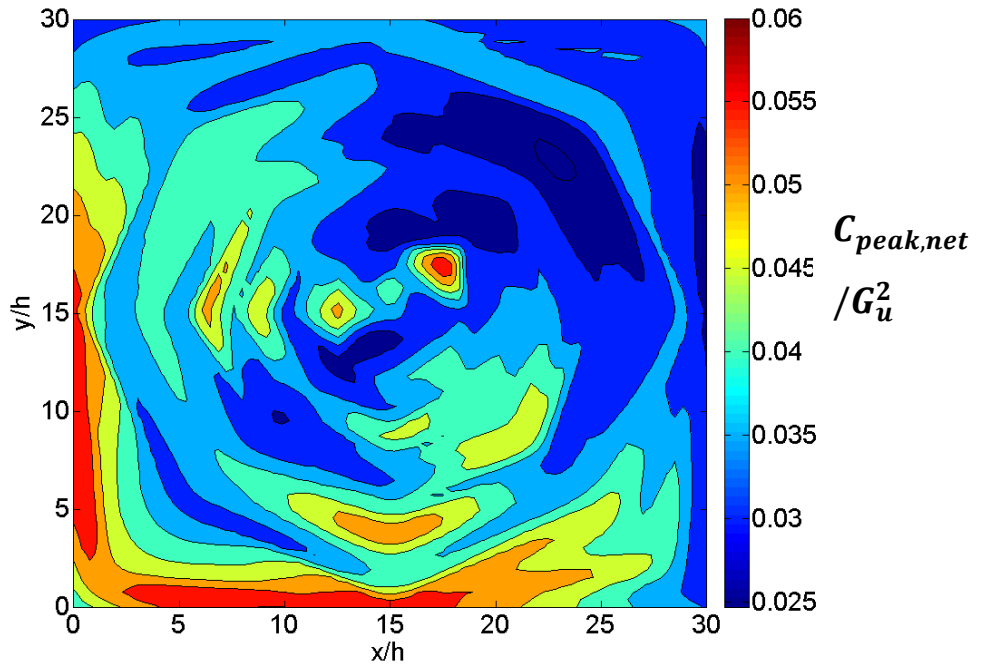
A.1 Roof Pressure Coefficient Contour Plots Model B (19% porosity)

A1.1 Model B, Roof R, $C_{peak.net}/G_u^2$ Maximum, $0^\circ, 15^\circ, 30^\circ, 45^\circ$ Wind Directions





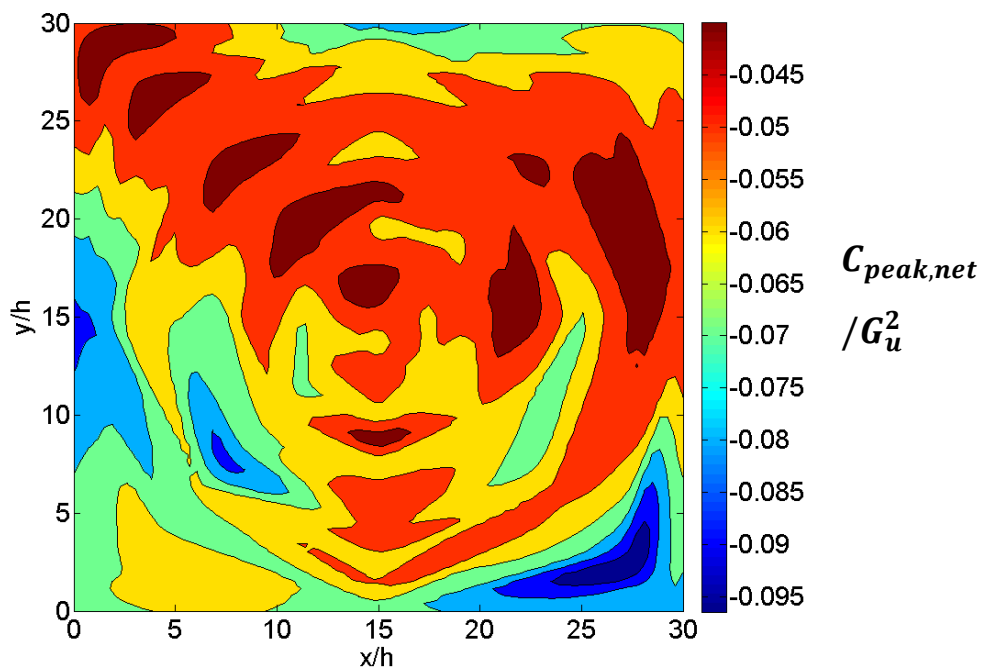
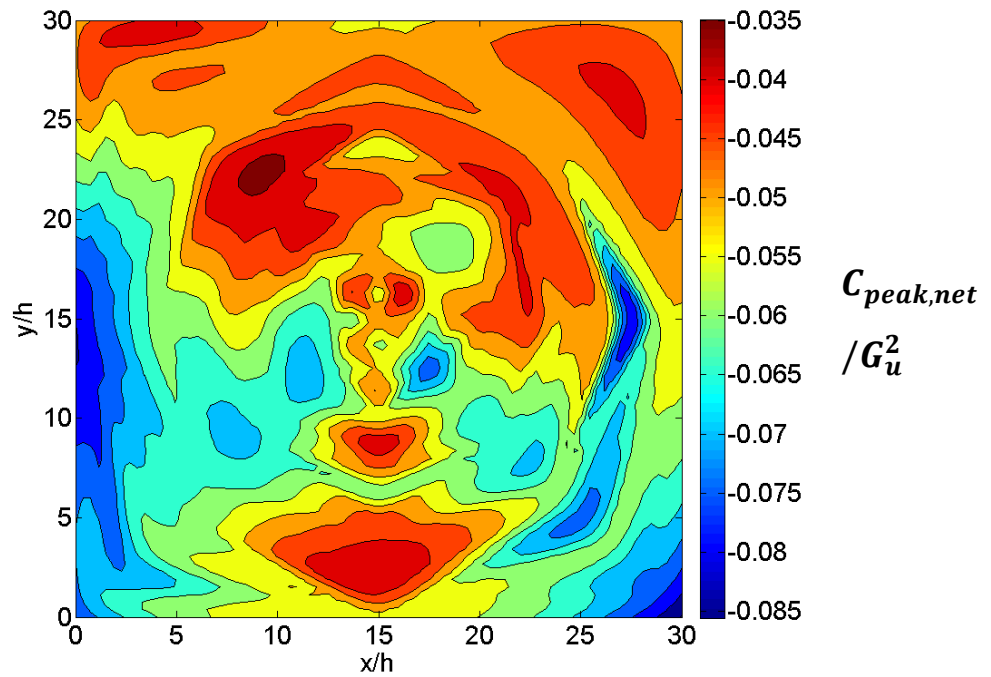
30°

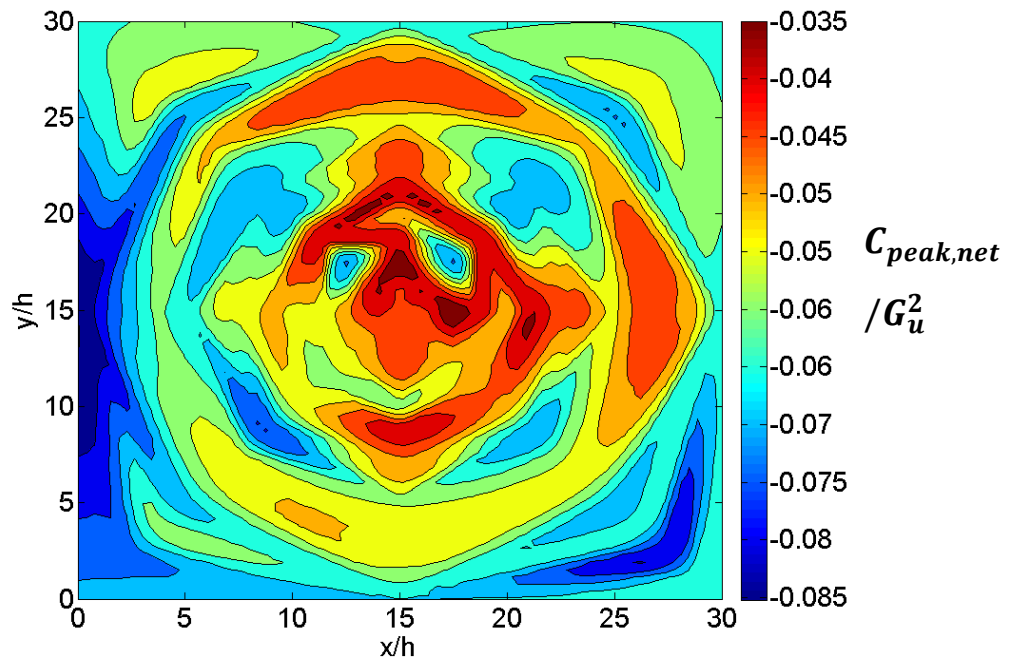


45°

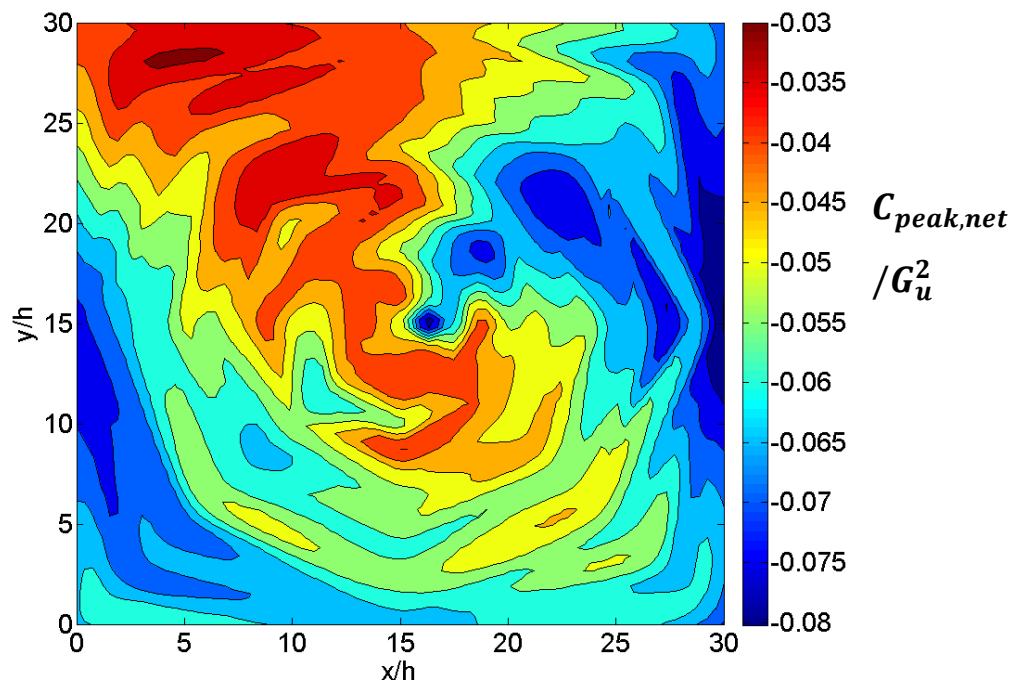
A1.2 Roof Pressure Coefficient Contour Plots

Model B, Roof R, $C_{peak,net}/G_u^2$ Minimum, $0^\circ, 15^\circ, 30^\circ, 45^\circ$ Wind Directions





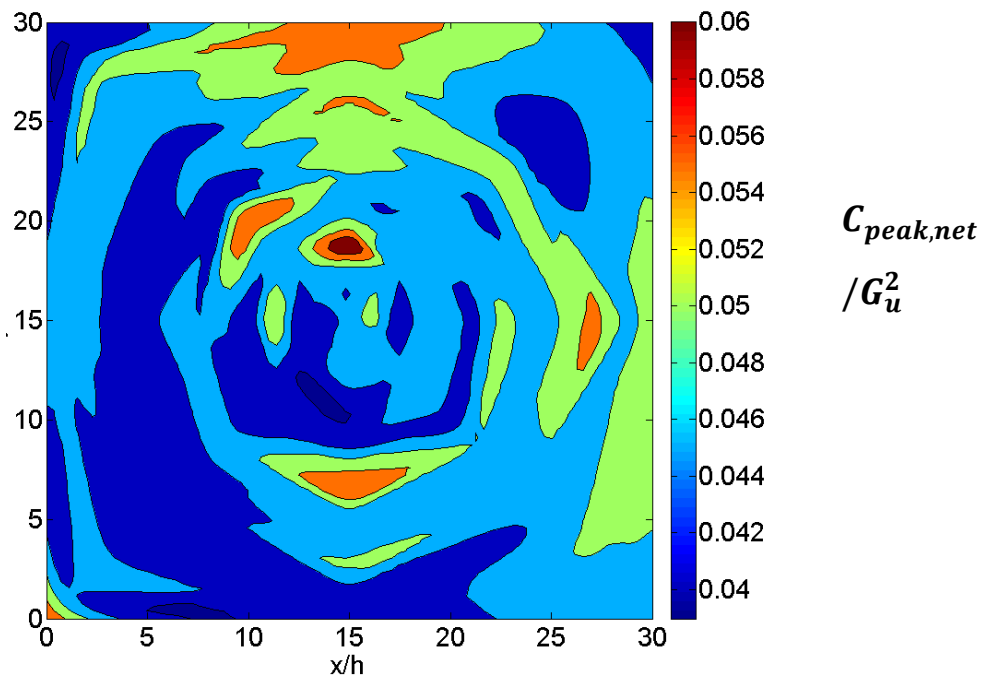
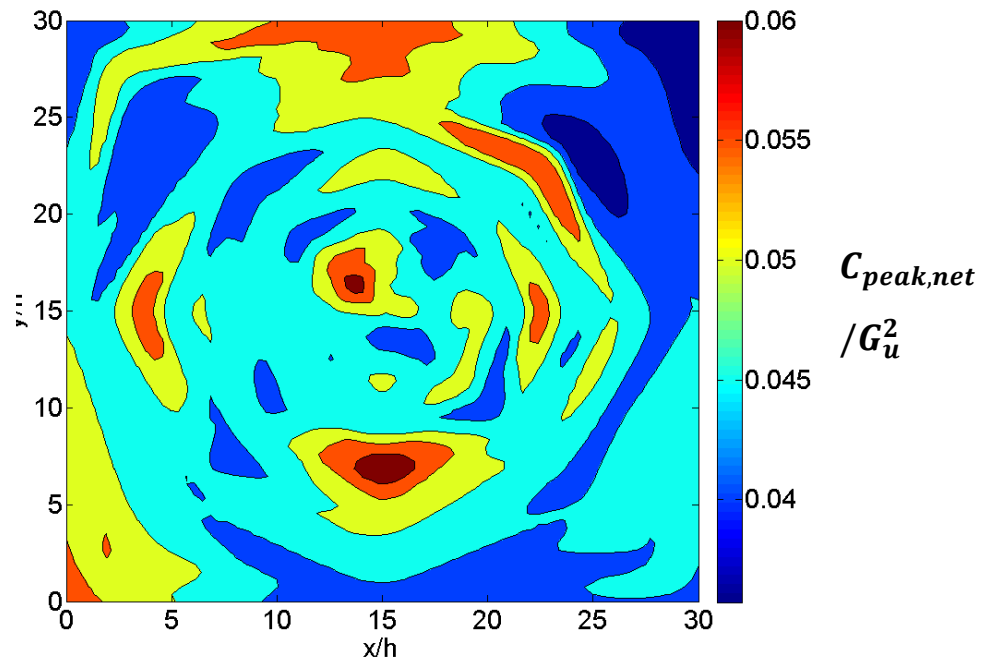
30°

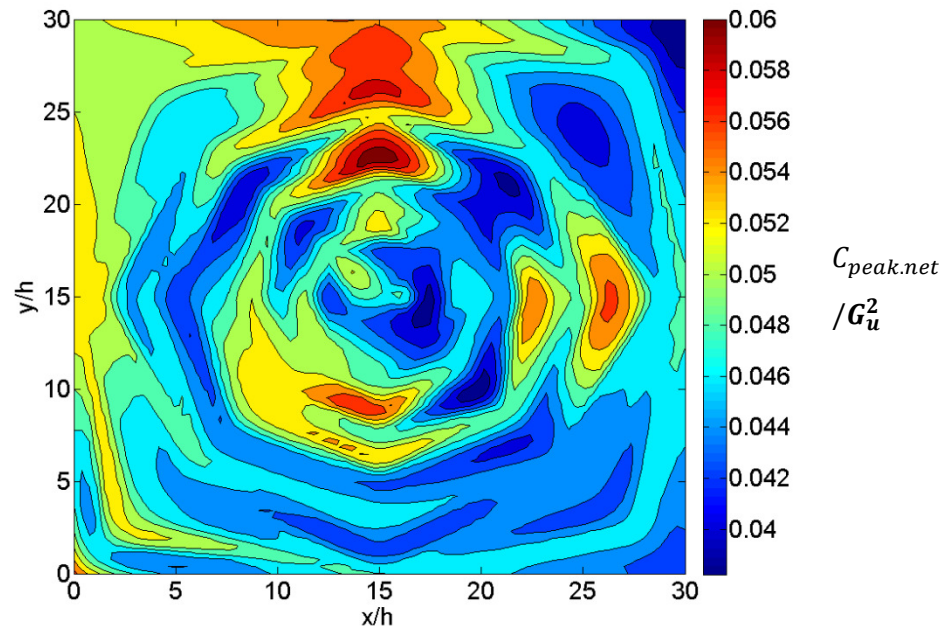


45°

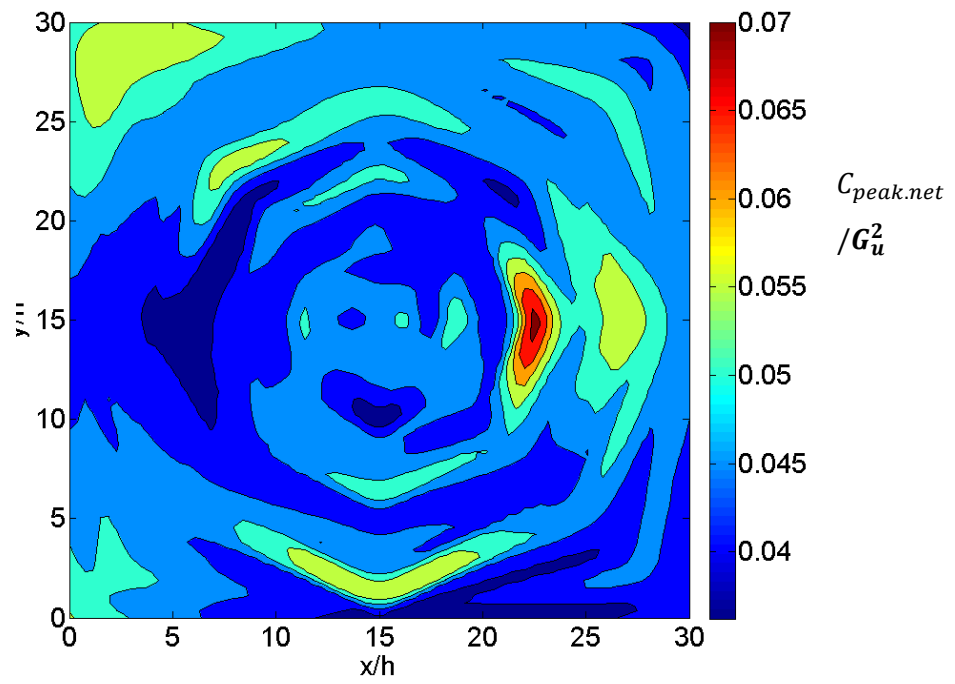
A2. Roof Pressure Coefficient Contour Plots, Model C (38% porous)

A.2.1 Model C Roof R, $C_{peak,net}/G_u^2$ Maximum, $0^\circ, 15^\circ, 30^\circ, 45^\circ$ Wind Directions





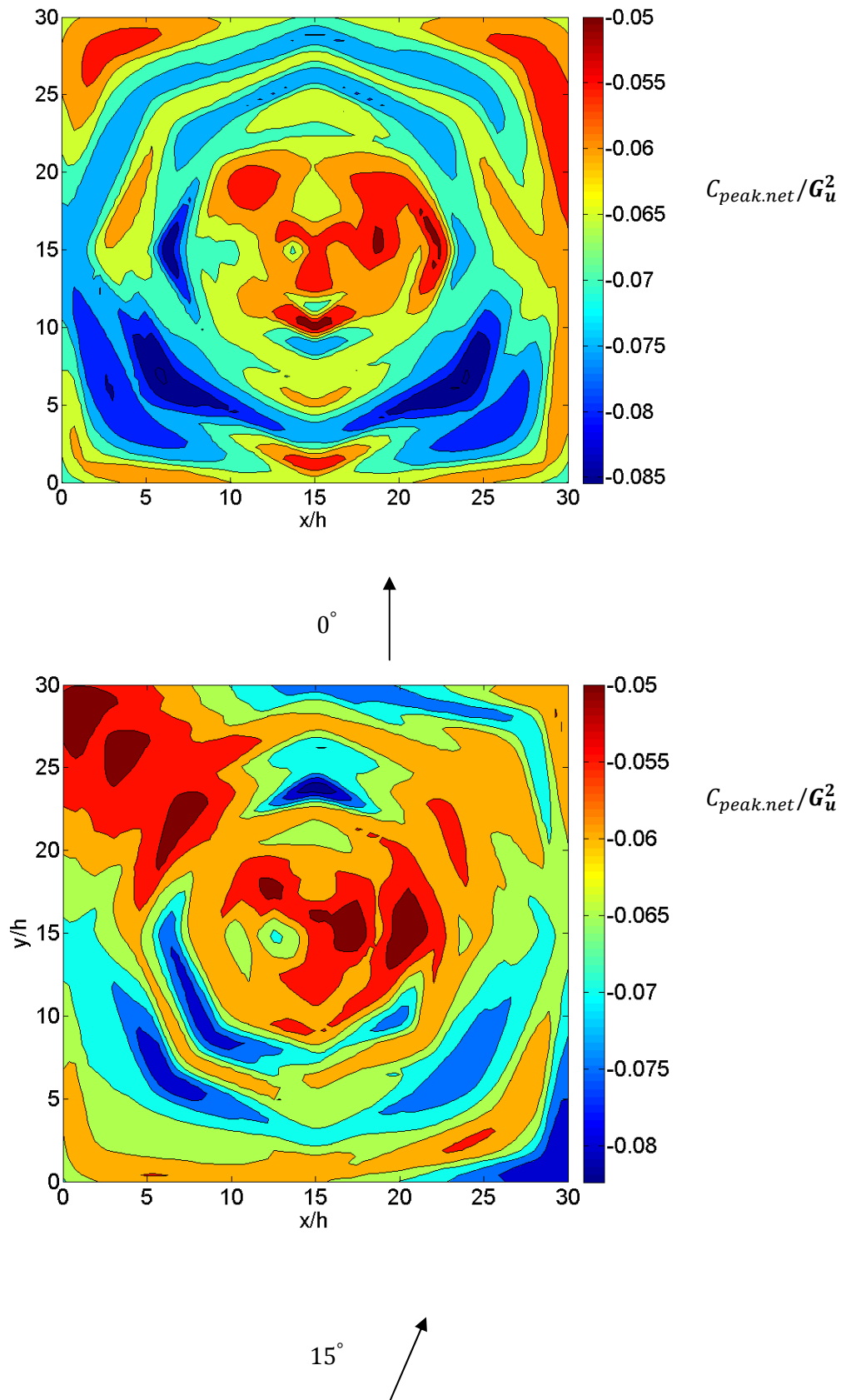
30°

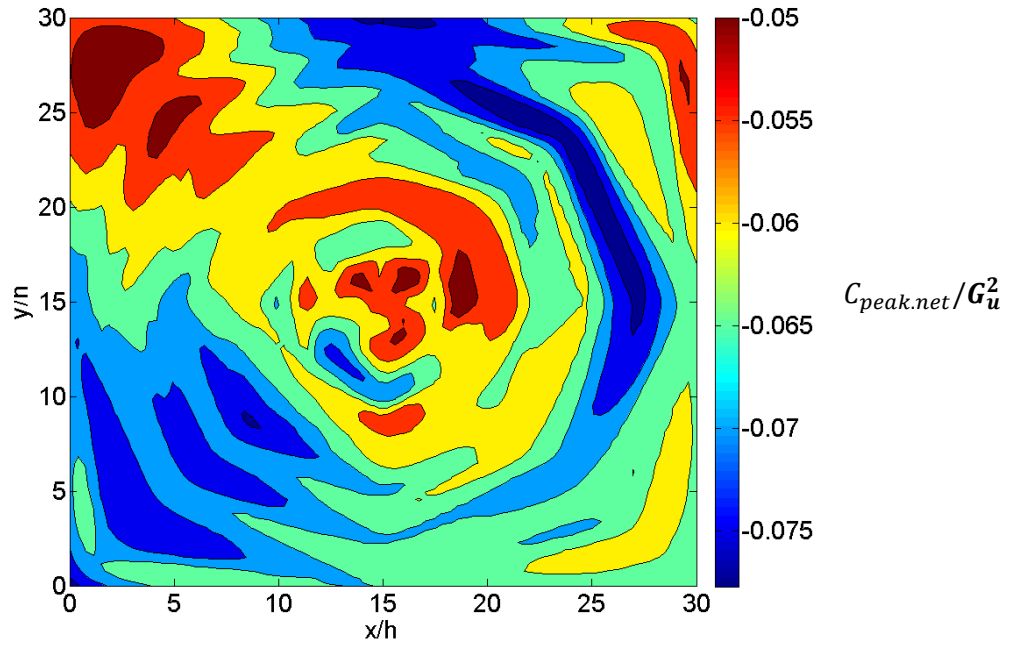


45°

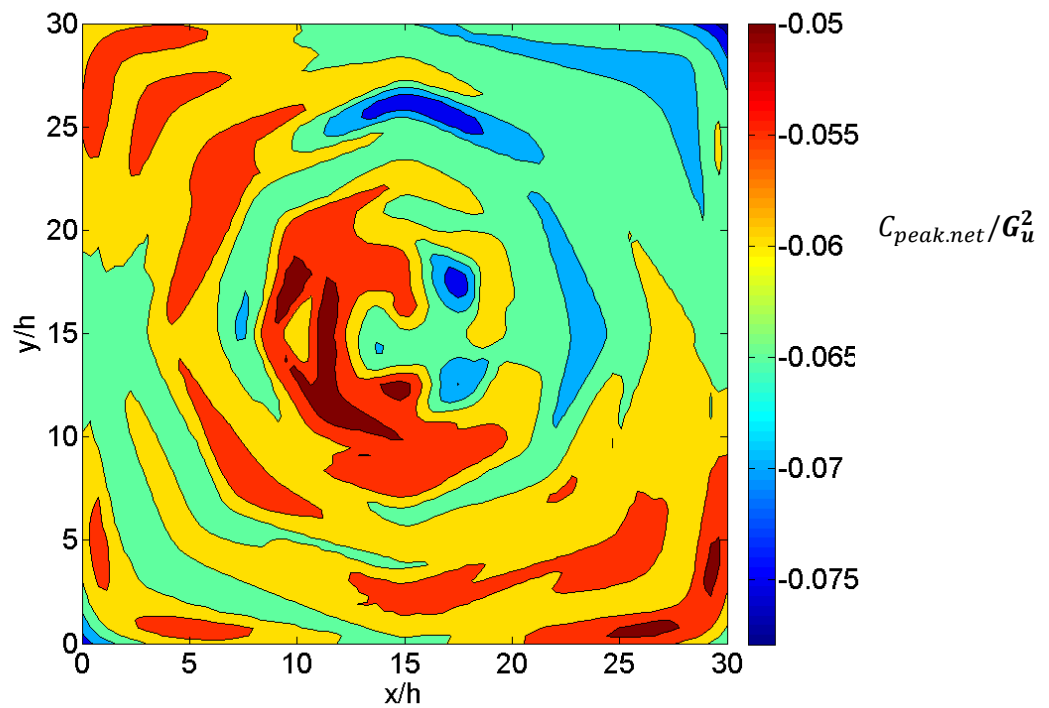
A.2.2 Roof Pressure Coefficient Contour Plots

Model C roof, $C_{peak.net}/G_u^2$ Minimum, $0^\circ, 15^\circ, 30^\circ, 45^\circ$ Wind Directions

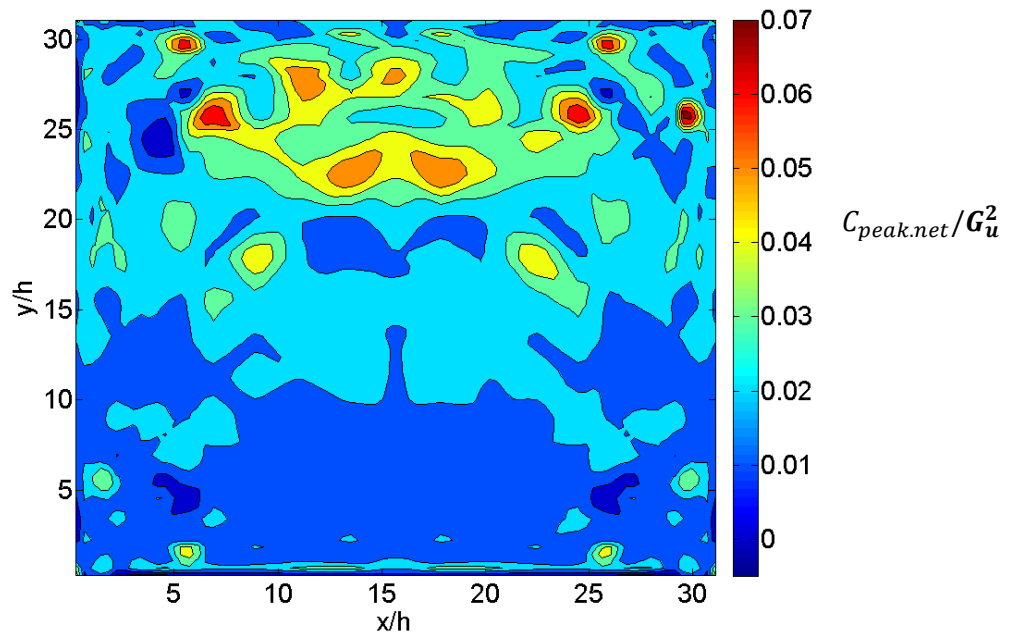
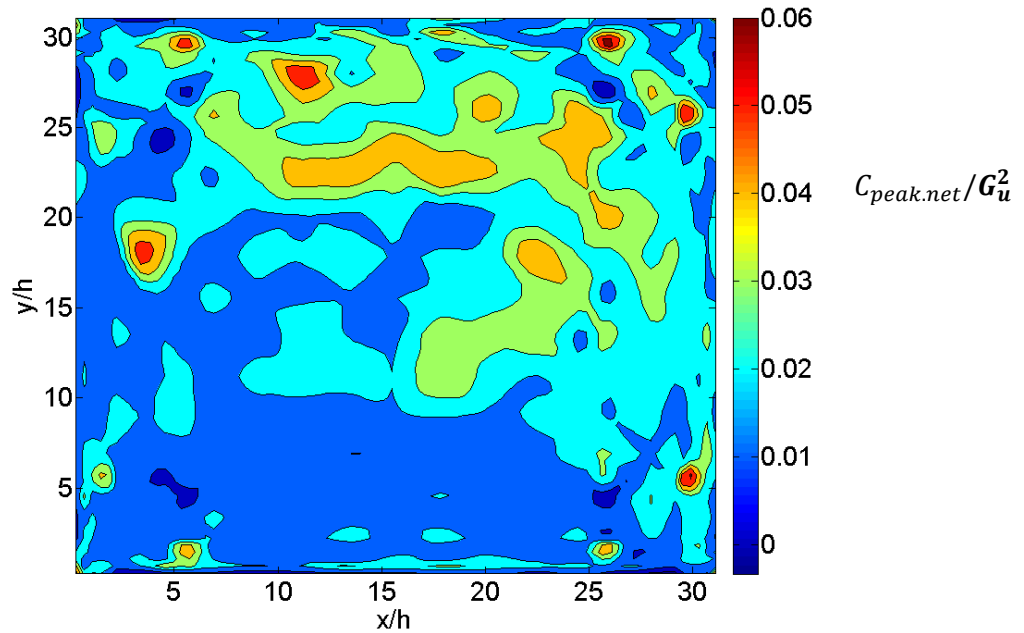


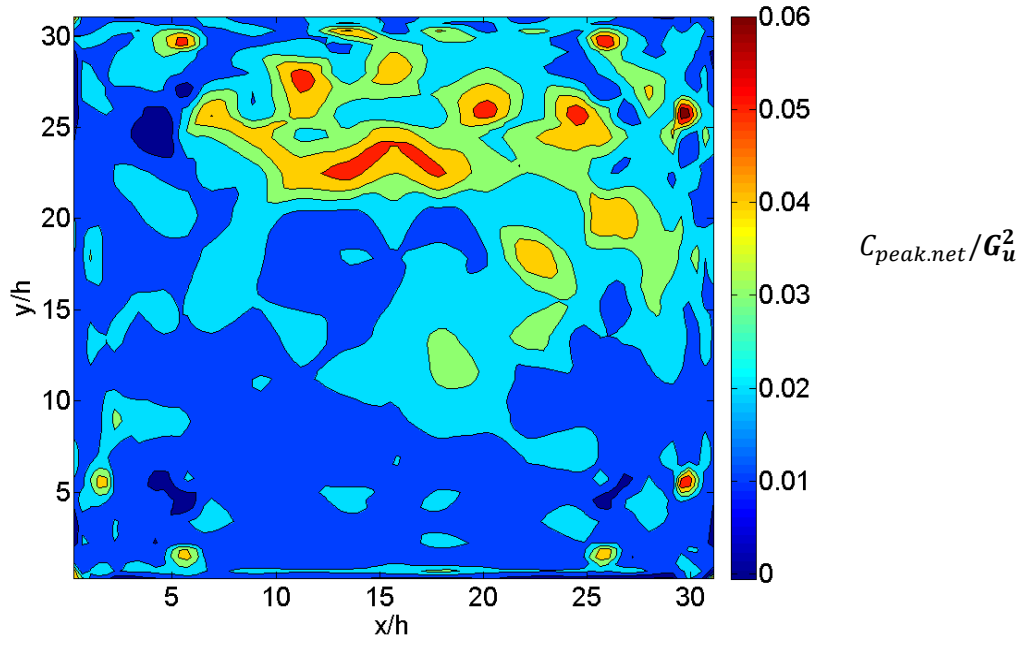


$\theta = 30^\circ$

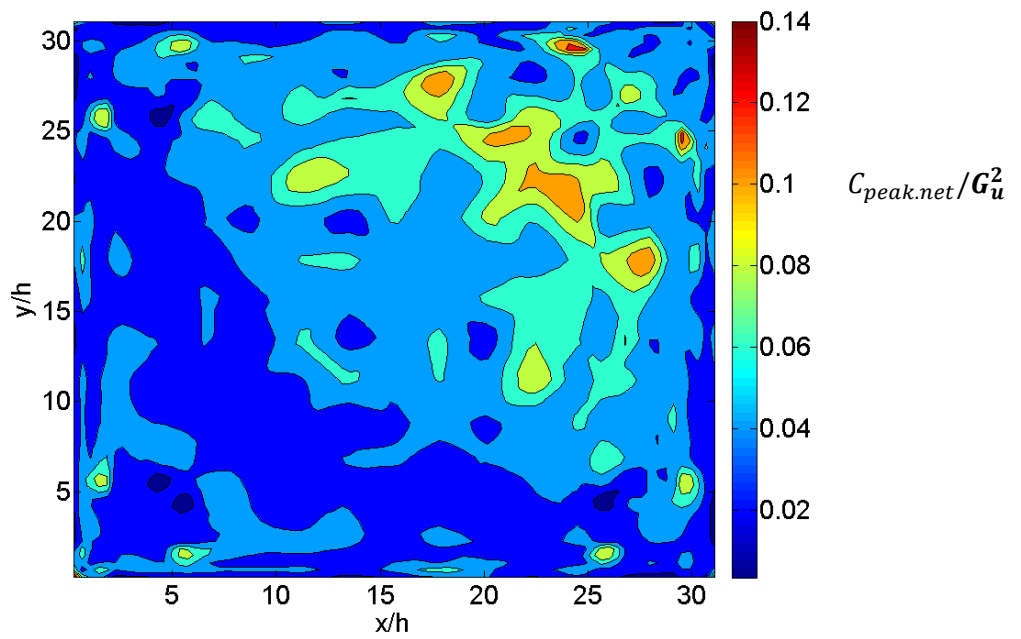


$\theta = 45^\circ$

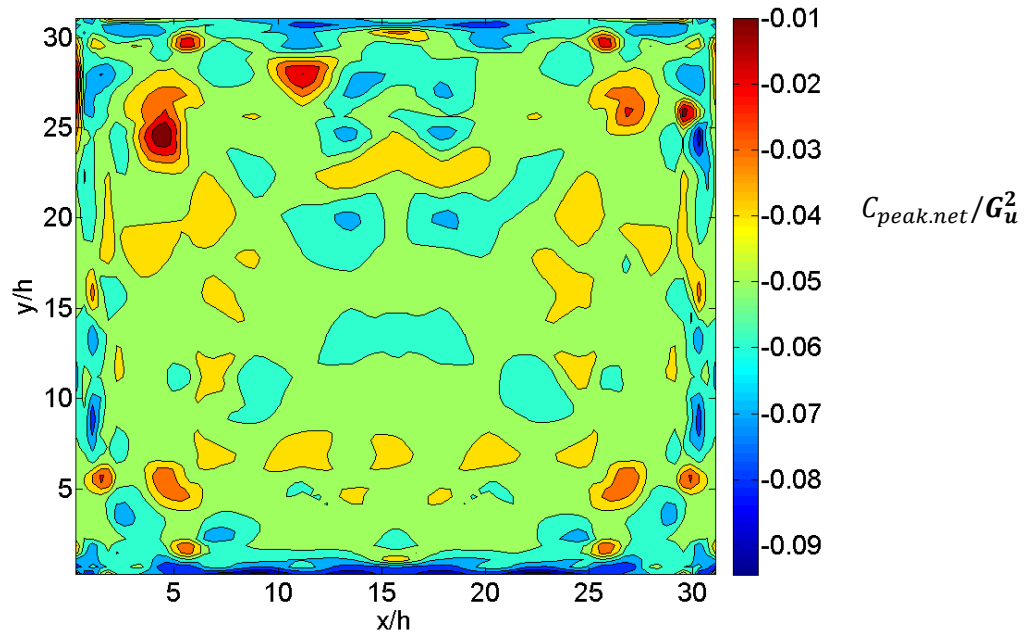
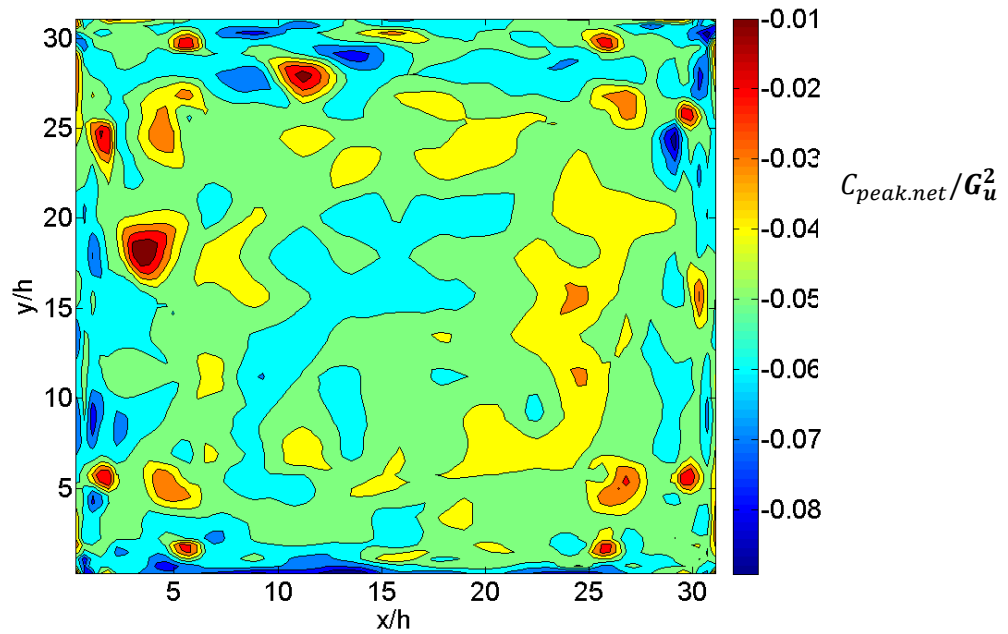
A3. Roof Pressure Coefficient Contour Plots, Model D (58% porous)**A3.1 Model D roof, $C_{peak.net}/G_u^2$ Maximum, 0° , 15° , 30° , 45° Wind Directions** $\theta = 0^\circ$  $\theta = 15^\circ$ 

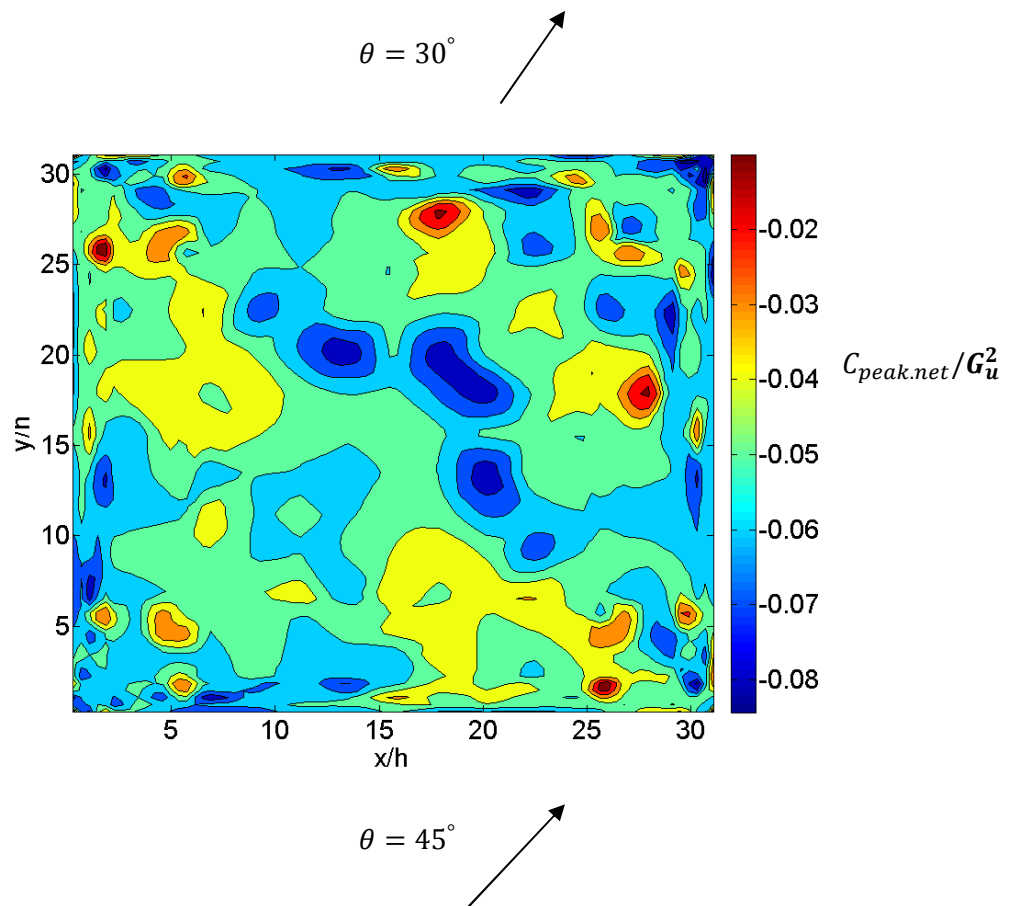
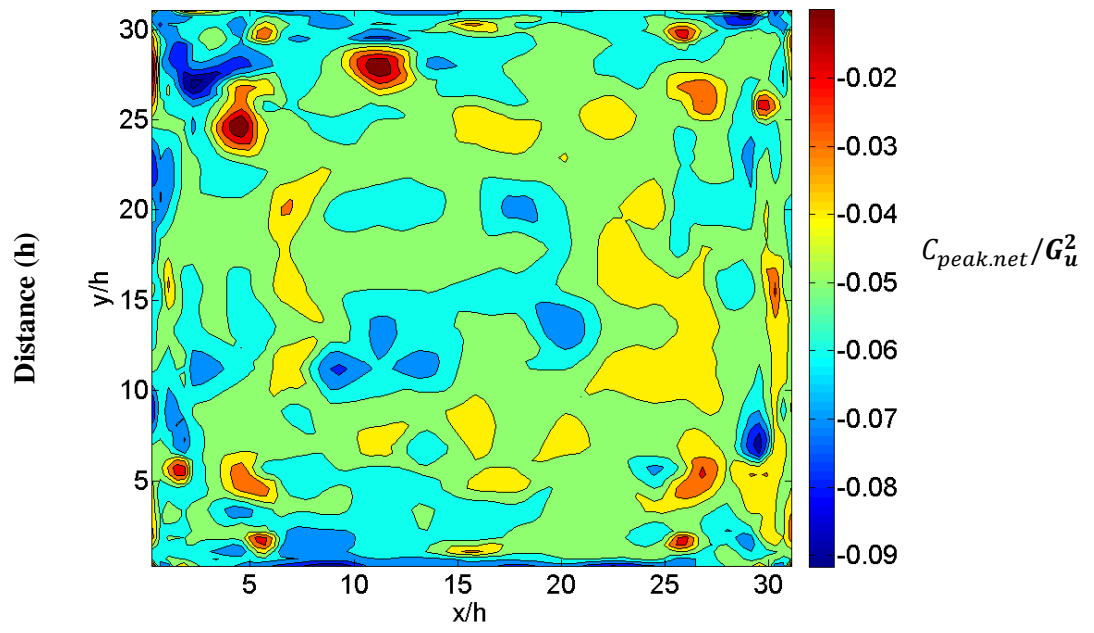


$\theta = 30^\circ$



$\theta = 45^\circ$

A3.2 Roof Pressure Coefficient Contour Plots**Model D roof, $C_{peak.net}/G_u^2$ Minimum, 0° , 15° , 30° , 45° Wind Directions** $\theta = 0^\circ$  $\theta = 15^\circ$



A4 Wall Pressure Coefficient Plots, Model B

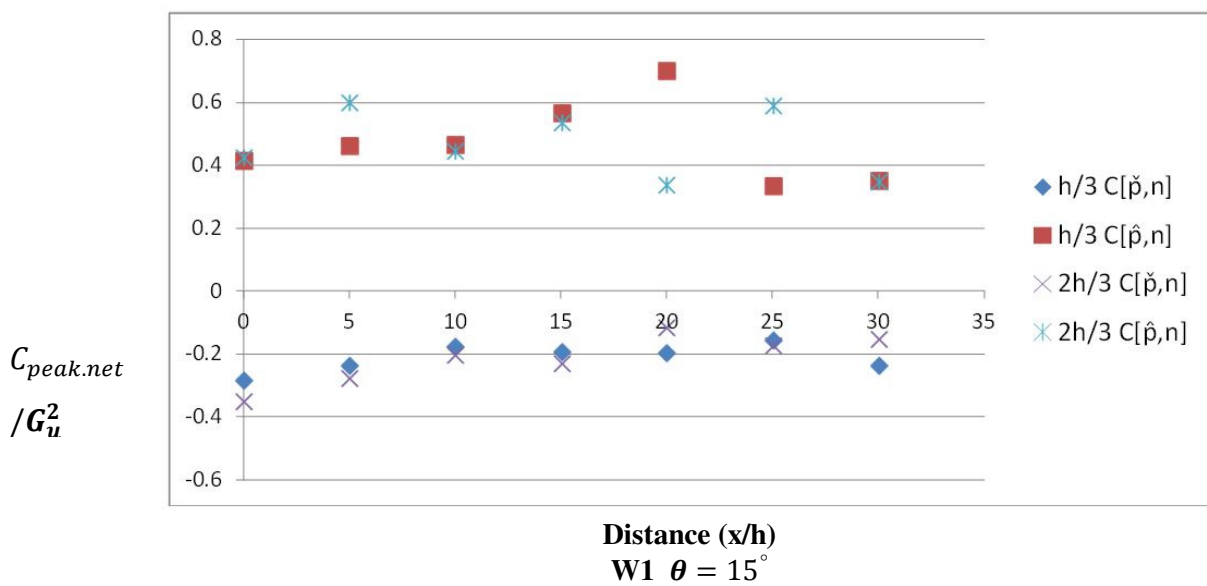
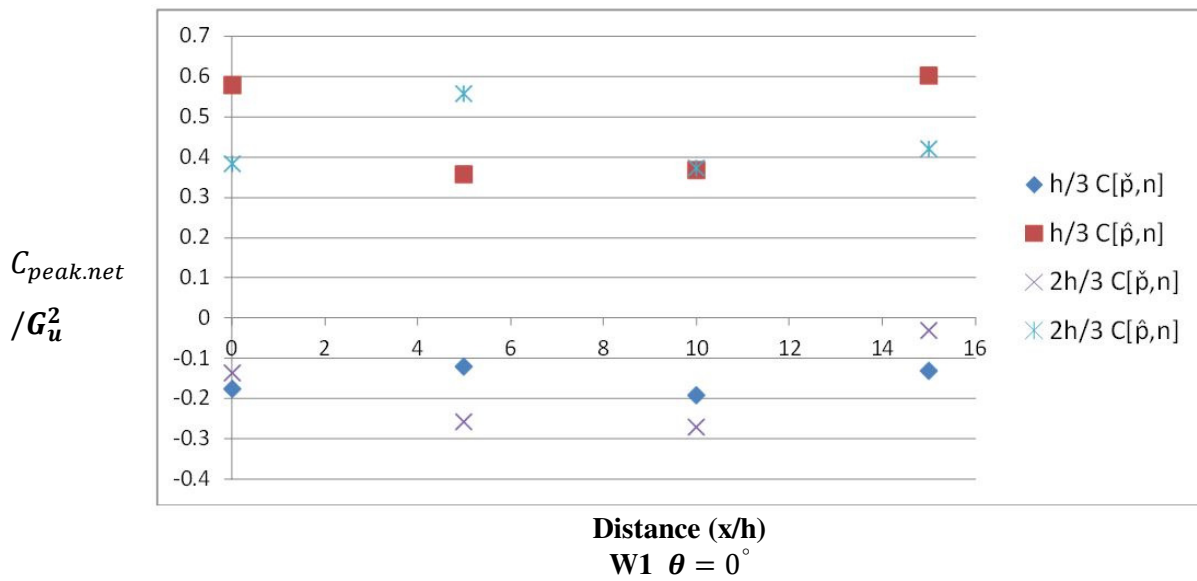
Note: for presentation purposes:

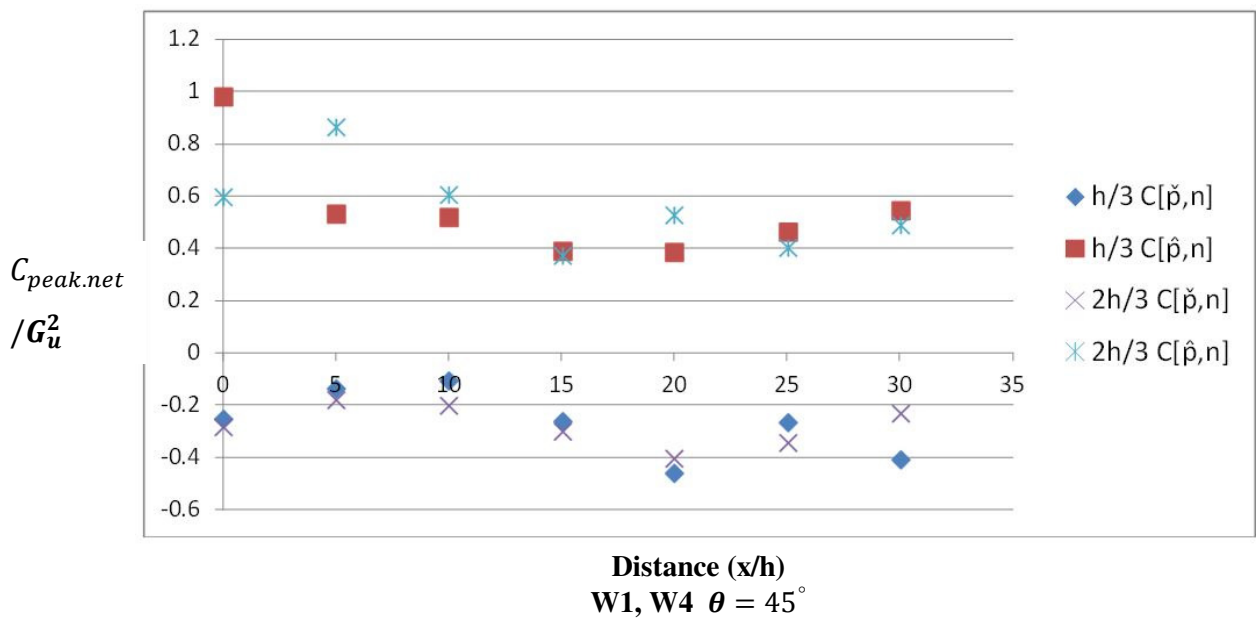
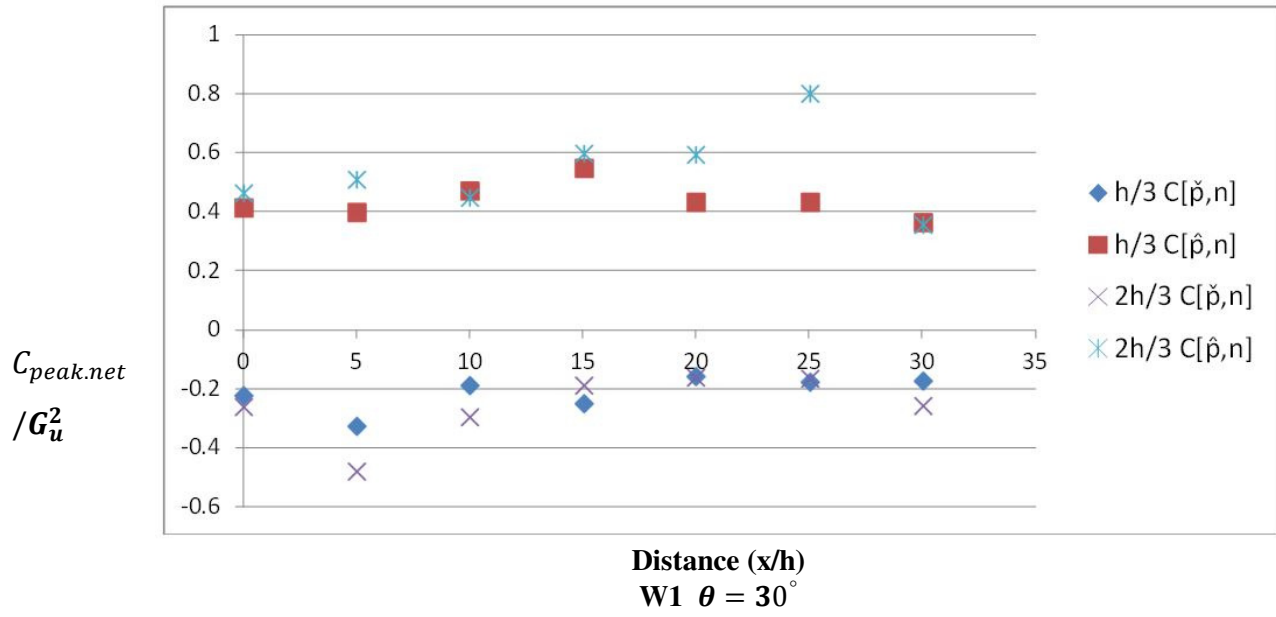
$$C_{peak.net}/G_u^2 \text{ maximum} = C[\hat{p},n]$$

$$C_{peak.net}/G_u^2 \text{ minimum} = C[\check{p},n]$$

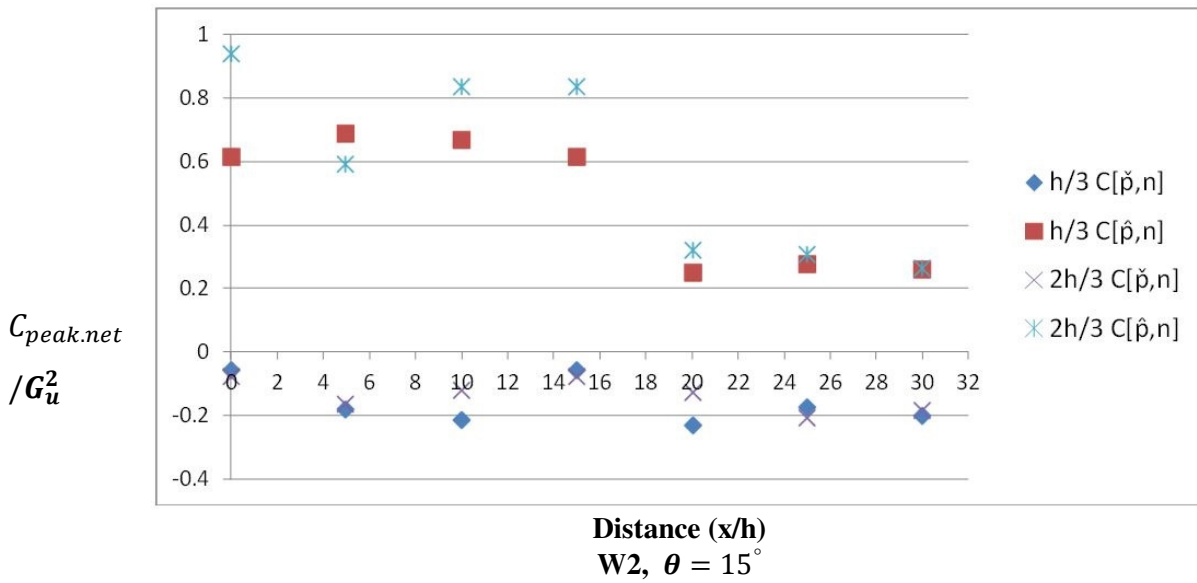
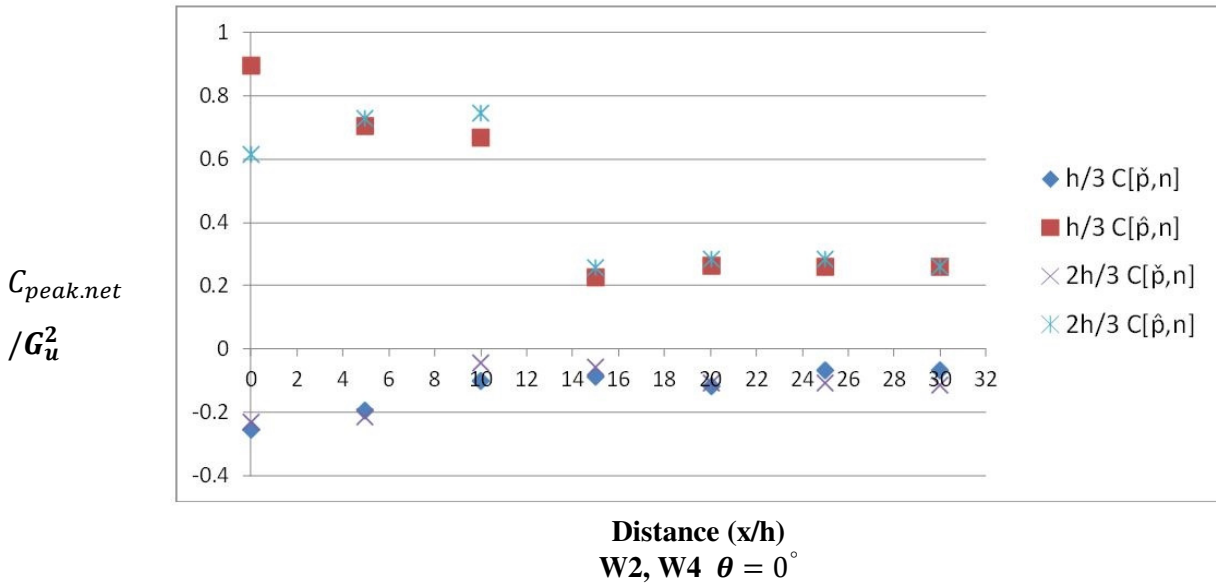
A4.1 Model B. (19% Porous)

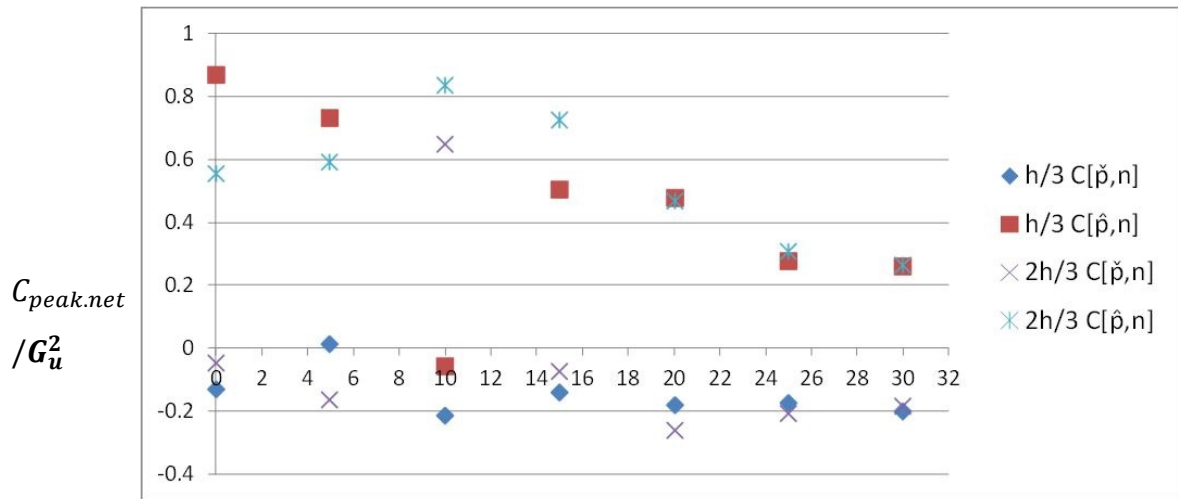
Windward Wall W1, $C_{peak.net}/G_u^2$, $\theta = 0^\circ, 15^\circ, 30^\circ, 45^\circ$



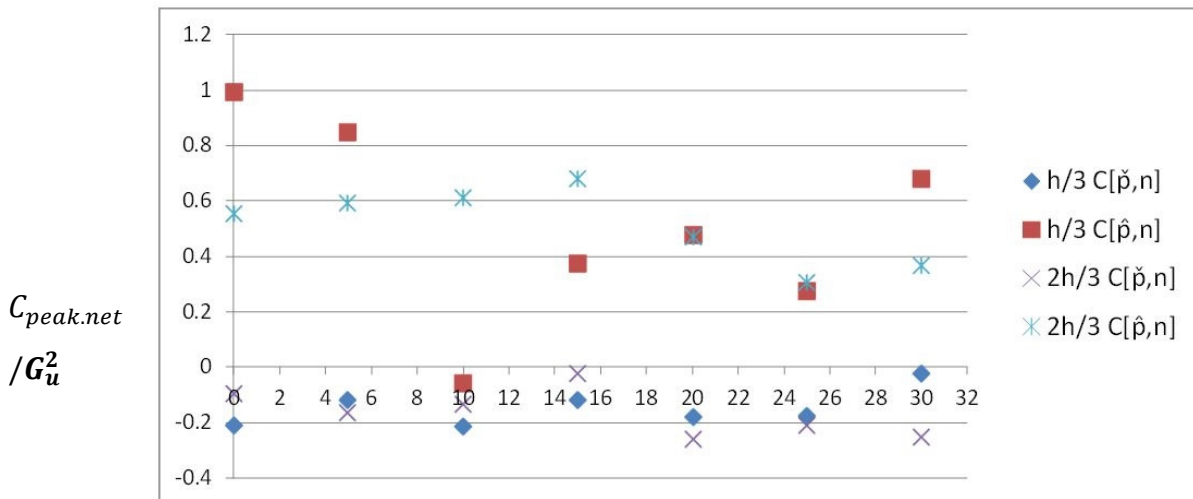


A4.2 Model B Side Walls W2, $C_{peak.net}/G_u^2$, 0° , 15° , 30° , 45° Wind Directions



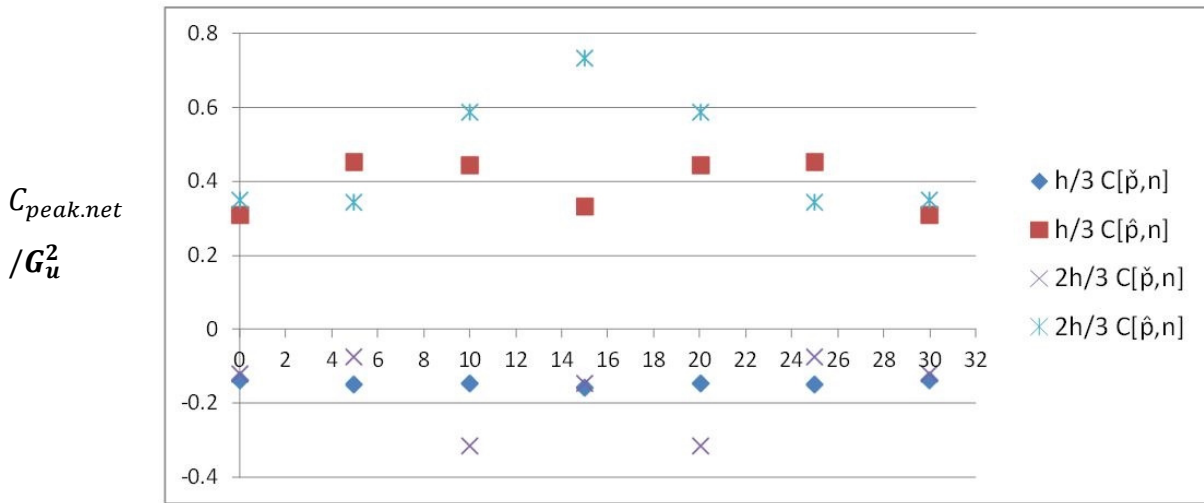


Distance (x/h)
W2, $\theta = 30^\circ$

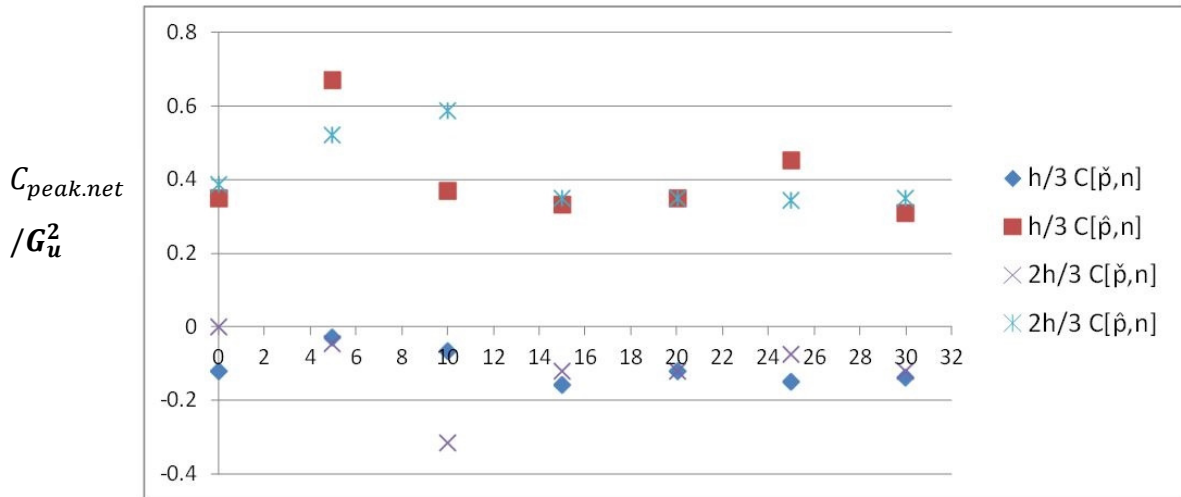


Distance (x/h)
W2, W3 $\theta = 45^\circ$

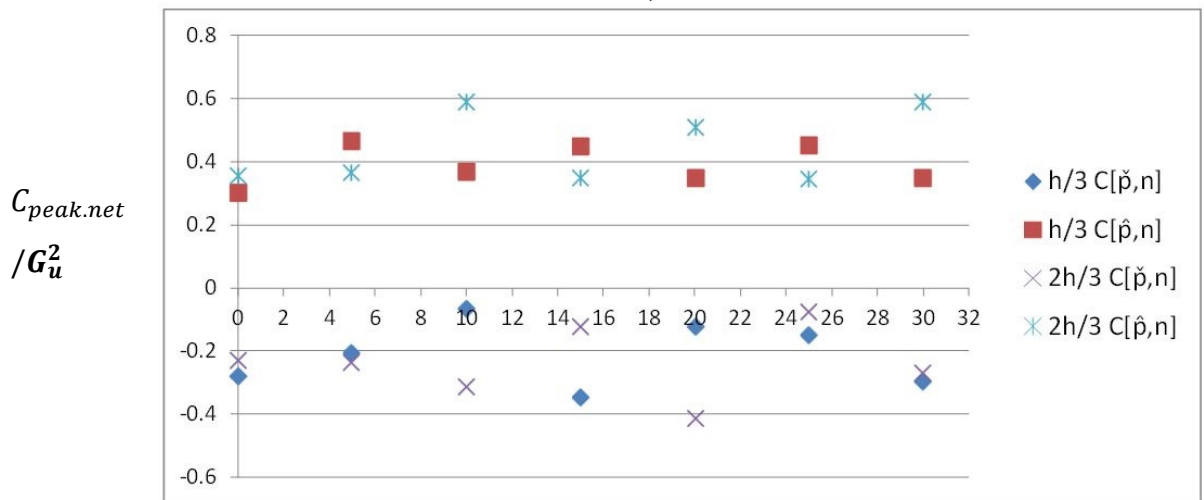
A4.3 Model B Wall W3, $C_{peak.net}/G_u^2$, $\theta = 0^\circ, 15^\circ, 30^\circ$



Distance (x/h)
W3, $\theta = 0^\circ$

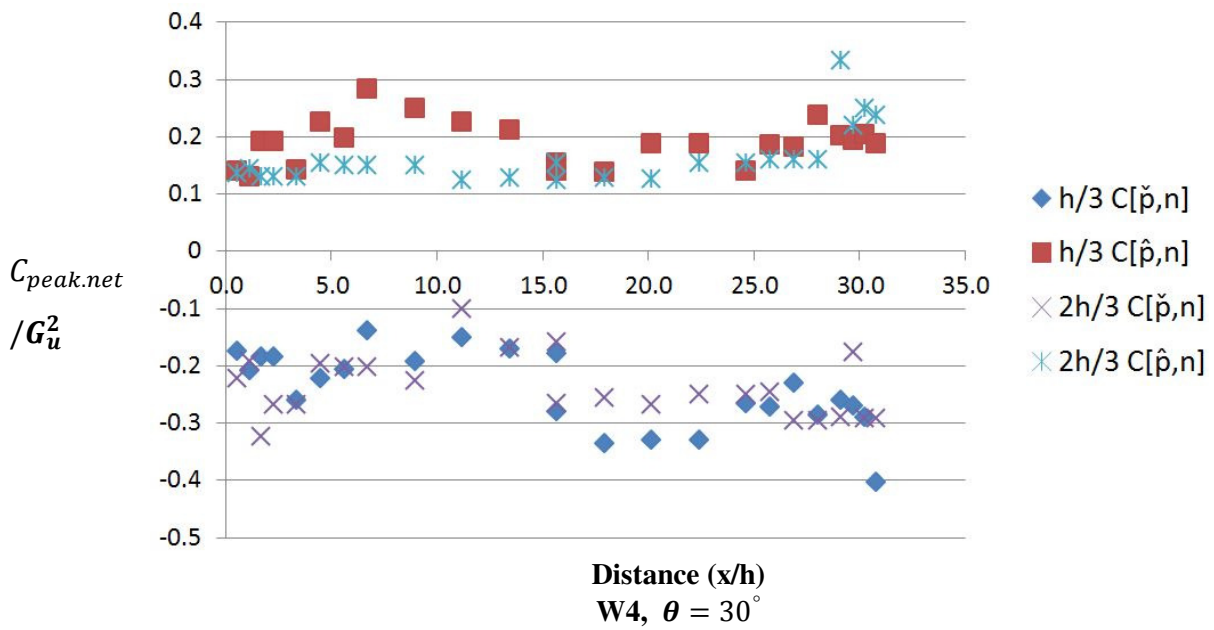
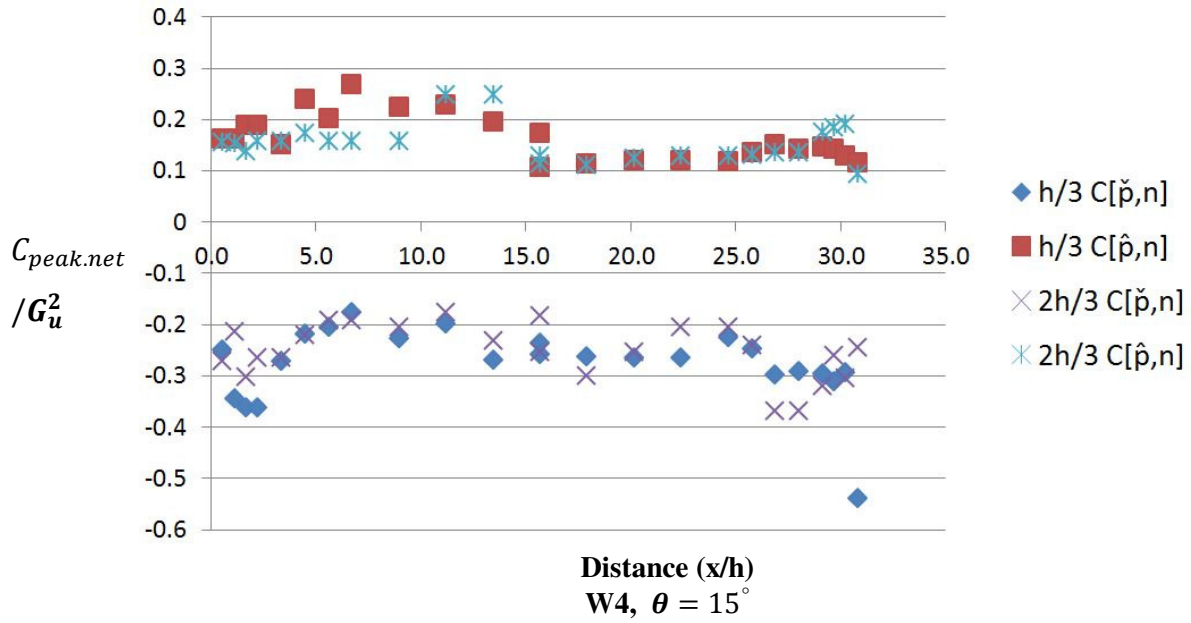


Distance (x/h)
W3, $\theta = 15^\circ$



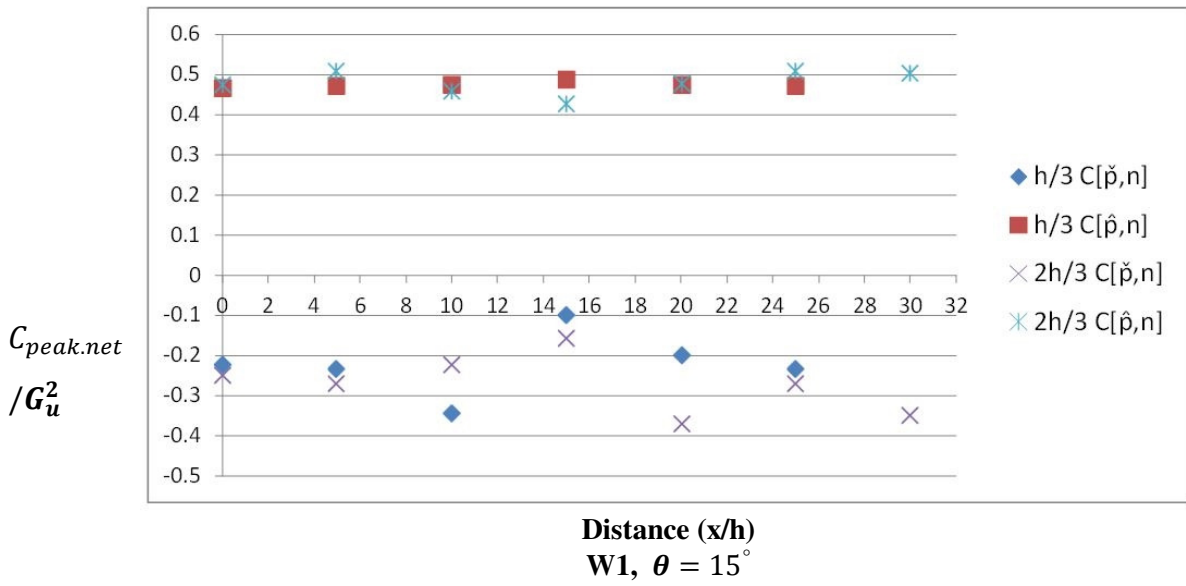
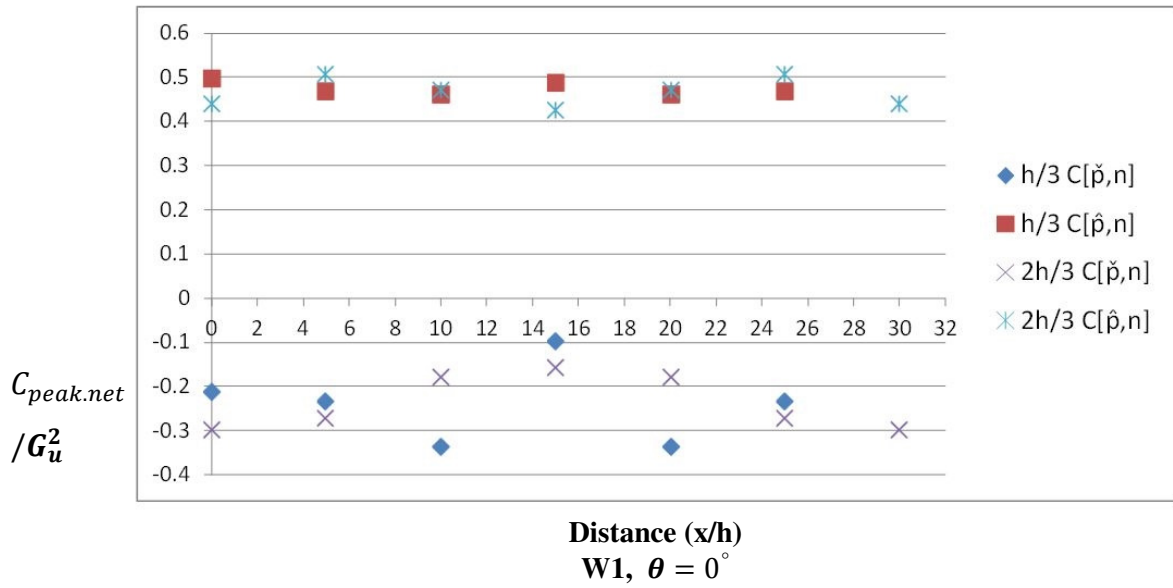
Distance (x/h)
W3, $\theta = 30^\circ$

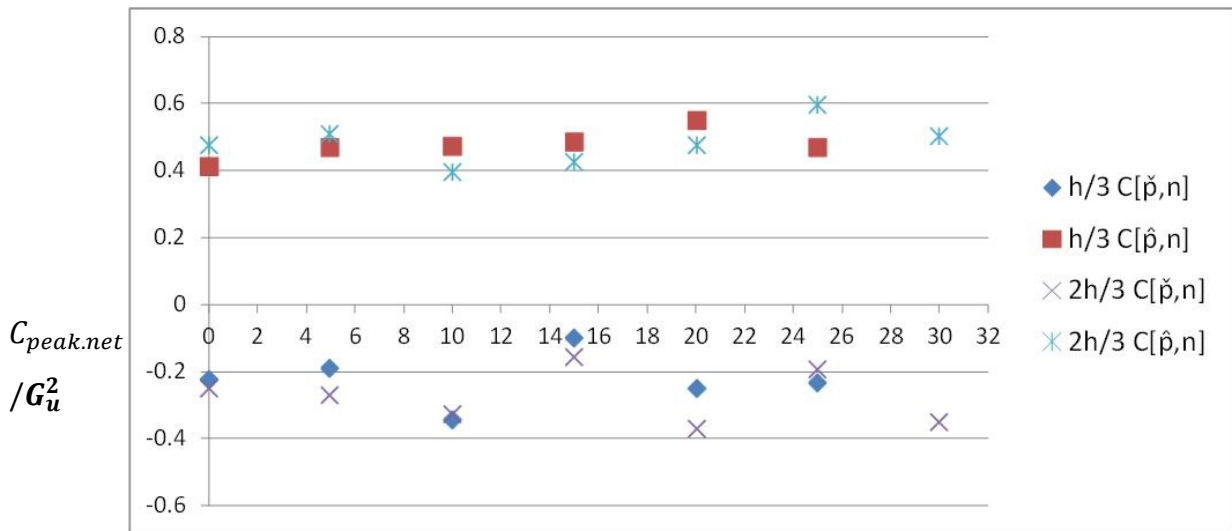
A4.4 Model B Wall W4, $C_{[p,n]}$, $\theta = 15^\circ, 30^\circ$



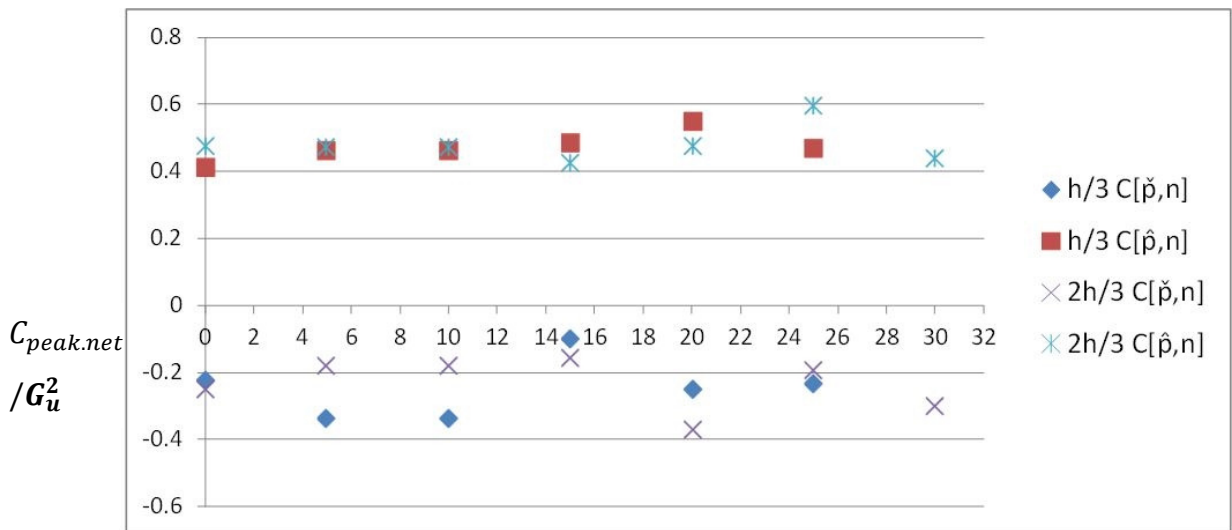
A5 Model C, (38°, Porous)

A5.1 Windward Wall W1, $C_{peak.net}/G_u^2$, $\theta = 0^\circ, 15^\circ, 30^\circ, 45^\circ$



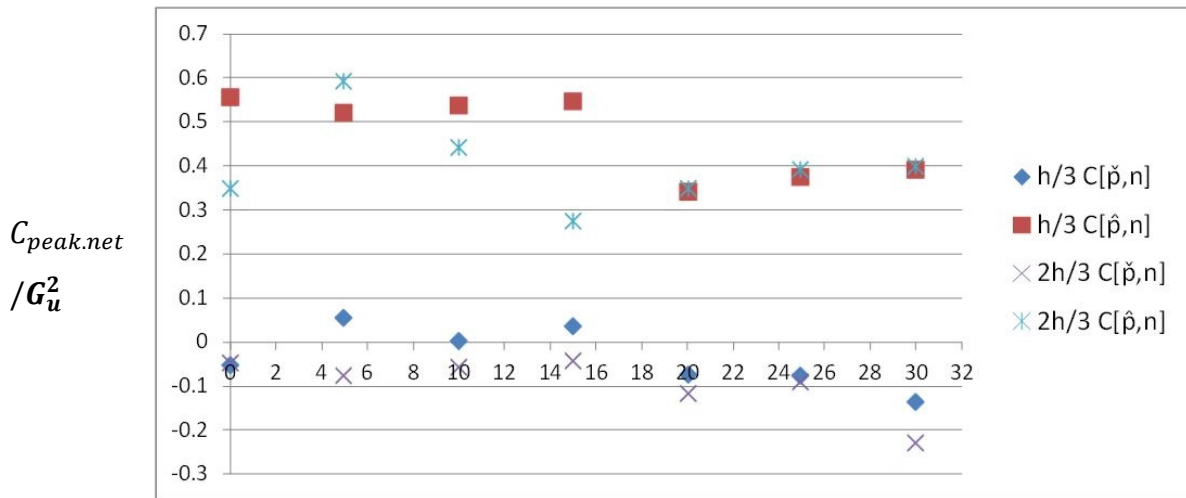


Distance (x/h)
W1, $\theta = 30^\circ$

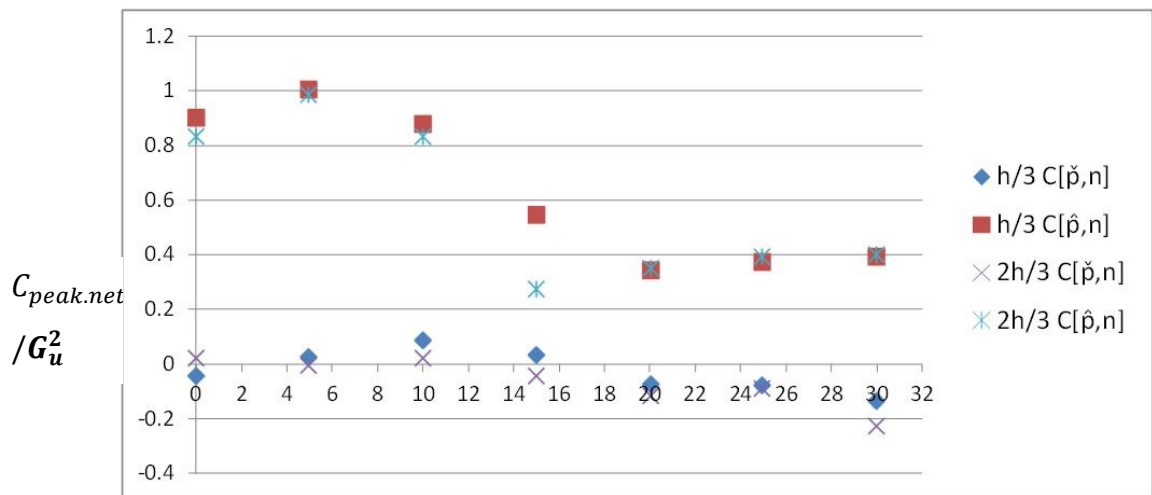


Distance (x/h)
W1,W4, $\theta = 45^\circ$

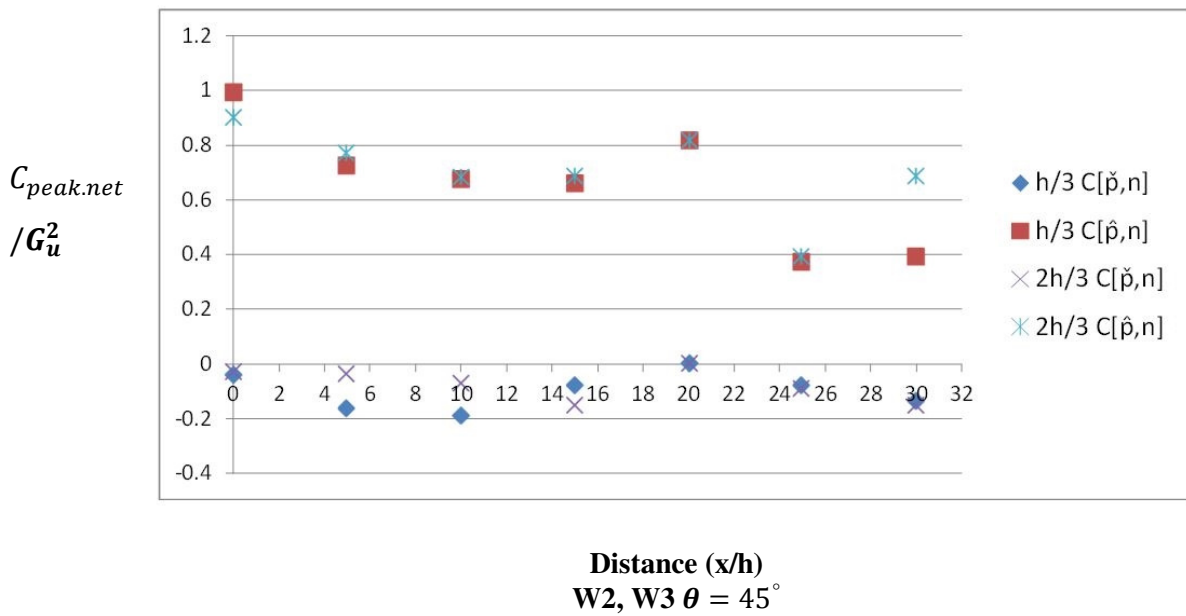
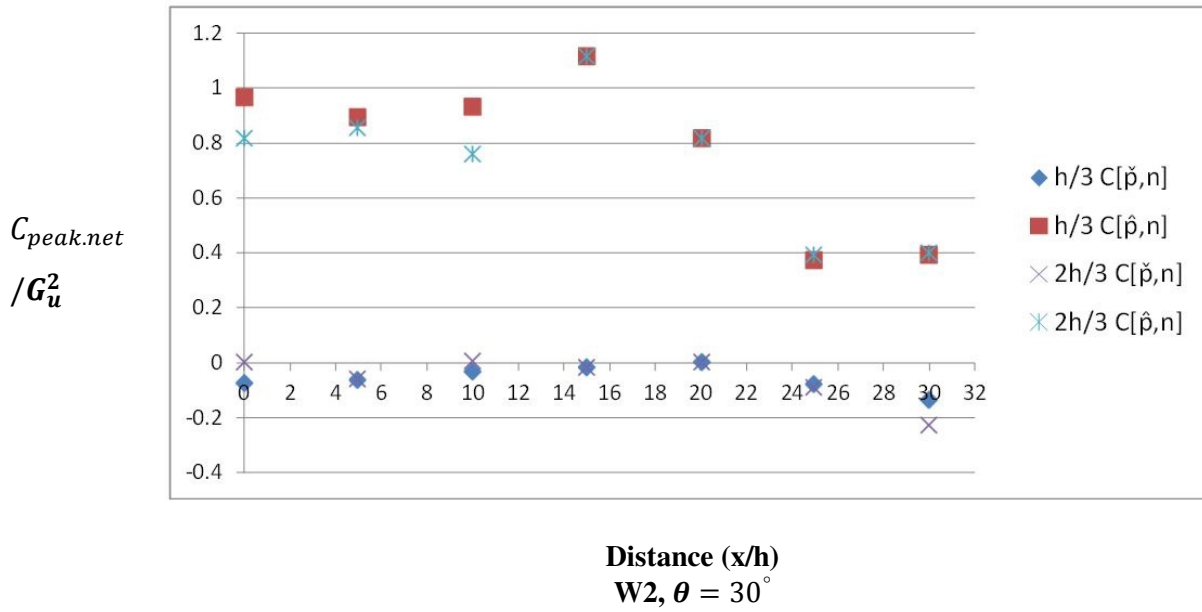
A5.2 Side Wall W2, $C_{peak.net}/G_u^2$, $\theta = 0^\circ, 15^\circ, 30^\circ, 45^\circ$



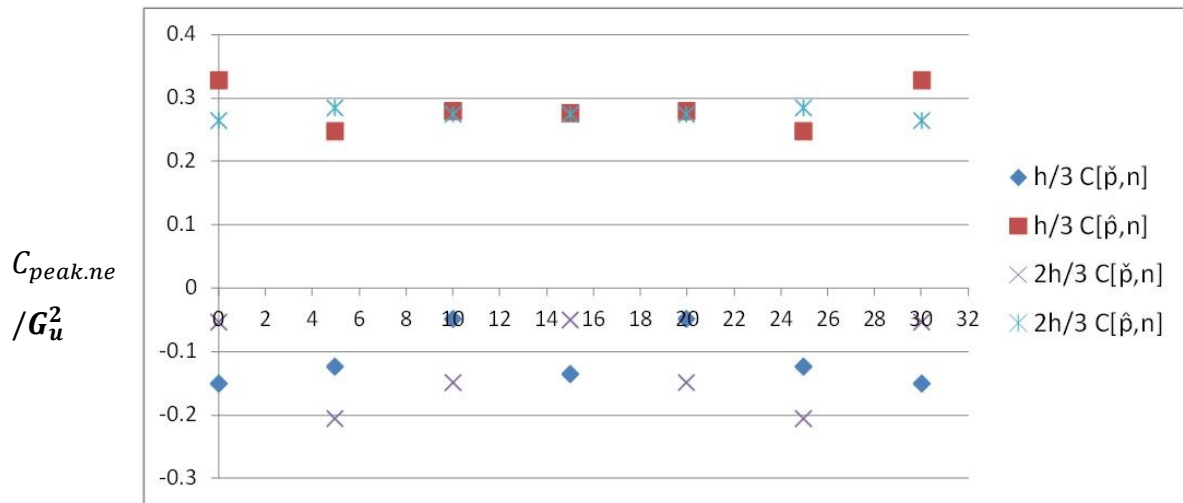
**Distance (x/h)
W2, W4 $\theta = 0^\circ$**



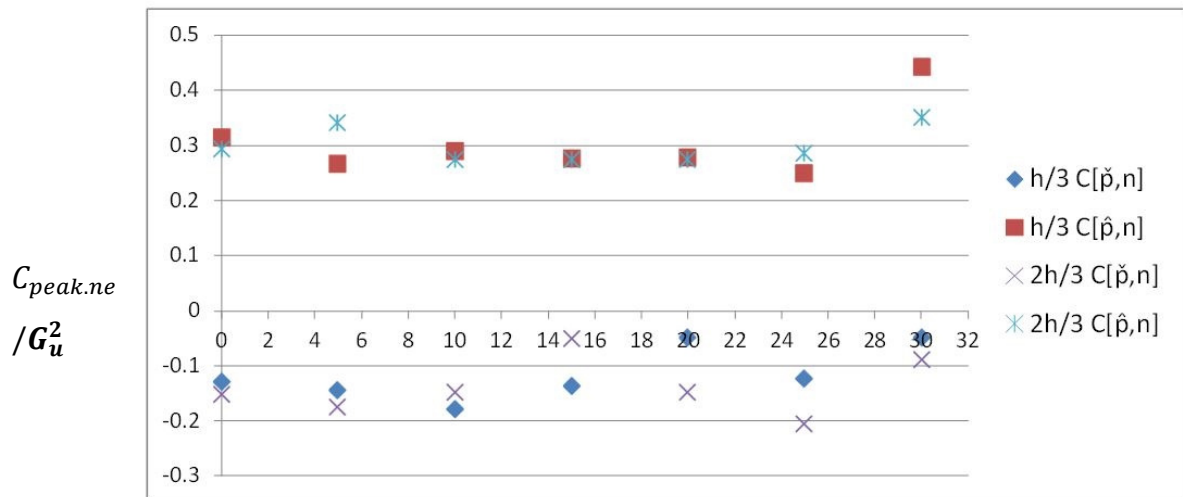
**Distance (x/h)
W2, $\theta = 15^\circ$**



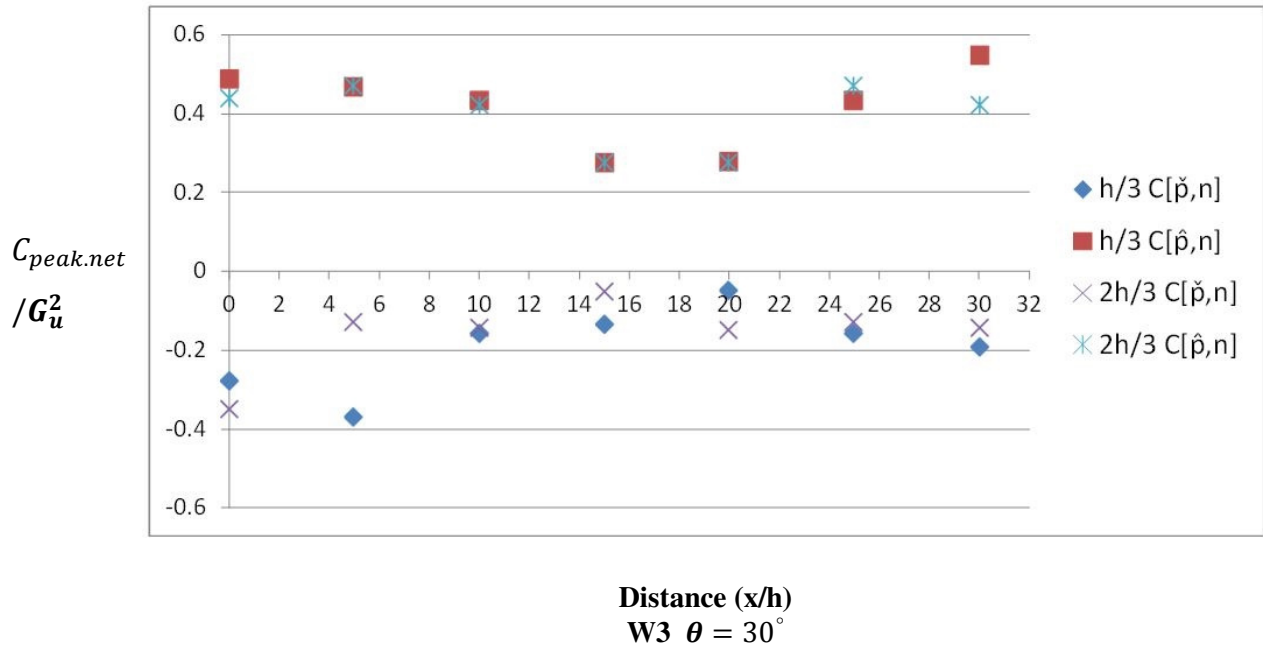
A5.3 Leeward Wall W3, $C_{peak.net}/G_u^2$, $\theta = 0^\circ, 15^\circ, 30^\circ$



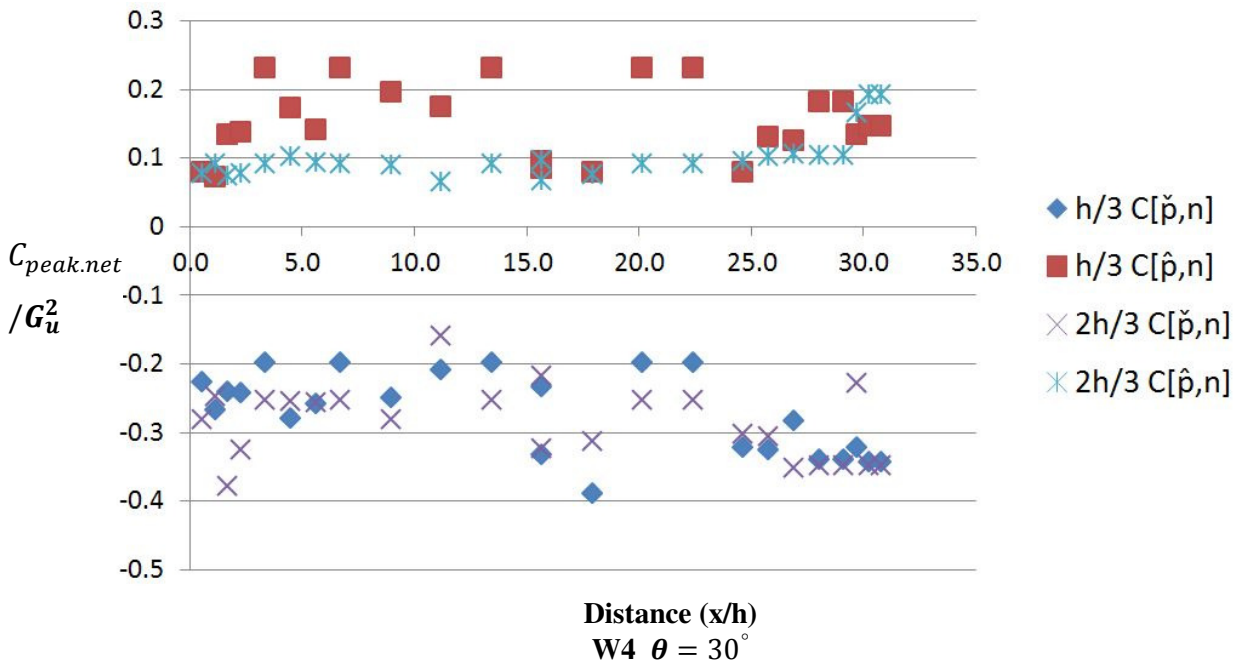
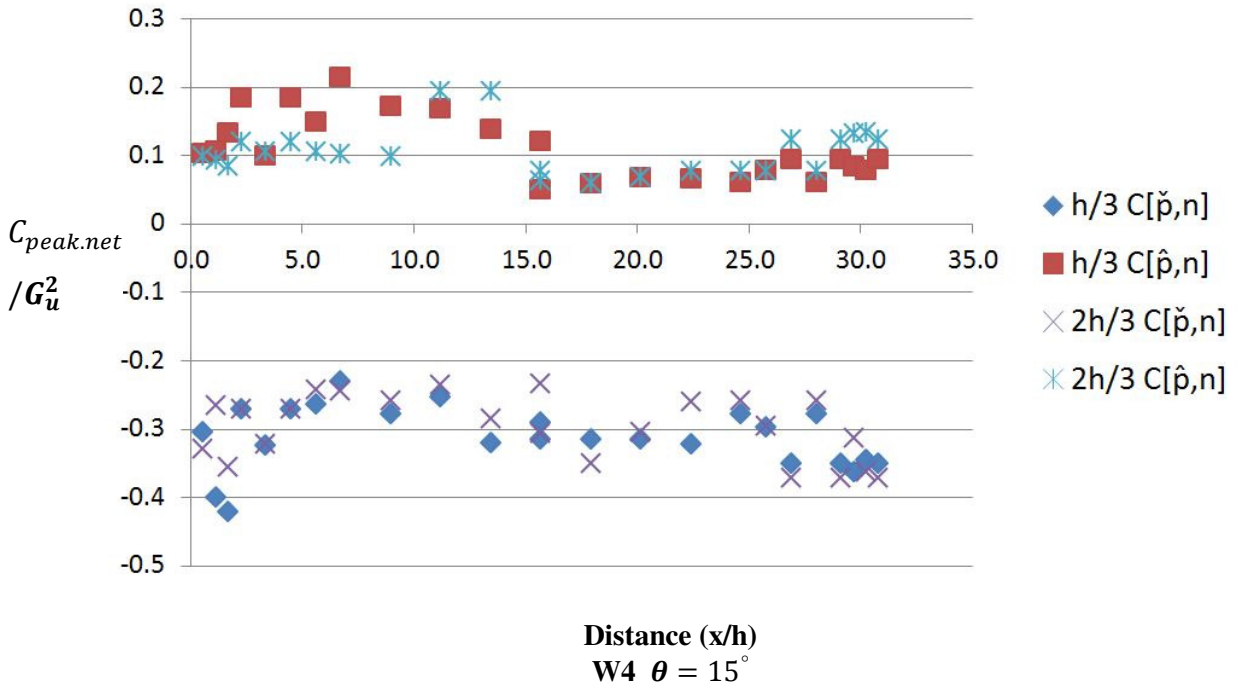
Distance (x/h)
W3 $\theta = 0^\circ$



Distance (x/h)
W3 $\theta = 15^\circ$

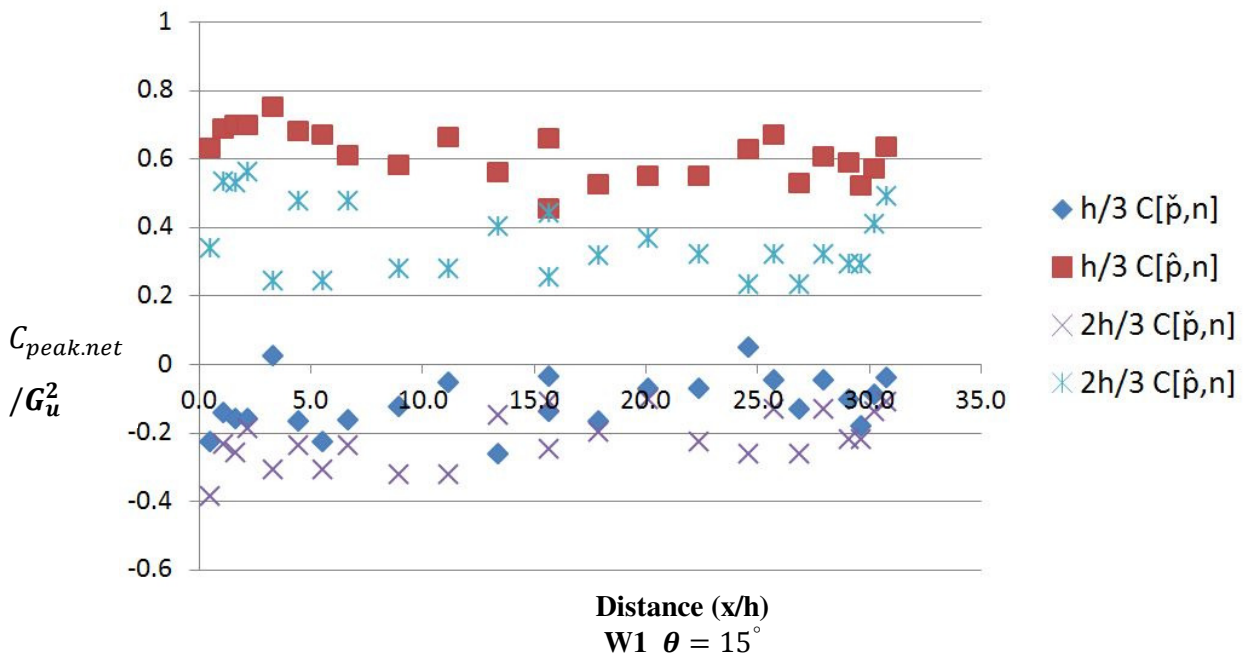
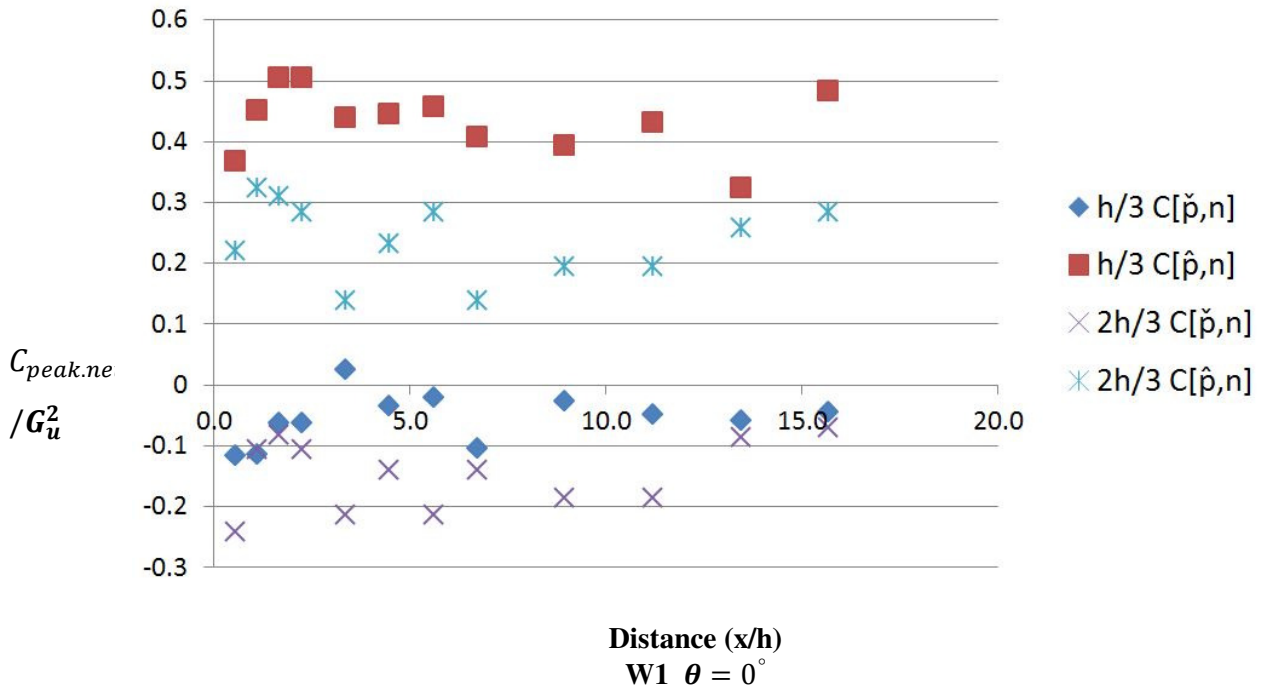


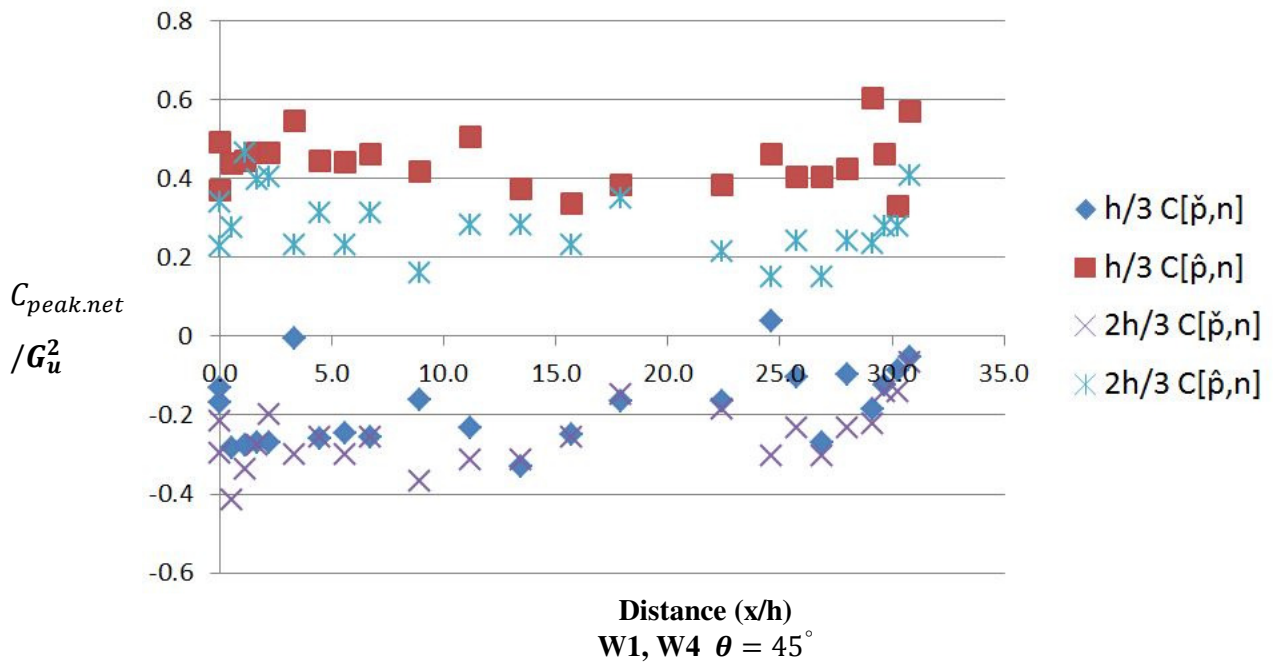
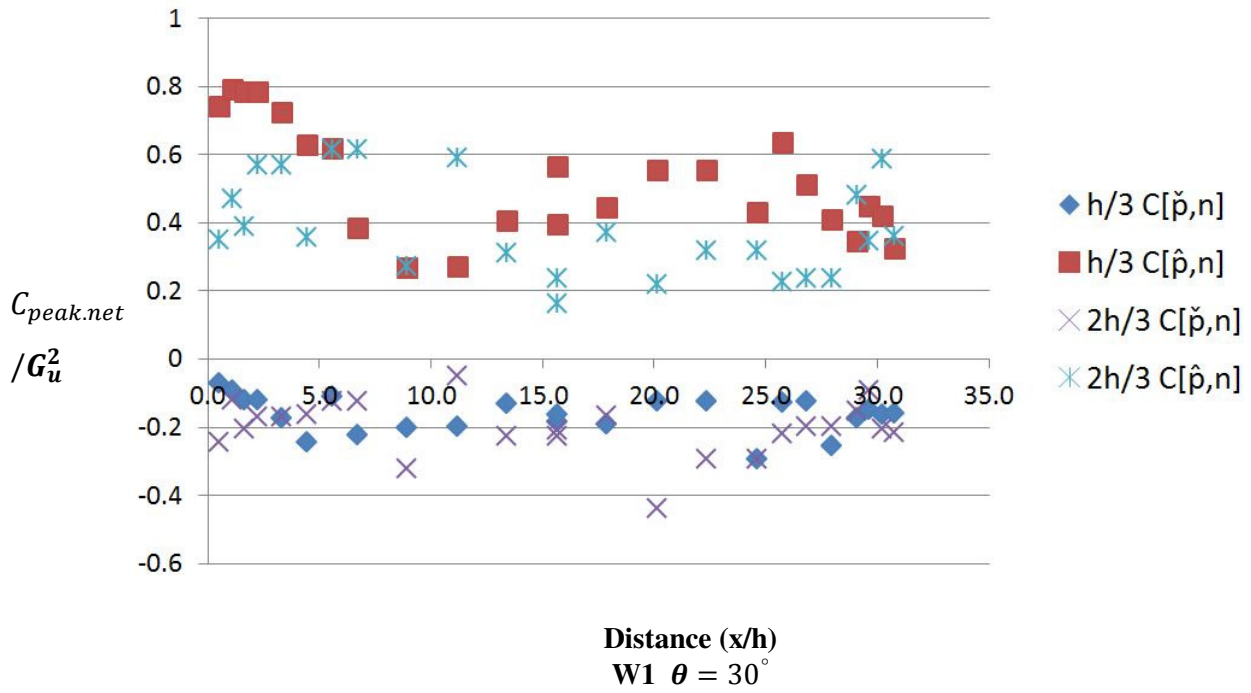
A5.4 Side Wall W4, $C_{peak.net}/G_u^2$, $\theta = 15^\circ, 30^\circ$



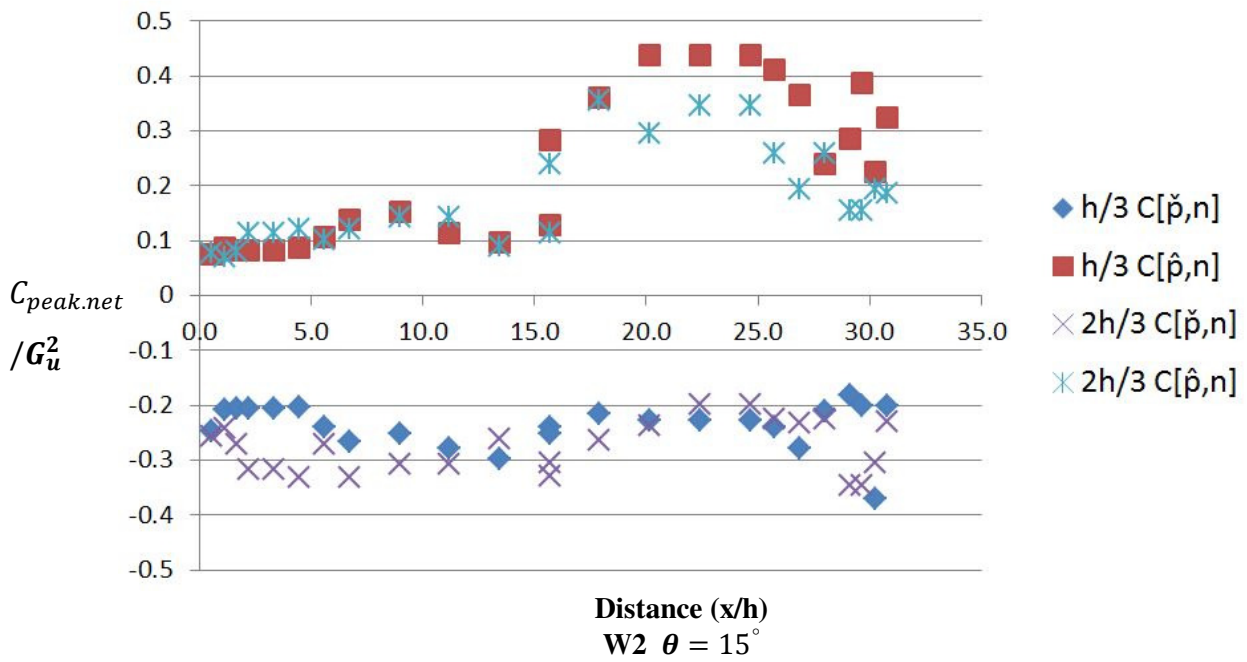
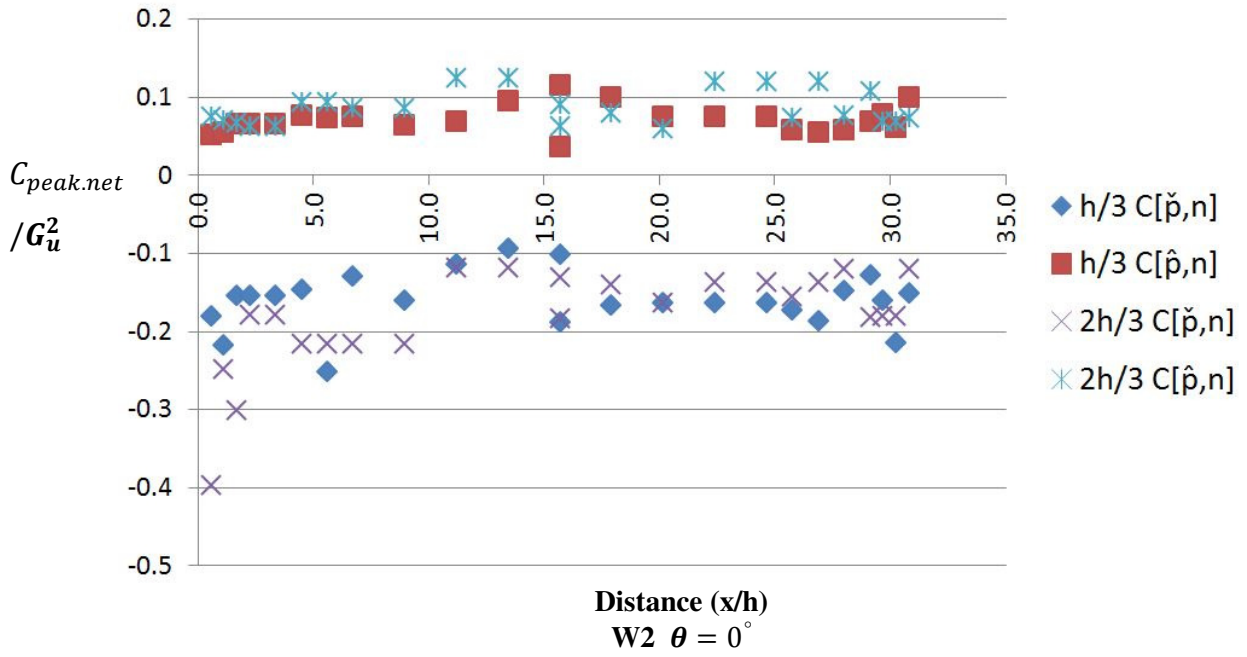
A6 Model D 58% Porous

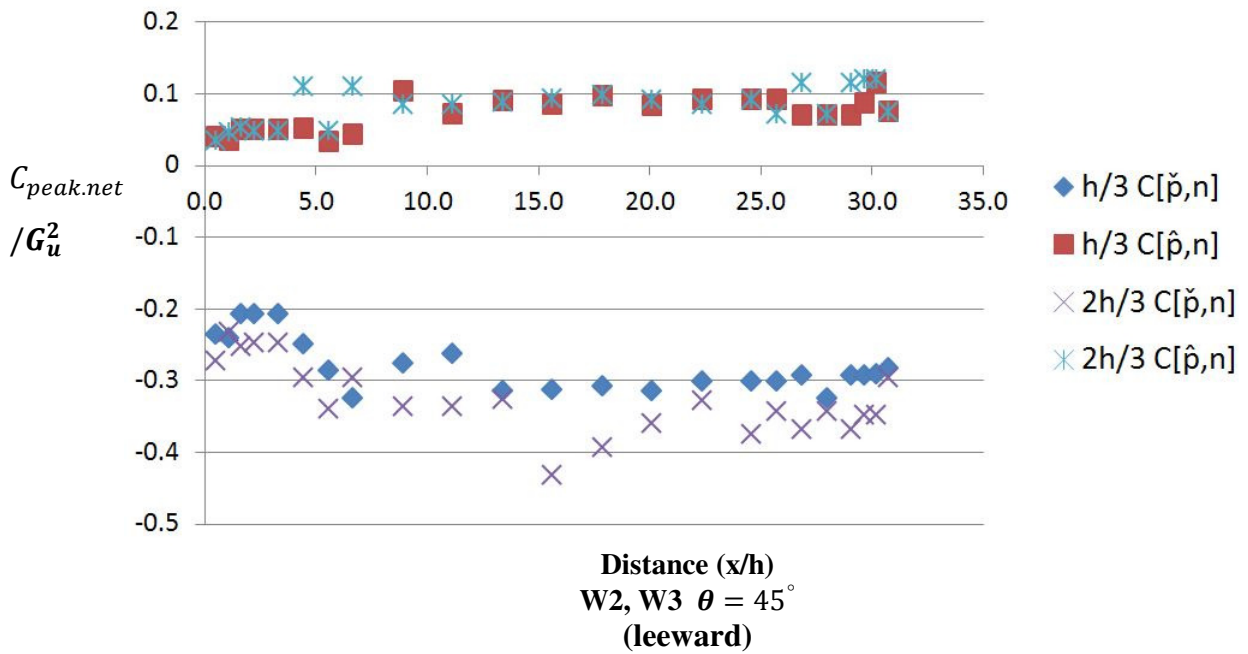
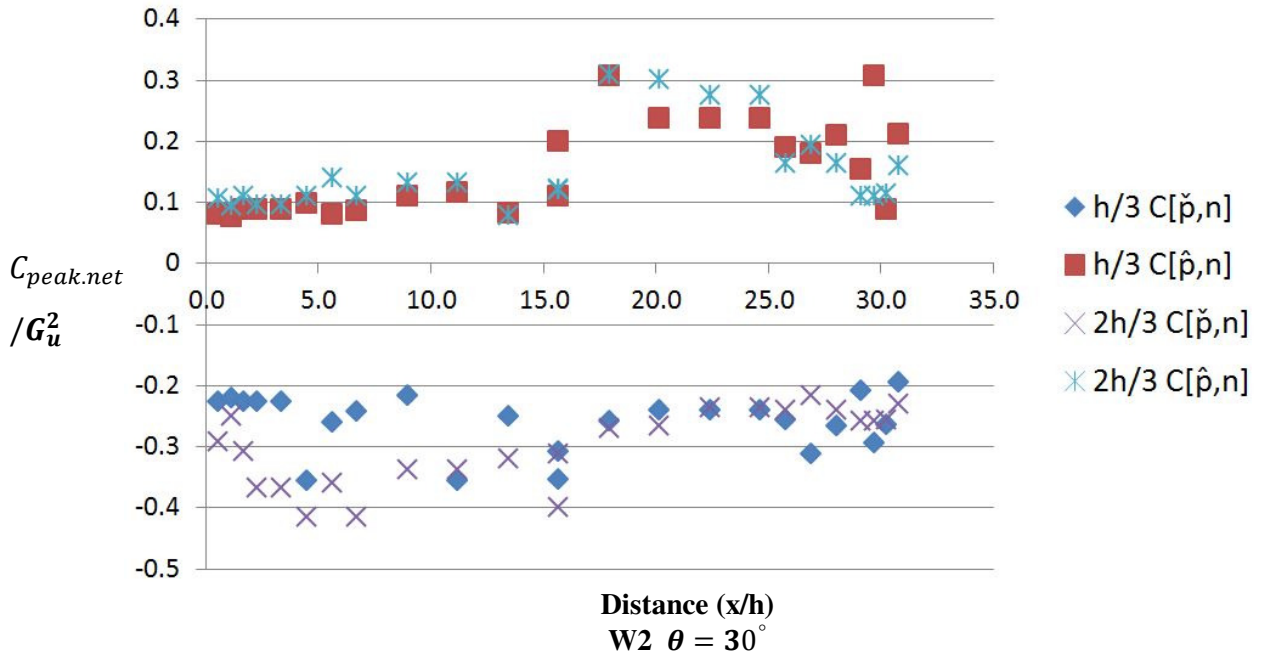
A6.1 Windward Wall W1, $C_{peak.net}/G_u^2$, $\theta = 0^\circ, 15^\circ, 30^\circ, 45^\circ$



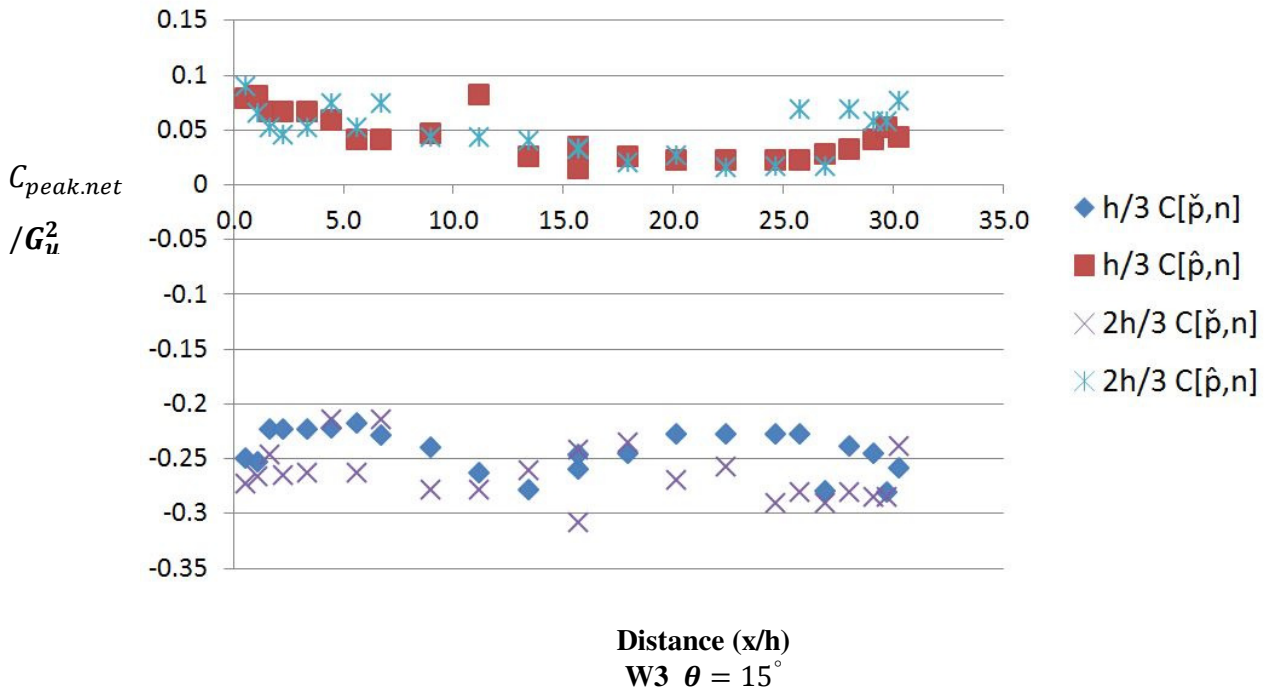
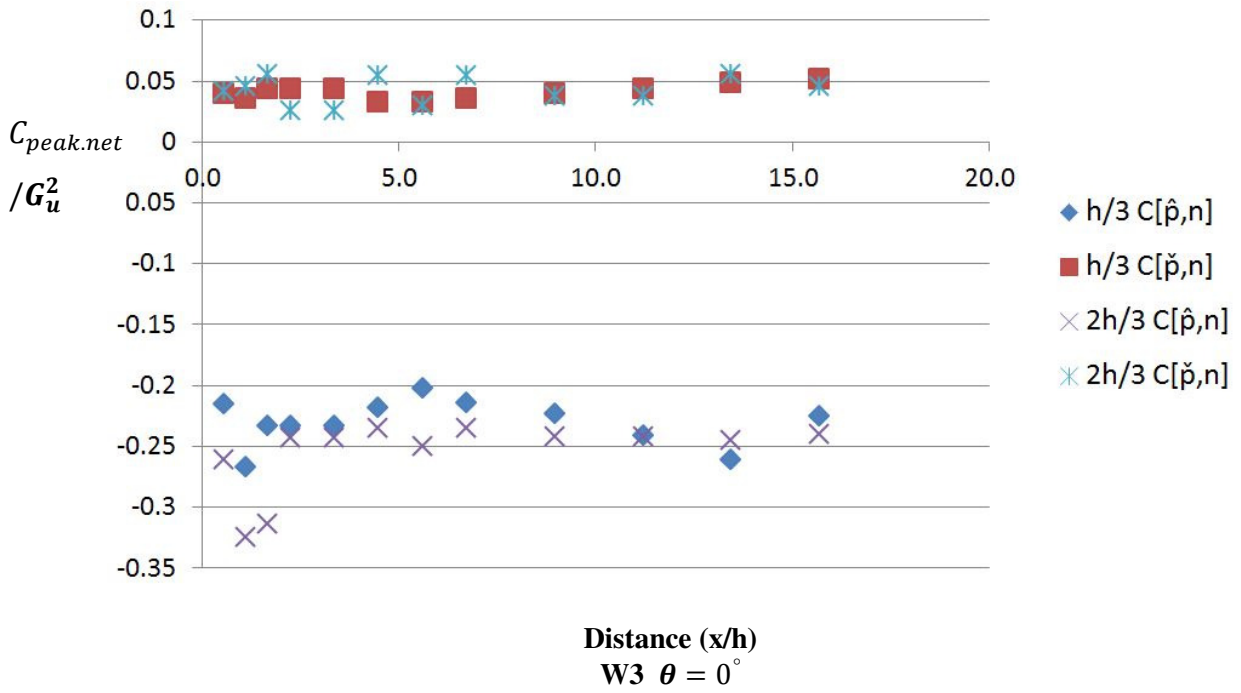


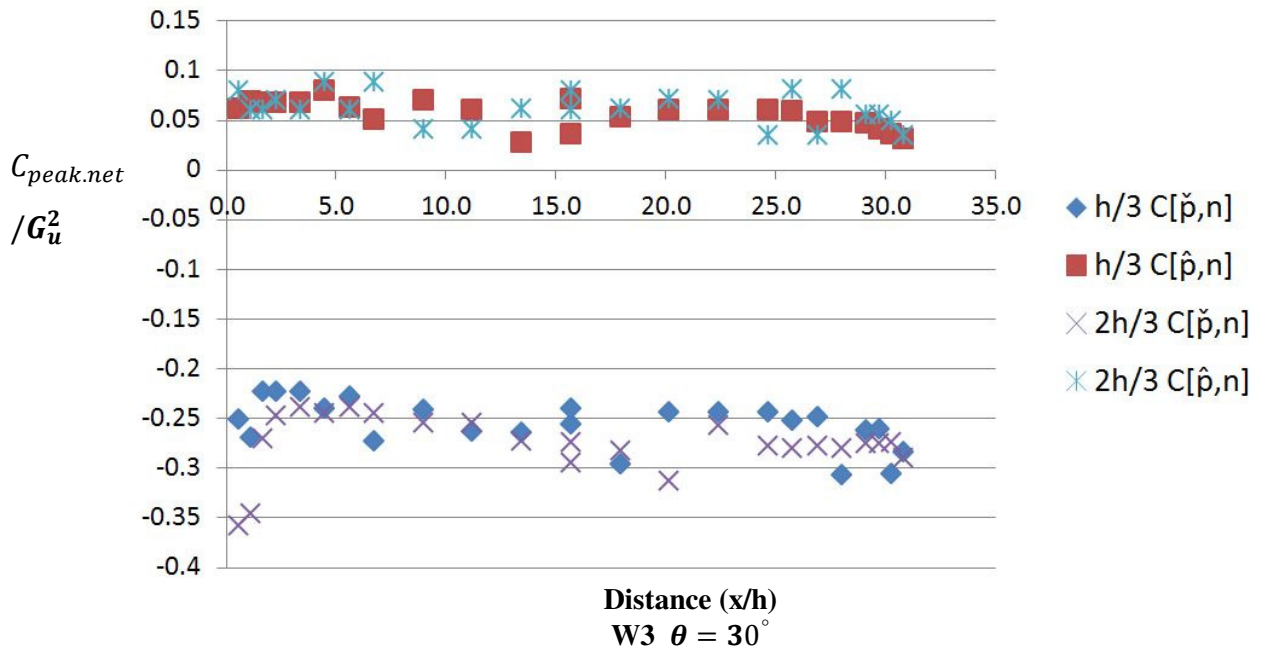
A6.2 Side Wall W2, $C_{peak.net}/G_u^2$, $\theta = 0^\circ, 15^\circ, 30^\circ, 45^\circ$





A6.3 Leeward Wall W3, $C_{peak.net}/G_u^2$, $\theta = 0^\circ, 15^\circ, 30^\circ$





A6.4 Side Wall W4, $C_{peak.net}/G_u^2$, $\theta = 15^\circ, 30^\circ$

